

Mechanistic Studies of Liquid Metal Electrode Solid Oxide Fuel Cells

Aliya Toleuova

A thesis submitted to University College London
for the degree of Doctor of Philosophy

September 2015

Department of Chemical Engineering
Torrington Place, London, WC1E 7JE



Declaration

I, Aliya Toleuova, confirm that the work presented in this thesis is my own. Where information has been derived from other sources, I confirm that this has been indicated in the thesis.

Signature

September 2015

*Dedicated to my parents, my sister and my loving husband,
who have always believed in me.*

Acknowledgements

Firstly, I would like to thank my supervisor – Dr. Dan Brett for giving me the opportunity to study at UCL and do my PhD. I had a great pleasure working with you, your constant belief in me and support throughout my studies was the driving force for the accomplishment of my research goals. Thanks for your encouragement and kindness not only in my studies, but also in my personal life. I would also like to thank my secondary supervisor – Dr. Paul Shearing for his supervision and guidance, particularly for useful comments during my Transfer Viva that helped me to set the rest of my work.

Secondly, I would like to express my deepest gratitude to the visiting academic at UCL - Dr. Bill Maskell, who is a true inspiration for me. I am so grateful that you have joined this project when I started and have led me through my research journey. My transformation from a chemical technologist to an electrochemical engineer could not be possible without your constant guidance, assistance and valuable experience. I am very thankful for your assistance in development of the electrochemical model and discussion of experimental results, as well as ideas on the Rotating Electrolyte Disc technique. Thank you for all your help.

My sincere thanks go to Dr. Vladimir Yufit for his help and assistance especially at early stages of this project, for constructive and critical view on the work in general and valuable comments on the papers.

Thanks to my sponsor “Center for International Programs”, Government of Republic of Kazakhstan and Nazarbayev University for awarding me BOLASHAK International Scholarship that covered full expenses at UCL.

I especially thank Graeme Smith and Erich Herrmann in the Workshop, Albert Corredera in Electronics Department for their professional help, Mike Gorecki and Simon Barrass for assistance with technical and safety aspects in the lab and the office. Thanks to Mae, Agata, Katy and Claire for processing of administrative jobs. I would like to thank all my PhD colleagues and postdocs at the Electrochemical Innovation Lab for their help and general support in the lab, particularly to Mithila, Jason, Toby, Tom and Ishanka. Special thanks to my office neighbours Amal, Lawrence, Mayowa, Quentin, Phil, Rhod and Chaoran for all the lovely moments we had together. I would also like to thank my friends in London – Assiya and Saule for wonderful time spent outside UCL, for sightseeing of London, for inspirational talks and discussions and many more. Thanks to all my friends back in Kazakhstan, in particular to Gulsamal who has encouraged and supported me throughout.

Finally, and above all, I would like to thank my parents, my sister for their love, support and prayers. Thank you for insisting on doing this PhD degree and encouraging me to believe in my dream, to be hard-working, persistent and strong in any situation. I cannot express my unfailing love and gratitude to my loving husband. I am so grateful that I met you during my PhD; my life without you would not be complete. Thank you for believing in me!

Abstract

Liquid metal electrode solid oxide fuel cells (LME SOFC) offer the advantage of high efficiency with the benefits of multi-fuel operation, the concept being particularly well-suited to the direct use of solid fuel. With respect to reported uncertainties in performance limitations of SOFCs with liquid metal anodes (LMA), in-depth understanding of the fuel oxidation mechanisms and transport processes within liquid metal electrodes is needed.

This study provides improved understanding of the operation of LME SOFCs using novel experimental and modelling approaches. H₂ oxidation in LMA SOFC in a specific potential range was chosen as the model system. A classification setting out four possible mechanisms of oxidation of H₂ is proposed. Two models are developed based upon Electrochemical (*E*) and Chemical-Electrochemical (*CE*) modes of operation of H₂-LMA SOFC under conditions that eliminate the detrimental effects of metal oxide layer formation at the electrolyte-electrode interface.

The *E* mode model of operation was found to be inconsistent with literature knowledge of H₂ solubility in liquid tin. A possible explanation considered is the generation of metallic foam effectively 'storing' hydrogen within its matrix, but this was not observed experimentally. Thus mode *E* (direct anodic oxidation of hydrogen in LMA SOFC) is not applicable to this system.

A major contribution of this work is the development and validation of a model for the *CE* mode. This is based upon fast dissolution of hydrogen in a molten tin anode, rate-determining homogeneous reaction of hydrogen with oxygen dissolved in the liquid tin, followed by anodic oxygen injection under diffusion control to replace the oxygen removed by chemical reaction. A new key parameter, related to the Damkohler number, termed the dynamic oxygen utilisation coefficient, (\bar{z}), evolved out of the model; its value is determined by geometric, mass-transport and kinetic factors in the cell, as well as the partial pressure of the supplied hydrogen fuel. Current output of the cell is proportional to the value of \bar{z} . This parameter is expected to have important implications regarding the design, development and commercialisation of the technology.

Additional validation of the *CE* mode model included development and application of a method named anodic injection coulometry (with similarities to anodic stripping voltammetry) for determination of the parameter \bar{z} , as well as measurement of the oxygen solubility in liquid tin. Feeding H₂ at 16 kPa partial pressure into the LME SOFC resulted in a \bar{z} value of 0.83 under the chosen conditions. This is consistent with a separate

estimate in this study using an unrelated method. The solubility of oxygen at 780 °C was found to be 0.10 at.%, which is comparable to literature values.

The possibility of application of the liquid metal electrode/ YSZ system for water electrolysis in solid oxide electrolysers (SOE) is explored. An electrochemical model is presented for interpretation of generated experimental results.

Application of a glassy carbon rod as a low-cost current collector dipping into the liquid tin electrode was successfully pioneered in this work; it showed stable operation without corrosion throughout the whole project at the chosen operating temperature of 780 °C.

A novel rotating electrolyte disc (RED) apparatus is proposed, which is an inverted arrangement of the well-known rotating disc electrode (RDE). The RED offers the prospect of measuring transport properties of active species within a liquid metal electrode. Initial studies towards the development of this technique have been undertaken.

List of Publications

Peer-reviewed journal papers:

1. A. Toleuova, V. Yufit, S. Simons, W. C. Maskell, and D. J. L. Brett, “A Review of Liquid Metal Electrode Solid Oxide Fuel Cells”, *J. Electrochem. Sci. Eng*, **3**, 91–105 (2013).
2. A. Toleuova, W. C. Maskell, V. Yufit, P. R. Shearing, and D. J. Brett, “Mechanistic Studies of Liquid Metal Anode SOFCs I. Oxidation of Hydrogen in Chemical - Electrochemical Mode”, *J. Electrochem. Soc.*, **162**, F988–F999 (2015).
3. A. Toleuova, W. C. Maskell, V. Yufit, P. R. Shearing, and D. J. Brett , “Mechanistic Studies of Liquid Metal Anode SOFCs II. Validation of Chemical-Electrochemical Mechanism and Determination of Oxygen Solubility using Anodic Injection Coulometry” (*submitted for publication*).

Peer-reviewed conference papers:

1. A. Toleuova, V. Yufit, S. J. R. Simons, W. C. Maskell, and D. J. L. Brett, “Rotating Electrolyte Disc (RED) for Operation in Liquid Metal Anode SOFCs”, *ECS Trans.*, **58**, 65 (2013).
2. A. Toleuova, W. C. Maskell, V. Yufit, P. R. Shearing, and D. J. Brett “Mechanistic Considerations of Liquid Metal Anode SOFCs Fuelled with Hydrogen”, *ECS Trans.*, **XX**, XX (2015) (*accepted for publication*).

Presentations:

1. 6th European Summer School on Electrochemical Engineering (2012), Zagreb, Croatia – Poster: “Studies Relating to Solid Oxide Fuel Cells with Liquid Metal Electrodes”.
2. 224th Electrochemical Society Meeting, (2013), San Francisco, USA - Presentation: “A Rotating Electrolyte Disc (RED) for Operation in Liquid Metal Anode SOFCs”.
3. H2FC Supergen conference (2013), Birmingham, UK, Poster: “A Rotating Electrolyte Disc for Operation in Liquid Metal Anode SOFCs”.
4. ECS Conference on Electrochemical Conversion and Storage with SOFC-XIV (2015), Glasgow, UK, Presentation: “Mechanistic Considerations of Liquid Metal Anode SOFCs Fuelled with Hydrogen”.

Table of Contents

Declaration	ii
Acknowledgements	iv
Abstract.....	v
List of Publications	vii
Table of Contents	viii
List of Tables.....	x
List of Figures	xi
1. Introduction	1
1.1. Research Aims.....	3
1.2. Thesis outline	3
2. Literature Review	6
2.1. Fuel Cells.....	7
2.2. Solid Oxide Fuel Cells.....	10
2.3. Liquid Metal Electrode Electrochemical Systems	25
2.4. Conclusions	45
3. Experimental methods and equipment	46
3.1. Experimental workstation	47
3.2. Electrochemical cell	50
3.3. Methodology	55
3.4. Experimental Methods: electrochemical techniques	56
3.5. Conclusions	60
4. Preliminary testing	62
4.1. Introduction	63
4.2. Background.....	63
4.3. Experimental procedure	65
4.4. Results and discussion	65
4.5. Conclusions	72
5. Experimental optimisation	74
5.1. Introduction	75
5.2. Background.....	75
5.3. Experimental procedure	78
5.4. Results and discussion	82
5.5. Conclusion.....	89
6. Proposed mechanisms for oxidation of hydrogen in LMA SOFCs.....	91
6.1. Introduction	92
6.2. Classification of modes of operation for H ₂ -LMA SOFCs.....	93
6.3. Thermodynamics of the modes of operation for LMA SOFCs.....	95
6.4. Experimental procedure	96
6.5. Oxidation of hydrogen in LTA SOFC operated in mode <i>EC1/EC2</i>	96
6.6. Conclusions	98

7. Oxidation of hydrogen in LTA SOFC in mode <i>E/CE</i>	99
7.1. Introduction	100
7.2. Experimental procedure	100
7.3. Oxidation of hydrogen in LTA SOFCs in mode <i>E/CE</i>	101
7.4. Electrochemical model for <i>E</i> mode	104
7.5. Investigation of a possibility of a metal foam in LTA SOFC.....	109
7.6. Electrochemical model for <i>CE</i> mode.....	120
7.7. Conclusion.....	134
8. Additional validation of <i>CE</i> model	135
8.1. Introduction	136
8.2. Background literature concerning oxygen and hydrogen solubilities	136
8.3. Experimental procedure	138
8.4. Results and discussion	138
8.5. Conclusion.....	147
9. Water electrolysis in reverse LME SOFCs	148
9.1. Introduction	149
9.2. Experimental procedure	149
9.3. Results and discussion	151
9.4. Conclusion.....	159
10. Rotating Electrolyte Disc system design and testing	161
10.1. Introduction	162
10.2. Development of the RED set-up.....	164
10.3. The RED modified for aqueous electrochemical systems	167
10.4. Application of RED to LME SOFCs.....	174
10.5. Conclusion.....	178
11. Conclusion and future work	180
11.1. Conclusion.....	180
11.2. Recommendations for future work.....	184
Nomenclature	188
References	193
Appendix	203
A. Electrical furnace temperature profile	203
B. Determination of permeability coefficient for plastic tubing	204
C. Electrochemical model for Anodic Oxidation of Hydrogen in Electrochemical mode	206
Model 1	206
Model 2.....	208
Additional Mechanistic Theory	210
Determination of the apparent solubility of H ₂ in liquid tin and the parameter <i>w'</i> using anodic stripping voltammetry.....	211

List of Tables

Table 2.1 Technical characteristics of five main fuel cell types ²⁵⁻²⁷	9
Table 2.2 Common metals properties and abundances, prices (adapted from Abernathy <i>et al.</i> ⁶)	34
Table 2.3 Thermophysical properties of tin ⁶	34
Table 2.4 Solubility of oxygen in liquid tin ⁷⁹	35
Table 3.1 Description of the parts a fuel cell.	54
Table 4.1 Ohmic resistance values for 6 mol. % YSZ symmetrical cell (Pt electrode area of 1.30 cm ²) with temperature.	70
Table 4.2 Conductivity values of YSZ electrolytes measured and given in the literature. ...	71
Table 5.1 Details of all the tubing employed in experimental work.	80
Table 5.2 Permeability in polymers at 25 °C for oxygen gas ¹²⁸	89
Table 7.1 Reciprocal time constants for various p_2 ' values.	125
Table 8.1 Q_1 values obtained from with 16 kPa $p(H_2)$ for Regime 1 operation.	142
Table 8.2. Q_2 values obtained with 16 kPa $p(H_2)$ for Regime 2 operation.	144
Table 9.1 Saturated water vapour pressure at set temperature values from standard tables.	151
Table 9.2 Q_1 values obtained from with 3.8 kPa $p(H_2O)$ for Regime 1 operation.	153
Table 9.3. Reciprocal time constants for various destination $p(H_2O)$ values.	158
Table 10.1 Comparison of diffusion coefficients for Fe^{2+} and Fe^{3+} ions with literature.	174

List of Figures

Figure 2.1 Individual fuel cell (one example of polymer electrolyte fuel cell).....	7
Figure 2.2 Flow of ions through different fuel cells electrolyte types.	8
Figure 2.3 Schematic view of SOFC operation using hydrogen as a fuel.....	11
Figure 2.4 Schematic of a typical current – voltage or polarisation curve that shows the operating cell voltage with activation, ohmic and concentration potential losses.....	13
Figure 2.5 Schematic view of tubular SOFC ²⁸	16
Figure 2.6 A schematic of cell-to cell connections in a cathode-supported tubular SOFC stack ²⁴	16
Figure 2.7 Schematic of cell configuration in an anode-supported planar SOFC stack ²⁴	17
Figure 2.8 Schematic view of planar SOFC ²⁸	17
Figure 2.9 A schematic of the ‘segmented-in-series’ design adopted by Rolls-Royce ²⁴	17
Figure 2.10 Schematic view of monolith-type SOFC ³³	18
Figure 2.11 Conductivity of yttria- and scandia-stabilised zirconia in air at 1000 °C ⁴⁰	21
Figure 2.12 An idealised Nyquist plot of a zirconia electrochemical cell with electrodes and its equivalent circuit. The three semi-circular arcs correspond to conductivity within the grain, grain boundaries and electrodes, respectively ⁴⁷	22
Figure 2.13 a) LLNL DCFC configuration with carbon particle anode, b) performance of LLNL DCFC ⁴	24
Figure 2.14 Configuration of the SRI direct carbon fuel cell (a), performance of SRI direct carbon fuel cell (b) ⁴	25
Figure 2.15 Operation of liquid metal electrode reactor in fuel cell and electrolyser mode.	25
Figure 2.16 Schematic of solid oxide membrane electrolyser for waste to hydrogen and syngas conversion ⁵³	27
Figure 2.17 Schematic showing operation of LMA SOFC with (a) hydrogen and (b) solid carbon, as the fuel.	28
Figure 2.18 Effect of temperature on standard equilibrium cell potentials for various metal oxidation reactions.	30
Figure 2.19 Ideal Nernst potentials for LTA SOFC for all three reactions ⁶²	32
Figure 2.20 Sn-O phase diagram determined at 1 bar ⁸¹	36
Figure 2.21 Sn-O system phase diagram calculated at 1 bar ⁶	37
Figure 2.22 Power curves for tin based cells operating on hydrogen and JP-8 (a); durability test on JP-8 (V, W) (b) ¹⁷	39

Figure 2.23 (a) Schematic of a LMA SOFC coupled to an external combustion reactor, (b) Schematic of a LMA Solid Oxide Electrolyser (SOE) coupled to an external combustion reactor ⁷⁰	40
Figure 2.24 (a) Schematic of liquid copper anode SOFC, (b) polarisation and power density curves for liquid copper anode SOFC ⁶⁰	42
Figure 3.1 Experimental workstation.	48
Figure 3.2 Schematic of experimental rig used for fuel cell testing.	49
Figure 3.3 Symmetrical cell: (a) 120 mm long 10YSZ cell for potentiometric measurements; (b) 6YSZ symmetrical cell for EIS measurements (front view) and side view (c).....	50
Figure 3.4 The 3D design of the fuel cell (a): closed end YSZ tube with fuel inlet, exhaust and current collector and pyrophyllite holder (b).....	51
Figure 3.5 Updated fuel cell design with YSZ thermocouple placed parallel to the vessel..	52
Figure 3.6 Schematic of a fuel cell used for electrochemical characterisation of LMA SOFC (held in furnace).....	55
Figure 3.7 Hydrodynamics profile of a rotating disc: (a) streamlines in solution; (b) coordinate system used in calculation (solid arrows denote the streamlines) ¹⁰⁸	59
Figure 4.1 Schematic of experimental rig used for oxygen sensor testing.	65
Figure 4.2 Schematic of experimental setup for potentiometric measurements (a) with 10YSZ symmetrical cell (b).....	66
Figure 4.3 Theoretical (using Equation (4.4)) and experimental EMF developed by the symmetrical cell.	67
Figure 4.4 Current – voltage characteristics that includes ionic conductivity of 10YSZ and overpotential on each Pt electrodes.....	68
Figure 4.5 Measured EIS data: at 315 - 422 °C frequency sweep: 10 kHz to 0.01Hz, 10 frequencies per decade, Voltage: 0 V, amplitude of oscillations: 10 mV.	69
Figure 4.6 Measured EIS data at 722, 890 and 1000 °C, frequency sweep: 10 kHz to 0.01Hz, 10 frequencies per decade, Voltage: 0 V, amplitude of oscillations: 10 mV.....	69
Figure 4.7 The electrical conductivity of 6 mol. % YSZ cell as a function of reciprocal absolute temperature.....	70
Figure 4.8 Experimental open circuit potential of the SOFC with a liquid tin anode compared to the theoretical equilibrium potentials for tin oxidation reaction.	72
Figure 5.1 Schematic of the oxygen permeation through silicone peroxide tubing (containing N ₂) with electrochemically pumped oxygen.	77
Figure 5.2 Electrical furnace for heating oxygen sensor and oxygen pump (closer look) in the overall set-up (a); oxygen sensor (b); oxygen pump (10YSZ symmetrical cell (closed at one end) with two Pt electrodes and Pt wires) (c).....	79

Figure 5.3 Electronic circuit with 10YSZ cell served to pump oxygen in and out of nitrogen flow (a); schematic of the operation of the oxygen pump using the electronic circuit (b)...	80
Figure 5.4 Process flow diagram for oxygen permeation and oxygen pumping into the nitrogen stream (a); schematic of experimental rig for the measurement of oxygen permeation and oxygen pumping in and/or out the nitrogen flow (expanded view) (b); schematic of an experimental setup of the LMA SOFC cell for oxygen permeation into the N ₂ stream (c).....	81
Figure 5.5 Concentration of oxygen diffused through silicone peroxide tubing of 88 and 8 cm and nylon tubing (8 cm) vs. inverse of the gas flow rate.	82
Figure 5.6 Concentration of O ₂ vs. pumped current with N ₂ flow rate of 1.67, 0.83 and 0.33 ml s ⁻¹ using 8 cm silicone peroxide tubing (a) and hard tubing (b).....	83
Figure 5.7 Intercepts obtained from Figure 5.6 against reciprocal of the flow rate for silicone peroxide and nylon tubing.....	84
Figure 5.8 Relationship between theoretical and measured injection rate of oxygen and gas flow rate with both silicone peroxide and nylon tubing.....	85
Figure 5.9 The effect of pumped in and pumped out current on cathodic current measured at -1.1 V vs. RE under flow of 1.6 ml s ⁻¹ of gaseous mixture of dry H ₂ and N ₂ (4: 96).....	86
Figure 5.10 Steady cathodic current (a) vs. pumped current and (b) vs. O ₂ concentration with total flow rate of 1.6 ml s ⁻¹	87
Figure 5.11 Concentration of O ₂ vs. pumped current at total flow rate of 1.6 ml s ⁻¹	87
Figure 6.1 Schematic showing operation of LMA SOFC with hydrogen. Yttria-stabilised zirconia (YSZ) is shown as a representative solid oxide electrolyte.	92
Figure 6.2. Proposed modes of operation for a LMA SOFC fuelled with H ₂ : (a) direct electrochemical oxidation of H ₂ at LMA / electrolyte interface; (b) chemical oxidation of H ₂ in the bulk of LMA by dissolved oxygen, followed by electrochemical injection of oxygen at LMA / electrolyte interface; (c) electrochemical oxidation of M followed by chemical oxidation of H ₂ in the bulk of the LMA; (d) extensive oxidation of M to insoluble MO _x that may create a blocking layer.....	93
Figure 6.3. Standard equilibrium potentials of H ₂ -H ₂ O, Sn-SnO and Sn-SnO ₂ redox systems (all based upon O ₂ at 1 atmosphere pressure and 21% concentration) as functions of temperature. Operating potential window in <i>E</i> mode (applied in the present work) is constrained by the onset of electronic conductivity in YSZ from the top and by SnO ₂ generation from the bottom at 780 °C.....	95
Figure 6.4. The effect of applied potential on current density in LTA SOFC in modes EC1 and EC2 with subsequent formation of a blocking layer (SnO ₂) at 760 °C.	97

List of Figures

Figure 7.1. Anodic current at -0.90 V vs. RE at 780 °C (immediately after switching from 3% to zero H ₂).....	102
Figure 7.2. Anodic current at -0.90 V vs. RE at 780 °C with increase of p(H ₂) from 0 to 26 kPa (a); and with decrease of p(H ₂) from 26 kPa to 0 (b).....	102
Figure 7.3. Anodic current with variation of p(H ₂) and of total flow rate (TF) at 780 °C.....	103
Figure 7.4. Steady anodic oxidation current as function of p(H ₂) with varying TF and direction of change of H ₂ composition (ascending / descending), all at 780 °C.....	103
Figure 7.5. Schematic of the step change in p(H ₂) during oxidation at applied potential in the E/CE mode of operation.	105
Figure 7.6 Electronic circuit with a 741 operational amplifier and a reversing switch for supply of current of both polarities (100 μA and -100 μA).....	112
Figure 7.7 Gas tight pyrophyllite holder with O-ring that enabled free movement of GC rod.	113
Figure 7.8 Apparatus for electrical resistance measurements: closer look of pyrophyllite holder with O-ring and moveable GC rod sheathed in alumina tube (a); complete cell with 8YSZ tube filled with tin shots, alumina inlet and outlet tubes, stationary and moveable GC rod sheathed in alumina tube (b).	114
Figure 7.9 Experimental cell for visualisation of the metal foam consisted of silica tube (filled with tin shots), alumina inlet and outlet tubes (a); identical s tube (filled with tin shots and 8YSZ chips), alumina inlet and outlet tubes during the operation at 300 °C (b).	115
Figure 7.10 Process flow diagram for observation of metal foam during the oxidation of hydrogen in LMA SOFC (foam shown subsequently found not to be present).....	116
Figure 7.11 Resistance measured between two probes inside molten tin at 300 °C (at no gas bubbling) and at 800 °C after gas bubbling as a function of height of liquid tin: using unsheathed GC probe (a) and using sheathed GC robe (b).	117
Figure 7.12 Silica tube apparatus <i>in-operando</i> with no metallic foam above tin: with inlet and outlet tubes (a) and with added 8YSZ chips (b).	118
Figure 7.13 Schematic of the dissolved oxygen concentration profile at a given applied potential in the CE mode of operation. The diffusion layer thickness is shown as δ.....	121
Figure 7.14. Step change in hydrogen partial pressure: from 0 to 8 kPa (total flow rate 2.6 ml s ⁻¹) (a); from 8 to 15 kPa (total flow rate 2.8 ml s ⁻¹) (b).....	126
Figure 7.15. Step change in hydrogen partial pressure: from 15 to 26 kPa (total flow rate 3.2 ml s ⁻¹) (a); from 26 to 15 kPa (total flow rate 2.8 ml s ⁻¹) (b).....	126
Figure 7.16. Step change in hydrogen partial pressure: from 15 to 8 kPa (total flow rate 2.6 ml s ⁻¹) (a); from 8 kPa to 0 (total flow rate 2.3 ml s ⁻¹) (b).....	126

List of Figures

Figure 7.17. The reciprocal time constant versus p_2'	127
Figure 7.18. Determined values of R^2 and intercept for the plots of i_2 versus $\mathbf{z2p2'}$ versus \mathbf{K} for a range of values.	129
Figure 7.19 Determined values for the slope of plots of i_2 versus $\mathbf{z2p2'}$ plotted as a function of \mathbf{K}	129
Figure 7.20. The ‘refined’ plot: steady anodic current versus $\mathbf{p2'}$. Compare Figure 7.4....	130
Figure 7.21. Anodic current versus time in LTA SOFC at 780 °C with instantaneous step change of $p(\text{H}_2)$ from 0 to 10 kPa, then to back to zero, repeated with 20 kPa and 30 kPa.	132
Figure 7.22. Current-time curves after switching the hydrogen partial pressure from 0 to 10 kPa (a); 20 kPa (b); 30 kPa(c). Slopes of the lines in (a-c) vs. $p(\text{H}_2)$ are shown in (d).....	133
Figure 8.1 Reported solubility of oxygen in liquid tin.	137
Figure 8.2 Schematic representation of Regime 1 conditions applied to the working cell: same hydrogen partial pressure, p_2' is applied from A to D; potential is held at a value E everywhere except in B - C.	139
Figure 8.3 Operation of the working cell under Regime 1 with 16 kPa $p(\text{H}_2)$ at 780 °C....	141
Figure 8.4. Schematic representation of Regime 2 conditions applied to the working cell flushed with constant flow of argon.....	142
Figure 8.5 Operation of the working cell under Regime 2 with 16 kPa $p(\text{H}_2)$ at 780 °C....	143
Figure 8.6 Schematic representation of Regime 3 conditions applied to the working cell flushed with constant flow of argon; potential is held at a value E everywhere except in B - C.....	144
Figure 9.1 Process flow diagram for dissociation of water in LMA SOFC cell followed by cathodic reduction of oxygen (with optional use of H_2 for additional removal of tin oxide).	151
Figure 9.2 Cathodic current at -1.1 V vs. RE at 810 °C with changes of $p(\text{H}_2\text{O})$	152
Figure 9.3 Steady cathodic current data as a function of $p(\text{H}_2\text{O})$ corrected for parasitic oxygen current.	152
Figure 9.4 Operation of LTA SOFC under Regime 1 with constant 3.8 kPa $p(\text{H}_2\text{O})$	153
Figure 9.5 Measured Q_i values as a function of OC intervals.	154
Figure 9.6 Schematic of the dissolved oxygen concentration profile at a given applied potential E during the water reduction process. The diffusion layer thickness is shown as δ . (Compare with Figure 7.13).....	155
Figure 9.7 Step change in $p(\text{H}_2\text{O})$: from 3.78(28 °C) to 0.61(0 °C) kPa (a); from 0.61kPa (0 °C) to zero (dry Ar) (b).....	158

Figure 9.8 Step change in $p(\text{H}_2\text{O})$: from zero (dry Ar) to 1.23 kPa (10 °C) (a); from 3.78 kPa (28 °C) to 1.23 kPa (10 °C) (b).	158
Figure 10.1 (a) Schematic of a rotating disc electrode of the classical Riddiford design where the electrode is a platinum wire of 1 to 3 mm radius ¹⁶⁸ ; (b) schematic of rotating ring-disc electrode ¹⁷¹ (the broken arrow indicates the electrolyte-flow lines induced by rotation).	163
Figure 10.2 Initial schematic of the cell containing Rotating Electrolyte Disc (Design 1).	166
Figure 10.3 The improved design of RED - Design 2.	167
Figure 10.4 Design for simplified RED setup in aqueous systems.....	168
Figure 10.5 The outer side of YSZ disc painted with Pt ink (a) and inner side (b) where Pt mesh and wire are attached.....	168
Figure 10.6 The prepared RED setup for aqueous electrochemical testing.....	170
Figure 10.7 Stages in making the gold disc electrode of 8 mm diameter.....	171
Figure 10.8 Experimental set-up for rotation speed measurement using Hall effect sensor and a time counter.....	171
Figure 10.9 LSVs with increasing rotation rate for the ferrous-ferric redox couple using 0.014 M Fe^{2+} / 0.014M Fe^{3+} in 3M KCl (data obtained via 6 mm Pt disc electrode).	172
Figure 10.10 Cyclic voltammograms for a range of rotation rates for the ferrous-ferric redox couple using 0.02 M Fe^{2+} / 0.02 M Fe^{3+} (a) and 0.02 M Fe^{2+} / 0.002 M Fe^{3+} in 1M KCl plus 0.01 M HCl (b) (data obtained via 8 mm Au disc electrode). The reference electrode was a dipping platinum wire so that potentials shown were versus the equilibrium potential of the particular ferrous-ferric couple under investigation.....	173
Figure 10.11 Cyclic voltammograms for a range of rotation rates for the ferrous-ferric redox couple using 0.002 M Fe^{2+} / 0.02 M Fe^{3+} in 1M KCl plus 0.01 M HCl (a); expanded view (b) (data obtained via 8 mm Au disc electrode). The reference electrode was as for Figure 10.10.....	173
Figure 10.12 Plots of limiting current density for Fe^{3+} reduction (a) and Fe^{2+} oxidation (b) vs. square root of rotation speed.	174
Figure 10.13 The ready RED set-up in operation of LME SOFCs.....	176
Figure 10.14 The latest design of RED - Design 3.	176
Figure A.1 Measured temperature profile inside the furnace for set points of 600 and 700 °C.	203
Figure B.1 Schematic representation of plastic tubing with external (r_1) and internal (r_2) radii and element radius, r and thickness, dr	204

List of Figures

Figure C.1 Schematic of Regime 1 conditions applied to the working cell (<i>E</i> mode). Same hydrogen partial pressure, p_2' is applied from A to D. Potential is held at a value <i>E</i> everywhere except in B - C.	212
Figure C.2 Schematic of Regime 2 conditions applied to the working cell (<i>E</i> mode) with constant flow of argon.	215
Figure C.3 Schematic of Regime 3 conditions applied to the working cell (<i>E</i> mode) with constant flow of argon. Potential is held at a value <i>E</i> everywhere except in B-C.	218

1. Introduction

This chapter presents an overview of the thesis. The motivation behind this study concerning investigation of the operation of liquid metal electrode solid oxide fuel cells (LME SOFC) is summarised together with research aims and objectives. Lastly the outline of the thesis is presented.

The world's growing energy demands have led to increasing environmental and resource availability concerns. In this regard, stabilisation of increasing anthropogenic carbon dioxide (CO₂) emissions is one of the most urgent issues associated with global climate change today. This problem may lead to the growth of average global temperatures by about 1.4 °C to 5.8 °C above 1990 levels by 2100 and have consequent severe impact on the environment¹. Regarding this matter, as part of the UK government's global strategy in response to the climate change, a target of 80% reduction in greenhouse-gas emissions by 2050 has been set².

According to the International Energy Agency (IEA), fossil fuels will continue to dominate the power generation sector despite the decline in their share from 68% in 2012 to 55% in 2040³. While low- or zero-carbon alternatives have been investigated in order to substitute the use of fossil fuels, in the short term there is no viable alternative to replace them completely. Among the common types of fossil fuels, carbon remains the most available and abundant fuel source around the world (60% of all global sources). As a result, highly efficient fuel technologies are required to minimize severe environmental impact of electric energy production from coal⁴.

In this regard, Solid Oxide Fuel Cells (SOFCs) is an emerging technology for clean and efficient power generation from various carbonaceous fuels with reduced levels of CO₂ emissions. High temperature solid oxide fuel cells are electrochemical devices capable of converting the chemical energy stored in gaseous fuels (including hydrogen, alkanes, alcohols, alkenes, alkynes, ketones, etc.) into electrical power⁵. The operational efficiency of such systems is higher than conventional heat engines since the process is electrochemical and not constrained by the Carnot efficiency limitation. Typical efficiencies obtained from SOFCs are in the range of 50-60% (LHV). The SOFC technology is highly scalable with systems in hundreds of kilowatts demonstrated⁵. Notwithstanding the reduction in greenhouse gas emissions brought about by high efficiency, fuel cells generate carbon dioxide free from diluting nitrogen which can be sequestered at lower cost compared with

the exhaust products from most electricity generation based upon combustion of fossil fuels.

However, durability and performance degradation due to impurities contained in hydrocarbon fuels continue to be a concern⁶. The performance of SOFCs is greatly limited by carbon deposition^{7,8} as well as sulphur poisoning⁹. Contaminants may react with anode materials via various mechanisms to decrease electrochemical reaction rates by increasing charge transfer resistance and result in mechanical failure of materials¹⁰. In order to mitigate the influence of fuel impurities on cell degradation, the supplied fuel should undergo pretreatment using a variety of adsorbents and filters¹¹.

Recent studies^{6,12,13} have presented a novel concept for direct electrochemical oxidation of carbon (coal or biomass) to electricity in liquid metal electrode solid oxide fuel cells (LME SOFC). Unlike conventional SOFCs, this class offers the advantage of high efficiency with the benefits of greater tolerance to fuel contaminants, the feature being particularly well suited to the direct use of solid fuel. The main principle lies in the liquid nature of the metal electrode (anode), which acts as a buffer to fuel impurities that dissolve in it and no longer affect the performance of the fuel cell, unlike in SOFC solid anodes (nickel-yttria-stabilised zirconia (Ni-YSZ)). Apart from exceptional tolerance to fuel impurities, the liquid metal anode is able to serve as an additional energy source that feeds the cell. This “battery” effect is particularly useful during interruption of the fuel supply.

Pioneering studies of liquid metal anode solid oxide fuel cells (LMA SOFCs) have been performed by Tao *et al.*¹⁴ at Cell Tech Power. In their prototype, liquid tin was used as the anode material^{12,13,15–17} where a power density of 170 mW cm⁻² on hydrogen and military logistic fuel, JP-8, has been demonstrated⁶. The projected efficiency of such a system operating on coal is 61%¹⁵. Subsequent investigation of alternatives to Sn (p-orbital electron metals - In, Pb, Bi and Sb) has been made at the University of Pennsylvania^{18–20}. Further characterisation of alloys of some of those metals (Sn-Pb, Sn-Pb-Bi) was performed by Labarbera *et al.*²¹.

Being a comparatively novel system, LME SOFC technology is some way from being fully commercialised due to technical challenges unique to this class of fuel cell. As such, there is a lack of knowledge on the mechanism and the species involved in the fuel oxidation process within the liquid metal media. The transport of active species within the liquid metal electrode is not yet well-understood.

In order to address these research questions a model system and novel technique are proposed in this study. First, to obtain a fuller understanding of the mechanisms of fuel oxidation in LME SOFCs the model system – oxidation of hydrogen in liquid tin anode

SOFC is suggested. To investigate transport phenomena that occur within the metal media a novel apparatus – Rotating Electrolyte Disc (RED) based upon the well-known Rotating Disc Electrode technique, where the electrode and electrolyte are inverted, is offered in this study.

1.1. Research Aims

The overall objective of this thesis is to obtain an improved understanding of liquid metal electrode SOFC in order to facilitate the development and commercialisation of the technology.

The system chosen for study is the oxidation of hydrogen in LMA SOFC due to its simplicity as a fuel compared to solid carbon or other gaseous fuels.

In line with the set objective, the aims are further described as follows:

- design and fabrication of the electrolyte-supported cell for the evaluation of LMA SOFC performance using a tin anode;
- experimental testing and optimisation of an electrochemical cell and workstation built for electrochemical characterisation of LMA SOFCs;
- understanding of oxidation of hydrogen in LMA SOFC;
- development of an electrochemical model for the analysis and interpretation of the obtained results on hydrogen oxidation in LMA SOFC;
- examine the possibility for water electrolysis in reverse LMA SOFC;
- initial work towards the development of a novel technique allowing strict control of the hydrodynamics conditions within a liquid metal electrode.

1.2. Thesis outline

The outline of the thesis is as follows:

Chapter 2 presents fundamentals of solid oxide fuel cells with the main focus on liquid metal electrode solid oxide fuel cells. It critically reviews the current status of this technology with various metallic anodes. Finally, a number of open research questions are postulated; an attempt is made to address some of these questions in this thesis.

Chapter 3 describes the design and development of an experimental workstation and electrochemical cell for testing and operation of LMA SOFCs. It also summarises the principles of electrochemical techniques that are applied in this study.

In Chapter 4 initial testing of the developed experimental rig along with materials and equipment is discussed.

Chapter 5 provides experimental results focused at optimisation of the developed experimental rig by measurement of permeation rates of air (oxygen) through plastic tubing. The effect of oxygen leaking into gas lines supplying fuel to the electrochemical cell on overall electrochemical performance of a fuel cell is also investigated and the method for separating of oxygen contribution to the fuel cell performance is demonstrated.

A classification of possible modes of operation of liquid metal anode SOFC fuelled with hydrogen based upon thermodynamic and electrochemical considerations is given in Chapter 6. Examples of each of the modes are also demonstrated.

Chapter 7 discusses the experimental results on oxidation of hydrogen in LMA SOFC, which was chosen as the model system for the testing of the RED. Two electrochemical models for electrochemical (***E***) and chemical-electrochemical (***CE***) modes of operation are proposed. A further re-consideration of a model involving ***E*** mode is accomplished based on investigation of the possibility of a metallic foam existing above the tin anode in LMA SOFC. Finally, the model developed for ***CE*** mode is presented as a theoretical framework for the obtained results on oxidation of hydrogen in LMA SOFC.

In Chapter 8 additional validation of the model for ***CE*** mode is carried out via determination of oxygen solubility in liquid tin and calculation of a new parameter, the dynamic oxygen utilisation coefficient, (\bar{z}), evolved from derivation of the ***CE*** model in Chapter 7. A methodology similar to anodic stripping voltammetry (but in this work involving anodic oxygen injection) is proposed and demonstrated.

Chapter 9 discusses initial experimental findings on water electrolysis using a liquid metal electrode solid oxide electrolyser cell (SOEC). An electrochemical model for interpretation of the obtained results is developed.

Chapter 10 presents the design and development of a novel rotating electrolyte disc (RED) apparatus, which is an inverted system based upon the rotating disc electrode technique. The results of testing of the engineering aspects of the RED apparatus in an aqueous system are presented. Chapter 11 concludes the thesis and summarises the main findings obtained in this study. Potential steps for future work are highlighted.

It has been shown that:

- i) The oxidation of hydrogen in LMA SOFC occurs via fast dissolution of hydrogen, rate-determining homogeneous reaction of dissolved hydrogen and oxygen and diffusion-controlled injection of oxygen to replace that removed by chemical reaction (so-called ***CE*** mechanism).

- ii) A critical design parameter, arising out of the *CE* model, herewith termed the dynamic oxygen utilisation coefficient, has been identified. Its value is governed by geometric, mass-transport and kinetic factors in the fuel cell.
- iii) A coulometric technique for determination of the dynamic oxygen utilisation coefficient has been developed.
- iv) The model for the *CE* mechanism has been validated via calculation of the solubility of oxygen in molten tin.
- v) Electrolysis of water has been demonstrated together with the development of a model for the interpretation of the obtained data.
- vi) A design for a novel Rotating Electrolyte Disc (RED) technique, proposed for fundamental investigations of the operation of the LMA SOFC, has been generated.
- vii) The RED design has been validated via its testing in an aqueous redox system.
- viii) Glassy carbon in contact with molten tin has been identified as a robust current collector.

2. Literature Review

This chapter summarises the fundamentals of fuel cells with the primary focus on solid oxide fuel cells. The current technological status of liquid metal electrode SOFCs is then discussed based on a critical review of the reported studies on liquid metal anode SOFCs. The main focus has been given to liquid tin anodes, as this metal is applied in the present work. Finally, the technological challenges that exist in the field of LMA SOFCs are highlighted. Possible solutions for some of the research questions are proposed, which is the main purpose of this thesis.

2.1. Fuel Cells

Conventional fossil fuels are likely to remain the primary energy sources for the next 50 years. With regard to recent energy policies, the conversion of hydrocarbons into energy has to be done in the most efficient and environmentally sustainable manner.

Fuel cells are electrochemical energy conversion devices that convert chemical energy in fuel directly into electricity (and heat) without involving the process of combustion^{22,23}. This technology is highly efficient, can be applied to a range of fuels (depending on the type of fuel cell), quiet in operation (the fuel cell itself has no moving parts) and scalable from mW to MW^{23,24}. As such, fuel cells are considered to be one of the most promising technological solutions for sustainable power generation. Fuel cells can be used in a broad range of applications, including: transportation, residential combined heat and power (CHP), large scale distributed power generation and battery replacement²³.

2.1.1. Fuel cell Principles

Fuel cells come in a range of architectures and material sets, but central to all is the electrolyte onto which there is attached the anode and cathode electrodes. Figure 2.1 illustrates the operation of a fuel cell using hydrogen and oxygen to electrochemically produce water. Hydrogen is fed to the anode, where it undergoes electrochemical oxidation into protons and electrons, promoted by the anode catalyst. Produced hydrogen ions then pass through the electrolyte, while the electrons follow the external circuit to the cathode, performing useful work.

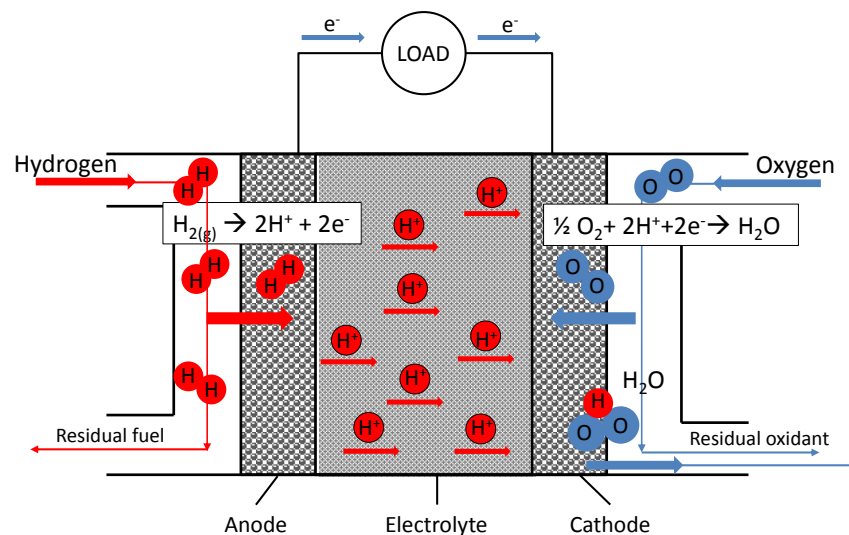


Figure 2.1 Individual fuel cell (one example of polymer electrolyte fuel cell).

Fuel cells vary in their design and material composition with respect to their application, though such properties as high efficiency, low or near zero emissions and quiet operation are common for all types.

2.1.2. Types of fuel cells

Fuel cell types vary from one to another in operating parameters and technical characteristics (e.g. power density, efficiency, etc.). However, the fundamental feature of the fuel cell which is different, and indeed names the fuel cell type, is the electrolyte. Fuel cell electrolytes are electronically insulating, but ionically conducting, allowing certain types of ions to transport through them. There are at least five main fuel cell types: Phosphoric Acid Fuel Cell (PAFC), Polymer Electrolyte Membrane Fuel Cell (PEMFC), Alkaline Fuel Cell (AFC), Molten Carbonate Fuel Cell (MCFC) and Solid Oxide Fuel Cell (SOFC). In the first two types, hydrogen ions (protons) flow through the electrolyte from anode to cathode to react with oxygen, and produce water; whereas in the last three types (Alkaline, Molten and Solid Oxide fuel cells) anions (OH^- , CO_3^{2-} , O^{2-}) migrate through the electrolyte from cathode to anode to react with fuel and similarly produce water (Figure 2.2).

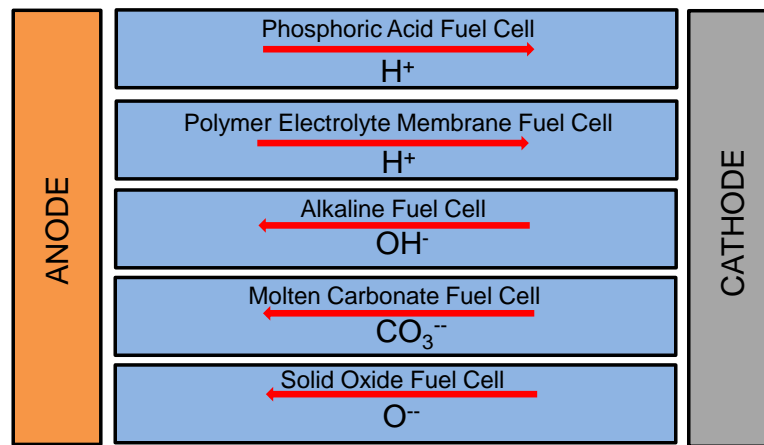


Figure 2.2 Flow of ions through different fuel cells electrolyte types.

The most common types of fuel cell systems and their main characteristics, including fuel efficiency, operating temperature, lifetime, etc. are summarised in Table 2.1. The type of fuel cell and its operating temperature range are primarily related to the electrolyte material. The first three types (AFC, PAFC and PEMFC) are considered as low temperature fuel cells, while the other two types (MCFC and SOFC) are known as high temperature fuel cells and require substantial amount of heat for initial operation. Low temperature fuel cells have the advantage of rapid start-up time though necessitate the use of precious metal electrocatalysts and high purity hydrogen as fuel.

Table 2.1 Technical characteristics of five main fuel cell types²⁵⁻²⁷.

Fuel Cell Type	Operating temperature ^{25,26} /°C	Power density ^{25,26} / Wcm ⁻²	Capital Cost ²⁶ / \$ kW ⁻¹	Fuel Efficiency ²⁶ / %	Lifetime ²⁶ / h	Applications ^{26,27}	Advantages ²⁷	Disadvantages ²⁷
PAFC	150-200	150-300	3000 \$/kW	55	> 40,000	Distributed Power;	Higher temperature enables CHP; Increased tolerance to fuel impurities	Platinum catalyst; Long start up time; Low current and power;
PEM FC	50-100	300-1000 (350 ²)	>200 \$/kW	45-60	> 40,000	Backup power; Portable power; Distributed generation; Transportation;	Solid electrolyte reduces corrosion & electrolyte management problems; Low temperature; Quick start-up	Expensive catalysts; Sensitive to fuel impurities; Low temperature waste heat
AFC	90-100	150-400	>200 \$/kW	40-60	> 10,000	Military; Space;	Cathode reaction is faster in alkaline electrolyte and leads to high performance; Low cost components	Sensitive to CO ₂ in fuel and air; Electrolyte management
MCFC	600-700	100-300	1000 \$/kW	60-65	> 40,000	Electric utility; Distributed power generation;	High efficiency; Fuel flexibility; Can use a variety of catalysts; Suitable for CHP;	High temperature corrosion and breakdown of cell components; Long start-up time; Low power density
SOFC	800-1000	250-350	1500 \$/kW	55-65	> 40,000	Baseload power generation; Auxiliary power; Electric utility; Distributed generation;	High efficiency; Fuel flexibility; Solid electrolyte; Suitable for CHP & CHHP; Hybrid/GT cycle	High temperature corrosion and breakdown of cell components; High temperature operation requires long start up time

Despite this variety of fuel cells, currently the greatest interest is shown primarily to PEMFC and SOFC. This thesis will discuss recent advances in SOFCs by considering the liquid metal electrode solid oxide fuel cells (LME SOFC), as a separate highly efficient and environmentally friendly fuel cell option that shares common features of SOFCs and molten carbonate fuel cells.

2.2. Solid Oxide Fuel Cells

The solid oxide fuel cell (SOFC) is one of the most promising fuel cells used to convert chemical energy stored in fuel directly into electrical energy. SOFC are primarily targeted at medium and large scale applications and considered to be a credible power source for automobiles and power plants²⁸. Solid oxide fuel cells are particularly designed for stationary and distributed power generation where they have advantages over conventional heat engines due to their compactness, modularity, durability and fuel flexibility. Therefore, as a result, over the last few decades SOFCs have become very attractive systems and are on the way to global commercialisation.

Solid oxide fuel cells can be applied to a range of fuels and are less affected by fuel impurities compared to low temperature fuel cells (e.g. polymer electrolyte membrane fuel cells). SOFCs have higher overall efficiency²⁸ compared to combustion engines, as they are not limited by the Carnot cycle. Higher efficiency promotes lower CO₂ emissions, which is a critical aspect on the way to a greener future power generation.

The operating temperature (typ. 700 - 1000 °C)⁵ of an SOFC activates the reforming of fuel and oxidation process and eliminates the poisoning of electrodes with carbon monoxide (CO), which is common for PEM fuel cells. Hence, highly active catalysts typical for other class of fuel cells (e.g. platinum in PEM fuel cells), are not required. The operating temperature not only facilitates rapid kinetics, but also allows production of high quality heat as a by-product²³, which can be further recovered or used secondarily in power generators²⁴. The efficiency of waste heat recovery combined with electricity production is in the range of 85-90% (compare to CHP systems)²⁴.

The solid electrolyte used in SOFCs avoids any corrosion issues arising typically from liquid electrolyte used in other high temperature fuel cells, for example molten carbonate fuel cell (MCFC) and hence, increases the durability of the SOFC systems²⁴.

Currently, SOFC technology remains at the R&D level (although commercial systems are available) due to two main obstacles – cost and reliability. These barriers are both related to the high operating temperature required to ensure sufficient conductivity of O²⁻ ions in the ceramic electrolyte. The operating temperature requires materials which are exceptionally

stable and robust. Therefore, although significant progress in SOFC development has been made over the last few decades, its practical application still relies heavily on materials development.

2.2.1. Principle of operation of the solid oxide fuel cell

The operational principle of SOFCs is very similar to other fuel cell types, though a difference is that the ceramic electrolyte conducts O^{2-} ions produced from reduction of oxygen at the cathode (Equation (2.1)). These negatively charged ions then migrate through the electrolyte to react with fuel at the anode (Equation (2.2)), and produce reaction products (e.g. water if hydrogen is used as fuel), power and heat. Equation (2.3) shows the global reaction for hydrogen oxidation in an SOFC. The generic fuel cell mode of operation for the SOFC is shown in Figure 2.3.

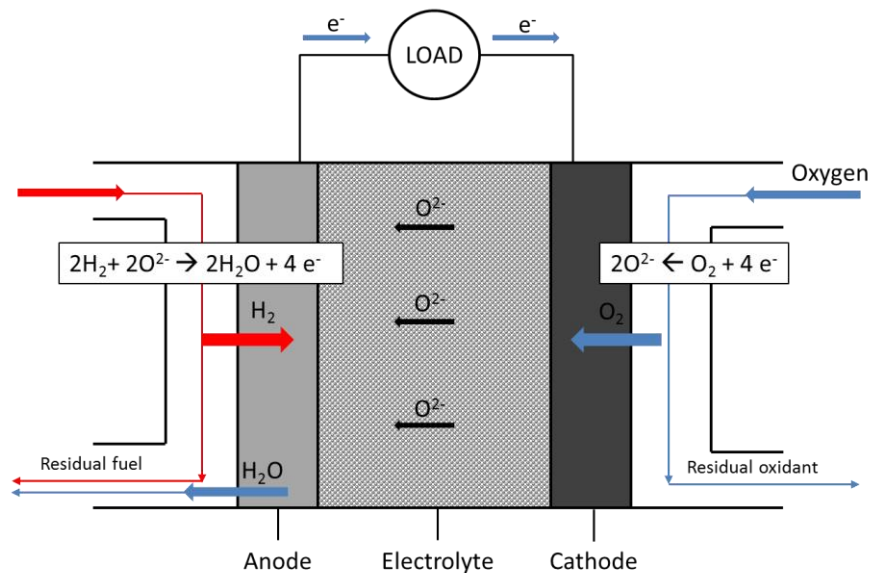
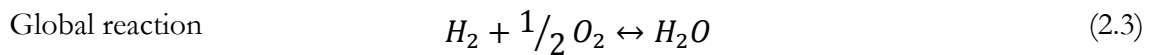
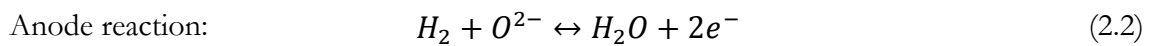
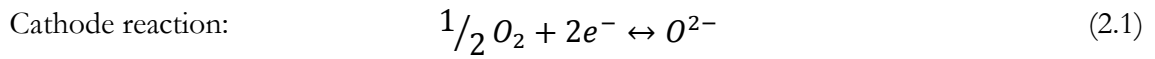


Figure 2.3 Schematic view of SOFC operation using hydrogen as a fuel.

2.2.2. Thermodynamics of ideal reversible SOFC

Treating a solid oxide fuel cell as a closed system operating at constant temperature and pressure, a general thermodynamic analysis can be carried out as follows.

From the first law of thermodynamics, the total change in internal energy, ΔU , of a closed system is:

$$\Delta U = Q - W \quad (2.4)$$

where Q – is the heat added to the system; W – work done by the system.

The total work produced by the system is divided into work associated with mechanical changes and work associated with other sources (e.g. magnetic, electrical, etc.)²⁹. Here, only electrical work is considered. Hence the Equation (2.4) is refined as follows:

$$\Delta U = Q - P\Delta V - W_{elec} \quad (2.5)$$

where $P\Delta V$ is the expansion/compression work; W_{elec} – electrical contribution to the work.

For a reversible change at constant temperature, the heat transferred is given by:

$$Q = T\Delta S \quad (2.6)$$

where ΔS – is the entropy change.

The change in Gibbs free energy, ΔG , for a system operating at constant temperature and pressure is given by:

$$\Delta G = \Delta H - T\Delta S \quad (2.7)$$

and the enthalpy change is defined as:

$$\Delta H = \Delta U + P\Delta V \quad (2.8)$$

Substitution of Equations (2.5) and (2.8) into (2.7) results:

$$\Delta G = -W_{elec} \quad (2.9)$$

This is the maximum electrical energy available in an external circuit, which is equal to the number of charges multiplied by the maximum potential difference, which is the reversible cell potential, E°_{rev} , and is given by:

$$E^{\circ}_{rev} = -\frac{\Delta G^{\circ}}{nF} \quad (2.10)$$

2.2.3. The Nernst Equation

The reversible cell potential given by Equation (2.10) is the potential for SOFC with reactants and products in their standard state with activities, $a_i=1$. Due to the temperature dependency of Gibbs free energy change (Equation (2.7)), the intrinsic temperature dependence of a reversible potential is evident.

In SOFC systems the activities of reactants and/or products are approximated to partial pressures. Deviation of the latter from their standard state is reflected in the Nernst potential, where the correction of the reversible cell potential is made as follows:

$$E_{rev} = E^{\circ}_{rev} - \frac{RT}{nF} \ln \frac{a_{products}}{a_{reactants}} \quad (2.11)$$

The Nernst equation for oxidation of hydrogen shown in Equation (2.3) is calculated using partial pressures in place of species activities with reaction stoichiometry 1, 0.5 and 1 for hydrogen, oxygen and water, respectively:

$$E_{rev} = E^{\circ}_{rev} + \frac{RT}{2F} \ln \left(\frac{p_{H_2} p_{O_2}^{1/2}}{p_{H_2O}} \right) \quad (2.12)$$

2.2.4. Fuel cell polarisation

Once a potential is applied to a fuel cell a current flows from anode to the cathode and the voltage of the cell changes, this process is known as polarisation. A schematic of a typical fuel cell polarisation curve as a function of current density is shown in Figure 2.4.

At open circuit (when no current is drawn from the cell) the cell voltage is lower than the thermodynamically predicted voltage due to energy loss under reversible condition, so-called open circuit losses (losses due to internal current and parasitic reactions), fuel crossover and mixed potentials.

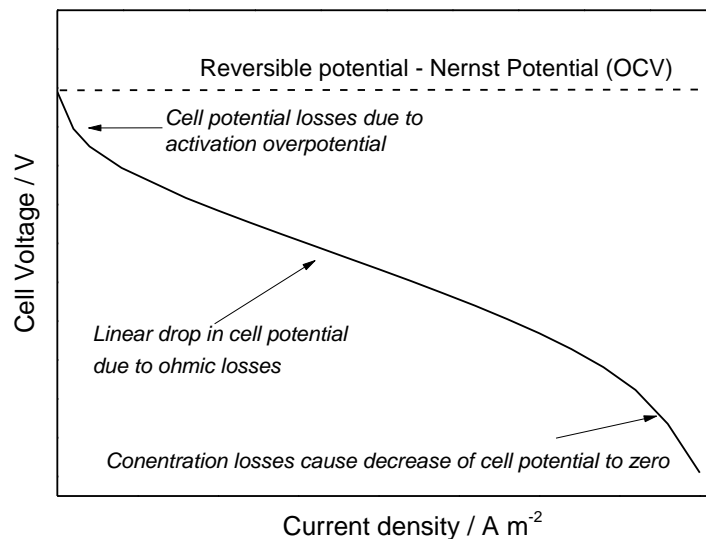


Figure 2.4 Schematic of a typical current – voltage or polarisation curve that shows the operating cell voltage with activation, ohmic and concentration potential losses.

The actual cell potential is lower than the reversible potential, E_{rev} , due to three different mechanisms of irreversible losses:

- activation polarisation
- ohmic polarisation
- concentration polarisation

Considering this the cell potential is then given by:

$$E_{cell} = E_{rev} - \eta_{act} - \eta_{conc} - \eta_{ohmic} \quad (2.13)$$

where η_{act} , η_{conc} , η_{ohmic} – are the activation, concentration and ohmic potential losses.

From Figure 2.4 it follows that activation polarization primarily occurs at low current density, while concentration polarization occurs predominantly at high current density. The next subsections describe each of the polarisation losses separately.

2.2.4.1. Activation overpotential

Activation overpotential is an additional potential required to overcome the energy barriers for oxygen reduction (Equation (2.1)) and hydrogen oxidation (Equation (2.2)) reactions at the electrode/electrolyte interfaces. Activation overpotential becomes significant at low current density region as the rates of those electrochemical reactions are low.

The Butler-Volmer equation relates the electrode activation overpotential, η_{act} and the current density, j as follows:

$$j = j_o \left[\exp\left(\frac{\alpha_a n F (E - E_{rev})}{RT}\right) - \exp\left(-\frac{\alpha_c n F (E - E_{rev})}{RT}\right) \right] \quad (2.14)$$

Or in simplified form:

$$j = j_o \left[\exp\left(\frac{\alpha_a n F \eta_{act}}{RT}\right) - \exp\left(-\frac{\alpha_c n F \eta_{act}}{RT}\right) \right] \quad (2.15)$$

where j_o is the exchange current density, α_a and α_c are the anodic and cathodic charge transfer coefficients respectively, n – number of electrons transferred in reaction, F – Faraday constant, R – Universal gas constant, T – operating temperature, E – cell voltage.

The limiting case of the Butler-Volmer equation is the Tafel equation, which expresses activation for cathodic reaction ($E \ll E_{rev}$) as follows:

$$\eta_{act} = a - b \log(j) \quad (2.16)$$

And similarly for anodic reaction ($E \gg E_{rev}$)

$$\eta_{act} = a + b \log(j) \quad (2.17)$$

where a and b are Tafel equation constants for a given reaction and temperature.

High electrocatalytic activity of electrodes with large values of j_o is favourable, as electrochemical reaction rate is fast and large current densities can be obtained with lower activation overvoltage.

2.2.4.2. Concentration overpotential

Concentration overpotential arises as a result of the slow mass transport of reactants reaching the reaction sites and the products leaving them. This leads to depletion of

reactants and accumulation of products at reaction sites. This overpotential is more dominant at high current densities when the slow rate of mass transport is unable to meet the required high demand of current output.

Concentration overpotential is induced by the concentration gradient which is caused by the differences in partial pressures/ concentrations of reactants and products between the bulk stream and reaction sites (electrode/electrolyte interface)³⁰.

The concentration overpotential at each electrode can be calculated from the local partial pressures of each reacting species (H_2 , O_2 and H_2O for typical SOFC operation) that are transported between the bulk and reaction sites (electrode/electrolyte interface)³¹:

$$\text{Cathode} \quad \eta_{conc} = \frac{RT}{2F} \ln \left(\left[\frac{p_{O_2}^{bulk}}{p_{O_2}^{react}} \right]^{1/2} \right) \quad (2.18)$$

$$\text{Anode} \quad \eta_{conc} = \frac{RT}{2F} \ln \left(\frac{p_{H_2}^{bulk} p_{H_2O}^{react}}{p_{H_2}^{react} p_{H_2O}^{bulk}} \right) \quad (2.19)$$

where *react.* – stands for reaction zone.

Application of Equations (2.18) and (2.19) for determination of concentration overpotential is not straightforward due to complexity associated with measurement of local reaction concentrations/ partial pressures.

An alternative equation for calculation of concentration overpotential as a function of limiting current density at which the partial pressures of reactants at the reaction sites tend to zero^{30,32} is as follows:

$$\eta_{conc} = 2.303 \frac{RT}{nF} \log \left(\frac{j_{lim}}{j_{lim} - 1} \right) \quad (2.20)$$

where j_{lim} is the limiting current density.

2.2.4.3. Ohmic overpotential

Ohmic losses are due to electrical resistance that arises from fuel cell components: cathode, anode, electrolyte, interconnects. From Ohm's law, the ohmic polarization is linearly dependent on the cell current, I , and can be found as follows:

$$\eta_{ohmic} = IR_{cell} \quad (2.21)$$

where η_{ohmic} is ohmic polarisation; R_{cell} is the overall resistance of the cell.

The ohmic losses can be improved by increase of conductivity of the cell components and reduction in the path length for current flow. Hence ohmic polarisation, η_{ohmic} , can be expressed as follows:

$$\eta_{ohmic} = I \sum_i \frac{l_i}{A_i \sigma_i} \quad (2.22)$$

where l_i – the corresponding path length in cell component i , A_i – the cross-sectional area of the component i , σ_i is the conductivity of the component i .

2.2.5. Geometry of solid oxide fuel cells

Depending on geometry there are three main configurations of SOFC: tubular, planar and monolithic^{23,28}. The schematic view of all three SOFC modifications are shown in Figure 2.5-Figure 2.10. Generally, both tubular and planar SOFC are designed as electrolyte-supported, anode-supported and cathode-supported cells, where the support is the thickest part of the cell²³. However, more attention has been devoted by planar SOFC, as it was reported to have more compact design and higher volume of specific power²³.

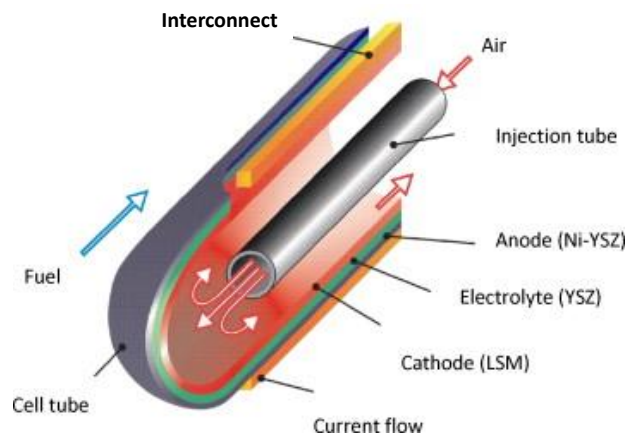


Figure 2.5 Schematic view of tubular SOFC²⁸.

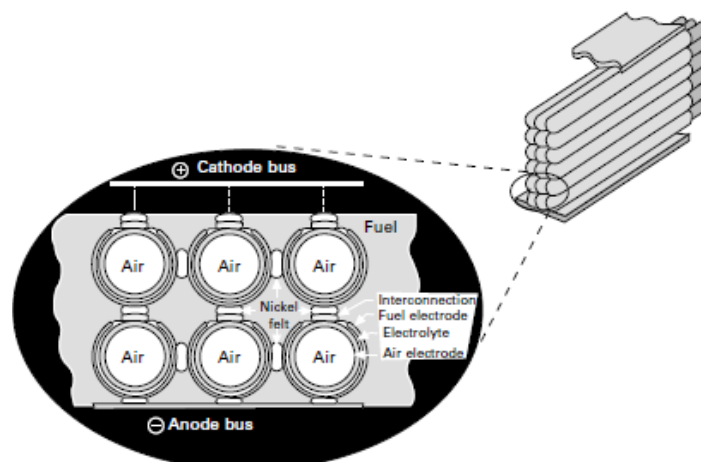


Figure 2.6 A schematic of cell-to cell connections in a cathode-supported tubular SOFC stack²⁴.

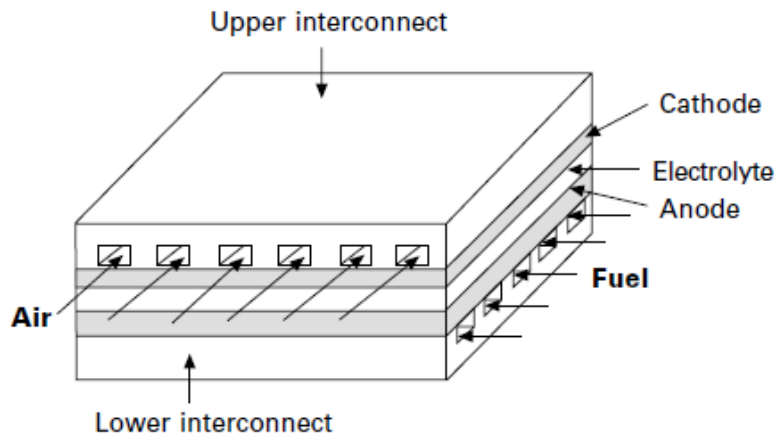


Figure 2.7 Schematic of cell configuration in an anode-supported planar SOFC stack²⁴.

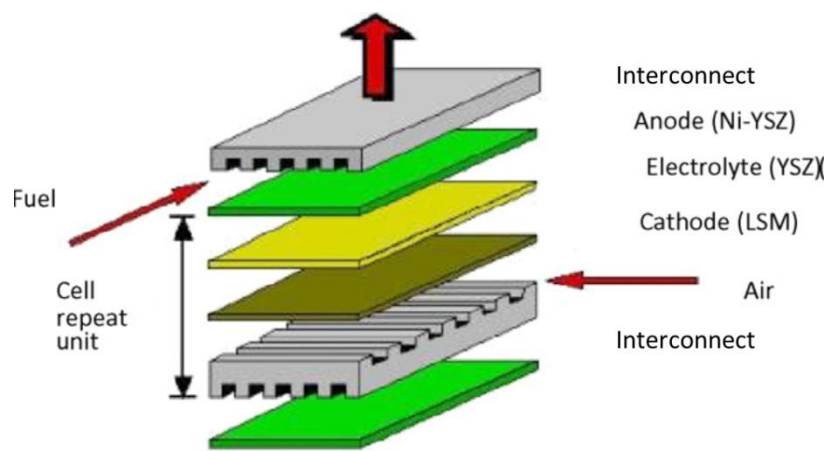


Figure 2.8 Schematic view of planar SOFC²⁸.

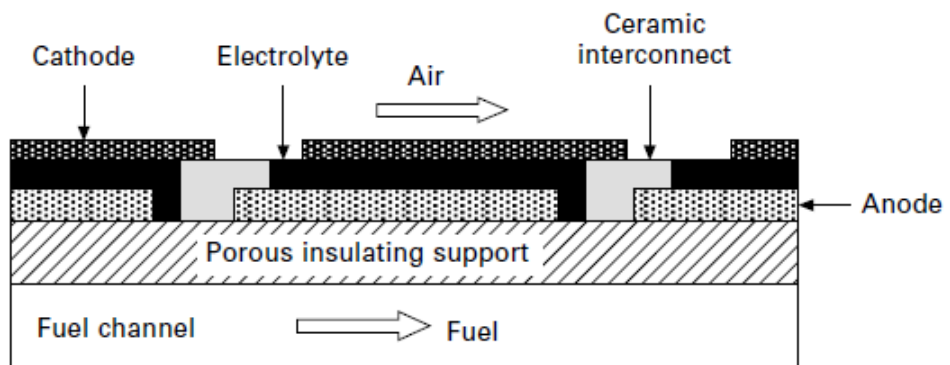


Figure 2.9 A schematic of the 'segmented-in-series' design adopted by Rolls-Royce²⁴.

In a monolithic SOFC, layers of electrodes are placed in a certain way so that anode and cathode form two channels for fuel and air. Three layers of the system are then sintered into one piece. Monolithic models combine some positive properties from both tubular and planar systems.

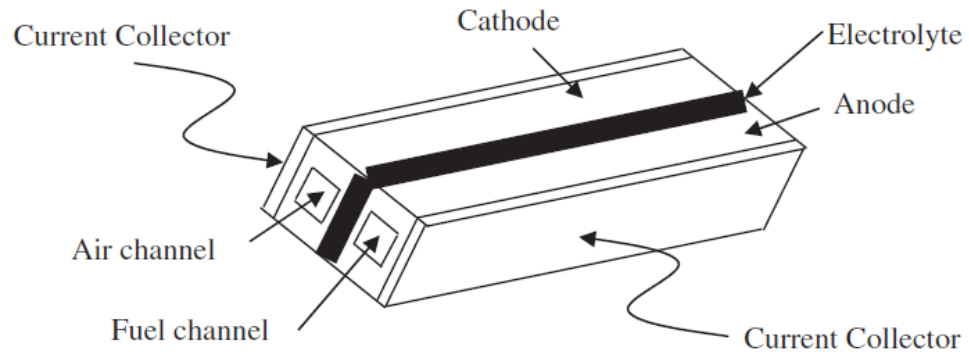
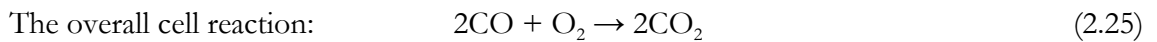
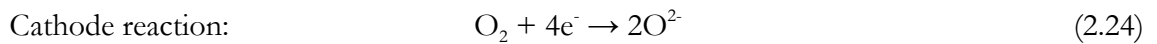
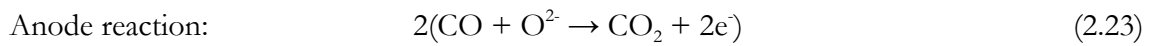


Figure 2.10 Schematic view of monolith-type SOFC³³.

2.2.6. Fuel flexibility of solid oxide fuel cells

Solid oxide fuel cells are flexible to a range of fuels, primarily due to the high operating temperature. They differ from PEM fuel cells which primarily operate on hydrogen gas (although other liquid fuels such as methanol are possible), whereas other hydrocarbons can be used instead in SOFCs. The following reaction equations illustrate electrochemical conversion of carbon monoxide and methane (used as fuels) in SOFCs.

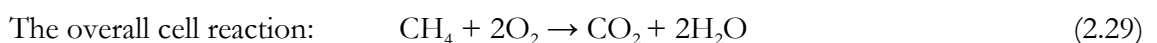
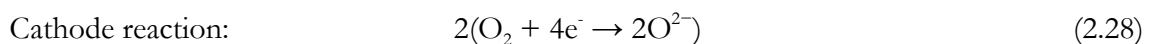
Carbon monoxide (CO):



At high temperature, there is a side reaction of oxidation of carbon monoxide with water to carbon dioxide and hydrogen gas, which is called the water-gas shift reaction²³:



Methane (CH₄):



2.2.7. Oxide-ion electrolyte in SOFCs

The performance of fuel cells largely depends on the electrolyte. It is generally preferable for electrolytes to have high ionic conductivity and stability. The nature of the electrolyte dictates the operating temperature of the fuel cell.

Apart from the relatively high oxygen-ion conductivity, there are other criteria for solid electrolytes such as: stability compared to other cell components, adequate thermal and mechanical properties (strength, toughness, mechanical and thermal shock resistance), structural and thermodynamic stability (in fuel and oxidising conditions). The thermal expansion coefficient of the electrolyte should match with other cell components. The ionic transport number of the electrolyte should be close to unity, otherwise there will be thermodynamic efficiency losses proportional to the electronic transport component³⁴.

There are four main electrolyte systems applied in SOFCs and they are based on zirconia (ZrO_2), ceria (CeO_2), lanthanum gallate (LaGaO_3) and bismuth (Bi_2O_3) oxides. With respect to fuel cell operating conditions, the most stable is the zirconia-based system, followed by lanthanum gallate, ceria and bismuth oxide systems³⁴. The oxides can be used separately or together (mostly two of them) to increase the stability in a reducing environment³⁴. For instance, bi-layer structures usually contain a layer of doped zirconia on ceria or bismuth oxide. Zirconia- and ceria-based electrolytes are relatively inert compared to doped bismuth oxides, which become reactive and thus their stability during the operational time of the stack significantly decreases.

Yttria-stabilised zirconia (YSZ)

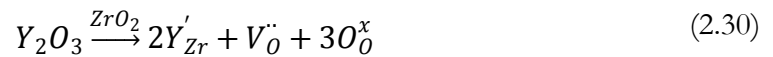
Zirconia-based electrolyte is commonly used in solid oxide fuel cells operated at high (800-1000 °C) and intermediate (600-800 °C) temperatures³⁵, as it fulfils the above mentioned electrolyte requirements. Zirconium is abundant in the Earth's crust (165 parts per million by weight³⁶) and consequently has relatively low cost. The electronic transport number of zirconia is small compared to other solid electrolytes in the oxygen partial pressure range ($>10^{-30}$ atm)³⁵. This is a typical pressure range in fuel cell applications.

Zirconium oxide exists in three different phases: monoclinic, tetragonal and cubic³⁷. Pure zirconium oxide (ZrO_2) is a monoclinic structured oxide at room temperature, with low ionic conductivity. Monoclinic zirconia (m- ZrO_2) is stable at ambient temperature, while cubic (c- ZrO_2) is stable from 2350 °C up to a melting temperature of 2680 °C and tetragonal (t- ZrO_2) is a metastable transition stage between m- ZrO_2 and c- ZrO_2 ³⁴. During the heating process, at around 1170 °C monoclinic ZrO_2 transforms to tetragonal and at 2350 °C from tetragonal to cubic³⁴. These transformations are reversible on reducing the temperature back to ambient, so that c- ZrO_2 reverts to t- ZrO_2 and then back to m- ZrO_2 . Reverse transformations are followed by rapid volume change and disintegration of material. Doping with a lower-valent oxide (e.g. yttria - Y_2O_3) can be applied to stabilise the cubic and tetragonal structures at low temperature where they are mostly used. As tetragonal phase is meta-stable and cubic phase is fully-stable the respective

dopant/stabiliser amount is needed for each of the phase. The tetragonal phase is stabilised by adding stabilisers up to 4 mole % of cation, while the cubic phase requires addition in excess of about 8 mole % of Y_2O_3 . Cubic zirconia is known to be the most ionically conductive among all three phases.

The following divalent and trivalent oxides can be used as potential zirconia dopants: CaO, MgO, Y_2O_3 , Sc_2O_3 , Yb_2O_3 , GdO_3 and some other rare earth metal oxides. However, it has been found³⁸ that the stabilisers which produce cubic zirconia with best ionic conductivity are those with a cation of similar size to that of Zr^{4+} . The lattice conductivity obtained after stabilisation is higher for trivalent metal compared to divalent metal oxide dopants³⁸. Among trivalent stabilisers the most common and well-developed is yttrium oxide (Y_2O_3).

A stabiliser has two main functions: the first one is to stabilise the structure of tetragonal or cubic phase, while the second is to generate oxygen-ion vacancies to allow oxygen ion diffusion. Substitution of Zr^{4+} ion with lower valent cation (e.g. Y^{3+}) in the crystalline lattice creates vacancies in the oxygen sub-lattice. This process can be expressed with Kroger-Vink notation as follows:



The created vacancy (V''_O) is mobile and allows oxygen ions to migrate through the lattice when a certain activation energy level is overcome. Equation (2.30) explains the phenomenon of oxygen ion conductivity by stabilised zirconia electrolyte, in this case yttria-stabilised zirconia (YSZ).

As dopant level is increased the conductivity of stabilised zirconia similarly increases. Higher amount of dopant leads to an increase in oxygen vacancy formation and hence ionic conductivity of solid electrolyte³⁹. At a certain level of dopant, created vacancies start to interact, thereby limiting their mobility in the lattice and hence inhibiting the overall conductivity^{35,39,40}. As demonstrated by Fergus⁴⁰ (see Figure 2.11) and other studies^{41,42} the 8 mol. % YSZ ($(ZrO_2)_{0.92}(Y_2O_3)_{0.8}$) is the minimum amount of yttria needed to stabilise cubic zirconia which exhibits the highest ionic conductivity.

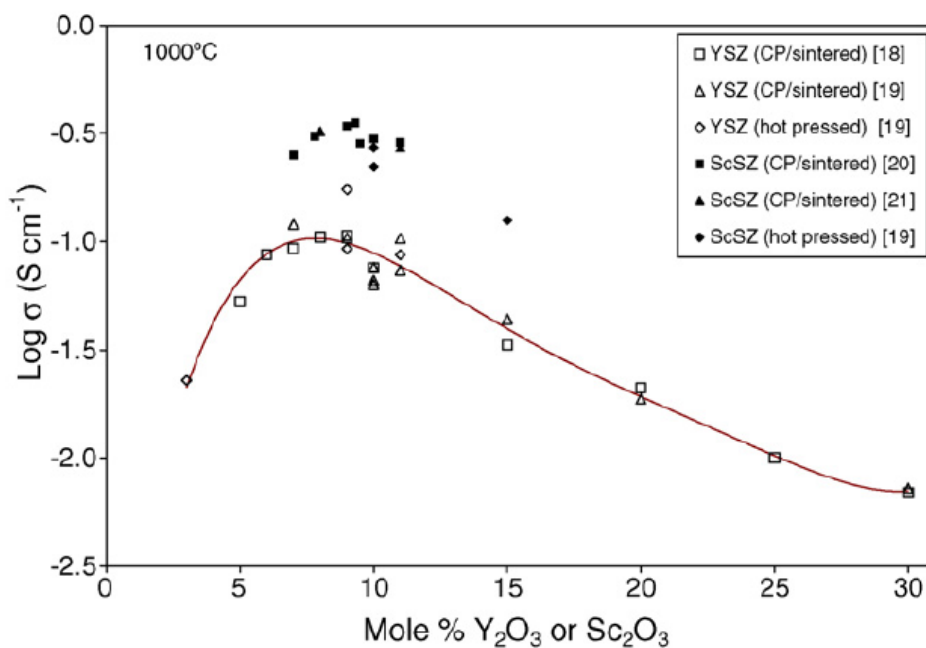


Figure 2.11 Conductivity of yttria- and scandia-stabilised zirconia in air at 1000 °C⁴⁰.

It has also been reported that the 9-10 mol.% ZrO_2 - Y_2O_3 system shows no or very low degradation of electrical properties³⁴. Hence the YSZ electrolyte is used in this research project. It has an adequate mechanical strength (about 250-300 MPa) with reduction at 1000 °C to about 150-200 MPa along with good ionic conductivity. The yttria content was changed at early stages of the project to find an optimum trade-off between the ionic conductivity, mechanical strength and cost of electrolyte material.

2.2.8. Diagnosis of solid oxide fuel cells using EIS

Electrochemical impedance spectroscopy (EIS) is an electrochemical technique that has been widely applied to distinguish individual losses in SOFCs, including oxygen reduction reaction kinetics, mass-transport and electrolyte membrane resistance⁴³⁻⁴⁵. Detailed overview of this technique is given in the next Chapter in Section 3.4.3. In this subsection the main focus is given to application of EIS in SOFC studies to the resistivity of the solid electrolyte.

One of the common applications of the EIS is the analysis of a YSZ conduction properties⁴⁶. In a solid electrolyte cell the overall electrolyte resistivity is governed by the migration of oxygen ions within the lattice and between the grains (so called intra-grain resistivity), and grain boundary (or inter-grain) resistivity, the latter explained by blocking of migrating oxygen ions at the grain boundaries. Intra-grain electrical conductivity of zirconia electrolyte is found to be mainly due to the dopant type and its concentration, and some other aspects such as phase assemblage, and grain porosity³⁴. An idealised impedance spectrum of a zirconia electrochemical cell with electrodes consists of three semi-circles in

the Nyquist plot⁴⁷ (Figure 2.12). A corresponding equivalent circuit for that system includes three parallel R-C elements connected in series.

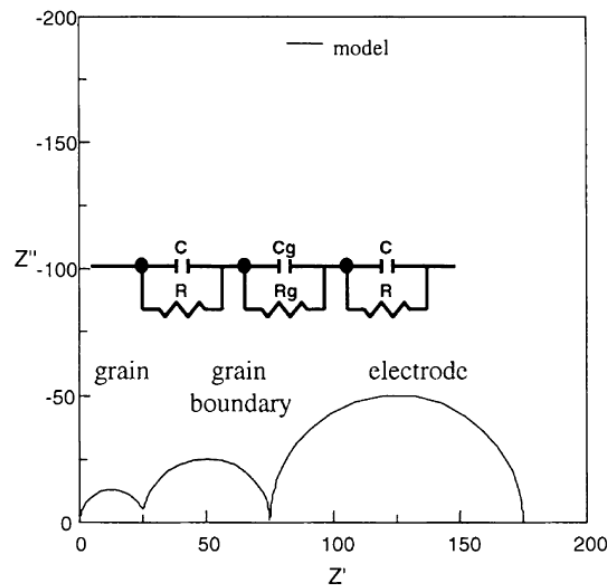


Figure 2.12 An idealised Nyquist plot of a zirconia electrochemical cell with electrodes and its equivalent circuit. The three semi-circular arcs correspond to conductivity within the grain, grain boundaries and electrodes, respectively⁴⁷.

The arcs attributing to the conductivity across the grain and grain boundaries in the solid electrolyte appear at higher frequencies, while the conductivity at the electrolyte/electrode interface is more prominent at lower frequencies^{46,47}. The first two semi-circles tend to diminish with increase of temperature due to significantly reduced intra-grain and inter-grain resistance of the electrolyte⁴⁷. As a result, the first two R-C elements are typically replaced by a single resistor that represents the overall electrolyte resistivity.

EIS is also widely used to diagnose performance of SOFCs with respect to operating conditions and cell components. For instance, humidification of supplied fuel significantly affects the operation of a fuel cell. This may be confirmed with measured in-situ EIS data where humidified fuel (e.g. hydrogen) results in lower resistance compared to dry fuel⁴³. Working temperature is another common parameter used to analyse performance of the SOFC.

Overall, EIS is being commonly used in SOFC studies because it provides individual fundamental information on each of the phenomena occurring at each interface as well as the bulk electrolyte conductivity. However, analysis and interpretation of impedance data is not straightforward, as data analysis has to correlate with other experimental information to verify the chosen equivalent electrical circuit for data fitting.

2.2.9. Direct Carbon Fuel Cell

In liquid metal anode SOFCs carbon (coal) can undergo direct electrochemical oxidation to carbon dioxide. A brief review of the common direct carbon fuel cells (DCFC) is given in this section to set the scene.

The direct carbon fuel cell (DCFC) was first reported by Sir William Grove in 1839^{48,49}. After several attempts, Dr. William Jacques was the first to build a direct carbon fuel cell in 1896, using a molten hydroxide electrolyte⁴⁹. Since that time, many researchers have worked to optimize this technology by applying new materials and improving the cell design. The most recent designs of DCFC are being developed and proposed by the Lawrence National laboratory, Cell Tech Power LLC and SRI International simultaneously with Scientific Applications & Research Associates (SARA), Inc.

The direct carbon fuel cell incorporates the characteristics of MCFCs and SOFCs, using solid carbon as a fuel instead of a typical gaseous fuel (e.g., hydrogen or methane).

According to the type of electrolyte used in the system, DCFCs are classified into three main types: those with molten hydroxide electrolyte, molten carbonate electrolyte and solid oxide electrolyte (typically YSZ). Electrical power is generated directly by introducing solid carbon, followed by its electrochemical oxidation to CO₂. The net cell reaction is:



DCFCs have numerous benefits, including high thermodynamic efficiency, which makes them advantageous over conventional molten carbonate or solid oxide fuel cells. The entropy change for the overall cell reaction is positive ($\Delta S = 1.6 \text{ J K}^{-1} \text{ mol}^{-1}$ at 600°C) resulting in higher Gibbs free energy change ($\Delta G = -395.4 \text{ kJ mol}^{-1}$ at 600°C) than the standard enthalpy change ($\Delta H = -394.0 \text{ kJ mol}^{-1}$ at 600°C)⁴. Therefore, theoretical electrochemical conversion efficiency of DCFC for the net cell reaction is greater than 100%.

Due to their low carbon emissions, DCFCs are considered to be a more environmentally friendly option than existing coal-firing plants. Cao *et al.*⁴ stated a 50% reduction in CO₂ emissions compared with conventional power plants. This is explained by direct electrochemical oxidation of carbon at the anode with no reaction with air. Therefore, the produced CO₂ is free from nitrogen as well as combustion products, such as SO₂, NO_x, etc., that are formed in combustion boilers. Almost pure CO₂ produced in a DCFC is then suitable for further applications or CCS (carbon capture and storage). This advantage makes this technology exceptionally promising in certain regions of the world, where coal

remains the primary energy resource (e.g. US, China, Former Soviet republics, etc.). To date, the US and China remain the highest CO₂ emitters around the world⁴.

The carbon required for DCFC systems is available from a variety of fuels, such as coal, biomass, and petroleum coke, which makes this technology even more attractive and promising. The system simplicity, absence of heat engines and reformers makes this technology adaptive directly near coal mines.

A schematic configuration of a direct carbon fuel cell constructed by Lawrence National Laboratory (LLNL, Livermore, CA) is shown in Figure 2.13. A 32% Li₂CO₃-68% K₂CO₃ molten salt mixture was used as the electrolyte. The operating current density varied from 58 to 124 mA cm⁻² at cell voltage of 0.8 V, which is 80% of its thermodynamic voltage⁴.

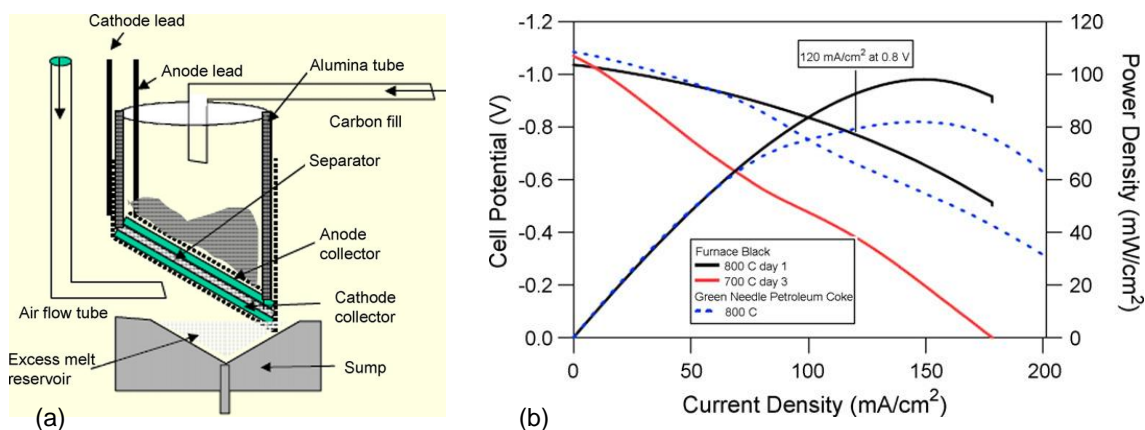


Figure 2.13 a) LLNL DCFC configuration with carbon particle anode, b) performance of LLNL DCFC⁴.

A novel arrangement for DCFC was patented by Balachov and co-workers⁴ at SRI International, where the main fuel cell component was a U-tube, consisting of a cathode current collector, cathode (lanthanum strontium manganite (LSM)), electrolyte – yttrium-stabilized zirconia (YSZ), anode current collector. The tube was immersed into a liquid anode (Li₂CO₃+K₂CO₃+Na₂CO₃). The design is illustrated in Figure 2.14a. The authors tested a variety of fuels (coal, tar, coke, acetylene, plastic, etc.). Reported power density was greater than 100 mW cm⁻² at 950°C (Figure 2.14b).

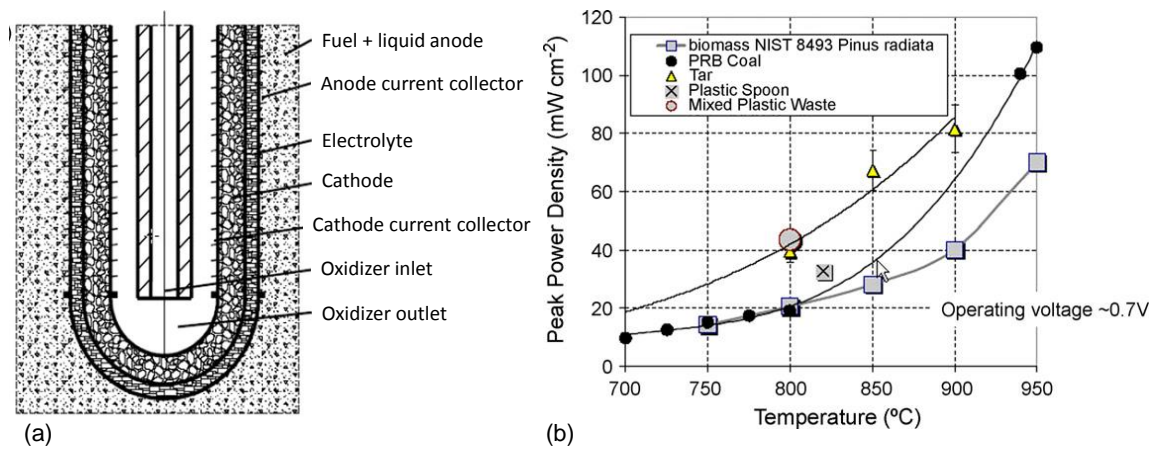


Figure 2.14 Configuration of the SRI direct carbon fuel cell (a), performance of SRI direct carbon fuel cell (b)⁴.

However, there are some ongoing technical challenges for DCFCs. They are primarily associated with high operating temperatures that require thermostable materials (e.g. ceramic, metal alloys) for stack components, which are typically expensive^{22,49}.

2.3. Liquid Metal Electrode Electrochemical Systems

The generic construction of a liquid metal electrode solid oxide fuel cell (LME SOFC) is illustrated in Figure 2.15. The arrangement is ostensibly identical to a conventional solid oxide fuel cell except that the anode is a molten metal. Fuel is fed to the electrode and oxidized products are generated in the same way. The difference is that both gaseous and solid fuel can be fed directly and effectively converted with no pretreatment stage.

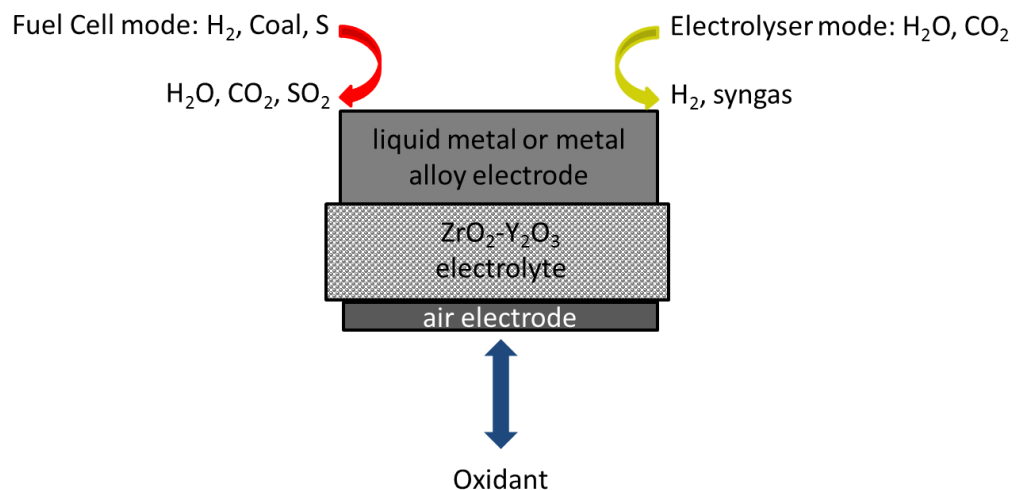


Figure 2.15 Operation of liquid metal electrode reactor in fuel cell and electrolyser mode.

Figure 2.15 also shows the potential for operation in electrolyser mode. This concept has the cell fed with CO_2 and steam (H_2O) that are electrochemically converted to synthesis gas

(a mixture of hydrogen and carbon monoxide), that can be used to produce liquid fuel (i.e. via the Fischer-Tropsch process) or used in a fuel cell directly⁵⁰.

2.3.1. Liquid Metal Electrode Solid Oxide Electrolyser

As shown in Figure 2.15 a molten metal anode can be applicable for electrolytic reduction of carbon dioxide and/ or steam in solid oxide electrolyzers (SOE). To understand how molten metal operates in electrolyser mode, conventional technological characteristics of SOE should be examined. Hence, this section briefly summarizes recent advances in SOE technologies using carbon dioxide and steam to produce a gaseous mixture of carbon monoxide and hydrogen, which is usually referred to as “synthesis gas” or “syngas”. The present study focuses mainly on application of a liquid metal electrode in fuel cell mode, though a possible application of molten electrode for water electrolysis has been also explored briefly (refer to Chapter 9).

High temperature electrolysis of CO₂ and steam for production of synthesis gas

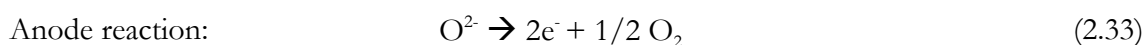
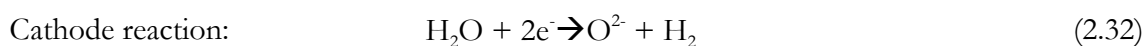
A significant amount of work has been done in this research area, as it seems to be a promising technological solution for production of hydrogen (alternative energy fuel) and carbon monoxide comprising the synthetic gas suitable for further applications⁵¹⁻⁵⁴. It is a favourable option that offers simultaneous reduction of carbon dioxide and steam that are usually released into the atmosphere in conventional power plants.

Pati *et al.*⁵³ have stated several advantages of SOE:

- Utilization of waste heat from nuclear waste and industrial processes to meet heat requirements of SOE;
- Production of pure hydrogen, free from typical impurities (sulphur and CO).

However, the main drawback remains high power requirement for electrolysis of steam⁵³.

Typical SOSE contains cathode and anode separated by oxygen-ion conducting YSZ electrolyte. Steam is fed to the cathode, where it dissociates into H₂ and O²⁻; the produced oxygen ions migrate through electrolyte layer to the anode and are oxidized to produce molecular oxygen:



By analogy to steam electrolysis the reduction of CO₂ to CO using conventional SOEs (with Ni-YSZ electrodes) has been reported recently⁵⁵ demonstrating relatively good

performance. The reduction reaction is carried out at the cathode side of the SOE as follows:



However, there are still concerns regarding the stability of Ni-YSZ components, as they can be damaged by a CO-CO₂ environment. Therefore, further investigation on more stable electrodes or lower energy requirements is needed.

The process of steam dissociation is regulated by applied potential difference between electrodes and requires significant power (ca. 70% of the total energy used). It was suggested that energy requirements might be reduced by introducing new anode materials, as liquid metals⁵³.

Several studies^{53,56} reported an adequate performance of solid oxide steam electrolyser (SOSE) where molten tin was employed as anode. This technological solution can be also applied for CO₂ electrolysis.

The design of such a steam electrolyser with liquid tin anode and Ni-YSZ cermet cathode is presented in Figure 2.16. Successful production of hydrogen at temperature range from 900 to 1000 °C was achieved whereby high temperature steam was fed to the cathode, while solid carbon - to the liquid tin anode.

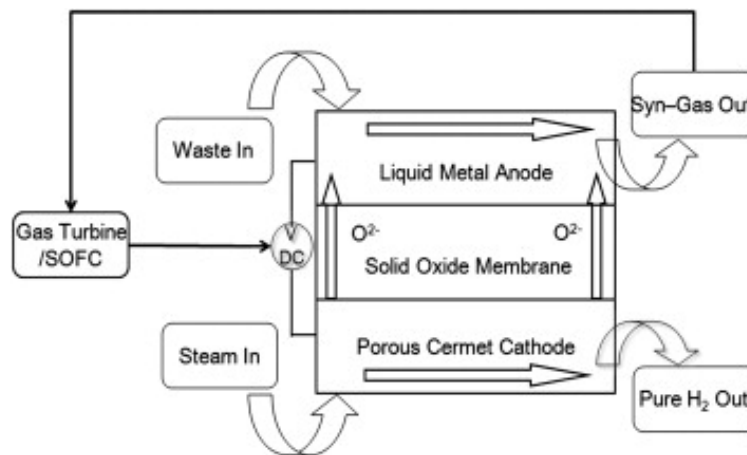


Figure 2.16 Schematic of solid oxide membrane electrolyser for waste to hydrogen and syngas conversion⁵³.

The main concept of such electrolytic cell was the introduction of a reductant that would lower the energy requirements for steam electrolysis by reducing the chemical potential of oxygen⁵³. SOE or SOFC with conventional solid electrodes cannot handle a solid reductant, except those that use molten metal electrodes, where reaction between solid and liquid is more favourable.

In such a SOEC system the liquid metal has been used as the anode. There are no literature studies that present solid oxide electrolysis using liquid metal as the cathode for reduction of species within the melt. Hence this field of the LME systems is open for further research. Early work on water/steam electrolysis using a molten tin electrode in solid oxide systems is demonstrated in Chapter 9 of this thesis.

2.3.2. Liquid Metal Anode SOFCs

The liquid metal electrode resides in a layer between the fuel chamber (gaseous or solid fuel) and the solid electrolyte (Figure 2.17). The oxygen reduction reaction occurs at the cathode/electrolyte interface generating oxygen ions, which then migrate through the solid electrolyte, typically represented by yttria-stabilised zirconia (YSZ), to the liquid metal anode. The O^{2-} ions react electrochemically with the liquid metal, generating metal oxide which is the active species for the oxidation of the fuel (gaseous or solid - carbon and hydrogen in the diagram), producing carbon dioxide or water respectively. However, the exact mechanism occurring and the species involved in the liquid metal anode media are not well defined and depend upon the metal used and operating conditions.

The molten metal blocks direct contact of electrolyte with gaseous impurities and hence reduces electrolyte degradation by inhibiting the reaction between contaminants and electrolyte⁶. Moreover, the fuel contaminants can become a fuel source themselves as they undergo electrochemical oxidation. All of the electrolyte surface in contact with the anode is available to supply a flux of oxide ions for reaction - there is no need to engineer a complex ceramic metal (cermet) electrode with optimized triple phase boundary (TPB) as is necessary in conventional SOFCs^{57,58}.

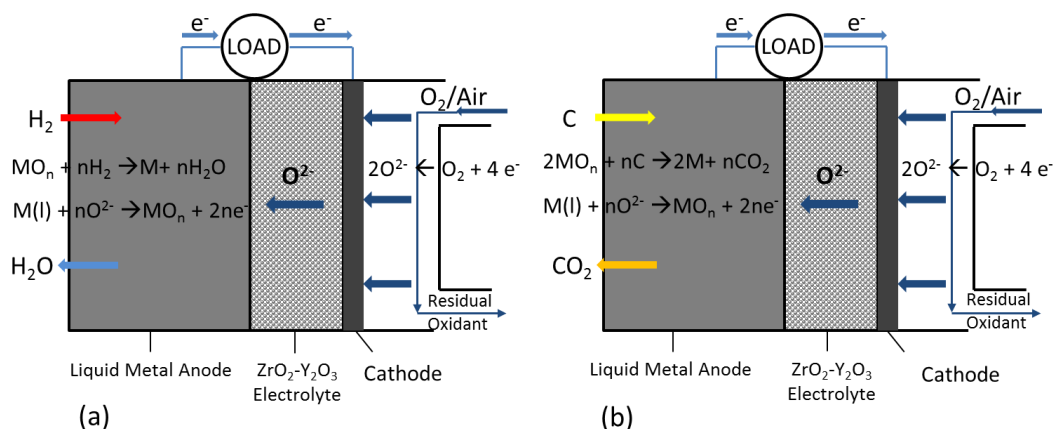
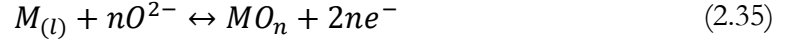


Figure 2.17 Schematic showing operation of LMA SOFC with (a) hydrogen and (b) solid carbon, as the fuel.

2.3.2.1. Operation of Liquid Metal Anode SOFCs

The liquid metal anode acts as an intermediary for the oxidation of fuel⁶. Taking a molten metal (M) and hydrogen as a fuel, the reactions at the LMA-SOFC anode follows the generic mechanism:



The first reaction (2.35) proceeds at the liquid anode-electrolyte interface, whereas the second reaction (2.36) occurs at the fuel-anode interface. The oxide ions (O^{2-}) are delivered from the cathode via the electrolyte. The state of oxygen in the metal varies with operating conditions. When using tin, oxygen may form oxide or suboxide, or remain dissolved in the melt⁵⁹. The state of oxygen may vary, though it has no particular effect on the overall reaction, which is the sum of the first and second reactions:



This reaction (2.37) is applicable to any liquid metal anode SOFC system including Sn or Cu⁶⁰.

2.3.2.2. Thermodynamics of LMA SOFC operation

The maximum electrical voltage generated by an electrochemical system can be determined via the equilibrium electrode potential (E_N), expressed by the Nernst equation (2.38) as follows:

$$E_N = E_{rev}^\circ - \frac{RT}{nF} \sum_i v_i \ln a_i \quad (2.38)$$

where a_i and v_i are the activities (fugacities for gases) and stoichiometric coefficients of all reactants and product species i , R is the molar gas constant, $8.314 \text{ J mol}^{-1} \text{ K}^{-1}$, T is absolute temperature and E_{rev}° is the standard electrode (equilibrium) potential of the reaction that can be defined from the Equation (2.39):

$$E_{rev}^\circ = \frac{-\Delta G_r^0}{(nF)} \quad (2.39)$$

where ΔG_r^0 is the Gibbs free energy change for the global reaction of H_2 oxidation ($H_2 + 1/2O_2 \rightarrow H_2O$), n – number of electrons transferred during electrochemical reaction and F is the Faraday's constant.

The standard equilibrium potentials of several metal-metal oxide couples as a function of temperature are shown in Figure 2.18. The data for the figure was generated using the chemical reaction and equilibrium software HSC Chemistry 6.1 (Outotec, Finland).

It can be seen that the cell voltage is expected to decrease with increasing temperature, as a result of the negative entropy change associated with the reactions. However, the voltage obtained under operating conditions (with a net current flowing) is difficult to predict. In addition to the usual loss mechanisms associated with reaction kinetics, ohmic and mass transport limitations, cell voltage will depend on the actual reaction at the anode: whether it is directly with dissolved fuel or the oxidation of the metal to oxide (electrochemical reaction) followed by oxidation of the hydrogen by the oxide (chemical reaction).

If the reaction is directly with the fuel then conventional fuel cell reaction OCVs will hold, which are generally higher than those for the reaction with the metal. Therefore, from a thermodynamic perspective, it may be preferable for the metal to have a low affinity for oxygen and a high solubility of fuel and oxygen.

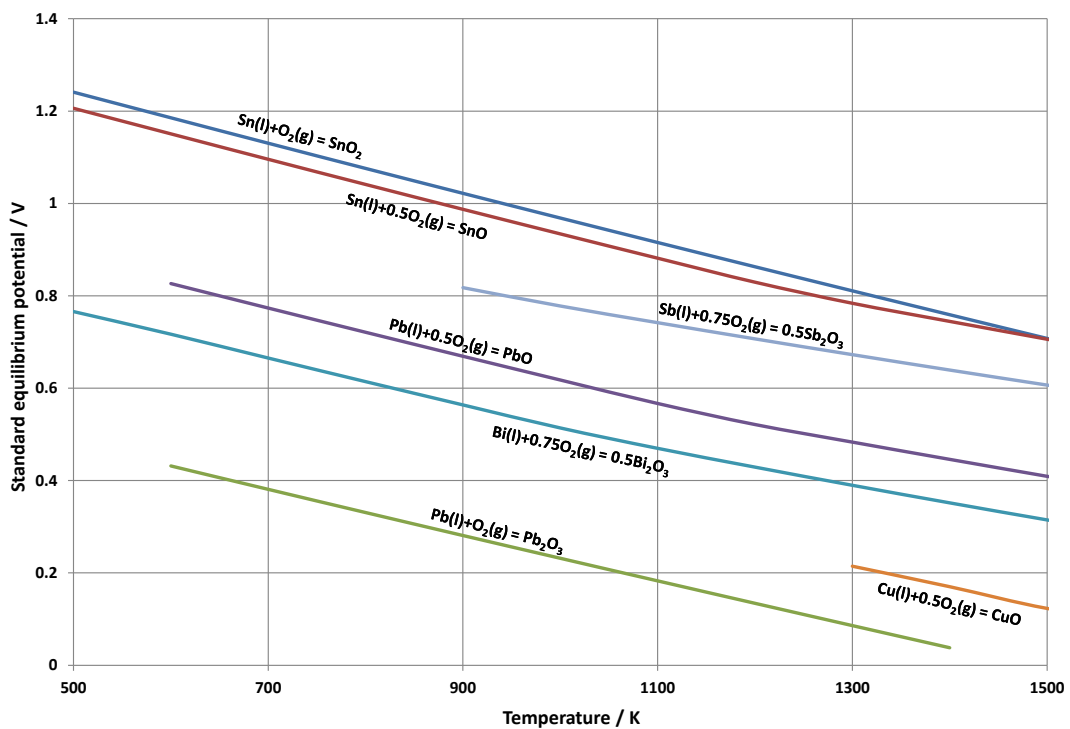


Figure 2.18 Effect of temperature on standard equilibrium cell potentials for various metal oxidation reactions.

Battery Effect

The use of LMAs can have an additional positive impact on fuel cell performance by creating the so-called ‘battery’ buffering effect. It is well known that SOFCs (similar to other fuel cells) can be detrimentally affected by power demand surges during operation, since such surges can cause fuel starvation, which in turn may cause irreversible structural changes at the electrodes. The presence of a certain amount of LMA acts as a metal-oxygen

battery, where the metal itself is oxidised to provide sufficient load^{6,12,61}. The oxidised metal can be reduced again by the fuel fed into the anode when normal load is resumed.

2.3.2.3. Ideal Potential

According to the Nernst Equation, the ideal potential for LTA SOFC can be derived similar to any kind of hydrogen fuel cell and expressed by the following equation⁶²:

$$E_N = \frac{-\Delta G^0}{2F} + \frac{RT}{2F} \ln \left(\frac{a_{H_2(a)} \times a_{O_2(c)}^{\frac{1}{2}}}{a_{H_2O(a)}} \right) \quad (2.40)$$

The simplified form of the above Equation (2.40) is presented below⁶²:

$$E_N = \frac{RT}{4F} \ln \left(\frac{a_{O_2(c)}}{a_{O_2(a)}} \right) \quad (2.41)$$

where E_N is the ideal Nernst potential, ΔG^0 is the Gibbs free energy change for the reaction of production of water from H_2 and O_2 ($H_2 + 1/2O_2 \rightarrow H_2O$).

In their fundamental analysis of the LTA SOFC, Gemmen *et al.*⁶² explained different types of electrochemical equilibrium that occur in the system, such as Anode Gas – Liquid Metal Equilibrium, Liquid Metal – Metal Oxide Equilibrium, and also suggested the pattern of non-equilibrium operation of the system.

For the first case of equilibrium it was assumed that the species in the anode gas phase are in equilibrium with species in the liquid metal. This is possible due to the equal chemical potentials of species in gas phase and in molten metal phase. And hence, at given concentrations of hydrogen and water in the anode gas, the given oxygen activity remains independent of the form in which the oxygen is incorporated (oxide, dioxide, sub-oxide or dissolved oxygen). Subsequently, Equation (2.41) can be written as⁶²:

$$E_N = \frac{RT}{4F} \ln \left(\frac{a_{O_2(c)}}{a_{O_2(m)}} \right) \quad (2.42)$$

where $a_{O_2(m)}$ is activity of oxygen within molten metal.

The activity of oxygen within the molten metal (Sn) is the same, and is equal to the activity of oxygen in the anode gas phase; hence the ideal potential of the system expressed by Equations (2.41) and (2.42) are equivalent.

The second case presented by Liquid Metal – Metal Oxide Equilibrium, where there is a case of formation of metal-oxide phase due to sufficiently large oxygen concentration in the anode. As a result, metal-oxide equilibrates with liquid metal and oxygen at the anode. Assuming that until there is enough oxygen at the anode side to consume all the metal (so

that there is no metal oxide), the ideal potential is only dependent on the activity of oxygen at the cathode side and working temperature⁶²:

$$E_N = \frac{-\Delta G^0_{M-MO_n}}{2F} + \frac{RT}{4F} \ln(a_{O_2(c)}) \quad (2.43)$$

where $\Delta G^0_{M-MO_n}$ is the change in Gibbs free energy for metal oxidation reaction ($M + (n/2) O_2 \rightarrow MO_n$).

In summary, it was shown that Equation (2.41) is applied for general cases; Equation (2.43) is used if it is evident that both metal and metal-oxide exist (e.g. for battery mode, where only conversion of M to MO_n is possible). And finally, the Nernst equation expressed by Equation (2.40) can be applied when H_2 is available for the reaction of hydrogen conversion to water.

In the following figure (Figure 2.19) Gemmen *et al.*⁶² presented the calculated Nernst potentials over a range of temperature for all three cases ($Sn + O_2 \rightarrow SnO_2$; $Sn + 1/2 O_2 \rightarrow SnO$; $H_2 + 1/2 O_2 \rightarrow H_2O$, where the system pressure is 1 atm; partial pressure of O_2 at cathode = 0.21 atm, hydrogen content is about 97%).

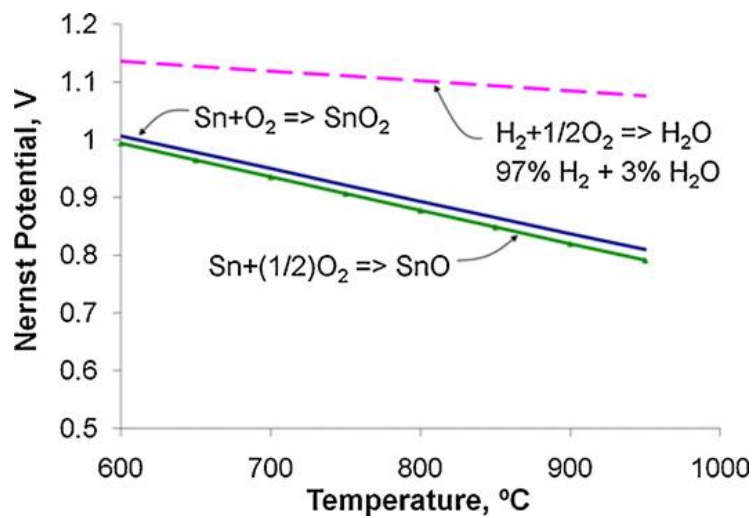


Figure 2.19 Ideal Nernst potentials for LTA SOFC for all three reactions⁶².

According to Figure 2.19, the actual OCV of the system is between two given potential lines. The potentials shown provide a rough estimate of fuel cell performance but in practice the system is not in equilibrium and as stated by Abernathy *et al.*⁶ a higher oxygen activity is present within liquid anode than within the anode gas stream (where H_2 is present) due to some resistance of oxygen flow in liquid melt. At a particular current density, oxygen activity grows considerably compared to oxygen activity in the anode gas phase, leading to formation of metal oxide. The metal oxide produced then blocks the electrolyte interface, reducing the overall cell performance and can pose significant problems⁶².

2.3.3. Liquid Tin Anode SOFC

Liquid tin anode SOFCs (LTA SOFC) have been demonstrated with a variety of fuels, including gaseous, solid and liquid carbonaceous fuels that do not require any processing, reforming or pretreatment to remove sulphur. The power density reported was $>160 \text{ mW cm}^{-2}$ with hydrogen and 120 mW cm^{-2} with JP-8 fuel⁶². Operated at $900 \text{ }^\circ\text{C}$, a layer of molten tin (6 mm) was exposed to humidified H_2 gas (3% H_2O). From the analysis of transient time characteristics, the oxygen (oxide) diffusion coefficient of $1 \times 10^{-3} \text{ cm}^2 \text{ s}^{-1}$ was deduced from test results. The value differs significantly from previously measured literature values⁶². Oxide diffusivity is one of the most critical fundamental parameter that determines cell performance. Inconsistencies in literature reported values call for further work to develop robust methods for the determination of this parameter.

Physical and chemical properties of tin and tin-oxygen systems

Abernathy *et al.* make the case for tin as a good candidate for LMA SOFCs⁶. A comparison table (Table 2.2) summarises physical properties and abundances of various metals that can be used as a liquid anode. The metal should have relatively low melting point (simplifying operational conditions) and high boiling point. Tin has a low vapour pressure ($9.87 \times 10^{-4} \text{ Pa}$ at $1000 \text{ }^\circ\text{C}$) and hence, low volatility¹⁷, i.e. the anode is not vaporised into the fuel exit stream during operation. Being technically easier to operate with, Sn remains the most commonly used anode material for such LMA SOFC systems, though some researchers are seeking alternative anode materials and suggest the use of metal alloys based upon tin. Such factors as metal abundances in the Earth's crust, annual production and associated prices also have to be taken into consideration. Research studies so far have shown results working with tin, copper and bismuth. Other metals may not be suitable due to health hazards (Sb), high price (Ag) or low abundance (In).

Table 2.2 Common metals properties and abundances, prices (adapted from Abernathy *et al.*⁶).

Metal	T_m , / °C	T_b , / °C	Price*/ \$ kg ⁻¹	Abundance in Earth's crust/ ppm	Reported studies using metal and/or metal alloys
Aluminum	660	2520	1.7	83,000	-
Antimony	631	1587	5.0	0.20	19,63 64-69
Bismuth	271	1564	16.3	0.063	21,60,63,70
Cadmium	321	767	2.7	0.10	-
Copper	1085	2563	5.2	79	60
Indium	157	2073	390	0.05	19
Lead	328	1750	1.7	7.9	Pb - ¹⁹ ; Sn-Pb alloy- ²¹ ; Sn-Pb-Bi alloy- ²¹ ; 6,12,13,15-17,20,59,62,64-73
Tin	232	2603	13.9	2.5	
Silver	962	2163	471	0.079	-
Zinc	420	907	1.7	79	-

*The metal prices are taken from US Geological Survey Minerals Information Team, Mineral Commodity Summaries 2010.

Table 2.3 shows the chemical and physical properties of tin at a range of temperatures, including the solubility of oxygen, hydrogen and sulphur. Electrical resistivity of tin at 1000 °C has a reasonable value of 67.1 $\mu\Omega$ cm compared to the resistivity of nickel (53.1 $\mu\Omega$ cm) used in conventional ceramic metal (cermet) SOFC anodes¹⁷. The density of tin and nickel at room temperature are 7.28 g cm⁻³ and 8.90 g cm⁻³, respectively. This makes tin an even more preferable metal on the basis of weight¹⁷. High solubility of sulphur at high temperatures⁷⁴ in the melt is an attractive property of tin, allowing 'dirty' fuels to be used without sulphur removal or fuel reforming.

Table 2.3 Thermophysical properties of tin⁶.

Property	Temperature / °C	Value
Surface tension	232	5.44 mN cm ⁻¹
Viscosity	232	1.85 mN s m ⁻²
Expansion on melting	232	2.3%
Density	800 1000	6.58 g cm ⁻³ 6.48 g cm ⁻³
Resistivity	800 1000	62.1 $\mu\Omega$ cm 67.1 $\mu\Omega$ cm
Gas solubility-oxygen	536 750	0.000018 wt% 0.0049 wt%
Gas solubility- hydrogen	1000 1300	0.04 cm ³ H ₂ /100 g Sn 0.36 cm ³ H ₂ /100 g Sn
Gas solubility - sulphur	800 1000	4.5 wt% 8.0 wt%

The viscosity of liquid tin is not much greater than of liquid water⁷⁵ at 20 °C, 1.002 mN s m⁻², hence the hydrodynamic properties of both fluids are similar. Low viscosity can be exceptionally valuable if for instance a vigorous stirring or rotation inside the melt is required. It may be also useful for circulation of liquid tin anode around the system.

One of the less attractive features of tin is its relatively high surface tension, and hence poor wetting properties. Nogi *et al.*⁷⁶ reported the surface tension of liquid tin measured by the sessile droplet method as a function of temperature and oxygen partial pressure. Surface tension values between 5.5 and 4.95 mN cm⁻¹ were reported for the temperature range of 227 and 827 °C at low oxygen partial pressure. This would primarily affect the liquid tin/ solid electrolyte (typically YSZ) interface when a thin layer of tin is anticipated. In order to resolve this issue an extra mechanical pressure has been applied by some researchers^{16-18,63} on top of the liquid tin to reduce its contact angle and wet the surface of electrolyte.

Reports on hydrogen solubility in liquid tin date back to the 1920's. Abernathy *et al.*⁶ have recently summarised the early papers on H₂ solubility in liquid tin: a value of 9×10⁻⁵ at.% H in tin at 1000 °C or 3.81×10⁻⁷ moles of H₂/100 g Sn was measured by Bever *et al.*⁷⁷ while Iwase⁷⁸ reported 1.4×10⁻² at.% H in tin at 1000 °C (5.9×10⁻⁵ moles of H₂/100 g Sn). Clearly a substantial difference of more than two orders of magnitude in the reported values is evident, possibly due to variation in methods applied, as well as general difficulty of the measurements.

The solubility of oxygen in liquid tin has been measured by Belford and Alcock⁷⁹ using electromotive force (EMF) measurements in the temperature range from 536 °C to 751°C and extrapolated to cover the range from 232 °C to 1100 °C. Measured and predicted values for oxygen solubility in liquid tin are shown in Table 2.4.

Table 2.4 Solubility of oxygen in liquid tin⁷⁹.

Temperature / °C	Direct values /at.% [O]	Method
536	0.0012	Measured
600	0.0042	Measured
700	0.0190	Measured
751	0.0360	Measured
780	0.0561	Predicted

Similarly Ramanarayanan and Rapp⁸⁰ have reported solubility of oxygen in liquid tin using (EMF) measurements in the temperature range of 750 to 950 °C. The following expression was derived from experimental data obtained:

$$N_O^s(\text{Sn}) = 1.3 \times 10^5 \exp\left(-\frac{30000}{RT}\right) \quad (2.44)$$

where $N_O^S(Sn)$ is the solubility of oxygen in at.%, R is the gas constant in $\text{cal K}^{-1}\text{mol}^{-1}$, and T is the absolute temperature in K.

At a temperature of 780 °C (the operating temperature in present work) Equation (2.44) predicts an oxygen solubility of 0.08 at.%.

The possible states of oxygen in liquid tin have been recently determined by Cahen *et al.*⁸¹ and presented in the form of Sn-O phase diagram (Figure 2.20). From the diagram the solubility limit of oxygen is about 2 at.% at 1000 °C. Beyond this point tin dioxide (SnO_2) precipitates in the solution (melt). This number is almost twice that calculated by the previous Equation (2.44) – 0.91 at.% at 1000 °C.

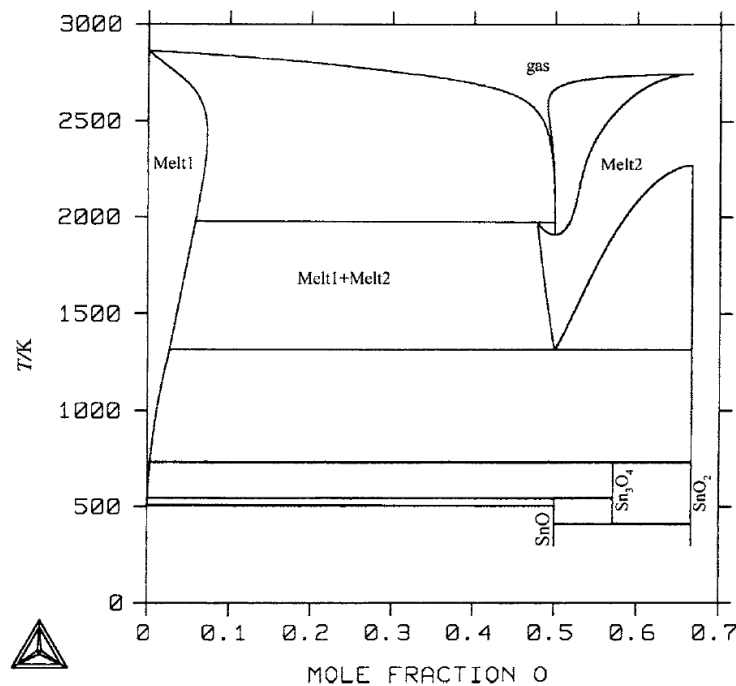


Figure 2.20 Sn-O phase diagram determined at 1 bar⁸¹.

Abernathy *et al.* have also attempted to determine the oxygen solubility in the liquid tin anode in order to further refine the existing data in the literature⁶. An oxide ion flux was assumed to be a measure for the dissolved oxygen concentration when currents of various magnitude were supplied to the LTA SOFC at an operating voltage of 0.78 V (the potential at which tin is suggested to convert to tin dioxide). As a result, a value of 0.8 at.% at 1000 °C was found to be in fair agreement with 0.91 at.% given by Ramanarayanan and Rapp. The phase diagram for Sn-O system was also composed by Abernathy *et al.* using the FactSage™ 5.6 thermodynamic modelling software (Figure 2.21).

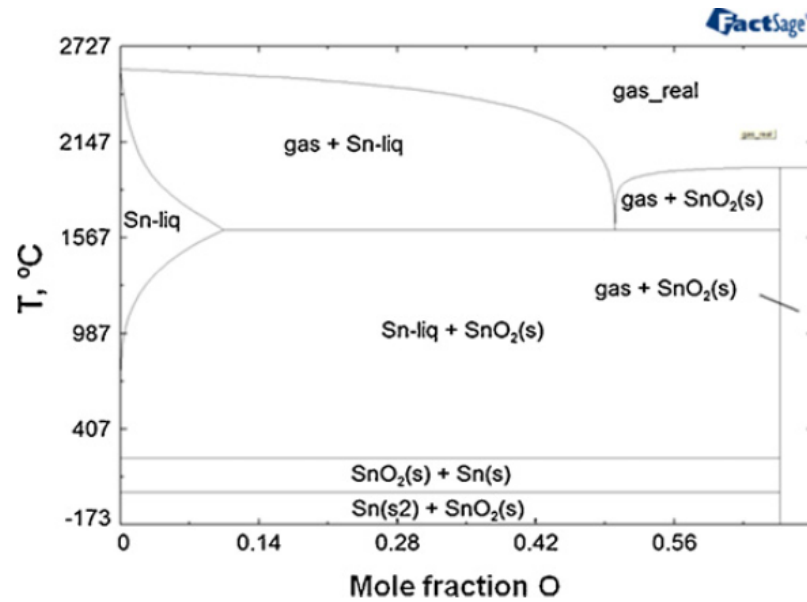


Figure 2.21 Sn-O system phase diagram calculated at 1 bar⁶.

From the obtained phase diagram, oxygen solubility at 1000 °C was found to be 0.5 at.% with a maximum oxygen concentration of about 10 at.% at 1600 °C. Both values for 1000 °C are closer to the value calculated using Equation (2.44).

Clearly there is a discrepancy in the literature data on oxygen solubility in liquid tin, including data obtained from thermodynamic modelling as well as experimental measurements. Saturated oxygen concentration is a parameter of technological significance for LMA SOFCs, as fuel oxidation rate is governed by dissolved oxygen in liquid tin. The enhanced solubility of oxygen in liquid metal results in greater power output from a fuel cell. Therefore, calculation of its value is essential for the development of LMA SOFCs.

Precipitation of tin oxides (SnO or SnO_2) occurs if oxygen is constantly added to liquid tin, exceeding its solubility limit. From differential scanning calorimetry measurements Bonicelli *et al.*⁸² confirmed that only SnO_2 is found in the system at temperatures greater than 525 °C. Precipitation of SnO_2 in liquid tin affects the performance of Sn-based SOFC systems due to a substantial difference in physical properties of a pure metal and its oxide. Tin dioxide is an n-type wide-gap semiconductor with a bulk conductivity of 0.3 S cm^{-1} at 1000 °C⁸³ for a dense structure of SnO_2 . Lower conductivity is found for less dense layers of SnO_2 ⁸⁴. Reduction of conductivity upon formation of even thin layers of SnO_2 may explain the decline in the performance of a Sn-based LME SOFCs. At high temperatures tin dioxide becomes denser than liquid tin with calculated densities of 6.98 and 6.58 g cm^{-3} at 800 °C for SnO_2 and molten tin, respectively^{6,85}. This difference in the density is another factor that may adversely influence the overall fuel cell performance. As a result of those factors the power output of liquid tin anode SOFCs (operated in a vertical orientation)

typically decline upon formation of even the first thin layers of SnO₂. The former aspect potentially increases the resistivity in a fuel cell. The latter is responsible for the fact that the SnO₂ layer will not float to the top of the molten tin, but sink and hence block the active liquid tin/electrolyte interface. Therefore, formation and precipitation of a dense and less conductive layer of SnO₂ should be monitored and ideally eliminated.

Fuels Investigated

Various fuels have been studied for LTA SOFCs including biodiesel¹², military fuels, such as JP-8^{13,15,16}, gasoline, methane, etc. All these studies confirm the LTA SOFC fuel flexibility. The measured efficiency of LTA SOFC operated on hydrogen, carbon and coal compiled 50%, followed by plastic with efficiency of 45%, diesel and natural gas- 40%¹³.

2.3.4. Electrochemical Characterisation of LME SOFCs

A significant amount of work has been done on electrochemical testing of SOFCs with a variety of liquid anodes. Tin, as explained in Section 2.3.3, remains the most common anode material. Hence, more liquid tin anode studies have been published recently. However, in this section studies on liquid tin and/or other anode metals, metal alloys anodes relevant to the current project are reviewed.

2.3.4.1. Electrochemical Characterisation of liquid tin anode SOFCs

The first studies on LTA SOFC were performed by Cell Tech Power LLC¹⁷ with subsequent focus on application of LTA SOFC for distributed power generation using natural gas. The next step was to test alternative fuels such as waste plastics and military logistic fuels (e.g. JP-8) applicable for portable applications, followed by studies where biomass and coal are considered to be directly converted in LTA SOFC. Tao *et al.*¹⁷ initially developed the Gen 3.0 cell and stack and demonstrated a power density of 40 mW cm⁻² with JP-8 fuel. Cell performance was significantly improved in the next generation cell - Gen 3.1, which was lighter by a factor of four. The operational power density was 120 mW cm⁻² with JP-8 fuel that contained 1400 ppm of sulphur¹⁷. This study confirmed the operation of LTA SOFC without fuel desulfurization or pre-processing. To overcome existing drawbacks of the previous cell design (Gen 3.0) an alumina porous separator was introduced to increase fuel mass transport to liquid tin. Prior to testing with JP-8, Gen 3.1 was tested with hydrogen to ensure proper cell operation (Figure 2.22a).

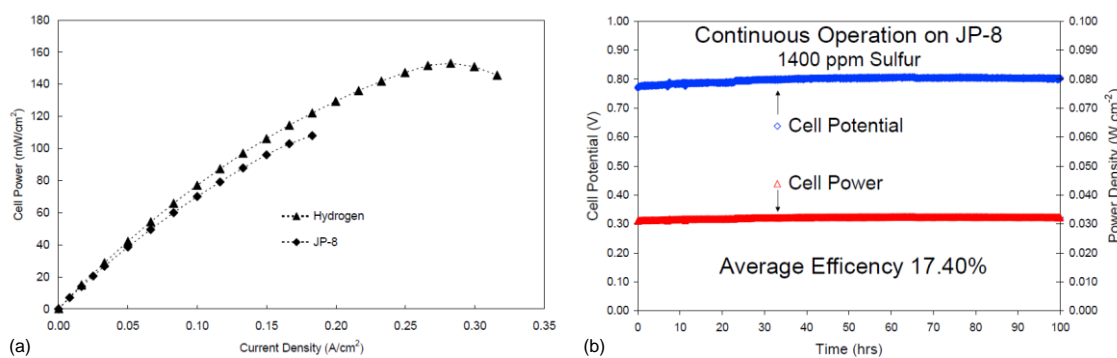


Figure 2.22 Power curves for tin based cells operating on hydrogen and JP-8 (a); durability test on JP-8 (V, W) (b)¹⁷.

At equal operating conditions the cell fed with JP-8 showed 70-80% of the cell performance compared with hydrogen: the maximum current density for hydrogen was 316 mA cm^{-2} and 220 mA cm^{-2} for JP-8, corresponding to a maximum power density of 153 mW cm^{-2} and 120 mW cm^{-2} , respectively. In terms of durability, Gen 3.1 with JP-8 demonstrated an average efficiency of 17.4% at 30 mW cm^{-2} for the 100 hour durability test. The whole durability test is illustrated in Figure 2.22b. The next generation of cells aims to reach $>200 \text{ mW cm}^{-2}$ power density with the military fuels. To achieve this a more detailed evaluation of separator properties such as porosity and stability for long-term operation is still needed¹⁷. It has been pointed out that interactions between the liquid tin anode and fuel have not been systematically studied and that better modelling and a fundamental study are needed.

Direct conversion of biodiesel has been demonstrated using the LTA SOFC¹². In an approach similar to that adopted for JP-8, a tubular LTA SOFC cell was tested for 4.5 h with biodiesel (B100) prepared from virgin and waste cooking oils¹². Peak power and current density values of 117 mW cm^{-2} and 217 mA cm^{-2} and overall cell efficiency of 40% were reported. The results of the study also verify the fuel flexibility of the LTA SOFC system.

An interesting approach of using a separate electrochemical reactor coupled to an external chemical reactor with liquid tin anode SOFC was proposed by Colet Lagrille *et al.*⁷⁰. The system oxidizes carbon directly in fuel cell mode and produces H_2 in the electrolyser mode. The schematic of two separate reactors is illustrated in Figure 2.23. The approach has the advantage of allowing the ‘combustion’ (fuel oxidation) process and the electrochemical oxidation of the melt to be optimized in two separate reactors; it also improves mass transport losses. The disadvantage is that pumping of liquid metal between the reactors is necessary. This study also reports a 2D model of a micro-tubular hollow fibre fuel cell to predict distribution of oxygen concentration within the liquid tin anode⁷⁰. The diffusion

coefficient of oxygen in tin was assumed and the authors highlighted the need for accurate determination of this parameter for reliable model prediction.

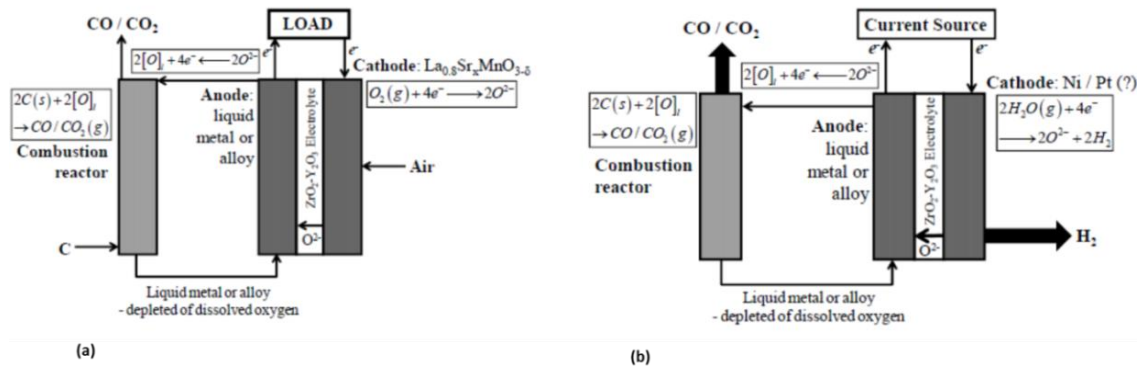


Figure 2.23 (a) Schematic of a LMA SOFC coupled to an external combustion reactor, (b) Schematic of a LMA Solid Oxide Electrolyser (SOE) coupled to an external combustion reactor⁷⁰.

Operation of LTA SOFC in a battery and fuel cell mode (fed with hydrogen and coal) was recently evaluated using the EIS technique by Khurana *et al.*⁷². From open circuit voltage (OCV) measurements reduction of SnO_2 with hydrogen was found to be more effective with respect to coal. This confirmed that H_2 remains the most efficient fuel in SOFC with liquid metal anodes. On the contrary, the fitting of EIS spectra revealed the lowest ohmic and charge transfer resistances when LTA SOFC was operated with argon (in battery-mode), followed by coal and finally with H_2 . The H_2 -fed cell resulted in the greatest overall resistance with extra mass-transfer resistance explained by more complicated fuel oxidation process compared to simplified oxidation of tin to tin dioxide in battery-mode.

A similar study to the above with opposing EIS results was reported by Wang *et al.*⁷³. Deterioration of LTA SOFC with a single crystal YSZ electrolyte was demonstrated using both the polarisation curves and EIS spectra. The Sn-based cell was operated in battery and fuel cell mode (fed with H_2 , CO and solid carbon). H_2 fuel was found to be the most efficient for reduction of SnO_2 which showed a better performance compared to all other fuels (from both OCV and I-V curves). Performance of a cell in a battery mode was the poorest, indicating that the presence of active fuel is essential for such systems (to reduce SnO_2 species in the melt). A constant ohmic component in battery mode and fuel cell mode (with H_2 and CO) contributed ca. 2.3Ω , whereas the non-ohmic contribution was maximum in battery mode, followed by CO and finally H_2 . Those losses were associated with the rate of reduction of SnO_2 via different fuels. Hence a cell with H_2 fuel showed the best performance compared to CO, carbon or without fuel (in battery mode). These findings contradicted those of Khurana *et al.*⁷². The EIS data reported by Wang *et al.* were supported by cyclic voltammetry tests that showed a deterioration of performance and limiting current densities, reducing upon using H_2 , CO and without fuel. Good correlation

between the results obtained by OCV, polarisation curves and EIS data provides more confidence in the findings demonstrated by Wang *et al.* The discrepancy found between these two studies indicates the need for further investigation with the EIS technique.

Degradation of LTA SOFC in both studies was claimed to be due to an accumulated layer of SnO₂ that blocked the active interface for diffusion of O²⁻ ions. Deteriorated LTA cell made of single crystal YSZ electrolyte was further evaluated with SEM and Energy-dispersive X-ray spectroscopy⁷³. Apart from porous and crystal layers of SnO₂, another layer of SnSZ was suggested to exist at the surface of the electrolyte. That SnSZ layer indicated the possible agglomeration of Sn with the surface of single crystal YSZ and its reaction with YSZ⁷³, which may be another operating challenge in LTA fuel cells. To confirm this there is a need for microstructural evaluation of liquid tin/electrolyte interface particularly after long-term operation of such systems.

2.3.4.2. Alternative metals and metal-alloy anodes for LME SOFC

Other metals and metal alloys have been demonstrated as interesting anode materials capable of direct carbon oxidation in novel SOFCs. As presented in Table 2.2, most common liquid metal anodes are made of tin, antimony, bismuth, lead, indium, copper, and rarely - silver.

Liquid antimony

Liquid antimony has been assessed as an anode for DCFCs¹⁸. Operating at 973 K and employing a scandia-stabilized zirconia (ScSZ) electrolyte, the system, incorporating an air electrode but with no input of fuel, has demonstrated an open-circuit voltage (OCV) of 0.75 V for the redox couple Sb - Sb₂O₃. Having an anode electrode resistance of 0.06 Ω cm², the operated power density was 350 mW cm⁻². As expected, the addition of sugar char immediately increased the cell voltage as the Sb₂O₃ was reduced with fuel, preventing formation of a metal oxide layer on the electrolyte surface. Scaling up of such liquid antimony DCFC technology may require an increase in the rate of reaction between fuels and antimony oxide, as some carbonaceous fuels (carbon black, rice starch) have not demonstrated any interaction with liquid Sb¹⁸.

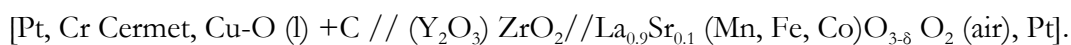
Substantial work has been done recently with Sb molten anodes by research group in Tsinghua University, China. The effect of electrolyte morphology on the performance of Sb-based cells was investigated⁶⁹. Increase of surface roughness of electrolyte resulted in improved performance of a fuel cell due to enhanced effective contact area of Sb anode. Formation of antimony oxide, which is liquid at operating temperature (800 °C), had a positive effect on the fuel cell performance due to intrinsic Sb₂O₃ electrical conductivity of

0.0792 S cm^{-1} at $828 \text{ }^\circ\text{C}$ ⁶⁶. In further studies (in battery mode) it was shown that changing the ratio of Sb to Sb_2O_3 (in the melt) to 50:50 resulted in reduced anode resistance of $0.8 \text{ } \Omega \text{ cm}^2$ which is similar to that for porous solid anodes⁶⁴. A numerical model was later developed to fit experimental characterisation of an Sb-cell operating in a battery-mode⁶⁵. Other studies of this group related to evaluation of Sb-based fuel cells for direct oxidation of coal⁶⁶⁻⁶⁸. As shown above by Jayakumar *et al.*, addition of a fuel (de-ashed coal) into molten Sb enhanced the fuel cell performance, although smaller coal particles were proposed to be used for further improvement. However, the problem with accumulated Sb_2O_3 layer at the interface remained un-changed since the first work on liquid antimony SOFCs.

Liquid Copper

Successful performance of LME direct carbon fuel cell (DCFC) has been demonstrated using a molten copper anode operating at 1373 K ⁶⁰. The overall conversion efficiency measured at maximum power density was 62.5%.

Design of this system was different to those discussed earlier in the way that the cathode-supported YSZ tube was immersed into liquid copper media. Figure 2.24(a) shows the schematic presentation of the system:



The fuel (coke particles) was added via an alumina inlet tube and stirred thoroughly with a stirrer; the entire cell was suspended in a vertical furnace. The OCV of the system was measured to be 1.2 V, and generated a maximum power density of 1.7 W cm^{-2} (2.25 A cm^{-2} at 0.75 V) as shown in Figure 2.24(b).

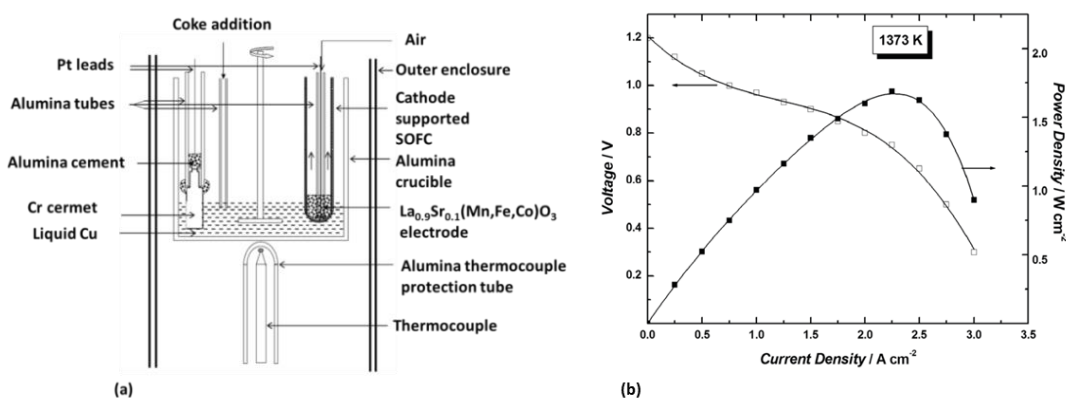


Figure 2.24 (a) Schematic of liquid copper anode SOFC, (b) polarisation and power density curves for liquid copper anode SOFC⁶⁰.

Despite good overall performance, liquid copper SOFCs are difficult to operate. The relatively high vapour pressure of copper, compared to tin and other metals, is a challenge for practical operation. In addition, copper anodes necessitate very high operating

temperatures (melting point at 1358 K), which inevitably complicates operation of the system.

Liquid bismuth

Liquid bismuth has been reported to have an inferior performance to tin anodes²¹. The OCV was reported to be slightly lower than theoretical (440 mV): 424 mV with hydrogen supplied and 408 mV without²¹. Being ion-conductive, bismuth oxide may solve the problem with oxide transport blockage through YSZ-anode media⁷⁰. However, operating at lower power densities, liquid bismuth SOFCs require in-depth investigation and are not considered to be a feasible alternative to SOFCs with a tin anode^{60,63}. Possible reaction of bismuth oxide with yttria (Y_2O_3) in YSZ electrolyte may affect the structure and the properties of electrolyte⁸⁷⁻⁸⁹. Similar to antimony bismuth has low vapour pressure⁹⁰, which is also toxic. This adds to the list of disadvantages of this anode.

Other metal anodes for LME SOFCs

Indium (In), lead (Pb), antimony (Sb)¹⁹ and silver (Ag)⁹¹ have also been examined in battery and fuel cell modes (if feasible) to test their anodic efficiency in LME SOFCs. Similar to tin, the performance of indium was adversely affected by formation of metal oxide at the electrolyte interface when higher current was drawn. This was not the case for Pb and Sb, where the melting points of their metal oxides were lower than the operating temperature. Direct oxidation of coal has also been proposed to operate in a liquid iron anode SOFC⁹².

The application of a liquid silver anode for DCFCs has been experimentally explored by Javadekar⁹¹ who achieved an OCV of 1.12 V with charcoal. Liquid silver has lower melting point and higher oxide solubility compared to other metals (e.g. copper) and therefore is advantageous. Another approach was to use a Ag-Sb alloy, where the high solubility of oxide in silver might be combined with the low melting point of Sb, to improve overall anode performance⁹¹.

Metal alloy anodes

In an effort to optimize anode properties, various alloy systems have been investigated. The work involving the pure metal anodes (bismuth) mentioned above was developed further to explore anodes of liquid tin-lead and liquid tin-lead-bismuth alloys in battery mode followed by direct oxidation of coal²¹. For the tin-lead alloy, performance degradation (from 11.7 mW cm⁻² to 10.1 mW cm⁻²) occurred within 13 hours, with an increase in performance to 14 mW cm⁻² when coal was introduced. The addition of bismuth to tin-lead alloy decreased the overall anode effectiveness.

2.3.5. Uncertainties and technological challenges of LMA SOFC

With increased interest in LMA SOFCs most of the early studies had focused on the operation of various LMA SOFCs in battery and fuel cell modes using various fuels. Significant efforts have been made in optimisation of electrochemical performance via replacement of anode materials (metals, metal-alloys), investigation of kinetics and thermodynamics, examining the effect of electrolyte roughness, etc.

Prior to commercialization of liquid metal anode solid oxide fuel cells, greater understanding of the electrochemical reactions, redox and transport processes within liquid metal electrodes is needed⁶². The following research challenges are particularly highlighted: the nature of oxidised species in liquid metal electrode media; transport of oxygen or oxidized species in LME SOFC; reaction kinetics between oxide and fuel within liquid anode; kinetics of oxygen transfer at liquid metal anode - electrolyte interface; oxygen (oxide) diffusivity / transport through liquid metal layer and solubility of oxygen and fuels in the melt.

As stated by Abernathy *et al.*⁶, improvement of oxygen transport within liquid metal media can be achieved by increasing oxygen solubility through alloying. Wetting characteristics of liquid metal with the electrolyte and fuel oxidation kinetics also need to be considered.

Most of the work so far has been focused on the testing of single cells, which limits its further application. In this regard, it would be beneficial to model the performance of LME SOFCs stacks and prototypes based on derived design guidelines.

In order to be able to model and later design practical LME SOFC systems the information on oxygen solubility and transport in liquid metals is essential as it is a central process that may limit the performance of the fuel cell. Fundamental investigation of these interactions within a liquid anode, as well as analysis of other physical metal properties with temperature (e.g. vapour pressure, melting point, surface tension, contact angle, etc.) will be beneficial in designing and building durable and stable fuel cells.

Other important factors requiring investigation include: aspects concerned with the introduction of solid fuel into the melt; optimization of thickness of the melt; prevention of unfavourable formation of metal oxide tending to result in blocking of the electrolyte; fundamental studies concerned with transportation of the oxide from the generation zone at the interface with the electrolyte to the reaction zone at the interface with the fuel (relevant aspects include melt thickness, diffusion of oxidised species and convection in the melt); effect and optimization (which may include surface structuring) of contact area between the liquid anode and electrolyte.

Engineering considerations include: matching of electrolyte composition to temperature of operation; choice of electrolyte thickness based upon optimization between mechanical properties and ionic conductivity; agitation of the melt; generation of suitable electrolyte surface structures; cell design; scale-up of laboratory cells to pilot and then to commercial plant.

LMA SOFCs are a highly efficient option for direct electrochemical conversion of solid fuels into electrical energy. A range of possible metal anodes have been reviewed with tin, the material on which most development work has been performed. Despite numerous studies, the understanding of the reaction kinetics at liquid metal-fuel and liquid metal-electrolyte interfaces, as well as oxygen diffusivity through the liquid metal layer needs further systematic investigation.

2.4. Conclusions

In the previous sections of this chapter recent advances in SOFC technologies, as one of the environmentally friendly and highly efficient options for direct electrochemical conversion of fuel energy into electrical energy were presented. The main focus of this review was to understand novel methods in SOFC technology using molten metals. The metal that received the greatest attention was tin; therefore, the working principle and operational conditions of Liquid Tin Anode SOFCs were addressed in detail. It was concluded that theory concerning thermodynamics and reaction kinetics in liquid metal – fuel and liquid metal-electrolyte media, as well as oxygen diffusivity through the liquid metal layer needs further investigation. Furthermore, the main difficulties and uncertainties associated with LTA SOFC and the ways they can be addressed are highlighted. Possible incorporation of LME SOFC into Solid Oxide Electrolyser (SOE) was described briefly. SOE offers simultaneous production of pure hydrogen gas and carbon monoxide via electrochemical processing of carbon dioxide and steam.

3. Experimental methods and equipment

This chapter demonstrates the design and development of an experimental workstation and electrochemical cells applied in LTA SOFC studies. The principles of electrochemical characterisation techniques such as Linear Potential Sweep methods, Chronoamperometry, Electrochemical Impedance Spectroscopy and Rotating Disc Electrode applied during this research project are also summarised.

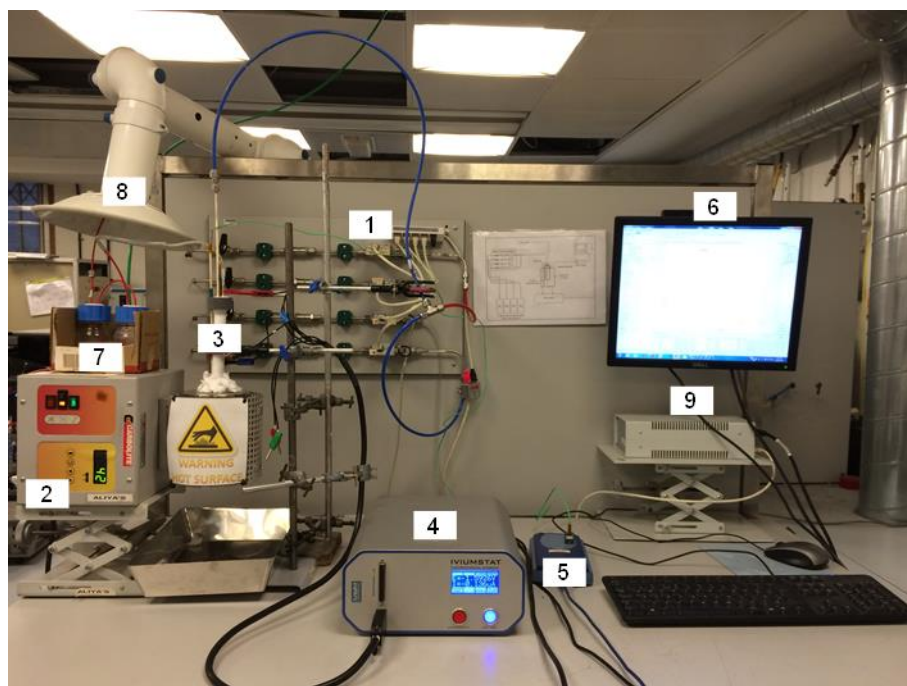
3.1. Experimental workstation

A new experimental workstation for carrying out experimental work was designed and built during the first year of the project. The workstation is shown in Figure 3.1 and comprises the mass flow controllers (EL-FLOW, Bronkhorst UK Ltd., UK) (mounted on a board) to maintain gas flow at the required set point up to 100 ml per minute (1.67 ml s^{-1}) for hydrogen and nitrogen and up to 140 ml per minute (2.3 ml s^{-1}) for argon. All gases (BOC, UK) used were zero grade purity of 99.998%, 99.995% and 99.999% for nitrogen, hydrogen and argon respectively. Inline micron gas filters (Swagelok Ltd., UK) were mounted on a board upstream of the mass flow controllers.

Gases were supplied under pressure of 4 bar from gas cylinders to the electrochemical cell in a 1/4" (6.35 mm) OD tubing made of stainless steel, nylon, vinyl (PVC) (Swagelok Ltd., UK) as well as 4 mm OD, 2 mm ID silicone peroxide tubing (VWR International Ltd., UK). Stainless steel valves, T-connectors, compression fittings (Swagelok Ltd., UK) were applied throughout the project to supply gases with minimum leakage.

The supply of fuel (typically a mixture of H_2/N_2 or H_2/Ar) direct into the liquid tin anode was achieved using 4 mm OD 2 mm ID alumina tube open both ends. Because of the delicacy of alumina material Teflon front and back ferrules (4 mm OD, Swagelok UK) were applied with stainless steel union to fit to the stainless steel piping.

An electrochemical cell was heated up to the required operating temperature in a MTF-10-25-130 (normally horizontal) tubular furnace (Carbolite Ltd., UK) operated in a vertical orientation. A K-type thermocouple (Omega Engineering Inc., UK) was placed parallel to the cell to measure its temperature independent of the furnace temperature controller. The readings from a thermocouple were recorded via a thermocouple data logger (TC-08 Pico Technology, UK) connected to a PC. Temperature data were recorded using a LabVIEW based software code written and used with the thermocouple data logger.



- | | |
|---|---|
| 1. Mass flow controllers mounted on a board | 6. PC Monitor |
| 2. Electrical furnace (held in vertical orientation) and controller | 7. Schott water bottles |
| 3. Electrochemical cell | 8. Extractor |
| 4. Potentiostat | 9. Power supply for mass flow controllers |
| 5. Thermocouple Data Logger | |

Figure 3.1 Experimental workstation.

An electrochemical cell was placed in the central part of the furnace and held from the outside of the furnace with laboratory clamps. Such positioning was necessary because, in accordance with the temperature profiles measured (refer to Appendix A), the maximum and uniform temperature region of the tubular furnace was located in the centre of the furnace.

Electrochemical measurements were made using an IviumStat potentiostat (Ivium Technologies B.V., The Netherlands). The unit has a potential range of ± 10 V and a current range of 5 A to 1 pA. The unit was used to control the voltage generated by the system (in a fuel cell mode) and measure the current (potentiostatic mode). Furthermore, the losses from the wires were accounted through the reference and sense electrodes. Electrochemical Impedance Spectroscopy measurements were performed using the IviumStat potentiostat.

The initial workstation shown in Figure 3.1 was modified throughout the project depending on various research objectives. As a result, each experimental chapter in this

this thesis provides a list of changes made to the original workstation, as well as detailed schematics of the particular experimental rig applied.

A schematic of the generic experimental rig employed most frequently (see Chapters 6,7,8 and 9) is shown in Figure 3.2, which demonstrates the final design of the rig station after considering the sizes and compatibility of the equipment.

According to Figure 3.2, dry or humidified argon was supplied to the oxygen sensor (Kent Industrial Measurements, UK) after which it was mixed with hydrogen and supplied to the cell held at operating temperature by an electric furnace. The oxygen sensor was added to the original rig to monitor the oxygen concentration in the flow to the main cell.

Water bottles placed at two different locations in the experimental rig (Figure 3.2) were used for two different purposes. The humidification of gases was achieved using the first two bottles; the other two bottles located downstream of the fuel cell were necessary to check that the system had no leaks and furthermore, stopped the diffusion of air (oxygen) back into the fuel cell. After exiting the fuel cell, the supplied gas bubbled through the water bottles providing an indication of positive pressure within the system.

Note that an empty bottle was incorporated into each line to ensure that water could not be sucked back into the fuel cell. Such an event could be catastrophic potentially causing cracking of a ceramic tube.

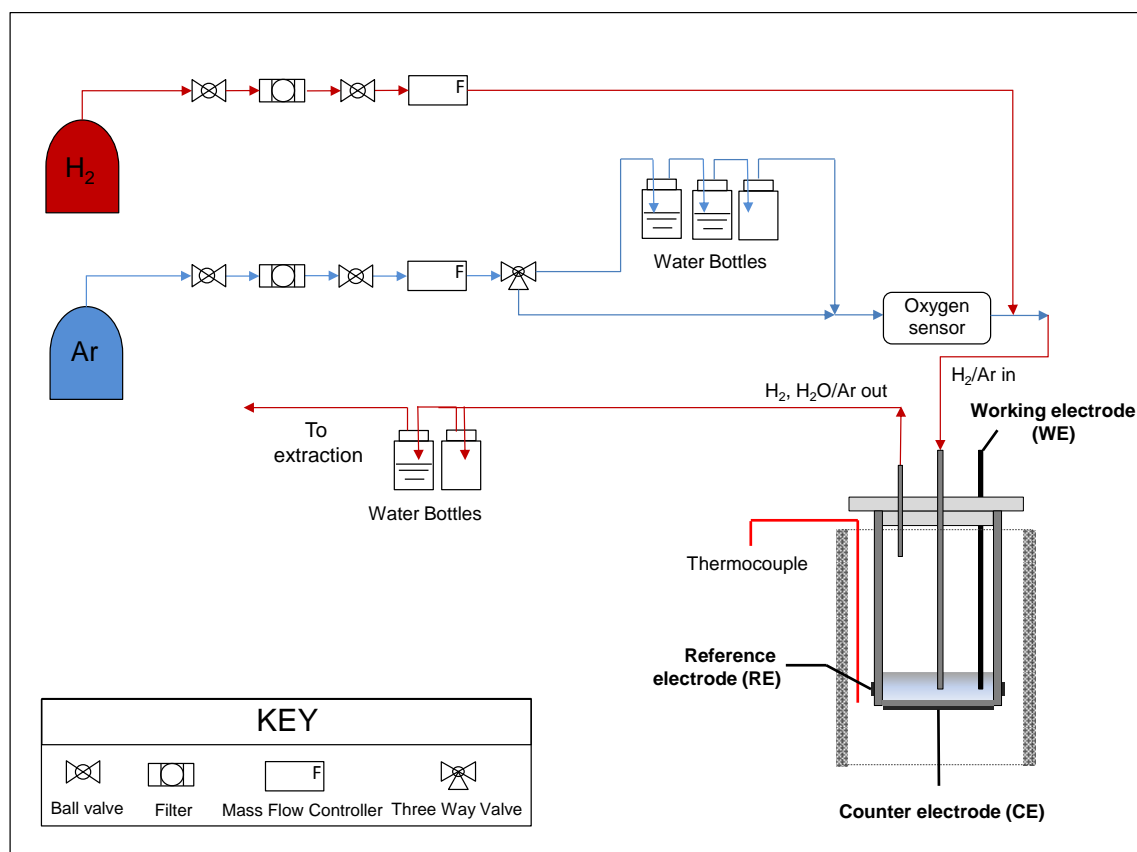


Figure 3.2 Schematic of experimental rig used for fuel cell testing.

3.2. Electrochemical cell

Experimental work undertaken throughout this project varied significantly. Therefore several working cells were developed, depending on the primary aim of their operation: *symmetrical cell* (used for operation of yttria-stabilised zirconia (YSZ) tube as oxygen sensor and to measure its ionic conductivity); *fuel cell* (electrochemical cell for testing of performance of LTA SOFC).

3.2.1. Symmetrical cell

In order to investigate ionic conductivity of the YSZ material (chosen for its good conductivity at high temperatures) with temperature two symmetrical cells were prepared. The first one was used in potentiometric measurements and operation of YSZ tube as an oxygen sensor. The second one was used to measure ionic conductivity of YSZ material using Electrochemical Impedance Spectroscopy (EIS).

The first symmetrical cell (Figure 3.3a) was made of 10 mm OD 8 mm ID 120 mm long 10 mol.% YSZ (10YSZ) tube, closed at one end, with two platinum electrodes on the outer and inner sides of the tube. Platinum wires were attached to each electrode for electrical connection. The method for preparation of Pt electrodes is provided in Section 3.2.3. The average electrode active area was 0.79 cm².

The second symmetrical cell was made of 6YSZ tube specifically for EIS measurements and had a greater and more defined electrodes area of 1.30 cm² with an electrolyte thickness of 0.5 cm (Figure 3.3b, c). Attached Pt wires were held in 5 mm OD two-bore alumina tube (Multi-Lab Ltd., UK) (open both ends) to provide electrical isolation and minimise inductive effects at high frequency during the EIS measurement.

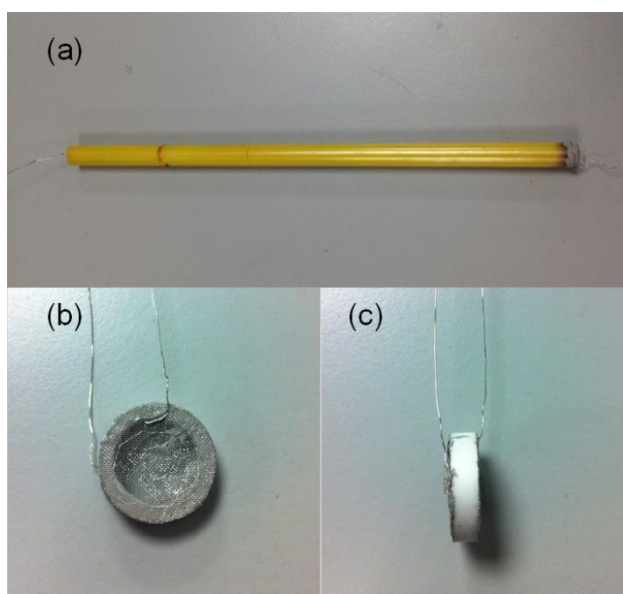


Figure 3.3 Symmetrical cell: (a) 120 mm long 10YSZ cell for potentiometric measurements; (b) 6YSZ symmetrical cell for EIS measurements (front view) and side view (c).

3.2.2. Fuel cell

Prior to fabricating actual fuel cells to be used at high temperatures ($> 800\text{ }^{\circ}\text{C}$) it was essential to make a robust design of the electrochemical cell. The 3D design of the cell was completed using CAD Rhinoceros 4.0 software (Figure 3.4). The working cell consisted of a closed-end 8YSZ tube (Dynamic-Ceramic Ltd., UK). The 8YSZ tube was used as a vessel to contain the liquid metal anode, current collector to the anode, alumina tubes for fuel inlet and exhaust, all held using a pyrophyllite (machinable ceramic) holder. Counter and reference platinum electrodes were painted on the outer side of YSZ tube at a later stage (cell preparation) and are not shown in the basic cell design.

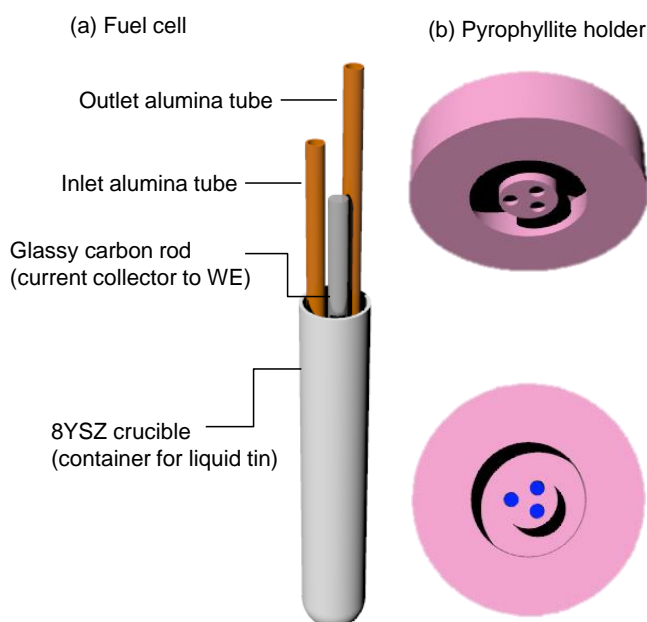


Figure 3.4 The 3D design of the fuel cell (a): closed end YSZ tube with fuel inlet, exhaust and current collector and pyrophyllite holder (b).

The heating zone inside the employed furnace was relatively short (ca. 140 mm). And the temperature profile inside that zone was found to be uniform only in the limited central part (refer to Appendix A). Therefore a separate K-type thermocouple was placed next to the YSZ tube for accurate temperature determination. As a result, the initial holder design was modified from that in Figure 3.4 to that in Figure 3.5, where the pyrophyllite holder was re-designed to accommodate an additional alumina tube for the thermocouple placed parallel to the main cell.

Figure 3.5 illustrates how all the parts of the cell were assembled together, where the YSZ tube cell is shown transparent to demonstrate at what levels the inlet, outlet tubes and glassy carbon rod were placed inside the YSZ tube to provide sufficient bubbling into the liquid tin and good electrical contact with the tin.

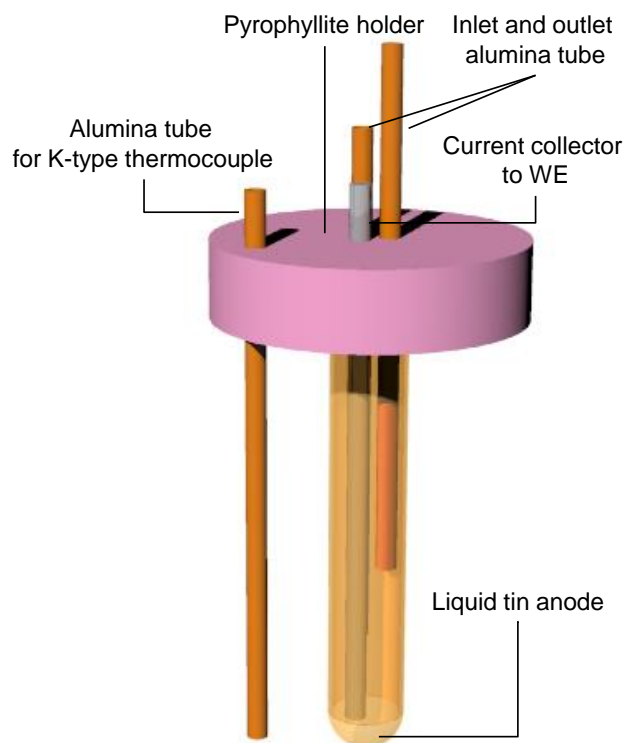


Figure 3.5 Updated fuel cell design with YSZ thermocouple placed parallel to the vessel.

3.2.3. Fuel Cell components

Electrolyte

The 8 mol.% yttria-stabilised zirconia (8YSZ) solid electrolyte was chosen due to its ability to operate at high temperatures and has been shown to have good mechanical strength and oxygen ion conductivity of 0.13 S cm^{-1} at 1273 K ⁹³.

In order to minimise the ionic resistance, the electrolyte thickness is usually in the range of $50\text{-}1000 \text{ }\mu\text{m}$ ⁹⁴. As one of the main objectives of this study is to clarify transport of oxidised species within the liquid anode and not to maximise the fuel cell performance, the electrolyte thickness chosen for this project was $2000 \text{ }\mu\text{m}$ in order to contain the molten anode (around 25-30 g) safely and securely.

Working electrode (Anode)

Tin was chosen as the anode material for this project due to its low melting point (232° C) and low vapour pressure. Tin shots of 3 mm dia., 99.99+% (metals basis) (Alfa Aesar, UK) were used. Once it is melted at ca. 240° C it can be immediately used as a liquid anode.

Counter and Reference Electrodes

A platinum electrode was chosen as the cathode, as it has high electrical conductivity and high catalytic activity for the oxygen reduction reaction⁵. Glass-free Pt ink (4082 Pt Vitro-Au-Less Conductor, Ferro Electronic Materials) was applied to the outer side of the YSZ tube followed by its sintering at 1000 °C for 1 hour at a ramping rate of 10 °C per minute. Pt mesh (10 mm diameter, Goodfellow Cambridge Ltd, UK) with spot welded Pt wires (0.25 mm diameter, 99.9% Pt, Peak Sensors Ltd) on it were attached with additional ink to cured platinum and sintered again under the same conditions to achieve good electrical conductivity across the whole surface.

A reference platinum electrode was placed 10 mm up from the bottom of the YSZ tube symmetrically around the tube. Attachment of Pt wire to the reference electrode was difficult to achieve and for that reason a groove was cut 0.5 mm deep around the outside of the ceramic tube to hold the wire in place. The wire was then twisted and fired at 1000 °C as described above.

Accurate location of the reference electrode is well established for aqueous electrochemical systems and can be less trivial in the systems with thin solid electrolytes⁹⁵. Minor errors in alignment of RE with respect to WE can create significant errors in measurement of the working electrode⁹⁶ particularly when rapid changes in potential are involved. In the present work the geometry of the symmetrical RE was similar to others used typically in the literature^{89,94} whereby the RE was adjacent to CE and therefore is considered to be suitable for this study.

Interconnects

Platinum wires together with Pt mesh were used for the electrical connections necessary for the operation of the cell. The wires of the mesh itself had a diameter of 0.06 mm and the mesh was 10-15 mm diameter with an open area of 65%.

A dipping glassy carbon rod was used as an electronic contact to the working electrode (anode). It provided good electrical connections with the cell with an average electrical resistance of the glassy carbon rod of 9 Ohms. The employment of glassy carbon as current collector was one of the achievements of this work. The applied GC rod showed no deterioration after numerous uses in fuel cell testing (at 800 °C under wide range of oxygen partial pressures). Unlike other metallic contacts it does not alloy with liquid tin at 800 °C⁹⁷. Glassy carbon, according to the supplier's specifications⁹⁷, shows no wetting by metallic and ceramic melts and is extremely resistant to thermal shock.

Fuel cell holder

The cap for the cell is made of Ceramit 14, an industrial name of the machinable mineral – pyrophyllite which possesses the properties of fired ceramics after heat treatment (firing), high thermal and mechanical stability, high dielectric strength, etc. Before the firing pyrophyllite is readily machined (milled, drilled or cut). Machining of a pyrophyllite cylinder was done using a computer numerical control (CNC) machine, applying precise dimensions according to the design made in Rhinoceros 4.0 CAD software taking into account volume contraction of material of around 1.0% on firing. It was then fired at 1400 °C for 1 hour at ramping rate of 1 °C per minute to achieve high chemical and thermal stability for later use at high operating temperatures.

The summary of the dimensions of the main fuel cell components with their purpose of use, chemical composition and commercial suppliers is presented in Table 3.1.

Table 3.1 Description of the parts a fuel cell.

Purpose of use / Material	Dimensions	Composition	Source
Electrolyte – closed one end 8YSZ tube	19 mm OD, 15 mm ID, LG 210 mm	8 mol. % Y ₂ O ₃	Dynamic-Ceramic Ltd., UK
Fuel inlet and exhaust – alumina tubes open both ends	4 mm OD, 2mm ID of various lengths	99.7% Al ₂ O ₃	Multi-Lab Ltd, UK
Liquid metal anode- tin shots	3 mm diameter	99.99+% (metals basis)	Alfa Aesar, UK
Current collection to WE - glassy carbon rod	3 mm OD, LG 250 mm	n/a	HTW Hochtemperatur-Werkstoffe GmbH, Germany
Counter and Reference electrode –platinum ink	n/a	Not less than 70% Pt by weight	4082 Pt Vitro-Au-Less Conductor, Ferro Electronic Materials, US
Interconnects-platinum wire	0.25 mm diameter	99.9% Pt	Peak Sensors Ltd, UK
Interconnects-platinum gauze (mesh)	Aperture 0.25 mm; wire diameter 0.06 mm	99.9% Pt	Goodfellow Cambridge Ltd., UK
Ceramic holder- pyrophyllite cap (Al ₂ O ₃ 4SiO ₂ H ₂ O)	60 mm OD cylinder with 20 mm height	silica 56.8% Alumina 33.37% Ferric oxide 0.79% Titanium dioxide 2.42% Magnesium oxide 0.24%	Ceramic Substrates & Components Ltd, UK
Detection of metallic foam- silica tube	19 mm OD, 15 mm ID, LG 210 mm	SiO ₂ 99.99%	Cambridge Glassblowing Ltd., UK

The ready-assembled fuel cell set-up that was applied in experimental work described in Chapter 6, 7, 8 and 9 is shown in Figure 3.6.

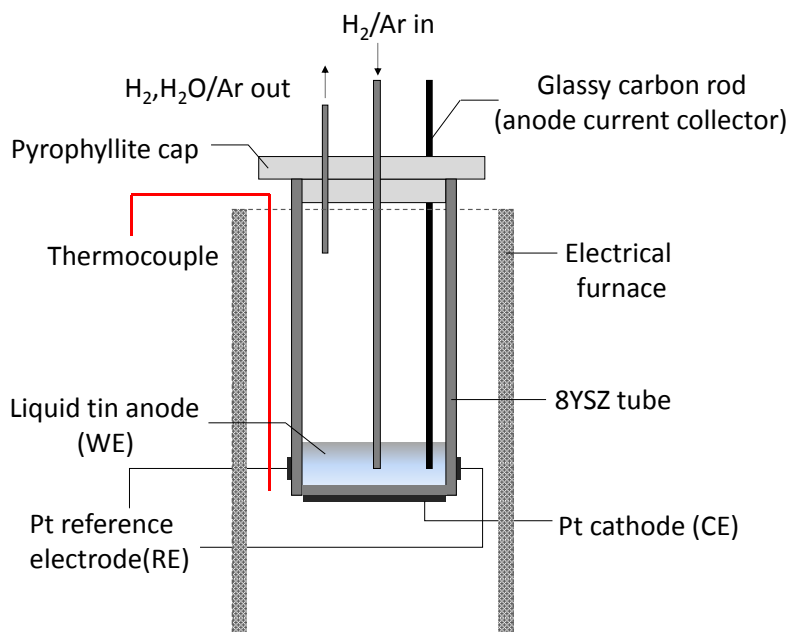


Figure 3.6 Schematic of a fuel cell used for electrochemical characterisation of LMA SOFC (held in furnace).

3.3. Methodology

Operating conditions used for testing the performance of the LTA SOFC are summarised in this section. Any additional changes to working conditions with regards to a specific experiment are listed separately in every chapter of this thesis.

The LTA SOFC was operated in battery and fuel cell modes under flow of inert gas (N_2 or Ar) to eliminate any oxygen leak to the anode and held at temperature >700 °C (typically at 780-800 °C) to reduce ionic resistance of solid electrolyte tube (8YSZ). The system was heated from room temperature up to the desired temperature (800 °C) at a ramping rate of 5 °C min^{-1} and likewise when cooled down to room temperature. This condition was necessary to avoid thermal shock of the components which can induce cracking of materials used in the rig. Any inevitable leak of oxygen was detected using a potentiometric sensor that was measuring O_2 concentration in the piping leading to the fuel cell.

During electrochemical characterisation of LTA SOFC, electrical connection from the anode was connected to the working electrode (WE), platinum paint on the outer side of the 8YSZ tube was connected as the counter electrode (CE) and a platinum ring electrode was connected as the reference electrode (RE) to the potentiostat.

3.4. Experimental Methods: electrochemical techniques

This section briefly describes the theoretical principles of the experimental techniques that were applied to characterize the performance of the electrochemical system of interest – LTA SOFC fueled with hydrogen.

The electrochemical characterization techniques were applied to provide details of the thermodynamic and kinetic aspects of the system based on the applied potentials and measured currents.

For investigation of the processes occurring in LTA SOFC the following electrochemical techniques were applied:

- Potential sweep methods
- Chronoamperometry
- Electrochemical Impedance Spectroscopy
- Rotating Disc Electrode

Note that the Rotating Disc Electrode (RDE) theory was applied to analyze an inverted system – Rotating Electrolyte Disc, which differed from standard hydrodynamic aqueous systems in many aspects (see Chapter 10 for more details).

3.4.1. Potential sweep methods

In potential sweep techniques, such as Linear Sweep Voltammetry (LSV) and Cyclic Voltammetry (CV) the electrode potential is swept linearly with time between two chosen values, while current is continuously recorded. Potentials at which species are oxidised or reduced are registered as current peaks on the voltammogram. The range of a potential scan is typically chosen so that the initial potential (E_1) has no electrochemical activity, whereas at final potential (E_2), the reaction is governed by mass transport⁹⁸. During LSV the potential scan stops at a final potential E_2 , while in CV, when final potential is reached, the sweep is then reversed back to E_1 (or a different potential) and this counts as one cycle. During CV numerous cycles can be run. The advantage of CV is the ability to identify redox couples. The cyclic voltammogram produced characterizes the individual reaction mechanism and kinetic conditions⁹⁸.

3.4.2. Chronoamperometry / Chronopotentiometry

Chronoamperometry and chronopotentiometry are commonly used electrochemical techniques that allow the observation of the current-time or voltage-time behavior of electrochemical system after potential or current step, respectively. In chronoamperometry

the potential of the electrode is held constant for a certain time period, while current is determined as a function of time. In the reverse process, constant current is applied between working and auxiliary electrode, while potential is measured with time between working and reference electrodes⁹⁹. In the present work, chronopotentiometry is useful to study kinetics of an electrochemical cell reaction at a desired voltage. Durability and stability of the system can also be evaluated using this method.

3.4.3. Electrochemical Impedance Spectroscopy

Electrochemical Impedance Spectroscopy (EIS) is one of the most powerful techniques for investigation of electrochemical systems as it is capable of separating out different mechanisms occurring with different time constants^{43,100-102}.

EIS is widely applied for fuel cells diagnosis⁴³ as it provides insight into different phenomena comprising the overall electrochemical process. The EIS measurements are typically performed in a large frequency range (usually from high frequency to low frequency, typically from 10^{-3} to 10^7 Hz) at which certain processes with different time-constants can be observed and distinguished. For instance, electronic conduction and electrochemical kinetics are relatively faster processes than diffusion (mass-transport) phenomena and hence can be monitored and evaluated separately via EIS.

In EIS the system under investigation is perturbed with sinusoidal voltage oscillations:

$$V(t) = V_m \sin(\omega t) \quad (3.1)$$

and the resulting current from the system is recorded accordingly as follows:

$$I(t) = I_m \sin(\omega t - \varphi) \quad (3.2)$$

where ω is the angular frequency, φ is the phase difference between voltage and current signal, V_m and I_m are the amplitudes of voltage and current, respectively.

The impedance is defined as the ratio between the output and input signal measured at any particular frequency. When current perturbations serve as input signal and voltage output is recorded the obtained impedance, $Z(i\omega)$, is formulated by:

$$Z(i\omega) = \frac{U(t)}{I(t)} = |Z|e^{j\varphi} = Z_{Re} + iZ_{Im} \quad (3.3)$$

where Z_{Re} and Z_{Im} are the real and imaginary parts of the impedance and $j = \sqrt{-1}$. If voltage is oscillated and current is measured, the resulting transfer function is called admittance, $Y(i\omega)$, and expressed as the inverse function of impedance:

$$Y(i\omega) = \frac{1}{Z(i\omega)} = Y_{Re} + iY_{Im} \quad (3.4)$$

The impedance data can be represented in a form of a Nyquist plot, where $-Z_{Im}$ is plotted vs. Z_{Re} or Bode plot, where magnitude of impedance $|Z|$ and phase φ are shown vs. $\log(f)$, where f is the measuring frequency.

The measured EIS data needs further interpretation using an equivalent electrical circuit that has an identical response to the measured system of interest and comprises a series of resistances, capacitances or inductances. The physical meaning of each element in the circuit should correspond with a particular process that occurs in the overall electrochemical system. The values calculated for circuit components can provide details for better understanding of the electrochemical systems^{100,103}.

EIS is a useful tool that allows electrical properties of materials, and their interfaces with electronically conducting electrodes, to be explored. It has been widely used to investigate different electrochemical processes: charge transfer of ionic or mixed-ionic conductors, semiconductors, corrosion processes, investigation of coatings on metals, characterisation of materials and solid electrolyte as well as solid-state devices¹⁰⁴.

It is worth mentioning that interpretation of impedance results is as important as experimental performance and accuracy. This is not a trivial procedure and depends on many factors relevant to that particular electrochemical system.

3.4.4. The Rotating Disc Electrode

The Rotating Disc Electrode (RDE) is one of the commonly used hydrodynamic techniques for analysis of electrochemical systems involving movement of electrode with respect to the bulk solution. It has been commonly used to study electrode reaction kinetics¹⁰⁵⁻¹⁰⁷.

The RDE theory resulted from the development of mathematical models based on the solution of the convective-diffusion equation, considering hydrodynamic boundary layer from the Navier-Stokes equation and other geometric equations¹⁰⁷. The velocity profile of a fluid (bulk solution) near a rotating electrode was developed by von Karman and Cochran solving the hydrodynamic equations under steady-state conditions⁹⁹.

The rotation of the electrode is determined via the angular velocity term, ω , which is a rotation rate parameter:

$$\omega = 2\pi f \quad (3.5)$$

where f - is frequency (number of revolutions per second).

As rotation of the disc increases, the hydrodynamic boundary layer is dragged by the centrifugal force of the spinning disc away from the centre of the electrode in the radial

direction, as shown in Figure 3.7a. A three-dimensional view of the flow is given in Figure 3.7b. This results in laminar flow of solution towards and across the electrode surface⁹⁹.

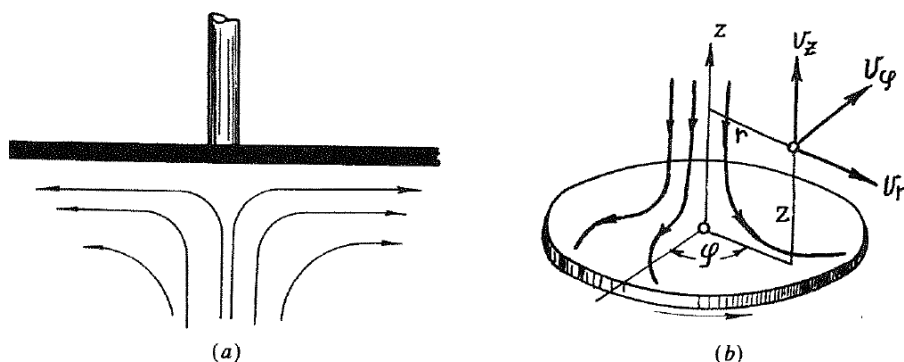


Figure 3.7 Hydrodynamics profile of a rotating disc: (a) streamlines in solution; (b) coordinate system used in calculation (solid arrows denote the streamlines)¹⁰⁸.

The reactant transport from bulk solution to the electrode surface is dominated by diffusion across a thin layer of solution adjacent to the electrode, which is known as the diffusion layer. The thickness of this layer is controlled by the angular velocity of the rotation, ω . The greater the angular velocity the thinner the diffusion layer will be and vice versa. An important feature of the system is that the surface of the electrode is uniformly accessible so that the diffusion layer thickness (dependent upon rotation speed) is constant across the surface.

The flowrate of the solution is governed by angular velocity and can be modeled mathematically. The RDE can therefore control the flux of solution (reactant species) via rotation speed, and can be used to quantify the kinetic constant for the rate-determining step¹⁰⁷.

The potential of the working electrode is scanned within a certain range, where reaction starts to occur. The measured current is then referred to the kinetics of the electrochemical reaction occurring and mass-transport of the reactants. Eventually diffusion limiting current is observed by way of a plateau when the applied potential is high enough and the reaction rate is determined by diffusion (mass transport) at a given rotation speed. This diffusion-controlled current, i_d is expressed by the Levich equation¹⁰⁹:

$$i_d = 0.62nFAD^{\frac{2}{3}}\omega^{\frac{1}{2}}\nu^{-\frac{1}{6}}C \quad (3.6)$$

where, n is the number of electrons transferred, F is the Faraday constant, A is electrode (disc) surface area, D -is diffusion coefficient, ν is kinematic viscosity of bulk solution given by ratio of viscosity of solution to its density, and C is the concentration of analyte in bulk solution.

Levich Analysis

When a series of voltammograms is obtained over the range of different rotation rates (from lowest to highest), and the rate of reaction is controlled by diffusion of reactant to the electrode surface, the magnitude of currents in the voltammograms normally increases with the square root of the rotation rate. The measured limiting currents are usually plotted vs. the square root of the rotation rate on a graph called a Levich plot. As predicted by the Levich equation, the limiting current, i_d , increases linearly with square root of the rotation rate, $\omega^{\frac{1}{2}}$, with the slope of $0.62nFAD^{\frac{2}{3}}\nu^{-\frac{1}{6}}C$. The diffusion coefficient of species in the bulk solution (electrolyte) can be determined from the slope. The Levich equation is usually rearranged to the following equation:

$$\frac{1}{i_d} = \left[\frac{1}{0.62nFAD^{\frac{2}{3}}\nu^{-\frac{1}{6}}C} \right] \omega^{-\frac{1}{2}} \quad (3.7)$$

Koutecky-Levich Analysis

When the rate of reaction is limited by both mass transport and kinetic processes (e.g. at reaction onset), the RDE technique allows kinetic information (such as standard rate of reaction) to be separated from mass transport (e.g. diffusion coefficient). The kinetic current is expressed by¹⁰⁹:

$$i_k = nFAk_f C \quad (3.8)$$

where k_f is the rate constant and is a function of the potential. Then the overall current measured over the entire potential window is given by the Koutecky-Levich equation¹⁰⁹:

$$\frac{1}{i} = \frac{1}{i_k} + \frac{1}{i_d} = \frac{1}{i_k} + \frac{1}{0.62nFAD^{\frac{2}{3}}\omega^{\frac{1}{2}}\nu^{-\frac{1}{6}}C} \quad (3.9)$$

A plot of reciprocal current versus the reciprocal square root of the angular rotation rate is called a Koutecki-Levich plot, which yields a straight line with an intercept equal to the reciprocal of kinetic current. Kinetic current is observed when there are no mass transport limitations.

3.5. Conclusions

The details of the development of the experimental rig are given. Various types of working cell were developed and applied in accordance with primary objectives. As such, symmetrical cells were made for potentiometric and EIS measurements that could provide information on the ionic conductivity of the YSZ material applied in this project as the

electrolyte. The fuel cell was developed for testing the performance of LTA SOFC fuelled with hydrogen. Details of fuel cell components were given.

A brief description of the applied electrochemical characterisation techniques was also provided. In particular, linear sweep potential, chronoamperometry and electrochemical impedance spectroscopy were presented. The application of the Rotating Disc Electrode (RDE) technique normally applied to liquid electrolyte systems is exceptionally important for the development of the inverted system, Rotating Electrolyte Disc (RED) technique, appropriate to systems with solid electrolytes.

4. Preliminary testing

This chapter describes the results of preliminary testing of the developed workstation along with the equipment and materials that are applied for the main experimental work. Testing of the furnace performance and calibration of the mass flow controllers has been done in the first instance. This is followed by the testing of conductivity properties of the electrolyte material chosen for this project, yttria-stabilised zirconia (YSZ). For this work the symmetrical YSZ cell was applied as a potentiometric oxygen sensor. A good correlation between experimental data and theoretical response for concentration of oxygen was found for the applied range of gas flow rates.

Then, ionic conductivity of YSZ was tested, applying a voltage from -1.0 V to 1.0 V and monitoring a current response. The procedure was repeated with increasing operating temperature. This resulted in the highest current density at 800 °C and from that it was confirmed that operation of the fuel cell at around 800 °C was described in order to get sufficient conductance of electrolyte.

For more accurate and precise calculation of ionic conductivity of YSZ, EIS was applied to a second symmetrical cell (made of 6 mol.% YSZ). From the high frequency intercept of the impedance semi-circle, the bulk resistance of the electrolyte was found for the temperature range from 300 to 1000 °C. It was found that the conductivity trend followed the well-known Arrhenius relationship and was in close agreement with the literature. Ionic conductivity of 6 mol.% YSZ was found to be $6.58 \times 10^{-2} \text{ S cm}^{-1}$ at 1000 °C.

Finally, once all the materials and equipment were tested separately, a measurement of the ready-assembled LTA SOFC cell was accomplished via OCP measurements with temperature. Experimentally-determined OCP was in accordance with that predicted by thermodynamics and demonstrated the readiness of the whole rig and each component for precise electrochemical characterisation of LTA SOFCs. It also demonstrated the stability of the glassy carbon rod used as the anode current collector.

4.1. Introduction

It is essential to test and validate the experimental rig prior any actual electrochemical characterisation of LTA SOFC. Equipment and materials selected for this project require a check to ensure operation in a safe and proper manner. Therefore, this chapter describes the results of preliminary testing of the equipment and materials to be utilised extensively during the project.

As part of the testing of materials, a potentiometric measurement involving the application of a symmetrical YSZ cell as potentiometric sensor was performed. To investigate the overall conductivity of symmetrical cell as a function of applied potential and temperature, a linear sweep (from -1.0 to 1.0 V vs. air reference) was applied.

The resistance of a solid electrolyte contributes significantly to the overall resistance of an SOFC. Hence, to investigate and measure ionic conductivity of the electrolyte itself EIS was applied to a symmetrical 6 mol.% YSZ cell. Resistivity data (from the impedance diagrams) enables calculation of conductivity at a specified temperature.

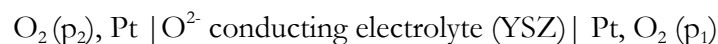
The final check of a ready assembled fuel cell and its components is the measurement of open circuit potential of a cell (OCV). A correct reading (corresponding to thermodynamics predictions) is an indicator for the proper operation of the whole rig and individual parts of it.

4.2. Background

4.2.1. Potentiometric measurements of oxygen concentration using YSZ

One of the common applications of YSZ material is the measurement of oxygen partial pressure, whereby YSZ is operated as a potentiometric gas sensor^{110,111}. Potentiometric zirconia sensors can measure oxygen pressure over a wide range from 10^6 to 10^{-25} Pa¹¹².

The potentiometric YSZ cell with two metal (typically platinum or silver) electrodes is typically expressed as follows:



The electrode reaction is:



Assuming reversibility¹¹¹ of Reaction (4.1) the cell develops an electromotive force (EMF) between two metal (Pt) electrodes, which is given by:

$$E = \left(\frac{RT}{nF}\right) \int_{p_2}^{p_1} t_{ion} d(\ln p) \quad (4.2)$$

where t_{ion} is the transport number of the mobile ion, n is number of electrons transferred during reaction, p_1 and p_2 are the partial pressures of oxygen on both sides of the electrolyte and R , T and F have their usual meaning.

Solid electrolytes generally have low electronic transport numbers, so t_{ion} is close to unity and hence Equation (4.2) rearranges as follows:

$$E = \frac{RT}{4F} \ln\left(\frac{p_1}{p_2}\right) \quad (4.3)$$

Or:

$$E = 2.303 \frac{RT}{4F} \log\left(\frac{p_1}{p_2}\right) \quad (4.4)$$

Usually one of the gases in oxygen sensors has known oxygen partial pressure, p_2 acting as a reference gas, while the other is the sample gas with oxygen partial pressure, p_1 . Therefore, Equation (4.3) can be applied in the following form:

$$E = E_1 + \left(\frac{RT}{4F}\right) \ln(p_1) \quad (4.5)$$

where E_1 is a constant of value of $-\left(\frac{RT}{4F}\right) \ln p_2$.

The reference gases are usually pure oxygen ($p_2=1$ atm) and air ($p_2=0.21$ atm). In the experimental set up the reference gas was ambient air, and a mixture of nitrogen and air was used as the sample gas mixture. The partial pressure of the oxygen was controlled with mass flow controllers for N_2 and air accordingly.

4.2.2. Ionic conductivity of YSZ electrolyte

Section 2.2.7 in the literature review (Chapter 2) provides the details of ionic conductivity of YSZ material among other solid electrolytes. It also explains the mechanism for transfer of charged species, which are oxygen ions, O^{2-} . Ionic conductivity of YSZ improves upon increasing the operating temperature^{40,113}. Therefore it can be expressed with Arrhenius relationship¹¹⁴ as follows:

$$\sigma = \frac{\sigma_0}{T} \exp\left(-\frac{E_a}{kT}\right) \quad (4.6)$$

where σ is the ionic conductivity, σ_0 is the pre-exponential factor, T is the absolute temperature, E_a is the activation energy, k is Boltzmann's constant.

Arrhenius relationship predicts linearity between measured conductivity data, $\ln(\sigma T)$ and reciprocal of temperature, $1/T$.

4.3. Experimental procedure

All primary investigations, including the operation of the 8 mol.% YSZ symmetrical cell as an oxygen sensor, measurement of its conductivity, etc. were performed in a workstation shown in Figure 4.1. The operating conditions varied from the conditions required for the main fuel cell studies that involves electrochemical characterisation of the liquid tin anode SOFC.

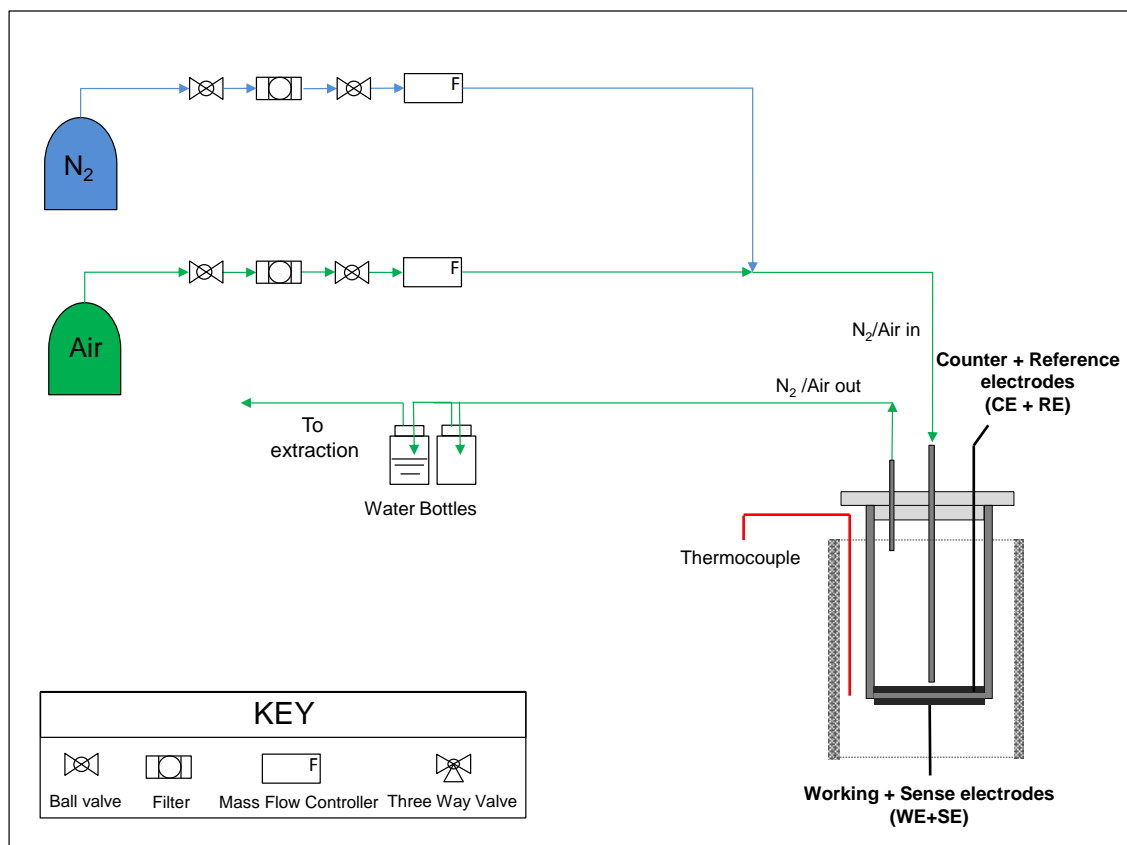


Figure 4.1 Schematic of experimental rig used for oxygen sensor testing.

4.4. Results and discussion

It was necessary to ensure that equipment was well-connected, in line with other laboratory stations (e.g. laboratory gas supply system, extraction system, etc.). Therefore the developed experimental rig for LME SOFC was tested prior to any work that involved high temperature, H_2 gas evolution, etc. The overall testing consisted of the following mini-steps:

- Testing and calibration of the furnace (set up of the ramping rate, testing of thermocouple accuracy, defining of the temperature profile inside the furnace, etc.);
- Testing and calibration of mass-flow-controllers;
- Leak check for all the gas connections.

4.4.1. Potentiometric measurements

In the applied experimental set up (Figure 4.2a) the reference gas was ambient air and hence remained constant, while the sample gas was made of a mixture of nitrogen and air. Varying the flow rates of nitrogen and air, and hence $p_1(\text{O}_2)$, the EMF across the symmetrical cell (assuming constant value of p_2 of 0.21 atm) was measured and compared to the value predicted by the Nernst equation (Equation (4.4)). A 10YSZ symmetrical cell (Figure 4.2b) (full details of the cell were given in Section 3.2.1, Figure 3.3a) was held in the central part of the electrical furnace and was heated to 700 °C. The flow of a gaseous mixture (N_2 +air) supplied to the inner electrode of YSZ was controlled with mass flow-controllers and varied from (1% air to 100% air). The outer side of the tube was left exposed to the ambient air with $p_2(\text{O}_2)$ of 0.21 atm. The outer electrode was connected to the working electrode (WE) terminal, while the inner one – to the counter (CE).

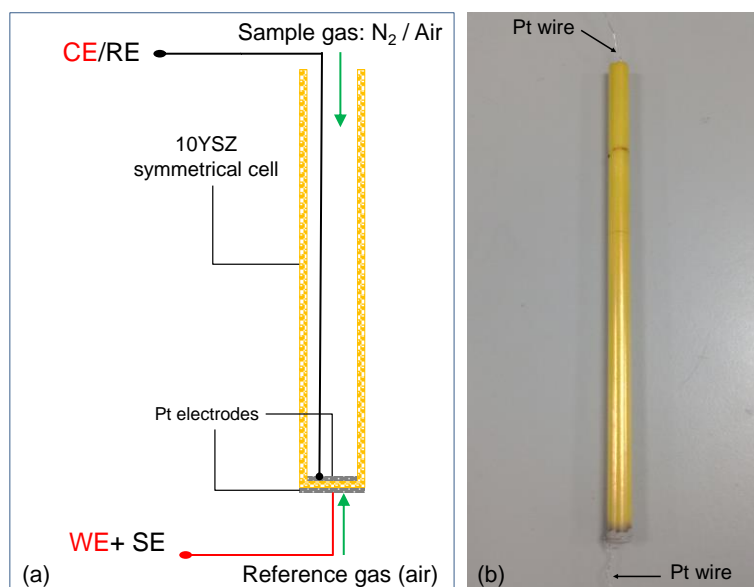


Figure 4.2 Schematic of experimental setup for potentiometric measurements (a) with 10YSZ symmetrical cell (b).

The experimentally measured and calculated EMF data obtained at 700 °C is shown in Figure 4.3. Overall there is a good agreement between the measured EMF values and theoretical data calculated using Equation (4.4). Good correlation between experimental and theoretical data provides confidence that the 10YSZ cell was a reliable and accurate sensor and the gas flow valves were operating correctly.

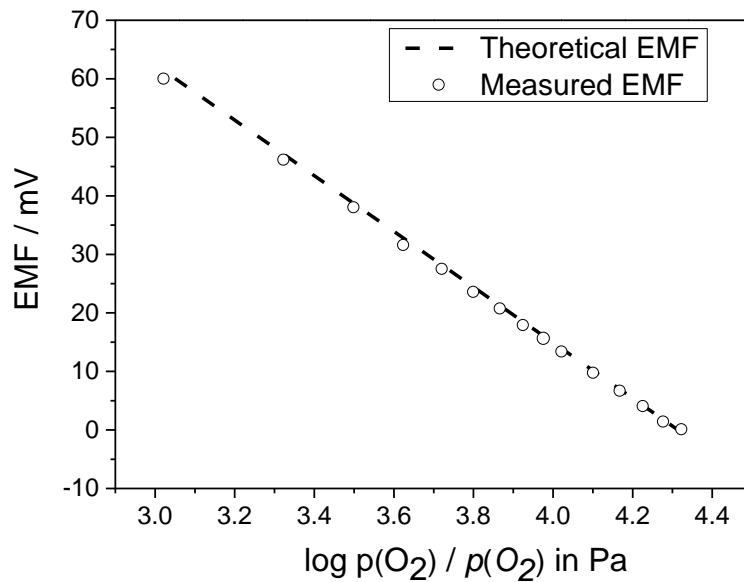


Figure 4.3 Theoretical (using Equation (4.4)) and experimental EMF developed by the symmetrical cell.

4.4.2. Ionic conductivity of YSZ measured as a function of applied potential

A relatively quick and simple measurement of solid electrolyte conductivity can be done by application of a voltage across two electrodes at both sides of the electrolyte and measuring the current response with step changes in operating temperature.

In order to validate sufficient ionic conductivity of chosen electrolyte material, its conductivity was tested as a function of applied potential and operating temperature. The recorded current is then an indication of ionic conductivity of electrolyte. For that the same symmetrical cell (Figure 4.2b) made of 10YSZ tube and two platinum electrodes described in details in Section 3.2.1 was held in the electrical furnace.

A linear sweep of voltage between -1.0 V to 1.0 V was applied at temperatures from 500 to 800 °C (connection were as shown in Figure 4.2a). The obtained results in Figure 4.4 demonstrate an increase in 10YSZ conductivity with temperature, as expected from the literature. At 800 °C there was a substantial increase in current density due to increased mobility of charges (O^{2-}) in the ceramic (Figure 4.4). The estimated accuracy of measured currents is $\pm 50 \mu A$. The obtained data also confirmed the typical operating range for YSZ (ca. >700 °C for 8-10 mol.% YSZ), as below 700 °C currents were small due to low conductivity of YSZ.

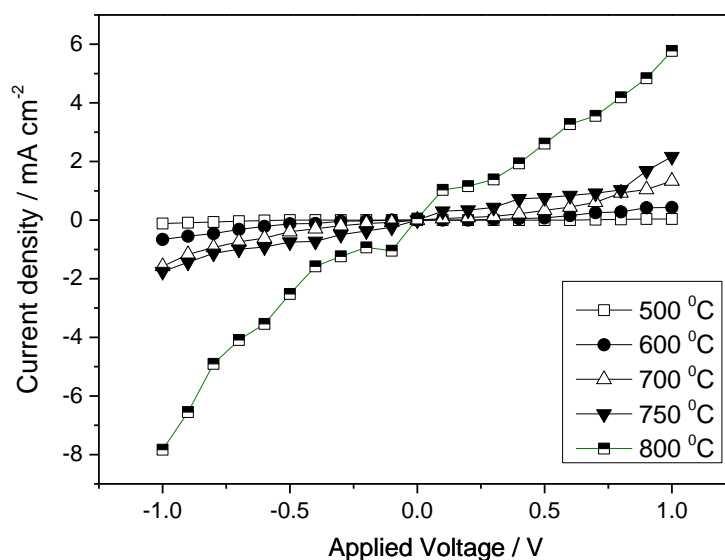


Figure 4.4 Current – voltage characteristics that includes ionic conductivity of 10YSZ and overpotential on each Pt electrodes.

The above results were complemented and confirmed using the EIS technique as described below under Section 4.4.3.

4.4.3. Ionic conductivity of YSZ using EIS technique

The next set of experiments was designed to explore the ionic resistivity of the YSZ solid electrolyte using EIS.^{101,115–117} As conductivity (reciprocal of resistivity) of solid electrolytes increases with temperature, the impedance measurements were performed over a wide range of temperature (from 300 to 1000 °C) with applied potential of 0 V and 10 mV AC perturbation over the frequency range from 0.01 Hz to 10 kHz. The symmetrical cell, made of 6YSZ with two Pt electrodes with overall electrode area of 1.30 cm² and 0.5 cm thickness, was used. More details are given in the previous Chapter (see Section 3.2.1; Figure 3.3b). The obtained EIS spectra are shown in Figure 4.5 for the low temperature range (315 - 422 °C) and in Figure 4.6 - for the high temperature range (722 - 1000 °C).

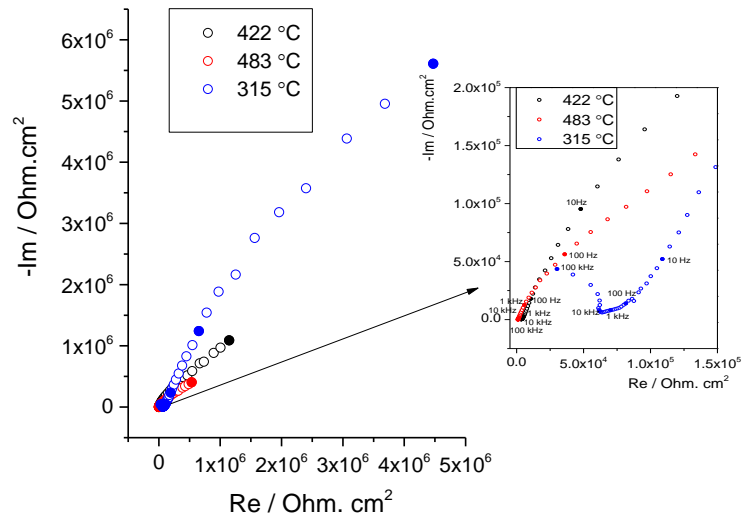


Figure 4.5 Measured EIS data: at 315 - 422 °C frequency sweep: 10 kHz to 0.01Hz, 10 frequencies per decade, Voltage: 0 V, amplitude of oscillations: 10 mV.

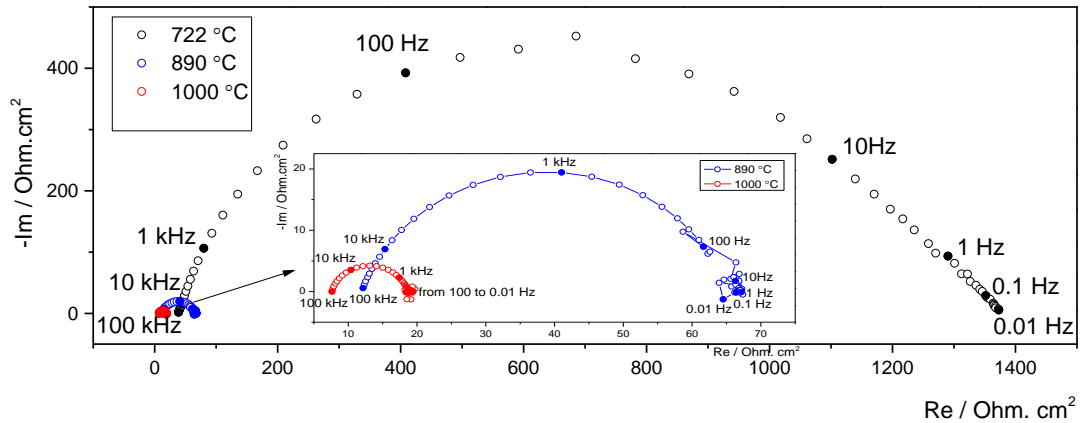


Figure 4.6 Measured EIS data at 722, 890 and 1000 °C, frequency sweep: 10 kHz to 0.01Hz, 10 frequencies per decade, Voltage: 0 V, amplitude of oscillations: 10 mV.

The obtained results were interpreted in accordance with commonly used SOFC impedance models reported by several studies^{116,118–121}. The overall impedance for SOFC systems comprises the bulk electrolyte impedance (Z_b), grain boundary impedance (Z_{gb}) and electrode impedance (Z_e)⁴⁶. In some studies relevant to impedance scanning of LSM-YSZ systems it is argued that at least two overlapping arcs should be expected, corresponding with two processes such as bulk or surface diffusion/adsorption or exchange of oxygen and transfer of charge¹¹⁸.

The expected bulk and grain boundary arcs can clearly be seen only at 315 °C (Figure 4.5). The bulk resistance was represented by the first arc at high frequency, while the second arc at high frequency was attributed to the grain boundary resistance. When the temperature was increased, the grain boundary arc diminished and it disappeared at significantly higher

temperatures. Hence, the other complex impedance plots obtained at higher temperatures (722 - 1000 °C in Figure 4.6) show only one overall depressed arc for all three types of resistances.

From the obtained impedance plots (movement of semi-circles towards the origin), and in general reduction in sizes of the arcs, indicates the reduction of the bulk YSZ resistance with increase of temperature.

High frequency intercept of the impedance arc on the real impedance axis provides the value of the resistance of electrolyte^{122,123}, ohmic resistance values are listed in Table 4.1.

Table 4.1 Ohmic resistance values for 6 mol. % YSZ symmetrical cell (Pt electrode area of 1.30 cm²) with temperature.

$\Omega_{\text{ohmic}} / \text{k}\Omega$	T / °C	T / K
23.2	316	589
3.94	405	678
2.50	422	695
0.73	483	756
0.65	492	765
0.14	588	861
0.03	722	995
9.34×10^{-3}	890	1163
5.87×10^{-3}	1000	1273

These data were used to calculate ionic conductivity of 6 mol.% YSZ electrolyte. The natural logarithm of ionic conductivity of 6YSZ is plotted against reciprocal of temperature in accordance with Arrhenius equation (Figure 4.7).

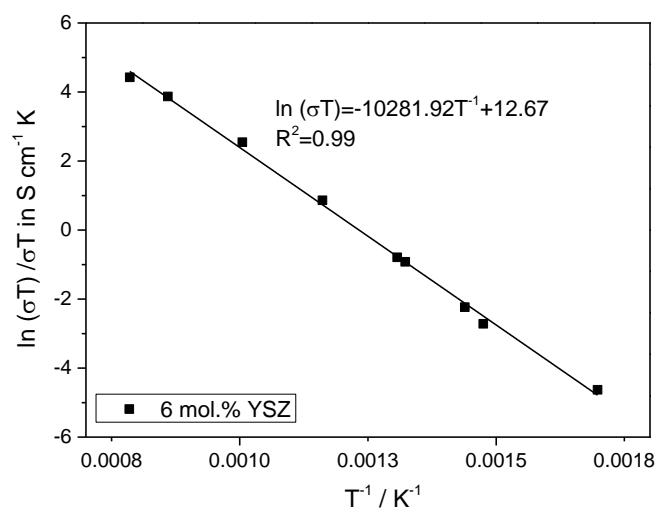


Figure 4.7 The electrical conductivity of 6 mol. % YSZ cell as a function of reciprocal absolute temperature.

A straight line was achieved, which confirms the expected Arrhenius behaviour between measured conductivity and the operating temperature. The slope from Figure 4.7 revealed the value of activation energy, E_a , for 6 mol.% YSZ sample, which was found to be 0.90 eV. This result is in a good agreement with the one obtained by Arachi *et al.*¹²² who

reported an activation energy of 1.0 eV for 6 mol.% YSZ for the similar temperature range of 350-1000 °C. These results are consistent with a recent study by Zhang *et al.*¹¹³, where for 8 mol.% YSZ activation energy was reported 0.85 eV in the temperature range of 700-1000 °C.

The conductivity values for some zirconia-based electrolytes including those measured at UCL in the present work are summarised in Table 4.2. From the findings it is clear that 6 mol.% YSZ electrolyte has inferior conductivity to 8 mol.% YSZ, and hence the latter is preferred for electrochemical work, although 6 mol.% YSZ possesses greater toughness. Therefore in the final design of LTA SOFC, an 8YSZ tube was used.

Table 4.2 Conductivity values of YSZ electrolytes measured and given in the literature.

Source	Y ₂ O ₃ content in ZrO ₂	σ at 1000 °C / $\times 10^{-2}$ S cm ⁻¹
UCL (present work)	6 mol.%	6.58
Yang <i>et al.</i> ¹²⁴	7.5 mol.%	6.67
Arachi <i>et al.</i> ¹²²	8 mol.%	14.0
Badwal ³⁷	8 mol. %	13.7

4.4.4. Open circuit potential of LTA SOFC

A fuel cell set-up developed previously for LTA SOFC studies (Figure 3.6) was heated from ambient temperature to 800 °C at the ramping rate of 5 °C per minute. The potential of working electrode was measured relative to the air reference electrode.

While constantly blowing nitrogen into the cell to maintain inert atmosphere, the open cell potential developed by the cell was measured with temperature. Figure 4.8 shows a comparison of theoretically predicted equilibrium potential differences with measured OCP values for LTA SOFC.

Experimental OCP data for temperatures less than 900 °C was slightly (ca. 40 mV) lower than theoretical equilibrium potentials. This is possibly due to the fact that saturation of liquid tin with oxygen had not yet been achieved. On the other hand, at temperature higher than 900 °C, equilibrium OCP is higher than theoretically possibly caused by oxidation of the glassy carbon current collector. For comparison, coal oxidation reaction has an equilibrium potential of ca. 1.02 V⁷⁰, which is higher than for the Sn-SnO₂ equilibrium potential.

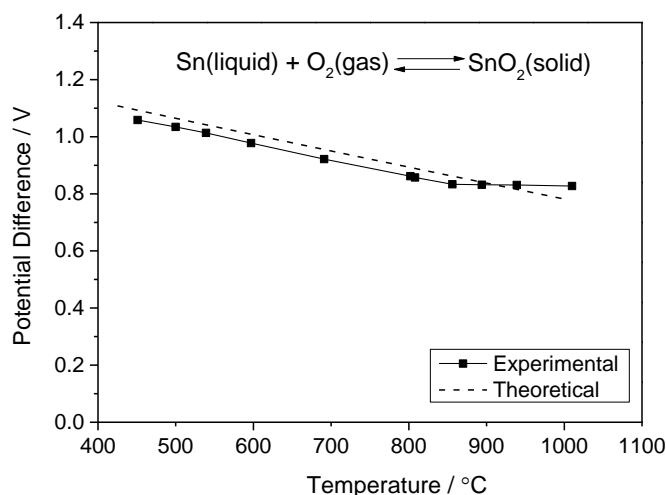


Figure 4.8 Experimental open circuit potential of the SOFC with a liquid tin anode compared to the theoretical equilibrium potentials for tin oxidation reaction.

Overall, glassy carbon showed itself to be an inert current collector up to 900 °C, which was suitable for the present study. All electrochemical characterisation of LTA SOFC was done at 780-800 °C (well below that point), but also normally with a supply of hydrogen fuel.

In case of constant supply of a fuel which is more reactive than the current collector material, glassy carbon can be considered as a reliable electronic probe. This situation is opposite to metallic contacts which tend to alloy with liquid tin at high temperatures and for that reason were not utilised.

4.5. Conclusions

Preliminary work was essential for validation of the developed workstation with equipment and material that are going to be applied throughout the project. Potentiometric measurements involving the application of YSZ tubular cell as an oxygen sensor were completed. Close agreement between the measured and theoretical EMF data obtained from a symmetrical cell confirmed that the developed cell was prepared correctly and operated accordingly.

Ionic conductivity of YSZ material as a function of operating temperature was investigated using two methods: one varying the applied potential and second, using the EIS technique. From current-voltage characteristics it was found that the YSZ cell exhibited the highest conductance at 800 °C in the temperature range considered; hence the temperature range for operation of LTA SOFC was chosen to be from 750 to 800 °C.

The EIS measurements confirmed the reduction in bulk resistance (attributed to electrolyte) with increase of temperature. Ionic conductivity of 6YSZ cell was calculated from the EIS data and was in a good agreement with values reported in the literature. From

the obtained result it was decided to utilise 8YSZ material rather than 6YSZ due to its enhanced conductivity.

The fuel cell developed in the previous chapter was operated in a battery mode (no fuel supply) and the OCP between the working electrode (anode) and reference electrode was measured with temperature. Good correlation between measured OCP and potential difference predicted by thermodynamics of the system was found. A deviation of experimental OCP from theoretical was found at extremely high temperatures (>900 °C) which may have been due to oxidation of the current collector.

5. Experimental optimisation

This chapter provides analysis of oxygen permeation rates through plastic tubing that was discovered at early stages of building the LTA SOFC set-up. Parasitic ingress of oxygen decreased upon reduction in the length of silicone peroxide tubing; later it was reduced via its complete replacement with hard nylon tubing. Concentration of leaked oxygen was found to be inversely proportional to the gas flow rate.

A methodology to account for the effect of leaked oxygen into the fuel cell on the overall fuel cell current was developed. In order to do that the LTA SOFC was operated at -1.1 V vs. RE when N₂ gas was supplied doped with some oxygen pumped in and/or out electrochemically. The amount of pumped oxygen was consistent with Faraday's law for both tubing materials. About 57% of the pumped current (due to oxygen) was attributed to the change in fuel cell reduction current. This showed that the liquid tin gettered 57% of the oxygen entering the cell via the supplied carrier gas; this is a surprisingly large fraction as the gas was in contact with the tin only for a short time (seconds or less). Importantly, it demonstrated that a substantial fraction of oxygen leaking into the gas supplied to the fuel cell dissolved in the tin and contributed to currents measured during electrochemical measurements. Thus, it is vital to ensure minimisation of parasitic oxygen into the carrier gas.

The developed mechanism not only showed considerable contribution of parasitic oxygen leaking into tin when LTA SOFC was run at -1.1 V vs. RE, but also indicated how measured currents could be corrected for parasitic oxygen; such a correction is applied in experimental chapters of this thesis.

Finally, the values of permeability coefficient for silicone peroxide and nylon tubing are determined and compared to literature values. Replacement of silicone peroxide tubing with nylon should have resulted in virtually zero permeability. The apparent permeability coefficient of $1.3 \times 10^{-11} \text{ cm}^2 \text{ s}^{-1} \text{ Pa}^{-1}$ measured for nylon tubing indicated that permeation occurred through the joints and connectors, where short sections of silicone peroxide tubing were used for making connections.

5.1. Introduction

One of the challenges in the operation of LMA SOFCs is to maintain the metal anode in an inert atmosphere. In order to flush the operating system and prevent any leak of oxygen to the anode the carrier gases N₂ or Ar were typically applied^{18,21,64,66,70}.

Electrochemical oxidation of liquid metal to metal oxide is one half reaction of the whole mechanism of the fuel cell, and therefore the level of oxygen present in the inert carrier gas should, if possible, be reduced virtually to zero in order to minimise any chemical oxidation of the anode.

At early stages of this project when the experimental rig was under construction using various types of plastic tubing, significant amounts of oxygen were detected in the carrier gas (nitrogen) after traversing the tubing.

Therefore, the aim of the work presented in this chapter is to quantify permeation of oxygen through the silicone peroxide tubing incorporated initially (and nylon tubing used subsequently). Traces of oxygen in the system were detected even after replacement of most of the soft tubing with hard impervious tubing. A methodology was developed whereby oxygen was electrochemically pumped in or out to the carrier gas supplied to the fuel cell. The methodology enabled investigation of the effect of pumped/parasitic oxygen on the fuel cell current.

5.2. Background

Transport of gases in polymer membranes has been studied widely over the past 150 years^{125–127}. The gas transport theory in synthetic polymeric membranes is dependent upon the morphology of the polymer and as such there are two main types of polymers for consideration: rubbery and glassy polymers¹²⁵.

The focus of this chapter is permeation through rubbery polymers (in particular silicone rubber). Permeation according to the ‘solution-diffusion model’¹²⁵ is governed by two processes: sorption (conforming to Henry’s law solubility) and diffusion (governed by Fick’s law of diffusion).

Combining sorption and diffusion, the steady state permeation rate (or flux) through a membrane of thickness τ is expressed as follows:

$$J = \frac{DS\Delta p}{\tau} \quad (5.1)$$

where D is the diffusion coefficient, S the absorption coefficient, and Δp the pressure difference.

Assuming that diffusion and solubility coefficients are independent of concentration of a gas in a membrane, the permeation flux is expressed as follows:

$$J = \frac{P\Delta p}{\tau} \quad (5.2)$$

And the permeability coefficient is then:

$$P = DS = \frac{J\tau}{\Delta p} \quad (5.3)$$

Apart from solubility and diffusivity of a small molecule in the polymer, other factors that affect permeability of a polymer are chain packing and side group complexity, polarity, orientation, fillers, humidity and plasticization¹²⁸.

Permeability of a membrane is used to characterise the permeation rate of a membrane and is typically expressed as follows:

$$P = \frac{V\tau}{At\Delta p} \quad (5.4)$$

where P is permeability for a given temperature, V is volume of gas which penetrates through a membrane, τ is thickness of a membrane, A is area of a membrane, t is time and Δp is partial pressure difference across the membrane.

Analysis of oxygen permeation through plastic tubing based upon ‘solution-diffusion’ theory in the present work is shown below. As all the experiments were run at ambient temperature (25 °C) and pressure (1 bar) and with the same permeant, namely oxygen, the dependence of permeability, solubility upon the gas type, temperature and pressure are not considered in the theoretical treatment of the results, which is shown below.

5.2.1. Theoretical analysis of oxygen permeation with the effect of pumping current

Based on studies of transport of gases and vapours in polymers¹²⁷, the following theoretical framework has been developed for the analysis of permeation rate of air (oxygen) through silicone peroxide tubing with a constant flow of nitrogen through it.

Consider permeation through plastic tubing (silicone peroxide), with length l , from air surrounding the tube to N_2 with O_2 content close to zero (Figure 5.1). Let the gas (nitrogen) input to the tube have O_2 content of \bar{a} ppm (from gas cylinder specification) and the output, \bar{c} ppm. Note that 1 ppm of O_2 is parts per million by moles but also by volume.

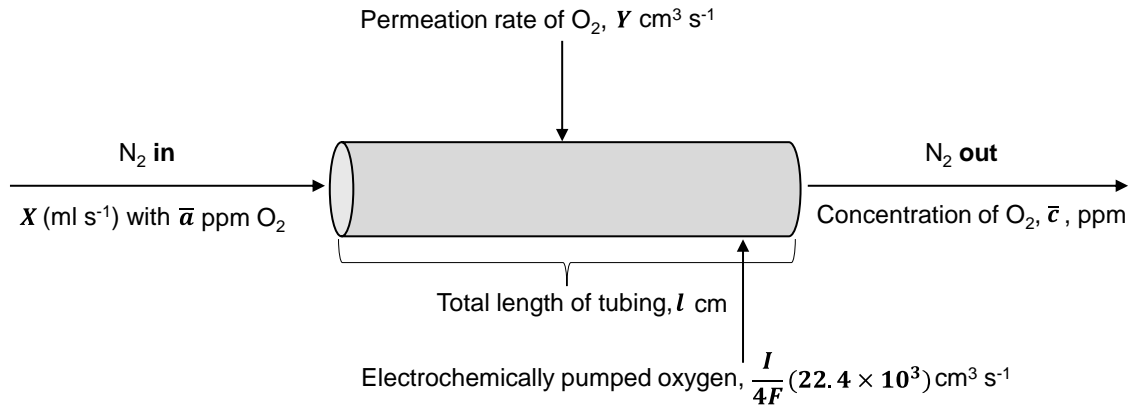


Figure 5.1 Schematic of the oxygen permeation through silicone peroxide tubing (containing N₂) with electrochemically pumped oxygen.

Permeation rate of oxygen through plastic tubing is shown as $Y \text{ cm}^3 \text{ s}^{-1}$, for the total length of tubing, l , where $X \text{ ml s}^{-1}$ is the flow rate of nitrogen gas and l is the total length of tubing and pumped current, I in A. The electrochemically pumped oxygen is treated below.

In order to quantify the amount of injected oxygen via the oxygen pump, the following reaction with four electrons transfer is considered:



So the rate of oxygen pumping is $\frac{I}{4F}$ mole s^{-1} of oxygen, which is $\frac{I}{4F}(22.4 \times 10^3) \text{ cm}^3 \text{ s}^{-1}$, where F is the Faraday constant, $0.965 \times 10^5 \text{ C mol}^{-1}$, and hence the volume of oxygen pumped (at STP) is equal to:

$$\frac{I \times (22.4 \times 10^3)}{4 \times 0.965 \times 10^5} = 0.058 I \text{ cm}^3 \text{ s}^{-1}$$

For a nitrogen (or argon) flow rate of $X \text{ ml s}^{-1}$, the following equation may be written:

$$\bar{c} = \frac{10^6}{X} (Y + 0.058 I) + \bar{a} \quad (5.6)$$

where \bar{c} is the concentration of oxygen in ppm.

For constant or zero current, a plot of oxygen concentration, \bar{c} vs. inverse of gas flow rate, X^{-1} should be a straight line with a slope of $10^6 Y$, and intercept, \bar{a} .

In case when additional oxygen is pumped in, for a fixed flow rate of nitrogen X , the plot of oxygen concentration, \bar{c} in ppm vs. pumped current, I , should result in intercept (units: ppm):

$$\text{intercept} = \bar{a} + \frac{10^6}{X} Y \quad (5.7)$$

and slope (units: ppm μA^{-1})

$$\text{slope} = \frac{0.0580}{X} \quad (5.8)$$

5.2.2. Calculation of oxygen concentration using potentiometric sensor

Oxygen concentration is determined from the EMF measured between two Pt electrodes located on each side of a YSZ cell, which is governed by the Nernst Equation as follows (see Chapter 4 for more details):

$$E = \frac{RT}{4F} \ln \left(\frac{p_{O_2 \text{ sample}}}{p_{O_2 \text{ ref}}} \right) \quad (5.9)$$

where R is universal gas constant, T is absolute temperature, $p_{O_2 \text{ ref}}$ is partial pressure of oxygen in dry, clean air (0.21 atm) and $p_{O_2 \text{ sample}}$ is the partial pressure of oxygen to be measured.

Assuming 210,000 ppm of O_2 in the ambient air (reference gas), Equation (5.9) could be written as follows:

$$E = 2.303 \frac{RT}{4F} \log \left(\frac{\bar{c}_{\text{sample}}}{210,000} \right) \quad (5.10)$$

where \bar{c}_{sample} is unknown oxygen concentration (in ppm) in the sample gas.

Equation (5.10) allows the determination of an unknown oxygen concentration (in ppm) in the sample gas, \bar{c}_{sample} from the measurement of EMF between two electrodes, E .

This chapter presents an investigation of oxygen permeation through silicone peroxide and nylon tubing. It also provides the methodology for doping of carrier gas with oxygen using an electrochemical pump. The effect of oxygen pumped in and out on the overall fuel cell current is also presented.

5.3. Experimental procedure

In the present chapter all experimental work entails operation of the LTA SOFC cell at an operating temperature of 760-780 °C. Experimental set-up and compartments of the working cell were similar to the ones described in Chapter 3. However, some modifications to the original set-up were made to fulfil the requirements for the practical work on the oxygen diffusion through plastic tubing as well as pumping of oxygen in and out of carrier gas prior to its entering the liquid tin electrode fuel cell. The carrier gas used in the measurements was zero grade (6 ppm O_2) nitrogen (BOC, UK).

The most important pieces of equipment that were added to the main set-up: potentiometric oxygen sensor (Kent Industrial Measurements, UK), oxygen pump (made of 10YSZ symmetrical cell (closed at one end) with Pt electrode on inner and outer side of the tube) and electrical furnace to heat up both sensor and pump (Figure 5.2). The outer

diameter of the 10YSZ tube was 10 mm with wall thickness of 1 mm and overall length of 120 mm. Platinum ink (4082 Pt Vitr-Au-Less Conductor, Ferro Electronic Materials, USA) for electrodes was painted on the inner and outer sides of the YSZ tube and sintered at 1000 °C for 2 hours (ramp rate of 10 °C per minute). Platinum wires were attached to each electrode prior to sintering, for electrical connections.

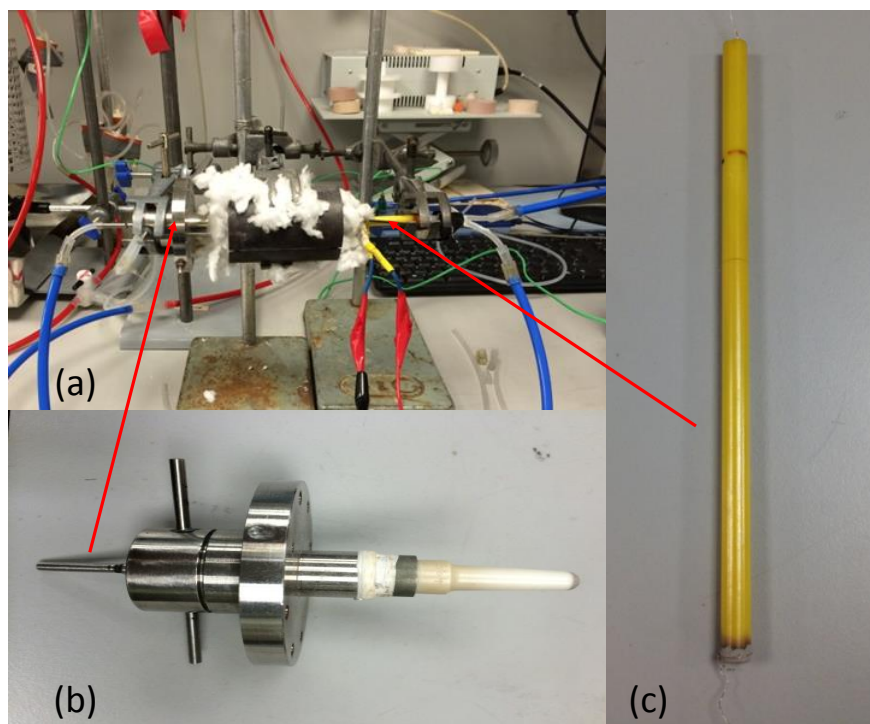


Figure 5.2 Electrical furnace for heating oxygen sensor and oxygen pump (closer look) in the overall set-up (a); oxygen sensor (b); oxygen pump (10YSZ symmetrical cell (closed at one end) with two Pt electrodes and Pt wires) (c).

During the practical work two types of tubing were used. During the early stages, 1/4" (6.35 mm) OD, 1/8" (3.18 mm) ID flexible vinyl (PVC) tubing (Swagelok, UK) suitable for operation from -40 to 73 °C was used together with 4 mm OD, 2 mm ID silicone peroxide tubing (VWR International Ltd., UK). At later stages, vinyl and silicone peroxide tubing were replaced by hard, lightweight, flexible nylon tubing of two sizes 1/4 (6.35 mm) OD and 1/8" (3.18 mm) OD (Swagelok, UK) suitable for operation from -40 to 93 °C. All types of tubing employed in this chapter are listed in Table 5.1.

Table 5.1 Details of all the tubing employed in experimental work.

Name of the tubing	Material	Dimensions	Supplier
Vinyl	Polyvinyl chloride (PVC) - $(C_2H_3Cl)_n$	1/4" (6.35 mm) OD and 1/8" (3.18 mm) ID	Swagelok, UK
Silicone peroxide	Basic elastomer – silicone; catalyst/filler - peroxide	4mm OD and 2 mm ID	VWR International Ltd., UK
Nylon	Nylon	1/4" (6.35 mm) OD, thickness 1.0 mm	Swagelok, UK
Nylon	Nylon	1/8" (3.18 mm) OD, thickness 0.5 mm	Swagelok, UK

An electronic circuit connected to the 10YSZ cell (oxygen pump) was inserted into the overall set-up to drive the pump. An electronic circuit was built specifically to be used with the oxygen pump (Figure 5.3), where the voltage (5 V) from the power supply unit was divided using four 1 k Ω resistors connected in series, which provided 1.25 V across each of the resistors (Figure 5.3a). The complete circuit consisting of ammeter, voltmeter and variable resistor (up to 1 M Ω) together with the oxygen pump is shown in Figure 5.3b.

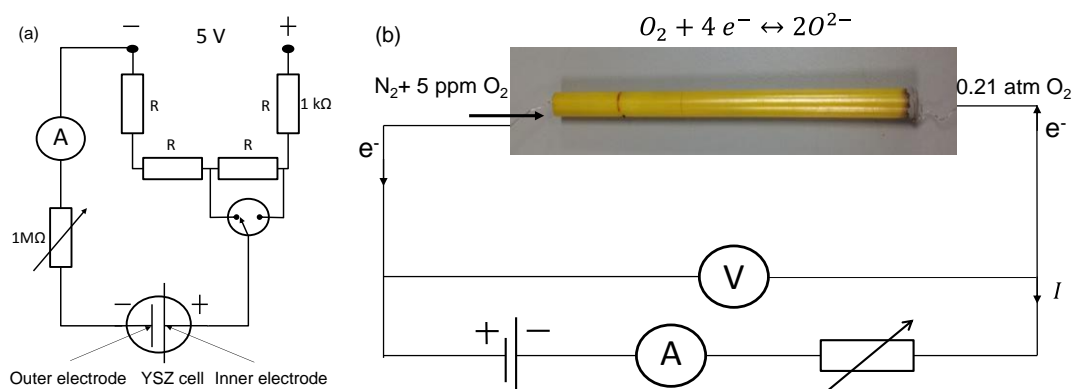


Figure 5.3 Electronic circuit with 10YSZ cell served to pump oxygen in and out of nitrogen flow (a); schematic of the operation of the oxygen pump using the electronic circuit (b).

A schematic of the experimental rig used in this work is shown in Figure 5.4a with detailed representation of the oxygen sensor and oxygen pump operable with in-house built electronic circuit, shown in Figure 5.4b. The flow of nitrogen was supplied to the oxygen pump (to pump oxygen in or out) followed by the oxygen sensor and then entered the fuel cell (Figure 5.4c) held at operating temperature by an electric furnace. Both oxygen sensor and oxygen pump were held inside a second electrical furnace (Kent Industrial Measurements, UK, 100 W), which was powered by two power supply units (PSU) connected in series (to achieve the required 12 V).

Experimental optimisation

Nitrogen gas entered and exited the fuel cell via alumina tubes with internal diameter 2 mm, the inlet tube being immersed in the liquid tin to a depth of approximately 15 mm so that the gas bubbled through the liquid tin.

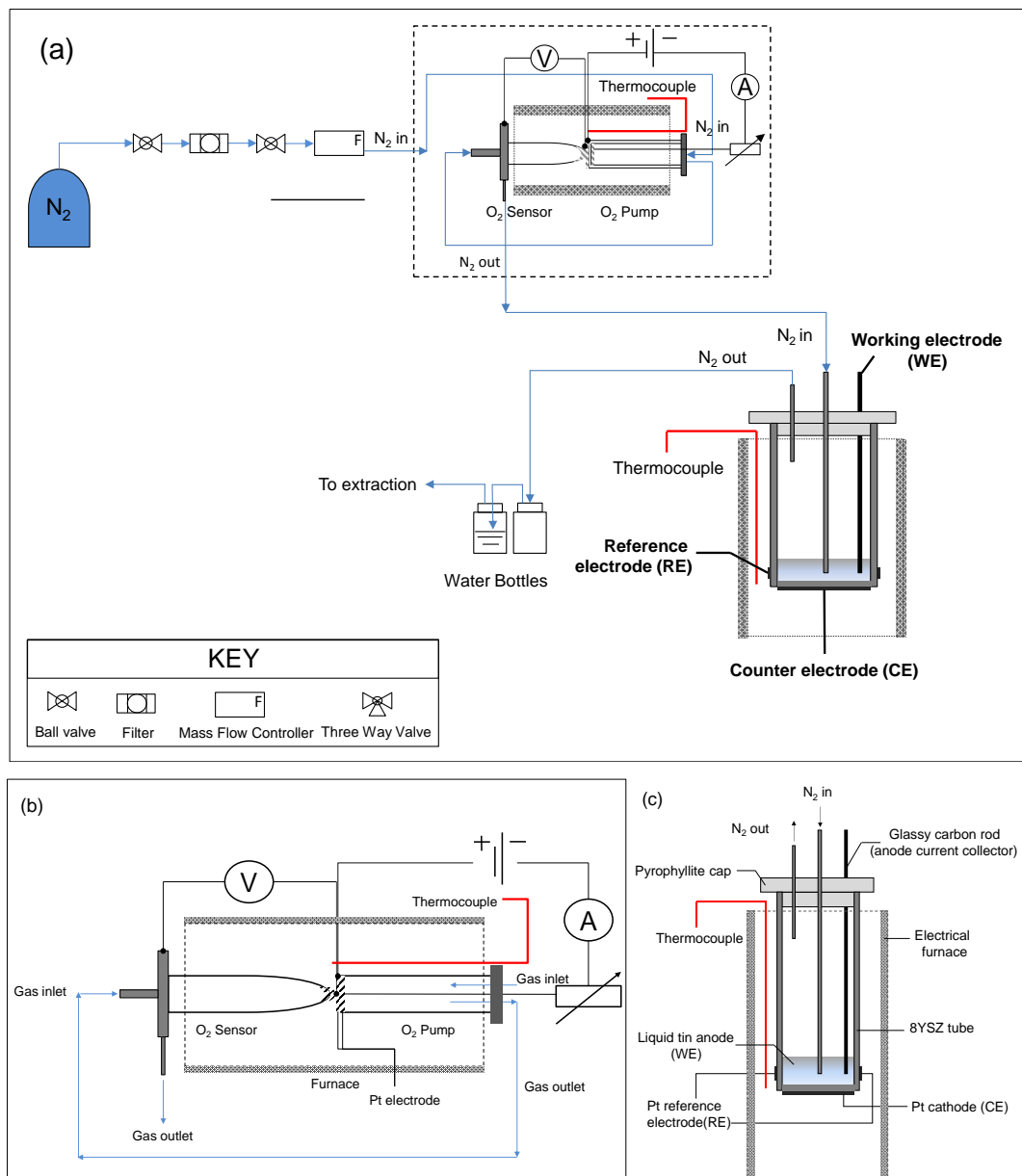


Figure 5.4 Process flow diagram for oxygen permeation and oxygen pumping into the nitrogen stream (a); schematic of experimental rig for the measurement of oxygen permeation and oxygen pumping in and/or the nitrogen flow (expanded view) (b); schematic of an experimental setup of the LMA SOFC cell for oxygen permeation into the N_2 stream (c).

5.4. Results and discussion

5.4.1. Permeation of oxygen through silicone peroxide and nylon tubing

Early measurements were carried out using the set-up shown in Figure 5.4. Oxygen concentration was measured using a potentiometric sensor in the N₂ line at a flow rate of 1.67 ml s⁻¹ and resulted in ca. 500 ppm of O₂ exceeding the O₂ concentration in the N₂ cylinder (6 ppm according to specification) by 100 times. Reducing the flow rate down to 0.83 ml s⁻¹ resulted in an almost doubled initial O₂ concentration (1045 ppm).

As a result the permeation rate of oxygen through silicone peroxide tubing was explored as a function of flow rate of supplied gas (nitrogen). The EMF (together with sensor temperature) was measured at 1.67, 0.83 and 0.33 ml s⁻¹ flow rates before and after reduction in length of silicone peroxide tubing from 88 cm down to 8 cm.

Subsequently, in order to reduce parasitic leakage of oxygen through soft silicone peroxide tubing most of the soft tubing was replaced with less permeable nylon tubing.

A plot of the concentration of leaked oxygen (into N₂ flow) versus the reciprocal of flow rate is shown in Figure 5.5 for the original and reduced length of silicone peroxide tubing, 88 and 8 cm respectively, as well as for nylon tubing.

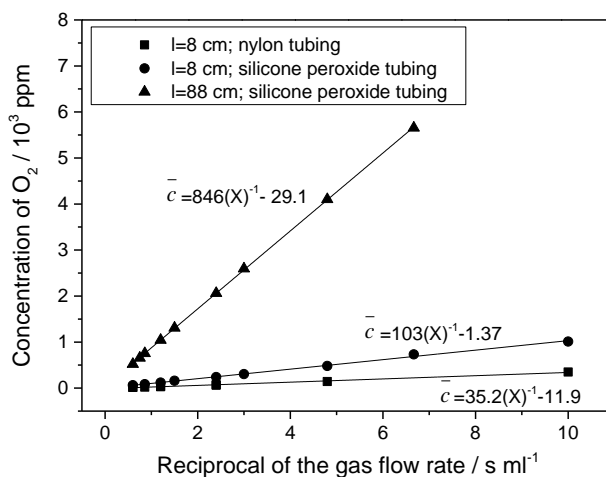


Figure 5.5 Concentration of oxygen diffused through silicone peroxide tubing of 88 and 8 cm and nylon tubing (8 cm) vs. inverse of the gas flow rate.

The obtained data (Figure 5.5) resulted in the straight lines, which provides confidence that the measurement of concentration using the potentiometric oxygen sensor was reliable and accurate. An indicated earlier, inverse proportionality between oxygen concentration and the flow rate of nitrogen predicted by the theory was confirmed (Section 5.2.1).

From the above theory it is expected that oxygen permeation rate should be proportional to the length of tubing, l . The difference in the slopes (almost 8 times) in Figure 5.5 upon reduction of length of tubing from 88 cm down to 8 cm serves as strong evidence to that, as no other parameter was changed during that experiment. Despite that reduction, precise ratio of the slopes according to theory should be 11:1 rather than 8:1. A possible explanation is that some leakage of oxygen was also occurring through the joints. Replacement of the soft by hard tubing resulted in significant reduction of oxygen permeation rates by a factor 2-3 for similar length of hard (nylon) and soft (silicone peroxide) tubing.

The oxygen permeation was investigated by application of the oxygen pump and electronic circuit illustrated in Figure 5.3 whereby oxygen was electrochemically injected and/or removed from the N_2 flow. Figure 5.6 shows the measured oxygen concentration vs. pumped current for silicone peroxide (reduced in length) and nylon tubing.

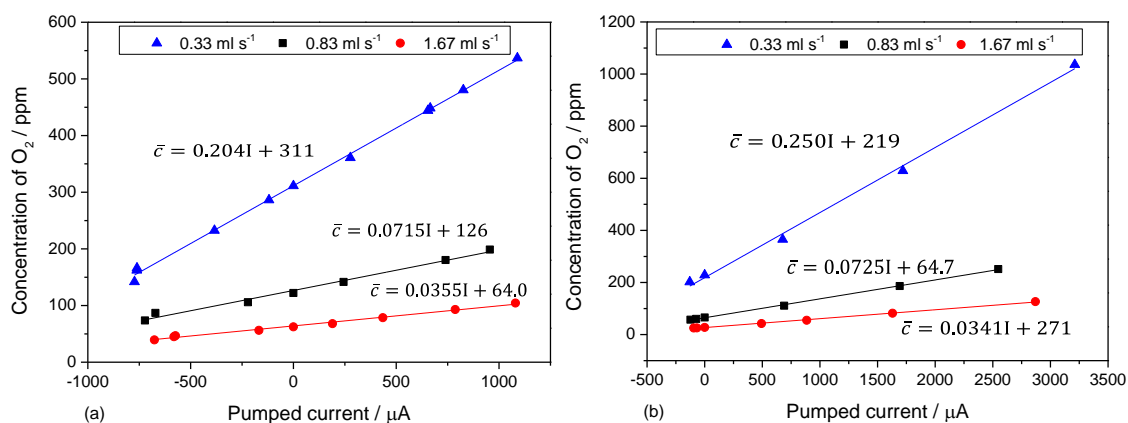


Figure 5.6 Concentration of O_2 vs. pumped current with N_2 flow rate of 1.67, 0.83 and 0.33 $ml\ s^{-1}$ using 8 cm silicone peroxide tubing (a) and hard tubing (b).

Plotting the intercepts from Figure 5.6 vs. the reciprocal of the flow rate resulted in straight lines for both silicone peroxide and nylon tubing. The obtained lines confirm the inverse proportionality between the experimentally measured intercepts (i.e. concentration of O_2 at zero pumped current) and the gas flow rate. This once again confirms that the concentration of oxygen is inversely proportional to flow rate as presented above in Figure 5.5., while the leakage rate was constant.

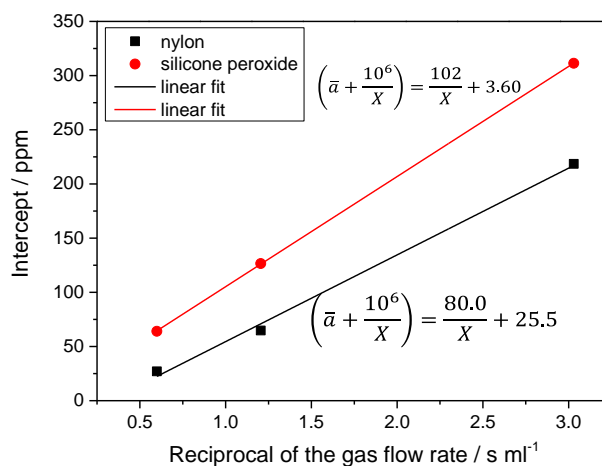


Figure 5.7 Intercepts obtained from Figure 5.6 against reciprocal of the flow rate for silicone peroxide and nylon tubing.

The positive effect from replacement of silicone peroxide tubing with less permeable nylon tubing was evident from the difference of two slopes of straight lines (i.e. 102 vs. 80.0 ppm ml s⁻¹). This would indicate the reduction in diffused O₂ concentration with nylon tubing compared to silicone peroxide at no pumping of additional oxygen.

Close agreement in the slopes obtained from Figure 5.7 and Figure 5.5 (102 and 103 ppm ml s⁻¹) is additional confirmation that same amount of oxygen was diffusing through 8 cm long silicone peroxide tubing during two separate measurements. This indicates consistency in the results obtained using different experimental methods.

In Figure 5.6, all the lines for each flow rate apart from those at 0.33 ml s⁻¹ are parallel (the slopes are in a good agreement), which confirms that the amount of oxygen pumped was consistent with Faraday's law shown in Equation (5.8) with both tubing materials. The following figure (Figure 5.8) provides additional confirmation to that. Two values with both materials obtained with slowest flow rate 0.33 ml s⁻¹ were not aligned with theoretical line. This could be due to some minor leak of oxygen at the joints, which was less influential at higher flow rates (1.67 and 0.83 ml s⁻¹).

Overall the obtained results with two materials confirmed that replacement of silicone peroxide tubing with nylon tubing led to a significant reduction of O₂ levels in the nitrogen flow.

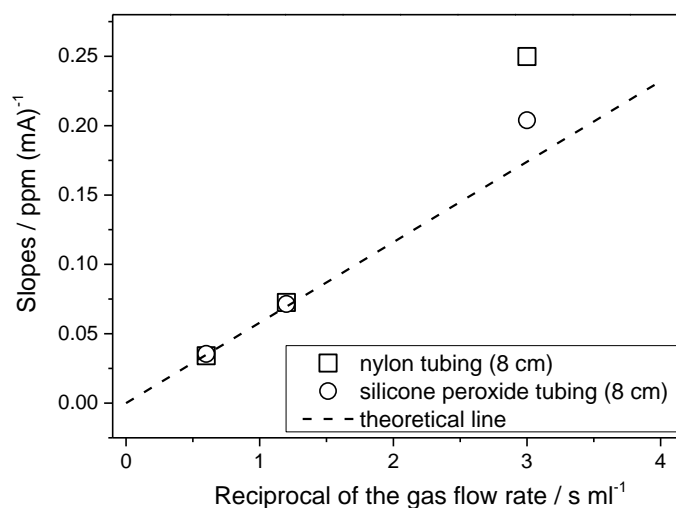


Figure 5.8 Relationship between theoretical and measured injection rate of oxygen and gas flow rate with both silicone peroxide and nylon tubing.

5.4.2. Oxygen pumping in and out of liquid tin anode during cathodic reduction of oxygen in LTA SOFCs

Replacement of silicone peroxide tubing with nylon reduced the amount of oxygen that leaked into the nitrogen line. Having reduced the levels of oxygen the effect of the remaining parasitic oxygen fed into the fuel cell during the electrochemical measurements in LTA SOFC was investigated.

The simplest reaction in LTA SOFC where parasitic leak of O₂ could be studied was cathodic reduction of oxygen (dissolved in tin) at some negative potential (with respect to Sn/SnO₂ redox couple). While measuring the current response from a fuel cell, some oxygen was added and/or removed using the oxygen pump. This enabled the effect of pumped oxygen on the overall fuel cell current to be explored.

The LTA SOFC cell (Figure 3.6) was heated in a vertical furnace to 761 °C under flow of 1.6 ml s⁻¹ of gaseous mixture of dry H₂ and N₂ (4: 96). The potential of the tin electrode was held at -1.1 V vs. RE and the current response was monitored with time, while O₂ was pumped into or out of the nitrogen stream supplied to the fuel cell (Figure 5.9). The estimated accuracy of measured currents is ± 50 μA.

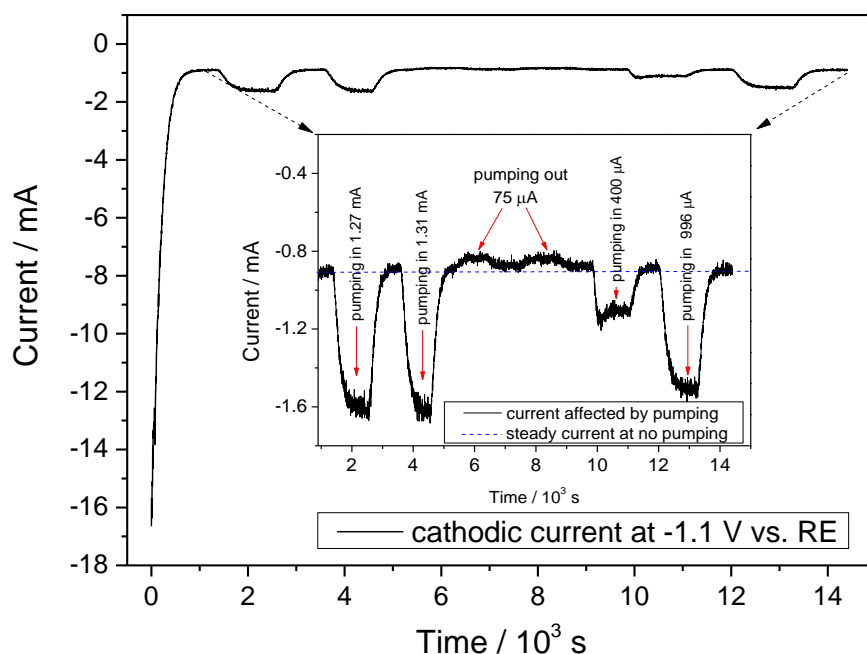


Figure 5.9 The effect of pumped in and pumped out current on cathodic current measured at -1.1 V vs. RE under flow of 1.6 ml s^{-1} of gaseous mixture of dry H_2 and N_2 (4: 96).

One of the limitations of the experiment was removal of greater amount of O_2 (the pumping out current could not exceed $75 \mu\text{A}$). Removal of more oxygen was possible only if higher voltage across the electrodes of the pump had been applied. That, however, could potentially induce electronic conductivity of ZrO_2 in the 10YSZ tube, which was not desirable¹²⁹ as Faraday's law does not apply for current carried electronically.

Figure 5.10a shows the linearity between pumped current and steady cathodic current at each O_2 injection rate into the N_2 flow. Increase in pumped current resulted in higher in magnitude fuel cell current, as more oxygen was supplied to the fuel cell to be reduced at liquid tin/ YSZ interface at -1.1 V. The obtained slope of ca. 0.57 indicates that around 57% of injected current had translated into the overall fuel cell current, and that the remained of pumped oxygen did not stay in the tin but was carried from the cell in the carrier gas. This is an interesting and important result because it shows that although the transit time of the bubbles was very short (the time it took for them to rise through 15 mm of tin) more than half of the oxygen was extracted into the tin. Extraction of the oxygen into the tin can only takes place at the interface between the bubble and the tin. So clearly the time constant for diffusion and oxygen getting within the dimensions of the bubbles is short. It would also suggest that oxygen reaching the interface dissolves or reacts with tin rapidly. This has implications regarding water reduction and will be recalled in Chapter 9.

The intercept of ca. 0.89 mA in Figure 5.10a was the value of the steady fuel cell (cathodic) current at zero pumping current and was due to the parasitic oxygen content of the carrier

gas. The amount of pumped oxygen had a primary effect on overall fuel cell current, which is shown in Figure 5.10b. One would expect that when zero oxygen was present in the system, the fuel cell current would also be zero. The intercept of -0.31 mA can be accounted as not significant as it was within the standard deviation of measured concentration.

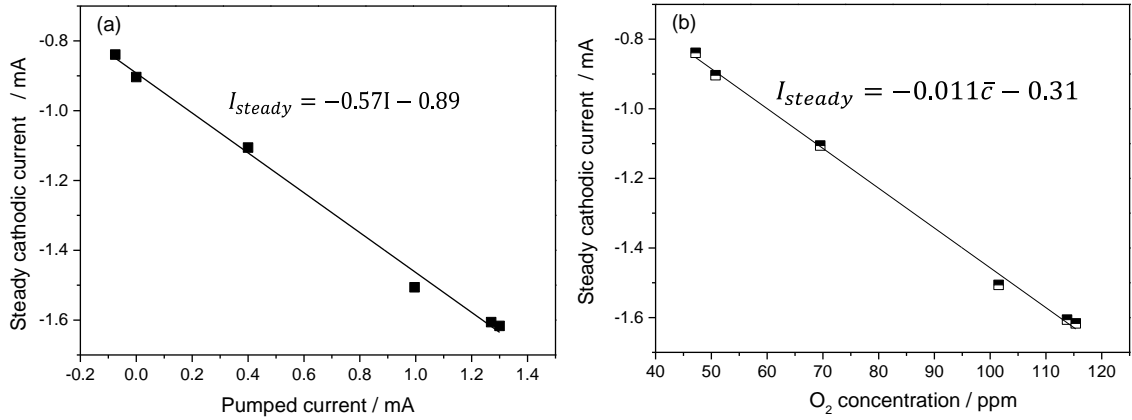


Figure 5.10 Steady cathodic current (a) vs. pumped current and (b) vs. O_2 concentration with total flow rate of 1.6 ml s^{-1} .

The plot of O_2 concentration versus the pumped current (Figure 5.11) resulted in a straight line with a slope of 50 ppm O_2 per 1 mA of pumped current. The intercept of 51 ppm indicated that this amount of O_2 was present in the tubing (when no O_2 was injected or removed electrochemically via the pump).

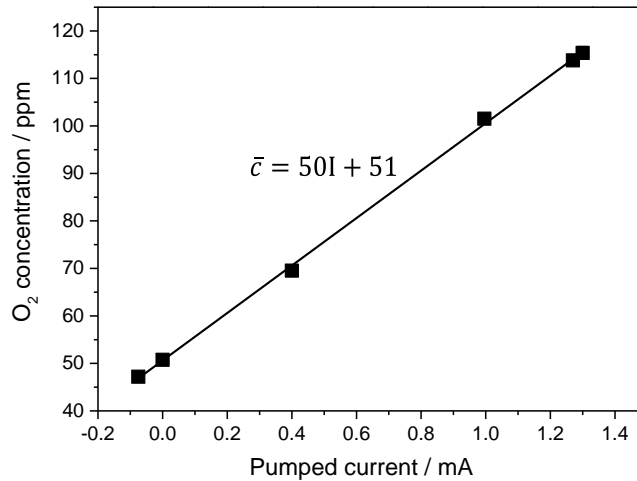


Figure 5.11 Concentration of O_2 vs. pumped current at total flow rate of 1.6 ml s^{-1} .

It is possible to compare the determined slope with the slope dictated by Faraday's law.

The volume of oxygen pumped in ml s^{-1} per 1 mA can be expressed as follows:

$$\frac{d\bar{N}}{dt} = \frac{I}{4F} \quad (5.11)$$

This is equivalent to a flow of oxygen in ml s^{-1} :

$$\frac{I}{4F} 22.4 \times 10^3 \quad (5.12)$$

Injecting this into a N₂ flow of 1.6 ml s⁻¹ results in oxygen concentration of $\frac{22.4 \times 10^3 I \times 10^6}{(1.6)4F}$ ppm or $\frac{22.4 \times 10^6}{6.4F}$ ppm mA⁻¹, i.e. 36.3 ppm (mA)⁻¹ compared to experimentally found 50.0 ppm per 1 mA (Figure 5.11). The discrepancy between the two values may indicate loss of N₂ before it flows through the pump because this would raise the O₂ concentration in the gas.

Overall the applied methodology when oxygen is pumped in or out of the fuel cell during chronoamperometric measurements was important. Using this technique, any inevitable leak of oxygen into the fuel cell can be taken into account and be separated from the overall fuel cell current.

Prior to any electrochemical measurements, steady oxygen reduction current should be measured when LTA SOFC is operated at some negative (with respect to OCV) overvoltage (say -1.1 V) and supplied only with carrier gas (N₂ typically). Then if the fuel cell is operated at positive overvoltage, the oxygen reduction current should be added to the overall anodic current. On the contrary, if LMA SOFC is operated cathodically then the oxygen reduction current should be subtracted from the overall current. This technique for addressing inevitable leak of oxygen into the system is applied in further experimental chapters of this thesis.

5.4.3. Determination of permeability coefficient for plastic tubing

Calculation of permeability coefficient for silicone peroxide tubing, P can be found using the equation (derived in Appendix B) as follows:

$$P = \frac{Y \ln(r_1/r_2)}{21,000 (2\pi l)} \quad (5.13)$$

where Y is permeation rate of oxygen, cm³ s⁻¹, r_1 and r_2 are the external and internal diameters of the tubing, l is total length of tubing, 21,000 is the concentration of oxygen outside the tubing/ Pa.

Recalling Figure 5.5 where for silicone tubing of total length of 88 cm, the slope of 846 ppm ml s⁻¹ was obtained, which according to Equation (5.6) is 10⁶ Y . Thus $Y=846 \times 10^{-6}$ cm³ s⁻¹. From dimensions of silicone peroxide tubing given in Table 5.1, the value of $\ln(r_1/r_2)$ can be found. Substituting all into Equation (5.13) obtain:

$$P = \frac{846 \times 10^{-6} \times 0.693}{0.21 \times 10^5 \times 2\pi \times 88} = 5.1 \times 10^{-11} \text{ cm}^2 \text{ s}^{-1} \text{ Pa}^{-1} .$$

Applying the analysis for nylon tubing, the permeability coefficient was found to be $1.3 \times 10^{-11} \text{ cm}^2 \text{ s}^{-1} \text{ Pa}^{-1}$, which about 4 times smaller than silicone tubing. This value was still higher than expected, as according to its technical specification is considered to be impermeable to oxygen. A possible explanation for the apparently elevated value for the nylon tubing is that there remained leakage via “soft plastic” connectors and joints, where it was not possible to connect directly between the metal fittings and the nylon tubing.

The obtained values for both silicone peroxide and nylon tubing in the existing set-up was higher than values for other polymers (see comparative Table 5.2). The actual permeability for nylon should be lower than most of the polymers, albeit the apparent permeability (measured taking into consideration all plastic connectors and joints) was relatively high.

Table 5.2 Permeability in polymers at 25 °C for oxygen gas¹²⁸.

Polymer	P/10⁻¹³ cm² s⁻¹ Pa⁻¹ at 25 °C
Polyethylene (LDPE)	2.2
Poly(ethyl methacrylate)	0.9
Poly (ethylene terephthalate)	0.04
Poly (vinylidene chloride)	0.004
UCL (present work)–silicone peroxide	510
UCL (present work)- nylon (polyamide)	130

So the tubing applied in early stages of this project was very permeable to oxygen compared with all other plastics shown above. And therefore was considered not a good plastic to be used for piping “oxygen-free” gases. Notwithstanding that some soft connectors and joints remained in the plumbing, the nylon tubing that replaced silicone peroxide tubing had significantly reduced permeation to oxygen compared to silicone peroxide.

5.5. Conclusion

Parasitic leakage of oxygen into the LTA SOFC cell was a serious problem that needed urgent solution prior to any accurate electrochemical measurement in LTA SOFC.

Several improvements made to the experimental rig enabled a reduction to be made to levels of O₂ in the nitrogen stream from 1045 ppm (initially) down to 50 ppm (finally) with 1.67 ml s⁻¹ flow rate of N₂ in both cases. This was achieved by firstly reducing the length of silicone peroxide tubing from 88 to 8 cm, and secondly by replacing most of the silicone peroxide tubing with less permeable nylon tubing.

Agreement between experimentally-measured permeation rate of oxygen through various tubing (silicone peroxide and nylon) and theoretical prediction (based upon Faraday’s law) provides confidence in accurate and reliable operation of both the potentiometric sensor and the electrochemical pump.

Using the oxygen pump and electrical circuit it was possible to remove O₂ and maintain its concentration in N₂ flow at acceptable levels. The technology developed to account the influence of parasitic oxygen on overall fuel cell performance showed that 57% of pumped oxygen current was translated to the overall fuel cell current, when LTA SOFC was operated at -1.1 V vs. RE and fed with dry N₂. That methodology considers some parasitic oxygen to be inevitable. It is shown that it is possible to correct for its contribution to fuel cell anodic or cathodic current measurements and this is done in the remaining chapters of this thesis.

Finally permeability coefficient for both types of tubing was calculated as 5.1×10^{-11} and $1.3 \times 10^{-11} \text{ cm}^2 \text{ s}^{-1} \text{ Pa}^{-1}$ for silicone peroxide and nylon tubing, respectively. The two values were higher than for other polymers. However, it is considered that the apparently high value measured for nylon was due to the use of short length of soft tubing to enable pipes to be fitted readily to metal connectors.

6. Proposed mechanisms for oxidation of hydrogen in LMA SOFCs

This chapter proposes the mechanisms for oxidation of gaseous fuel (hydrogen) in liquid metal anode SOFCs depending on the reaction conditions such as applied potential and operating temperature. The proposed mechanisms are suggested to be applicable to all metal anodes associated with formation of solid metal oxide upon polarisation of a fuel cell. There are four different modes of operation (and hence mechanisms for oxidation): direct electrochemical oxidation of fuel gas at the liquid metal anode/ YSZ interface; homogeneous oxidation of fuel in the bulk of the liquid anode by dissolved oxygen, followed by electrochemical injection of oxygen to replace the consumed oxygen; electrochemical oxidation of liquid metal at the anode/ electrolyte interface, followed by chemical oxidation of fuel by metal oxide in the bulk of the metal and electrochemical oxidation of liquid metal at a rate significantly higher than metal oxide reduction with fuel, which may lead to the formation of a blocking metal oxide layer. This chapter presents experimental results on oxidation of hydrogen in LMA SOFC under the fourth mode of operation, as the most common one applied in the literature. Investigation of other mechanisms for hydrogen oxidation in LMA SOFC is made in further chapters, Chapters 7 and 8.

6.1. Introduction

The operation of the liquid metal anode SOFC fed with hydrogen fuel is shown in Figure 6.1. Oxygen is reduced at the cathode to oxygen ions, which migrate through the solid electrolyte to the molten metal anode. Molten metal is electrochemically oxidised to metal oxide, which is reduced back to metal via chemical reaction with hydrogen supplied into the melt.

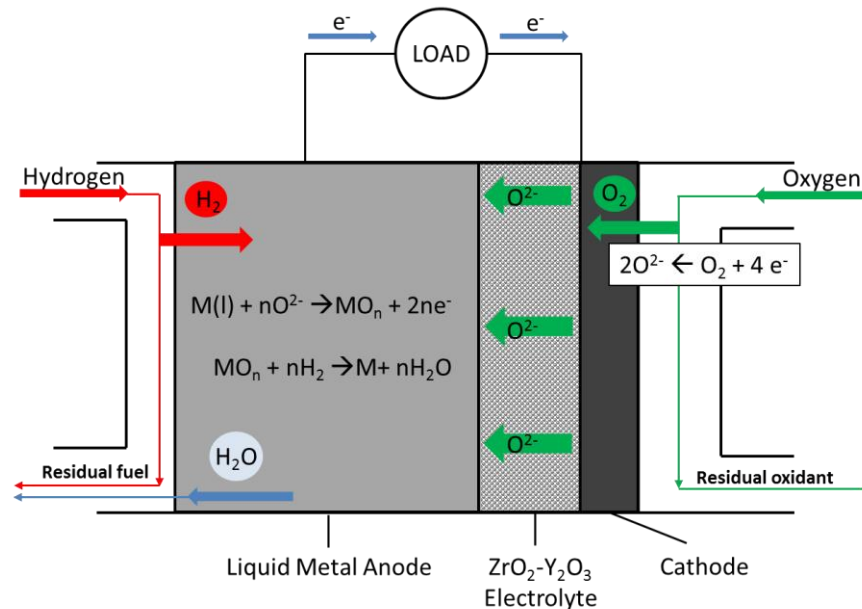


Figure 6.1 Schematic showing operation of LMA SOFC with hydrogen. Yttria-stabilised zirconia (YSZ) is shown as a representative solid oxide electrolyte.

So far, the most widely studied metal anode is tin and its alloys,¹³⁰ and is the subject of this work. The approach employed with tin is applicable to a range of molten metals (M) under investigation. As indicated in the review of LMA SOFC technology (refer to Chapter 2) numerous studies on liquid tin anode SOFCs have established deterioration in cell performance due to the formation of a blocking layer of SnO_2 ^{6,20,72,73,91}. Therefore, it was decided to operate the liquid tin anode SOFC in conditions where an insoluble SnO_2 layer is not formed and yet the fuel oxidation may be observed. This mode of operation will be applied in the present study (refer to Chapters 7 and 8) to gain more knowledge on the fuel oxidation process within the molten anode with no complexity associated with formation of metal oxide.

However, prior to any discussion of this mode of operation (without generation of oxide layer), a general classification of possible modes of operation of LMA SOFC is appropriate as is summarised below, which is the main purpose of this chapter. An example of one of the common modes of operation for LMA SOFCs is considered and presented in detail.

Other modes have not been applied yet in the literature and will be explored in further chapters of this thesis (Chapters 7 and 8).

6.2. Classification of modes of operation for H₂-LMA SOFCs

Depending upon the reaction conditions, in an LMA SOFC four different modes of operation (as example of hydrogen fuel) are proposed (Figure 6.2):

- Direct electrochemical oxidation of fuel at the liquid anode / electrolyte interface – classified as ***E*** (Electrochemical mode).
- Homogeneous oxidation of fuel in the bulk of the liquid anode by dissolved oxygen, followed by electrochemical injection of oxygen to replace the consumed oxygen – classified as ***CE*** (Chemical – Electrochemical mode).
- Electrochemical oxidation of liquid metal at the anode / electrolyte interface, followed by chemical oxidation of fuel by metal oxide in the bulk of the metal – classified as ***EC1*** (Electrochemical – Chemical mode 1).
- Electrochemical oxidation of liquid metal at a rate significantly higher than metal oxide reduction with fuel, which may lead to the formation of a blocking metal oxide layer – classified as ***EC2*** (Electrochemical – Chemical mode 2 - blocking). This mode is only applicable for metal oxides that are in solid phase at operating temperature.

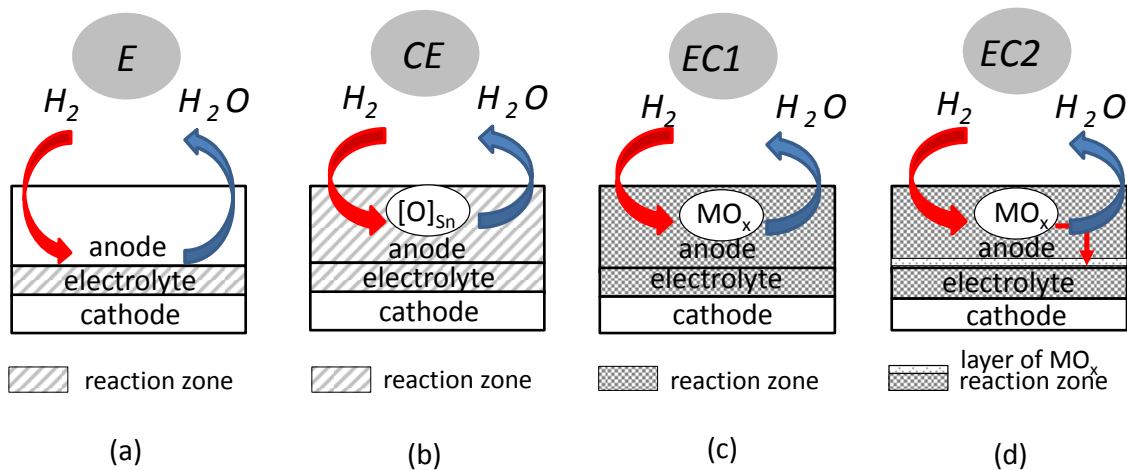


Figure 6.2. Proposed modes of operation for a LMA SOFC fuelled with H₂: (a) direct electrochemical oxidation of H₂ at LMA / electrolyte interface; (b) chemical oxidation of H₂ in the bulk of LMA by dissolved oxygen, followed by electrochemical injection of oxygen at LMA / electrolyte interface; (c) electrochemical oxidation of M followed by chemical oxidation of H₂ in the bulk of the LMA; (d) extensive oxidation of M to insoluble MO_x that may create a blocking layer.

In the first two modes (***E*** and ***CE***) the fuel cell is operated within a potential window in which the LMA is electrochemically inert (i.e. not oxidised by the oxide ion flux) and hence electrochemical oxidation of the fuel occurs directly at the LMA / electrolyte interface (in

the case of mode **E**). However, if the concentration of dissolved oxygen in the melt is sufficient (as in the case of mode **CE**), H_2 dissolves in the liquid metal and undergoes homogeneous oxidation with dissolved oxygen, reducing the concentration of dissolved oxygen, $[O]_{Sn}$ via Reaction (6.1):

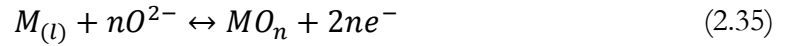


Consumption of dissolved oxygen drives the anodic generation of oxygen at the liquid tin / YSZ interface via Reaction (6.2):



Due to the reported low solubility of H_2 in liquid tin⁶ (0.9×10^{-4} at.% $[H]_{Sn}$ at 1000 °C) compared with that measured by Ramanarayanan and Rapp⁸⁰ for oxygen (0.91 at.% $[O]_{Sn}$ at 1000 °C) the rate of reaction in the **E** mode is likely to be insignificant compared with the **CE** mode. The latter mechanism (dominant **CE** mode), entails homogeneous oxidation of hydrogen in the bulk of tin as the chemical and rate-determining process (see Figure 6.2b).

In **EC** modes the liquid metal is electrochemically oxidised, and then chemically reduced back to the metal via fuel oxidation, as follows:



The rate of electrochemical oxidation of M is clearly greater than or equal to the rate of chemical reduction of MO_n . The ratio of the two rates is given by x :

$$x = \frac{a}{b} \geq 1 \quad (6.3)$$

where a is the rate of electrochemical oxidation of M to MO_n at the electrolyte interface; b is the rate of chemical reduction of MO_n to M in the bulk LMA.

In **EC1** the MO_n generated is totally reduced by fuel dissolved or present in liquid tin (i.e. $a = b$, $x = 1$). The fourth mode (**EC2**) is the case where the rate of electrochemical oxidation of M is greater than the rate of chemical reduction of MO_n (i.e. $a > b$, $x > 1$). During **EC2** mode there is more MO_n produced than can be readily reduced by the fuel. Taking the well-studied liquid tin anode system as an example, a layer of solid tin dioxide is accumulated at the electrolyte surface, which blocks the flow of O^{2-} ions and electrons and, as a result, inhibits further operation^{19,60,72,73}. In modes **E** and **CE** there is no formation of

MO_n (e.g. SnO_2) involved in the overall process, so parameter x is not relevant for these cases.

6.3. Thermodynamics of the modes of operation for LMA SOFCs

For the liquid tin anode (LTA) hydrogen-fuelled SOFC, the standard equilibrium potentials of the H_2 - H_2O , Sn - SnO and Sn - SnO_2 couples as functions of temperature are shown in Figure 6.3. Standard equilibrium potentials were calculated based on the Gibbs free energy of each reaction (with 21% O_2 at 1 atmosphere as oxidant). Required thermodynamic data were generated using the chemical reaction and equilibrium software HSC Chemistry 6.1 (Outotec, Finland)¹³¹.

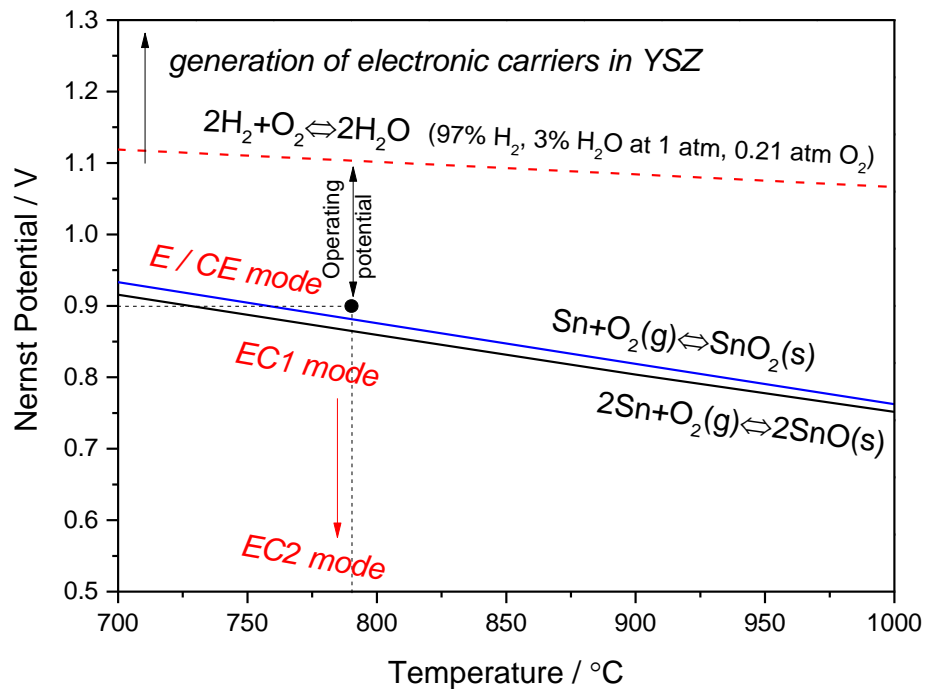


Figure 6.3. Standard equilibrium potentials of H_2 - H_2O , Sn - SnO and Sn - SnO_2 redox systems (all based upon O_2 at 1 atmosphere pressure and 21% concentration) as functions of temperature. Operating potential window in E mode (applied in the present work) is constrained by the onset of electronic conductivity in YSZ from the top and by SnO_2 generation from the bottom at 780 °C.

Modes E and CE in this system can be achieved by applying a potential to the working electrode above the Sn - SnO_2 and Sn - SnO redox potentials. In this way, the tin anode is maintained in an effectively “inert” state and does not interfere in electrochemical reactions at the electrolyte interface. Consequently, no blocking layer of SnO_2 can be generated in these modes. $EC1$ is initiated if the cell voltage is below the Sn - SnO_2 or Sn - SnO redox potential, with $EC2$ becoming more likely with increasing current density / anodic overpotential (Figure 6.3).

Operation in mode *E* or *CE* provides a simpler system compared to *EC* modes. It most importantly sets aside concerns with blockage of electrolyte with metal oxide. However the most common mode of operation for LMA SOFCs in the literature remains to be *EC* mode whereby formation of an oxide layer (in solid form in case of tin^{72,73} or in liquid form – in case of antimony^{66,67}) causes subsequent deterioration of the cell.

Consequently, this chapter aims to demonstrate typical operation of LTA SOFC in *EC* modes whereby electrochemical oxidation of liquid metal at the anode / electrolyte interface, followed by chemical oxidation of fuel by metal oxide in the bulk of the metal takes place.

6.4. Experimental procedure

Experimental work has been done by operating SOFC with liquid tin anode in mode *EC* (Figure 6.2 c, d). In modes *EC* there was no lower potential limit which is set by the Sn-SnO₂ couple in case of *CE* mode and the upper limit was set by generation of electronic carriers in YSZ¹²⁹.

A gaseous mixture of hydrogen and dry nitrogen (4% H₂ : 96% N₂) was supplied to the working cell (Figure 3.6) held at operating temperature (760 °C) by an electric furnace.

The working electrode (25 g of tin) was contained within a closed-end 8YSZ tube. Electrical connection to the working electrode (WE) was achieved using a glassy carbon rod immersed within the liquid tin inside the YSZ tube. Platinum counter and reference electrodes were painted on the outer side of the YSZ tube and sintered at 1000 °C for 2 hours. The total electrode (cathode) area was 1.54 cm².

6.5. Oxidation of hydrogen in LTA SOFC operated in mode *EC1/EC2*

Operation of LTA SOFC in mode *EC1/EC2* was performed to demonstrate how the formation of a blocking layer affects the performance. The applied potential was stepped from OCV (-1.0 V to -0.2 V vs. air electrode (RE)). The current response was monitored with time for 600 s at each set potential.

Since the measurements were performed using the anode (tin) as working electrode and the cathode (air electrode) as counter and reference, the OCV value measured was negative. However to be in agreement with theory and convention, the voltage values are shown positive (Figure 6.4). The current values were dependent upon the effective potential sweep rate and as a result, an uncertainty on the current values has no real significance.

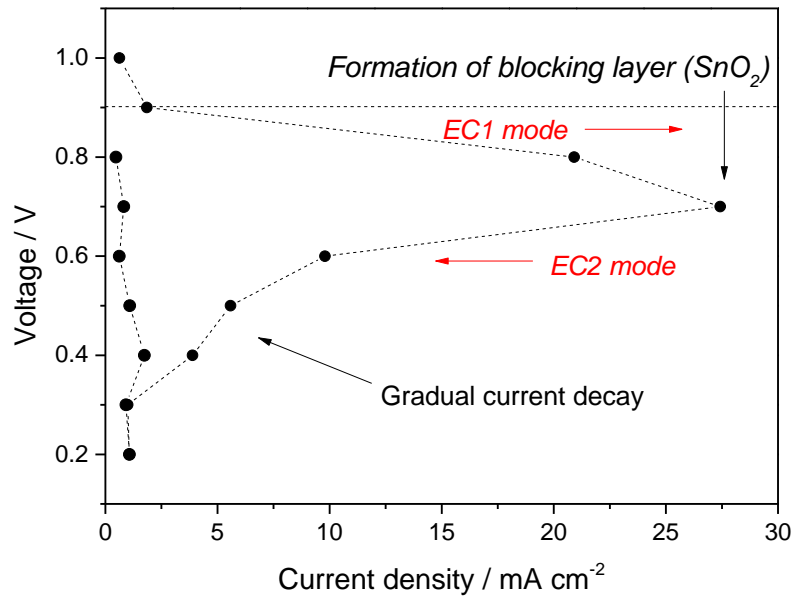


Figure 6.4. The effect of applied potential on current density in LTA SOFC in modes EC1 and EC2 with subsequent formation of a blocking layer (SnO_2) at 760°C .

The obtained OCV of 1.0 V indicated relatively fast dissolution and transport of H_2 within the melt to the liquid tin/ electrolyte interface to participate in electrochemical reactions, which was in agreement with findings reported earlier⁷³. Upon polarisation of the anode the current density has reached its maximum point of 27.5 mA cm^{-2} at ca. 0.7 V and gradually reduced back to nearly zero. At that point the decline in current density was due to formation of blocking layer of SnO_2 which could not be consumed by H_2 due to slower oxidation reaction kinetics and also limited diffusion of H_2 within the melt^{73,89}. When potential was reversed the cell did not recover with constant low current density.

Similar I-V curve for H_2 fuelled LTA SOFC was reported by Wang *et al.*⁷³ whereby the forward scanning curve was much greater than the backward curve in the polarisation curve. Wang *et al.* suggested that greater diffusion rate of hydrogen in liquid tin compared to consumption rate of hydrogen was evident. This argument indicated that hydrogen consumption rate of metal oxide was lower than rate for oxidation of tin to tin dioxide, as suggested earlier in the classification of modes of operation.

The shapes of reported and present (Figure 6.4) polarisation curves was similar albeit the “turning point” due to accumulation of SnO_2 layer was higher than in the case of Wang *et al.*⁷³ (0.70 V vs. 0.25 V). The measured current density respective to this point (ca. 27.5 mA cm^{-2}) was significantly lower compared to 400 mA cm^{-2} . This was probably due to variations in loading of tin and enhanced electrolyte specifications. As such a single crystal 13 mol.% YSZ electrolyte with increased roughness loaded with only 2.0 g of tin (vs. 25 g of tin in present work) was applied. As stated by Wang *et al.*⁷³, the electrolyte roughness enhances the reactive area and thus improves the performance of a LMA SOFC⁶⁹. Since

the aim of this experiment was not to maximise performance, but to clarify the transport of H_2 within molten tin and demonstrate its oxidation, the cell was designed with thicker anode as well robust and thick electrolyte (2000 μm vs. 500 μm) to withstand the weight of tin. As a result, upon increase of the thickness the electrolyte, the membrane resistance was also greater in the present work.

Operation in mode **EC1/EC2** is not the main focus of this thesis. Careful probing in operation of LMA SOFCs in mode **EC1/EC2** is needed and further experimental studies are required to provide better understanding of the system.

6.6. Conclusions

Four possible mechanisms for oxidation of gaseous fuel (hydrogen) in liquid metal anode SOFCs depending on the reaction conditions were proposed. In order to investigate fuel oxidation process within the molten metal operation of LMA SOFC in **CE** mode is advantageous compared to other modes, as it simplifies the system and no blocking layer can be formed.

However, typical characterisation of LMA SOFCs is performed by application of **EC** modes, where electrochemical oxidation of liquid metal at the anode/ electrolyte interface, is followed by chemical oxidation of fuel by metal oxide in the bulk of the metal. Upon extensive polarisation of a LMA SOFC, the rate of electrochemical oxidation of liquid metal increases and exceeds the rate of metal oxide reduction with fuel, which leads to the formation of a blocking oxide layer.

Therefore, operation of LTA SOFC in **EC** modes was demonstrated. The measured polarisation curve contained a so-called “turning point” of potential, after which the current density reduced dramatically and the fuel cell performance did recover. The decline in current density was explained by the formation of a SnO_2 layer which blocked the reactive liquid tin/ electrolyte interface. The shape of the measured polarisation curve was similar to those reported in the literature⁷³.

In order to eliminate the problems with a blocking layer albeit investigate significant parameters for fuel oxidation within the liquid metal the LTA SOFC will be run in **CE** mode, which is presented in the next Chapter.

7. Oxidation of hydrogen in LTA SOFC in mode *E/CE*

This chapter investigates oxidation of hydrogen in LTA SOFC operated in electrochemical (*E*) and/or chemical - electrochemical mode (*CE*). An electrochemical model developed originally was based on solubility of hydrogen governed by Henry's law, followed by diffusion of H₂ to the liquid anode / electrolyte interface and its direct electrochemical oxidation. The model required substantial volume of hydrogen to be trapped above the liquid tin anode. This could only be possible if H₂ and bubbled gases form a metallic foam above the tin.

To examine the possibility of a foam, two main experiments were performed: the first involved detection via electrical resistance of a possible foam; the second involved application of a silica tube for visualisation of a liquid tin anode bubbled with H₂/Ar mixture. As no foam was found, the first model that considered the *E* mode (direct anodic oxidation of H₂) was considered incorrect and replaced by the model developed for *CE* mode operation.

A refined electrochemical model is then developed based upon fast dissolution of hydrogen in a molten tin anode, slow, rate-determining homogeneous reaction of hydrogen with oxygen dissolved in the liquid tin, followed by anodic oxygen injection under diffusion control to replace the oxygen removed by reaction. Experimentally-generated data are used to validate the model. The model has introduced a new key parameter, the dynamic oxygen utilisation coefficient (\bar{z}), which takes a value between zero and unity; its value is determined by geometric, mass-transfer and kinetic factors in the cell as well as the partial pressure of the supplied hydrogen fuel. Current output of the cell is proportional to the value of \bar{z} .

7.1. Introduction

Despite the remarkable advantages of LMA SOFCs there are certain technological challenges which inhibit commercialisation¹³⁰. One of the main issues is the lack of fundamental understanding of the mechanisms of reaction and transport of active species (i.e. reactants and products) within a liquid metal electrode⁶.

Development of molten anode SOFCs requires detailed investigation of the fundamentals of operation. As such, a first step towards operation on direct solid fuel is the use of a simple gaseous fuel such as hydrogen operated in *E* or *CE* mode, (Chapter 6, Figure 6.2a,b). Such an approach is adopted here. Other approaches to the elucidation of anode processes in LME SOFCs include the Rotating Electrolyte Disc (RED)¹³² which offers the prospect of allowing the parameters controlling mass transport of dissolved species in the melt to be studied. Operation in mode *E* or *CE* provides a simpler system compared to other modes. It most importantly sets aside concerns with blockage of electrolyte with metal oxide.

Therefore, this chapter aims to explore the dissolution of hydrogen and its subsequent oxidation in LMA SOFC. The approach used here is also applicable to other fuel gases (e.g. CO). The electrochemical model developed in this work provides a framework for the interpretation of the generated experimental data. In developing the theory, an important parameter, \bar{z} , is introduced which takes a value between zero and unity; the factors determining the value of \bar{z} , are discussed in Section 7.6.

7.2. Experimental procedure

In the present chapter, all experimental work entails operation in mode *E* / *CE* (Chapter 6, Figure 6.2a,b). The lower potential limit of mode *E* / *CE* was set by the Sn-SnO₂ couple and the upper limit by the generation of electronic carriers in YSZ¹²⁹.

The system was operated at a constant temperature of 780 °C; dry or humidified hydrogen/ argon was bubbled into the tin and the working electrode was held at -0.90 V versus an air reference. A schematic of the experimental rig used in this work is shown in Figure 3.2. Dry or humidified (3% water) argon was supplied to the oxygen sensor after which it was mixed with hydrogen and supplied to the cell (Figure 3.6) held at operating temperature by an electric furnace. Gases entered and exited the cell via alumina tubes with internal diameter 2 mm, the inlet tube being immersed in the liquid tin to a depth of approximately 15 mm so that the gas bubbled through the liquid tin.

The working electrode (25 g of tin shot) was contained within a closed-end 8YSZ tube. Electrical connection to the working electrode (WE) was achieved using a glassy carbon rod immersed within the liquid tin inside the YSZ tube (Figure 3.6). Platinum counter and reference electrodes were painted on the outer side of the YSZ tube and sintered at 1000 °C for 2 hours (ramp rate of 10 °C per minute). Current collection from the cathode and reference electrode was achieved using platinum mesh and wires. The total electrode (CE) area was 1.54 cm².

7.3. Oxidation of hydrogen in LTA SOFCs in mode *E/CE*

Dissolution of hydrogen and its oxidation in LMA SOFC was investigated using the working cell operated in mode *E / CE*. Experimental investigations were first performed to assess the effect of hydrogen partial pressure in terms of current generation and dynamics associated with changes in hydrogen concentration. These results were then used in support of an analytical modelling analysis. However, before conducting these experiments, it was necessary to assess the low levels of oxygen present in the system which cannot be totally excluded, and take account of the effect on the electrochemistry.

7.3.1. Assessment of the effect of residual oxygen

A potentiometric oxygen sensor enabled the level of oxygen into the argon line to be monitored. In order to account for the contribution of oxygen reduction current to the overall measured current, the following procedure was performed and repeated prior to each test run in this work.

Initially, to remove residual SnO₂ present in the working cell, a mixture of 3% H₂ and 97% Ar was supplied for 600-900 s. A potential of -0.90 V vs. air electrode (RE) was then applied to the working electrode while simultaneously switching the gas flow to argon with no added hydrogen (Figure 7.1).

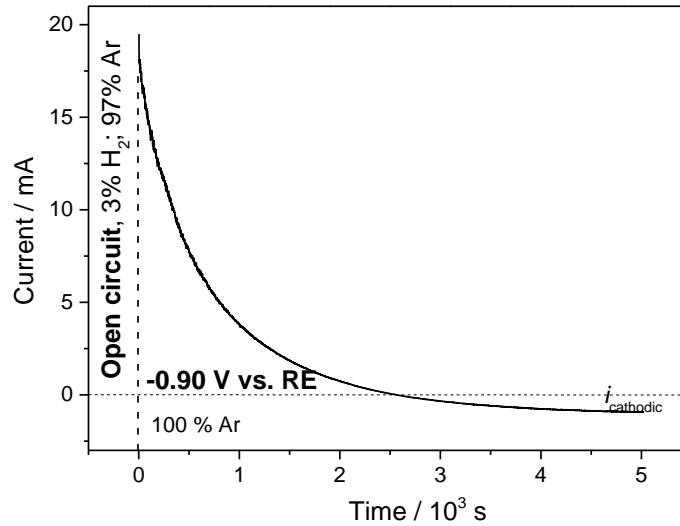


Figure 7.1. Anodic current at -0.90 V vs. RE at 780 °C (immediately after switching from 3% to zero H₂).

The current decreased slowly to zero and then eventually to a steady negative current, $i_{cathodic}$; this negative current was due to the parasitic level of oxygen in the system (-1.0 mA in Figure 7.1).

The current at zero hydrogen input, $i_{cathodic}$, was measured throughout the experiments presented in this work; anodic current data were corrected in each case for the individual measured value of $i_{cathodic}$.

7.3.2. Oxidation of hydrogen in LTA SOFC

Hydrogen of partial pressures from 8 to 26 kPa was supplied to the LMA at 780 °C. A potential of -0.90 V vs. air electrode (RE) was applied. The anodic current was monitored with time while $p(\text{H}_2)$ was increased step-wise from zero to 8, 15 and 26 kPa (Figure 7.2a) and likewise was reduced from 26 kPa to zero (Figure 7.2b).

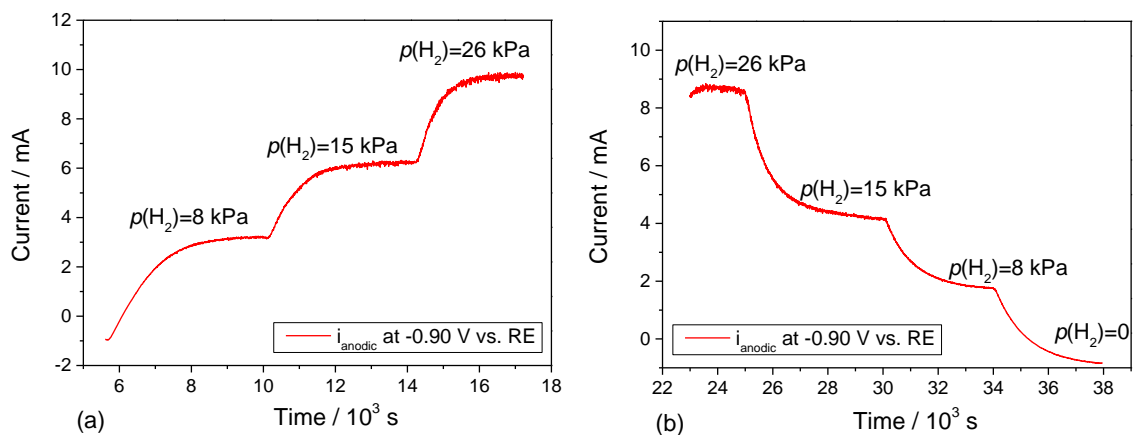


Figure 7.2. Anodic current at -0.90 V vs. RE at 780 °C with increase of $p(\text{H}_2)$ from 0 to 26 kPa (a); and with decrease of $p(\text{H}_2)$ from 26 kPa to 0 (b).

The same procedure was repeated, varying the total flow rate while maintaining a constant $p(\text{H}_2)$, as shown in Figure 7.3.

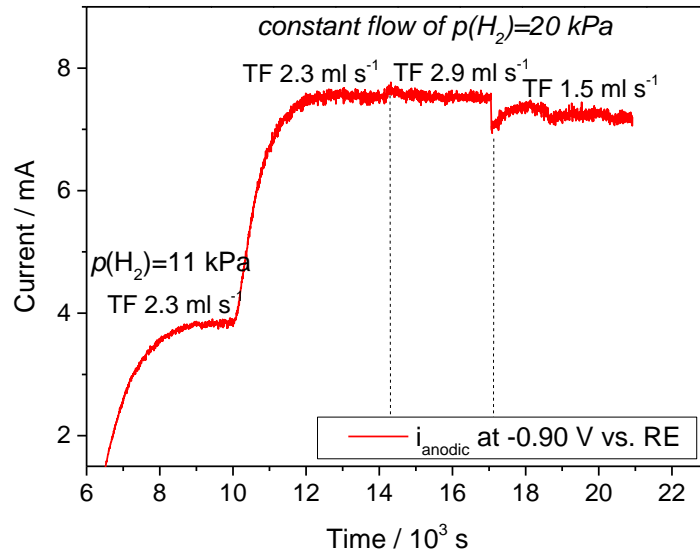


Figure 7.3. Anodic current with variation of $p(\text{H}_2)$ and of total flow rate (TF) at 780 °C.

The results in Figure 7.3 confirm that changes in total flow rate (shown as TF in Figure 7.3) had only a minimal effect on the measured steady anodic current.

Steady anodic currents as a function of $p(\text{H}_2)$ with various total flow rates and direction of $p(\text{H}_2)$ modulation are summarised in Figure 7.4. The currents shown have been corrected for parasitic oxygen reduction current, i_{cathodic} (see Section 7.3.1). The estimated accuracy of measured currents is $\pm 50 \mu\text{A}$.

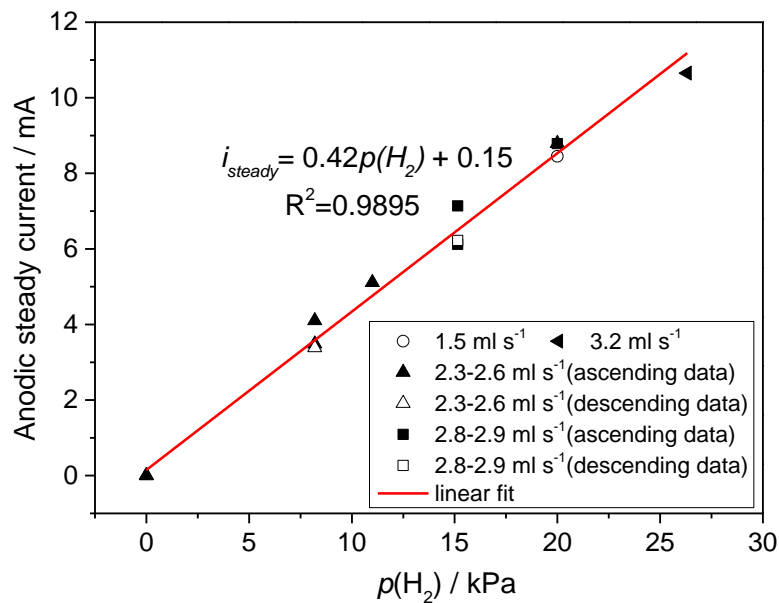


Figure 7.4. Steady anodic oxidation current as function of $p(\text{H}_2)$ with varying TF and direction of change of H_2 composition (ascending / descending), all at 780 °C.

Proportionality between steady oxidation current and H₂ partial pressure with no hysteresis and no significant sensitivity to total flow rate was evident (for the range of flow rates studied, 1.5 – 3.2 ml s⁻¹). Further refinement of the analysis is performed in Section 7.6.1.

7.4. Electrochemical model for *E* mode

Initial results, shown in Figure 7.2 -Figure 7.4, demonstrate three significant points:

- i) steady anodic currents were proportional to hydrogen partial pressure (this is refined later in the chapter);
- ii) steady anodic currents were essentially independent of total gas flow rate;
- iii) following step changes in hydrogen partial pressure, the current-time behaviour displayed a gradual and progressive change between the two endpoints, which appeared to be exponential in character.

In order to encompass these indicative effects an electrochemical model for *E* mode operation has been developed with the assumptions made as follows:

- a) the process (anodic oxidation) is diffusion-limited so that the concentration of hydrogen at the interface is close to zero at the chosen operating potential of the anode;
- b) the solubility of hydrogen in tin accords with Henry's law (bearing in mind point i);
- c) the dissolution of hydrogen in tin is governed by a first-order rate equation;
- d) diffusion of H₂ to the electrolyte interface occurs through a diffusion layer of constant thickness, δ , as a result of convection induced by bubbling and thermal effects;
- e) the system is considered to be in quasi-equilibrium.

A summary of the model is shown below. Complete derivation of the model is shown in Appendix C.

In the theoretical treatment in this series, hydrogen is denoted by single prime superscript, for example c' . Consider the following: hydrogen is bubbled through the liquid tin at partial pressure p_1' , a potential, E , is applied to the Sn / YSZ interface and a steady current, i_1 , is observed. The partial pressure of H₂ is then increased to p_2' and the current, i , increases with time and eventually stabilises at i_2 (Figure 7.5).

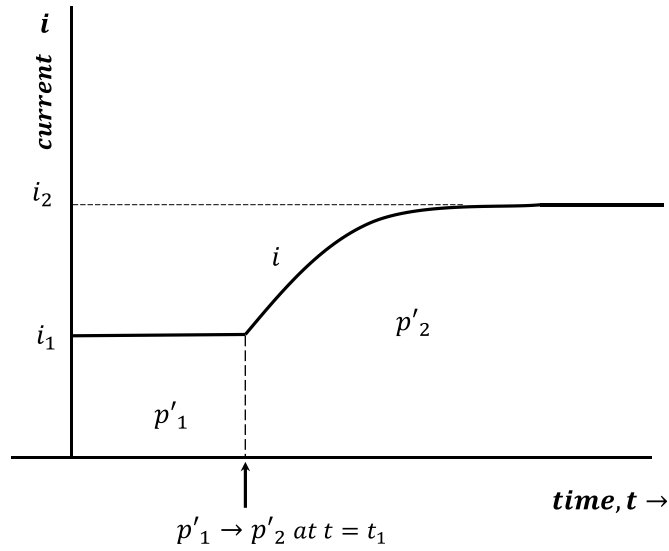


Figure 7.5. Schematic of the step change in $p(\text{H}_2)$ during oxidation at applied potential in the E/CE mode of operation.

When H_2 at partial pressure of p_2' is bubbled through tin, it dissolves in the tin and eventually saturates the solution; the saturated concentration of H_2 is c_2^{*} . The general unsaturated concentration is written as c' . The anodic oxidation of H_2 at the liquid tin / YSZ interface is as follows:



For a sufficient total flow rate of gas, the rate of dissolution of hydrogen in the tin is proportional to the difference of the saturated concentration and the actual concentration at any given time.

The rate of anodic oxidation of H_2 via reaction (7.1) is (i/nF) where n is the number of electrons transferred per hydrogen molecule, i.e. $n = 2$. If the amount of H_2 (in moles) in the tin is expressed as N' , we may write:

$$\frac{dN'}{dt} = k_1'(c_2^{*'} - c') - \frac{i}{nF} \quad (7.2)$$

where k_1' is the rate constant for dissolution.

When $c' = c_2'$, $i = i_2$ and $\frac{dN'}{dt} = 0$; note that $c_2' < c_2^{*}$

It follows that:

$$k_1'(c_2^{*'} - c_2') = \frac{i_2}{nF}$$

and

$$c_2' = c_2^{*'} - \frac{i_2}{nF k_1'} \quad (7.3)$$

Based on assumption (i) the current, i , is controlled by diffusion through the diffusion layer of thickness δ . The flux, J' , is given by Fick's first law, which is expressed as:

$$J' = -\frac{D'Ac'}{\delta} \quad (7.4)$$

where D' is the diffusion coefficient, A is the area of the interface and c' is the concentration of hydrogen.

Equating the flux with current, i via Faraday's law:

$$J' = -\frac{i}{nF} \quad (7.5)$$

Combining (7.4) and (7.5) leads to:

$$i = \frac{nFD'Ac'}{\delta} \quad (7.6)$$

This will be written as:

$$i = k'_2c' \quad (7.7)$$

where k'_2 is given by:

$$k'_2 = \frac{nFD'A}{\delta}$$

From (7.7):

$$i_2 = k'_2c'_2 \quad (7.7 \text{ a})$$

Eliminating i_2 between (7.3) and (7.7 a):

$$c'_2 = c_2^{*'} - \frac{k'_2c'_2}{nFk'_1} \quad (7.8)$$

Rearranging:

$$c'_2 = \frac{c_2^{*'}}{\left(1 + \frac{k'_2}{k'_1nF}\right)} \quad (7.9)$$

Write:

$$w' = \left(1 + \frac{k'_2}{k'_1nF}\right)^{-1} \quad (7.10)$$

Then

$$c'_2 = w'c_2^{*'} \quad (7.11)$$

By the same reasoning:

$$c'_1 = w'c_1^{*'} \quad (7.12)$$

Eliminating i between (7.2) and (7.7):

$$\frac{dN'}{dt} = k'_1 c_2^{*'} - k'_1 c' \left(1 + \frac{k'_2}{k'_1 nF} \right)$$

Using (7.10) and (7.11) leads to:

$$\frac{dN'}{dt} = \frac{k'_1}{w'} (c_2' - c') \quad (7.13)$$

Furthermore:

$$\frac{dc'}{dt} = \frac{1}{V} \frac{dN'}{dt} \quad (7.14)$$

where V is the volume of the solution.

Combining (7.2) and (7.14):

$$\frac{dc'}{dt} = \frac{k'_1}{Vw'} (c_2' - c') \quad (7.15)$$

Rearranging and integrating (the switch from p_1' to p_2' occurs at t_1):

$$\int_{c_1'}^{c_2'} \frac{dc'}{(c_2' - c')} = \frac{k'_1}{Vw'} \int_{t_1}^t dt$$

$$-\ln \frac{(c_2' - c')}{(c_2' - c_1')} = \frac{k'_1}{Vw'} (t - t_1) \quad (7.16)$$

From (7.7) it follows that:

$$-\ln \frac{(i_2 - i)}{(i_2 - i_1)} = \frac{k'_1}{Vw'} (t - t_1) \quad (7.17)$$

In a steady-state condition $\frac{dN'}{dt} = 0$ and equation (7.11) shows that $c' = w' c^{*}$; using (7.7)

$$i_2 = w' k'_2 c_2^{*'} \quad (7.18)$$

Applying the assumption that Henry's law is applicable to the system:

$$c^{*'} = k'_3 p' \quad (7.19)$$

where k'_3 is a constant for a given temperature.

Thus:

$$i_2 = w' k'_2 c_2^{*'} = w' k'_2 k'_3 p_2' \quad (7.20)$$

Predictions from model for E mode:

- i) Steady current is proportional to hydrogen partial pressure (Equation (7.20)).
- ii) Plot of $\ln \frac{i_2 - i}{i_2 - i_1}$ versus t should show a straight line of slope $-\frac{k'_1}{Vw'}$ through the origin (according to Equation (7.17)). Note that $\frac{Vw'}{k'_1}$ is the time constant for the curve of i versus t when a step-change is made in hydrogen partial pressure.

Comments regarding the parameter w'

The significance of the parameter w' requires brief consideration; it does not have fundamental significance as it depends upon geometric factors of the cell. However, it is important, as its value is required for analysis of the data as is shown later. Equation (7.10) indicates that the value of w' is a measure of the balance between k'_1 and k'_2 , in other words between the rate of dissolution of hydrogen in tin and its rate of removal by anodic oxidation.

Three possible situations may be identified:

- a) $w' \approx 1$ - at steady state, concentration of hydrogen in the bulk of the tin electrode is close to the saturation value for a given hydrogen partial pressure;
- b) $w' \ll 1$ - at steady state, concentration of hydrogen in the bulk is very small (much less than saturated value) and current is removing hydrogen by anodic oxidation at the same rate as hydrogen is dissolving into the tin at its maximum rate (because the bulk concentration is close to zero);
- c) $0.1 < w' < 0.7$ this is the intermediate case

7.4.1 Determination of the apparent solubility of hydrogen in liquid tin using model for E mode

Electrochemical modelling of hydrogen dissolution and anodic oxidation in liquid tin suggested the way for the apparent solubility of hydrogen in molten tin to be calculated. Calculation of apparent solubility is employed in this section. An expression for the number of moles of dissolved hydrogen in tin may be derived using the Equations (7.7 a), (7.10) and (7.11) presented above.

Eliminating C'_2 between (7.7 a) and (7.11) leads to:

$$i_2 = k'_2 w' c_2^{*'} \quad (7.21)$$

Rearranging (7.10)

$$k'_2 = k'_1 nF \left(\frac{1 - w'}{w'} \right) \quad (7.22)$$

Substituting for k'_2 from (7.22) to (7.21):

$$i_2 = (1 - w') nF k'_1 c_2^{*'} = \left(\frac{k'_1}{V w'} \right) w' (1 - w') V nF c_2^{*'}$$

Or

$$c_2^{*'} = i_2 \left(\frac{Vw'}{k_1'} \right) [w'(1-w')VnF]^{-1} \quad (7.23)$$

This is an expression for the solubility of hydrogen in tin in terms of the steady current, i_2 , the time constant, Vw'/k_1' , the volume of tin, V , and the parameter w' . Alternatively, the number of moles of hydrogen dissolved in the tin is given by $c_2^{*'}V$ as follows:

$$c_2^{*'}V = i_2 \left(\frac{Vw'}{k_1'} \right) [w'(1-w')nF]^{-1} \quad (7.24)$$

Initial measurements indicated that for an applied potential of -0.90 V vs. RE, w' lies within the range 0.2-0.8; thus, $w'(1-w')$ lies in the range 0.16-0.25.

The mean value of k_1'/Vw' , which is the inverse of the time constant was reported to be $(1.2_4 \pm 0.1_3) \times 10^{-3} \text{ s}^{-1}$ (see Table 7.1). The slope of the line of anodic steady current i_{steady} vs. $p(\text{H}_2)$ (Figure 7.4) indicated that for 100% hydrogen at 0.1 MPa pressure, i_2 is 42 mA in tin at 780 °C.

Inserting these values into equation (7.24) reveals a value for $c_2^{*'}V$ of $0.7\text{-}1.1 \times 10^{-3}$ moles of hydrogen in 25 g of tin. This figure translates into $(2.8\text{-}4.4) \times 10^{-3}$ moles of H_2 in 100 g of Sn or 0.47 – 0.75 at.%. Hence the lower limit of this range (0.47 at.%) exceeded the solubility of [H] in 100 g of tin reported by Iwase⁷⁸ 34 times and by 5200 times value given by Bever *et al.*⁷⁷ reported by Abernathy *et al.*⁶(see Chapters 2 and 8 - Sections 2.3.3 and 8.1, respectively).

Considerable difference between measured and reported solubility of H in liquid tin could be explained if all volume of H_2 along with carrier gas were trapped inside liquid tin in a form of foam. The foam would effectively store hydrogen and for a given volume of foam, behave as if the gas were dissolved with solubility proportional to the partial pressure of the supplied H_2 . An investigation aimed at the detection of foam was undertaken and described in the Section below.

7.5. Investigation of a possibility of a metal foam in LTA SOFC

Two mechanisms for oxidation of hydrogen in LTA SOFC in the potential window where SnO_2 cannot be formed have been proposed in the previous Chapter (*E* mode and *CE* mode). Experimental work presented in this section has been done to validate or rule out one of the mechanisms (*E* mode) which would necessitate the existence of persistent metallic foam above liquid tin anode. This requires that foam is induced by bubbling of gaseous mixture of H_2/Ar through liquid tin at high temperatures. A specially-made set-up

was developed to measure electrical resistance between two glassy carbon rods (one of them inserted into tin and one above the pool of liquid tin). Development of an apparatus with moveable electrical probe was of technological significance. It allowed the GC rod to move freely vertically while maintaining the atmosphere above tin free of oxygen.

A metal foam would display electronic conductivity though with lower magnitude than that of the liquid tin¹³³. Initial measurements with an unsheathed dipping GC probe indicated some conductivity above the tin pool suggesting the presence of a foam. However, when the dipping probe was subsequently sheathed with a alumina tube leaving only the tip of the GC exposed, preventing the probe from contacting the inside surface of the zirconia tube directly, electronic continuity was no longer found. This latest experiment showed that the continuity initially observed was due to conduction via the zirconia tube together with some electrochemical reaction at the surface of YSZ tube. Absence of a foam was confirmed by viewing liquid tin, through which gas was bubbled, using a transparent silica tube in place of the zirconia tube; no metal foam was observed above the liquid tin pool (with and without zirconia chips in the tin). Hence the *E* mode, requiring the existence of a persistent tin foam, was rejected as a primary mechanism for the oxidation of hydrogen.

7.5.1. Introduction

In Section 7.3 the oxidation of hydrogen in a LTA SOFC was investigated involving the bubbling of a hydrogen / argon mixture into molten tin. The obtained results suggest two possible mechanisms:

(i) The first mechanism involves the anodic oxidation of hydrogen at the YSZ / tin interface (*E* mode). The model developed requires that dissolution or incorporation of hydrogen into the tin occurs according to Henry's law, i.e. the amount of hydrogen 'stored' in the tin is proportional to the hydrogen partial pressure in the gas mixture. Furthermore, the amount of hydrogen 'stored' is 2 or 3 orders of magnitude greater than literature values for the solubility; also dissolution is known to obey Sievert's law, i.e. the solubility is proportional to the square root of the hydrogen partial pressure. A possible explanation of the findings is that the hydrogen / argon gas is incorporated in the molten tin in the form of a persistent foam.

(ii) The second mechanism involves homogeneous oxidation of hydrogen (the concentration of which obeys Sievert's law) by oxygen dissolved in the molten tin with no requirement for foaming (*CE* mode).

Thus the presence or absence of a foam provides a means of distinguishing between the two proposed mechanisms. It is the purpose of the work set out in this chapter is to show

whether or not a foam is formed when hydrogen/ argon gas mixtures are bubbled through liquid tin at the operating temperature of a LTA SOFC.

7.5.2. Background

Solid foams are highly porous materials with useful mechanical properties such as high stiffness, low specific weight, high gas permeability and low thermal conductivity^{134,135}. Among man-made cellular materials, polymeric foams attain widest applications in almost every sector of the industry¹³⁴. The phenomenon of foaming in metals and metal alloys was discovered only recently¹³⁶.

There are many production methods of cellular metallic materials depending on the state of the metal from which the foam should be manufactured (i.e. metal vapour, liquid metal, solid metal in powdered form and metal ions)¹³⁴. From liquid metal (which is the interest in the current study) foams can be manufactured via direct foaming with gas, direct foaming with blowing agents, powder compact melting, casting, etc.¹³⁴

Direct foaming of metals is based upon bubbling of gas into liquid metal while adding fine ceramic powders used to stabilise bubbles and prevent their escape increasing the viscosity of the melt¹³⁴. Direct foaming with gas can be achieved using two methods: injection of gas into liquid metal and in-situ gas formation via addition of gas blowing agents that release gas during in the melt¹³⁴.

Potentially most of the metals such as zinc, lead, tin, and even gold can foam¹³⁷ with the aid of blowing agents that decompose at certain temperature (usually close to the melting point of the metal or metal alloy) causing formation of bubbles in metallic structure. The rapid cooling of such structures is then required to obtain the desired metallic foam. The typical blowing agents for zinc and aluminium based alloys are zirconium hydride and titanium hydride¹³⁸.

Metallic foams are widely used for various applications, such as automotive and aircraft industry, construction of lightweight materials, military armour vehicles, etc.^{135,138} The structure of metal foams (2D or 3D) is investigated using various *in-situ* and *ex-situ* physical characterisation techniques such as X-ray radiography, electron and optical microscopy, X-ray tomography, etc.)^{137,139,140}.

Several studies have attempted to examine the effect of porosity (relative density), size and cell morphology on electrical conductivity of foamed metals¹⁴¹⁻¹⁴⁴. Unlike pure metals, metallic foams have reduced relative density (greater porosity). As a result, the cross section for the conduction path in the foam is reduced¹⁴¹ which leads to a decreased electrical

conductivity. Hence, with increased tortuosity¹⁴⁵ of the current path, electrical resistance in foams is increased.

This section presents experimental results that lead to clarification as to whether there was any tin foam generated by bubbling of hydrogen and argon mixture through liquid tin anode. Due to the porous nature of metal foam, lower electrical conductivity compared to pure metal is expected. Therefore an existence of tin foam is investigated by measuring electrical resistance between two electronically-conducting probes: one of which is inserted deep into the liquid tin, and the other one moved freely above the liquid tin. To confirm the results obtained from electrical resistance measurements visualisation of any potential foam was also carried out.

7.5.3. Experimental procedure

Experimental set-up and major parts of the cell containing tin were similar to the ones described in Chapter 3. Some modifications to the original set-up were made to observe metallic foam above the liquid tin. The cell holding the tin was either yttria-stabilised zirconia (YSZ) or silica. The former was applied in the measurement of electrical resistance of the foam, while the latter enabled a visual examination for evidence of a foam above the tin pool.

7.5.3.1. Electrical resistance apparatus

Electrical resistance of metallic foam has been measured using an apparatus that contained a custom-built holder and 8YSZ tube. Electrical resistance was obtained via supply of a constant current ($100\ \mu\text{A}$) of both polarities via the circuit with two GC rods inserted into the 8YSZ tube: stationary rod was in contact with tin, while moveable rod was supposed to be in contact with foam. The supply of constant current was achieved using either an in-house built electronic circuit with negative feedback loop shown in Figure 7.6 or a potentiostat.

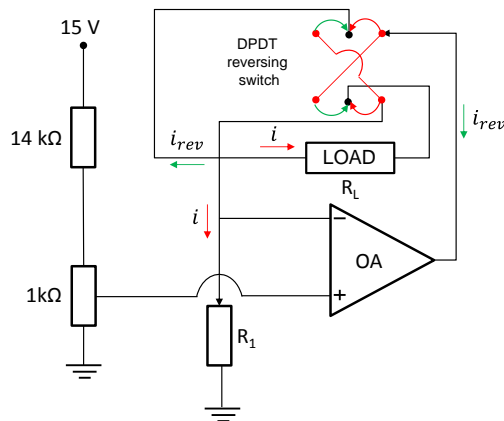


Figure 7.6 Electronic circuit with a 741 operational amplifier and a reversing switch for supply of current of both polarities ($100\ \mu\text{A}$ and $-100\ \mu\text{A}$).

7.5.3.2. Gas tight holder for moveable GC rod

Electrical contact to tin was achieved using a 3 mm diameter GC rod throughout the project. Initially two GC rods of the same size were applied in contact resistance measurement. To move one of GC rods freely inside the tube (as precise level of foam above tin pool was unknown), a custom-built holder made of pyrophyllite was developed. Pyrophyllite cylinder (30×20 mm) was cut and drilled using a CNC machine to the desired size. The holder had to accommodate not only usual fuel cell compartments (inlet and outlet alumina tubes, fixed GC rod, thermocouple probe), but one extra moveable GC rod. The holder had to be gas tight and allow the moveable rod to be lifted up and down easily. Both requirements were met with the aid of 2.5 mm inner diameter, 1.5 mm cross section Nitrile O-ring (Polymax Ltd., UK) glued to the top of pre-drilled pyrophyllite holder with silicone sealant (Silicoseal 152, ACC Silicones Ltd., UK) (Figure 7.7). The Nitrile O-ring chosen for its wide operating temperature range of -30 to 120 °C¹⁴⁶ prevented any gas leak yet allowed the GC rod to be moved up and down freely. The ready holder was glued to the top of 8YSZ tube with silicone sealant.

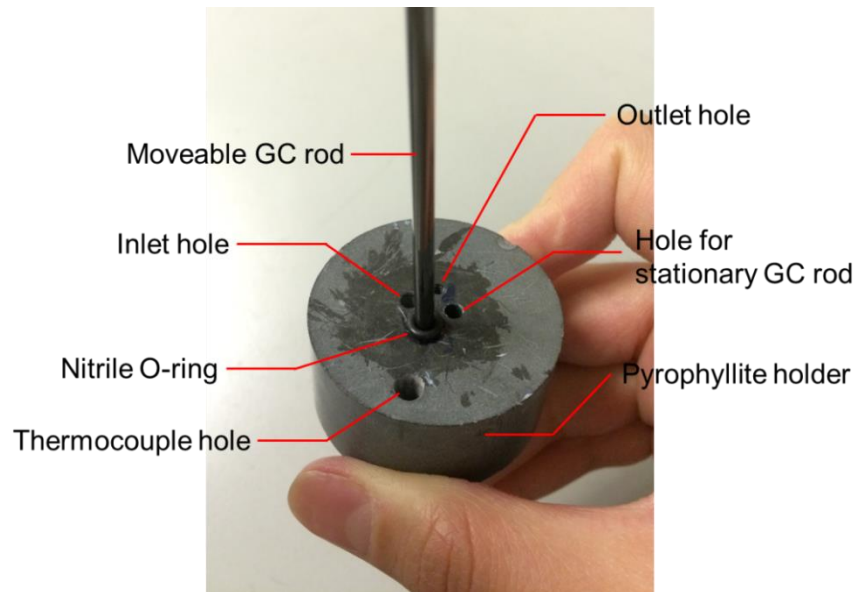


Figure 7.7 Gas tight pyrophyllite holder with O-ring that enabled free movement of GC rod.

In a second arrangement to prevent any electrical contact between moveable GC rod and 8YSZ tube, the former was placed inside a sheath made of alumina tube. Due to a limited space smaller GC rod (1 mm diameter) was placed inside 3 mm outer diameter alumina tube (Multi-Lab Ltd., UK) protruding only 5 mm at the bottom end to ensure no contact with the YSZ tube. Sheathed GC rod could be lifted up and down to check upon the level of foam and/or tin in the same manner. Because of the delicacy of 1 mm thick GC rod a

platinum wire (0.25 mm diameter) (Peak Sensors Ltd., UK) was glued to the top of the rod using the silver loaded epoxy adhesive (RS Components Ltd., UK) and used for electrical connection (Figure 7.8).

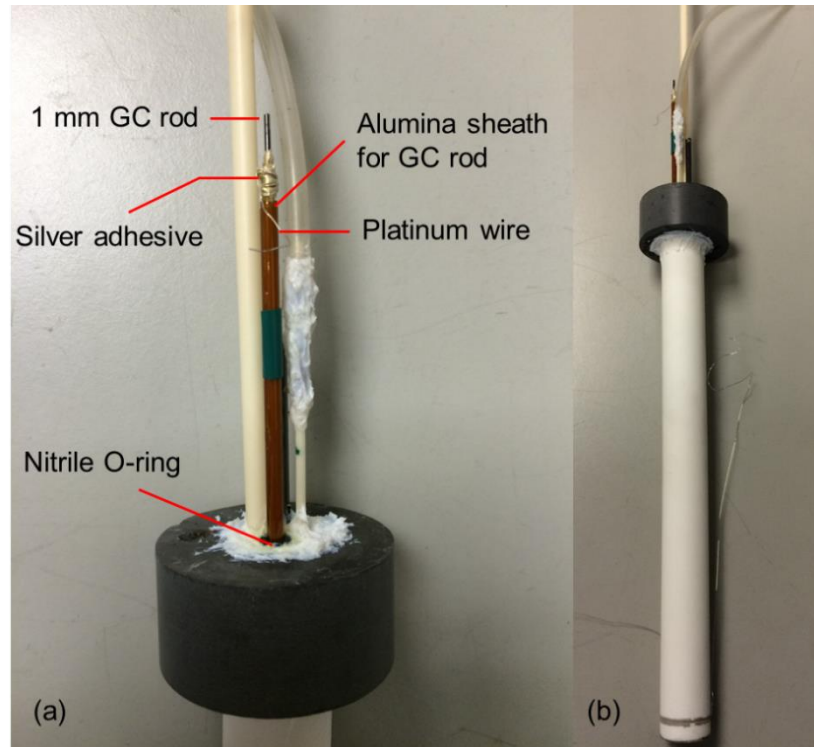


Figure 7.8 Apparatus for electrical resistance measurements: closer look of pyrophyllite holder with O-ring and moveable GC rod sheathed in alumina tube (a); complete cell with 8YSZ tube filled with tin shots, alumina inlet and outlet tubes, stationary and moveable GC rod sheathed in alumina tube (b).

7.5.3.3. Silica tube apparatus

For visualisation of foam 19 mm outer diameter and 15 mm inner diameter silica tube (Cambridge Glassblowing Ltd., UK) was applied. Silica tube was chosen due to its transparency, ability to operate continuously at 1000 °C and high resistance to thermal shock¹⁴⁷.

The cell was filled with 25 g of tin shots and contained one inlet (4 mm outer diameter) and one outlet (2 mm outer diameter) alumina tubes for gas inlet and outlet and pre-drilled pyrophyllite holder (Figure 7.9a). The second silica cell employed in this work was identical to the first one with extra 5g of 8YSZ chips (Dynamic-Ceramic Ltd., UK) mixed with tin shots (Figure 7.9b).

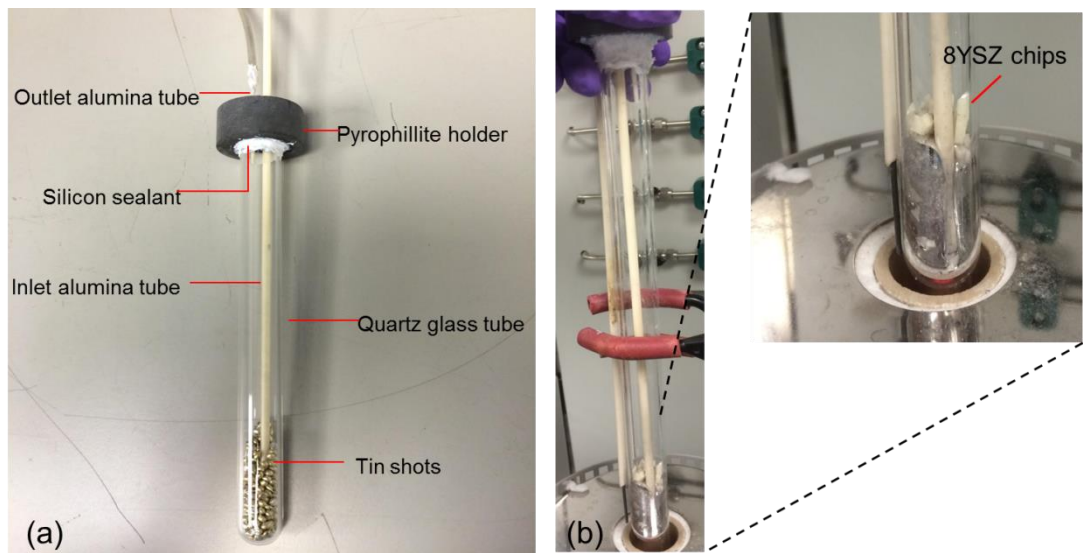


Figure 7.9 Experimental cell for visualisation of the metal foam consisted of silica tube (filled with tin shots), alumina inlet and outlet tubes (a); identical s tube (filled with tin shots and 8YSZ chips), alumina inlet and outlet tubes during the operation at 300 °C (b).

A schematic of the experimental rig used in this work is shown in Figure 7.10. Dry argon (zero grade, BOC UK) was supplied to the oxygen sensor (Kent Industrial Measurements, UK) after which it was mixed with hydrogen (zero grade, BOC, UK) and supplied to the cell (made of either silica or 8YSZ tube) held at operating temperature by an electric furnace (Carbolite, UK). Gases entered and exited the cell via alumina tubes with internal diameter 2 mm, the inlet tube being immersed in the liquid tin to a depth of approximately 15 mm so that the gas bubbled through the liquid tin. The use of stationary and moveable GC rods (unsheathed and sheathed in alumina tube) was optional.

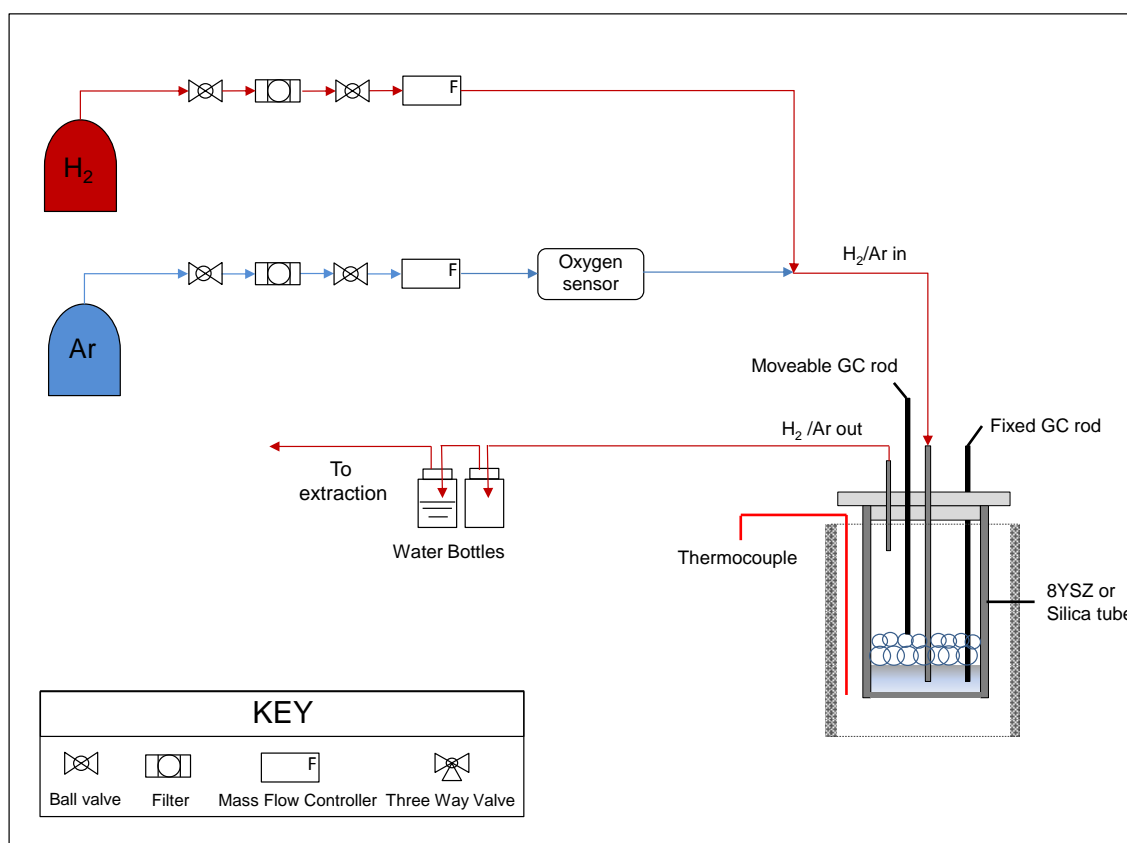


Figure 7.10 Process flow diagram for observation of metal foam during the oxidation of hydrogen in LTA SOFC (foam shown subsequently found not to be present).

7.5.4. Experimental results and discussion

The following experiments were performed to investigate the possibility of formation of tin foam when gaseous mixture of H₂ and Ar was supplied to the liquid tin anode SOFC. The measurement of electrical resistance between two glassy carbon probes in 8YSZ tube was conducted. Continuity detected above the tin pool was initially attributed to the presence of metallic foam. Electrical resistance was re-measured in 8YSZ tube with moveable GC rod in alumina sheath. The later result confirmed a negative result of existence of metallic foam above the tin pool. To confirm this finding a silica tube cells filled with tin shots and later with 8YSZ chips were applied. No foam was found in silica tube apparatus, which confirmed observations found in 8YSZ tube.

7.5.4.1. Electrical resistance measurements

The LTA SOFC cell was heated up to 800 °C at a ramping rate of 5°C per minute with no supply of gas. Once tin was completely melted (at 300 °C) a 100 μA current was passed through two probes using potentiostat and small electronic circuit and resistance between two probes (glassy carbon rods) was measured by lifting one of the rods up and down to detect the level of pure tin (Figure 7.11). After 300 °C, the flow of 0.77 ml s⁻¹ H₂/Ar

gaseous mixture was supplied to the cell to bubble through liquid tin until the cell temperature reached 800 °C. The flow of gases was then stopped, and resistance between two probes was measured again (Figure 7.11a). Note that resistance measured using both potentiostat and built electronic circuit was the same.

From Figure 7.11 it can be deduced that the height of pure tin was ca. 25 mm (which corresponds to 25 g of tin in 15 mm inner diameter tube). When continuity was measured at 800 °C there was some high resistance measured above 25 mm (i.e. above the level of pure tin). That high resistance was attributed initially, though incorrectly, to the presence of metallic foam above tin layer.

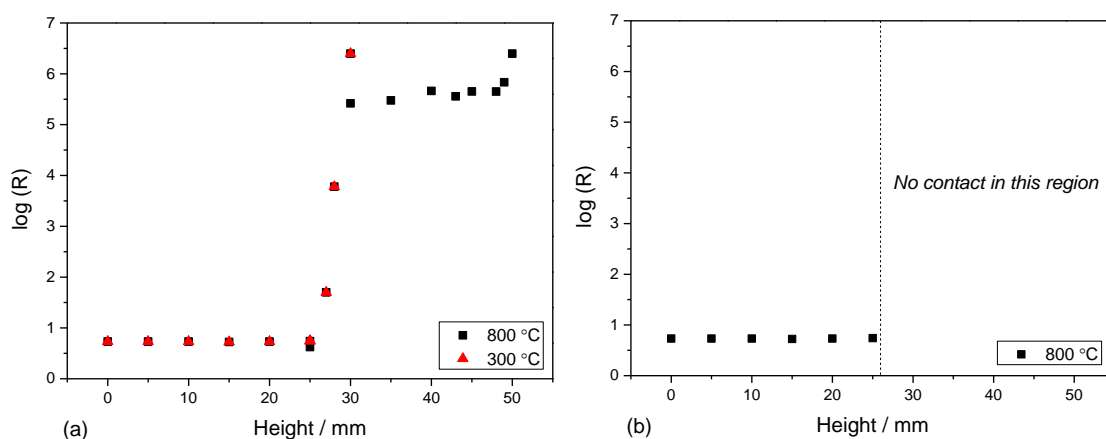


Figure 7.11 Resistance measured between two probes inside molten tin at 300 °C (at no gas bubbling) and at 800 °C after gas bubbling as a function of height of liquid tin: using unsheathed GC probe (a) and using sheathed GC probe (b).

The experiment was repeated with 8YSZ tube with sheathed moveable GC rod illustrated in Figure 7.8. No continuity was detected between probes above tin layer (Figure 7.11b). The obtained results served as an important confirmation for the absence of foam during the oxidation of hydrogen in LTA SOFC. Further confirmation was obtained using a silica tube apparatus.

7.5.4.2. Elucidation of tin foam in silica tube

The LTA SOFC cell was heated up to 800 °C at a ramping rate of 5°C per minute with no supply of gas initially. Once tin was completely melted at 300 °C, the flow of 0.77 ml s⁻¹ H₂/Ar gaseous mixture was supplied to the cell to bubble through liquid tin until the cell temperature reached 800 °C. After 2 hours of bubbling gases into liquid tin the cell was lifted up to check for the formation of foam (Figure 7.12a). As no evidence of foam was found, 5 g of 8YSZ chips were added to the silica tube to see if that aided the formation of a foam (Figure 7.12b). However, in both cases no foam was observed.

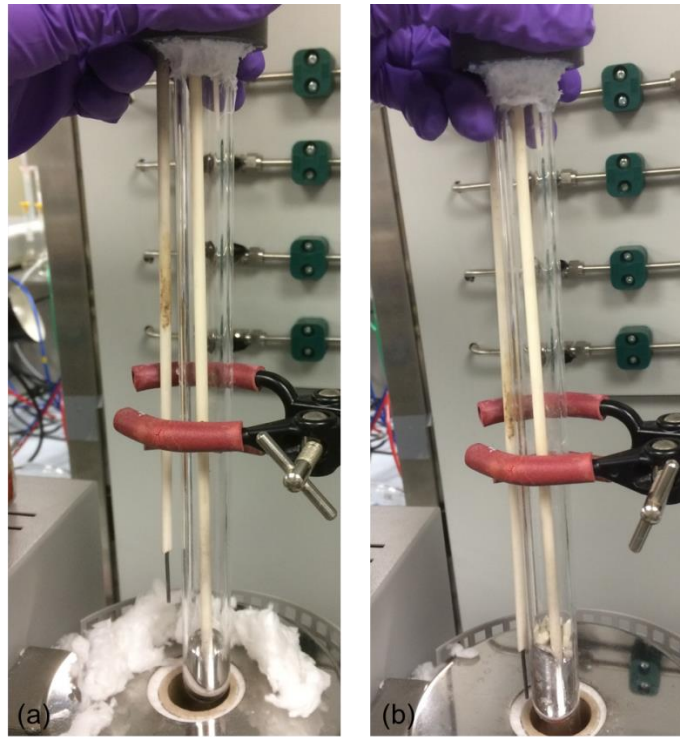


Figure 7.12 Silica tube apparatus *in-operando* with no metallic foam above tin: with inlet and outlet tubes (a) and with added 8YSZ chips (b).

The result shown in Figure 7.11a was a false indication of the existence of a foam. Upon movement the GC rod was in contact with YSZ surface. An electrochemical reaction that takes place at the surface of YSZ could lead to a current flow in that circuit.

One possible reaction at the surface of YSZ can be as follows:



As supplied gas (H_2) was dry (no water was present to be reduced) the other reaction that takes place at YSZ surface is as follows:



Hence the observed continuity was not due to foam, but due to the flow of current caused by some electrochemical reaction taking place at the YSZ surface.

Interestingly, when polarity of the current flow was altered using both potentiostat and/or built electronic circuit the resistance measured in the directions was significantly different. In one direction certain resistance (from 0.3 to 2.5 M Ω) (Figure 7.11) was measured, while in other direction – extremely high resistance was obtained (and for that reason those data were not included). The observed ‘diode phenomenon’ could be explained by the fact that one of the proposed reactions was of high impedance compared to the second one.

In addition, as operating temperature was raised, the ionic conductivity of 8YSZ tube was increasing¹⁴⁸ that lead to a reduced resistance between two probes in Figure 7.11a with temperature.

To sum up, no metallic foam was formed during the supply of H₂/Ar gaseous mixture into the liquid tin. The work conducted allowed the first mechanism for anodic oxidation of hydrogen at YSZ/ tin interface to be ruled out. Therefore, the second mechanism on homogeneous oxidation of hydrogen in liquid tin is going to be considered instead.

7.5.5. Concluding remarks

The presence or absence of metallic foam caused by bubbling of hydrogen/ argon gaseous mixture through the liquid tin in LTA SOFC has been examined using two experimental set-ups.

First, formation of a foam above tin level was tested using a custom-built electrical resistance apparatus in which resistance between two GC rods inserted into YSZ tube was measured. This was achieved using a special holder to fix GC rods whereby one of them was in contact with tin, while the other moved freely to detect the level of foam. The significance of the set-up was that it allowed one GC rod move freely, while kept the internal tube's atmosphere inert.

Electrical continuity detected between two probes appeared to indicate that some foam was formed above the tin layer. This observation was later re-considered when a set-up with sheathed GC rod was applied and no continuity was detected.

Initially observed continuity was not due to expanded volume of tin and formation of a foam, but due to electrochemical reaction taking place at the YSZ surface and the fact that moveable GC rod was in electrical contact with the surface of the YSZ.

To confirm the absence of the foam above the tin layer, a similar experiment was performed using a transparent silica tube apparatus. Supply of hydrogen/argon mixture into liquid tin held in silica tube showed that no foam can be formed. Addition of 8YSZ chips to the silica tube had no effect on formation of foam either.

The obtained findings served as a basis for the elimination of one of the proposed mechanisms for oxidation of hydrogen in LTA SOFC. Following that, the electrochemical model (and its assumptions) developed for the analysis and interpretation of oxidation of hydrogen in liquid tin anode SOFC in the previous Section would require re-consideration in accordance with the second proposed mechanism. The revamped model (with new concepts and assumptions) is presented in the next Section.

7.6. Electrochemical model for *CE* mode

The model for *E* mode was based upon dissolution of hydrogen according to Henry's law, followed by its diffusion to the interface and anodic oxidation. That model encounters two challenges: the first is that it is known^{149–151} that dissolution of hydrogen follows Sievert's law and not Henry's law; the second is that it requires the solubility of hydrogen in liquid tin to be 2 or 3 orders of magnitude greater than reported in the literature. An investigation aimed at the detection of a foam above the liquid tin was undertaken but yielded a negative result. Thus model *E* (direct anodic oxidation of hydrogen) in LMA SOFC is not applicable to this system.

The second mechanism (mode *CE*) involves fast dissolution of hydrogen in liquid tin according to Sievert's law^{149–151} followed by slow (rate-determining) homogeneous reaction with dissolved oxygen: the observed anodic current is then driven by the reduction in dissolved oxygen concentration in the melt, resulting in injection of oxygen via the YSZ-tin interface to replace the oxygen consumed in the chemical reaction.

The chemical reaction for homogeneous reaction of hydrogen and oxygen:



The anodic reaction is:



The oxygen injected diffuses into the bulk of the tin from the interface.

Intuitively, it was clear that in order to get the required proportionality between steady currents and partial pressure of hydrogen (found experimentally) and compliance with Sievert's law, the following two assumptions were employed:

- The concentration of dissolved hydrogen in liquid tin is the saturated concentration appropriate to the partial pressure of the hydrogen supplied (bubbled) as a gas and obeys Sievert's law.
- The rate of homogeneous oxidation of hydrogen by dissolved oxygen is the rate-determining step and is governed by a rate equation which is first-order with respect to monatomic oxygen.

Then to address the mass-transport (diffusion) of dissolved oxygen during its electrochemical injection the remaining two assumptions were added as follows:

- The electrochemical kinetics of the electrode reaction are fast so that the concentration of dissolved oxygen at the YSZ-tin interface is fixed by the applied potential and is not disturbed by the current flow.
- Diffusion of oxygen away from the YSZ-tin interface, to replace that removed by reaction with hydrogen, occurs through a diffusion layer of constant thickness as a result of convection induced by bubbling and thermal effects.

Finally the following assumption was necessary in order to achieve an analytical solution:

- The system is considered to be in quasi-equilibrium.

Consider the same process as in the model for the **E** mode (Figure 7.5): hydrogen is bubbled through the liquid tin at partial pressure p'_1 , a potential, E , is applied to the Sn / YSZ interface and eventually a steady current, i_1 , is observed. The partial pressure of H_2 is then increased to p'_2 and the current, i , increases with time and eventually stabilises at i_2 . Oxygen concentrations within the liquid tin are described schematically in Figure 7.13. In the theoretical treatment, hydrogen concentration is denoted by a single prime and oxygen concentration is denoted by a bar.

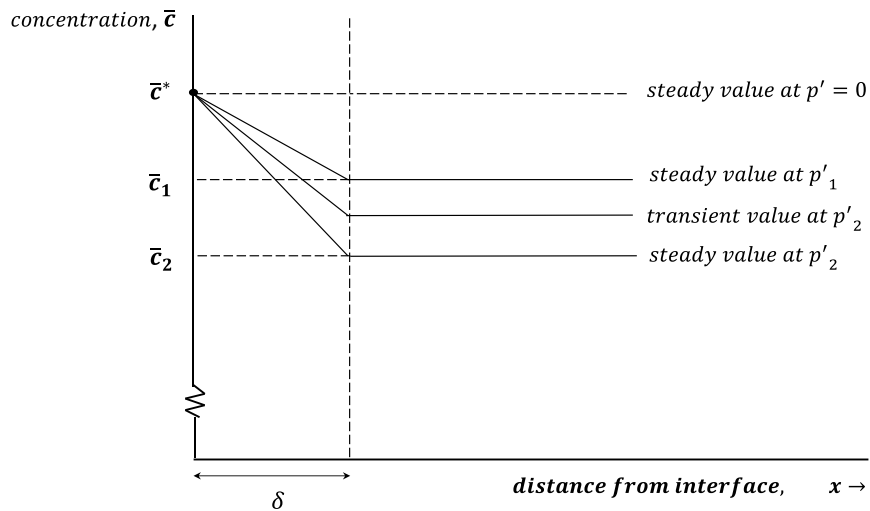


Figure 7.13 Schematic of the dissolved oxygen concentration profile at a given applied potential in the CE mode of operation. The diffusion layer thickness is shown as δ .

The rate of removal of oxygen via Reaction (7.27) is $Vk_1\bar{c}(c')^2$, (i.e. $k_1\bar{c}(c')^2$ per unit volume of tin) where k_1 is the rate constant for the reaction and V is the volume of tin.

The rate of injection of oxygen via Reaction (7.28) is i/nF ($n=2$). Thus the net rate of removal of oxygen via the two reactions is $Vk_1\bar{c}(c')^2 - i/nF$. The concentration of hydrogen, c' , for given hydrogen partial pressure, p' , is given by (according to Sievert's law¹⁵⁰):

$$c' = k_2(p')^{1/2} \quad (7.29)$$

where k_2 is a constant for a given temperature (Sievert's constant).

Expressing the total amount (gram atoms) of [O] in tin as \bar{N} , it follows that

$$\frac{d\bar{N}}{dt} = -Vk_1(k_2)^2\bar{c}p' + \frac{i}{nF} \quad (7.30)$$

Applying Fick's first law to the diffusion of [O] from the interface, the flux, \bar{J} , is given by:

$$\bar{J} = -\bar{D}A \frac{d\bar{c}}{dx} \quad (7.31)$$

where \bar{D} is the diffusion coefficient, A is the area of the interface and $\frac{d\bar{c}}{dx}$ is the concentration gradient within the diffusion layer. So Equation (7.4) becomes (see Figure 7.13):

$$\bar{J} = -\bar{D}A \left(\frac{\bar{c} - \bar{c}^*}{\delta} \right) \quad (7.32)$$

Equating the flux with current via Faraday's law:

$$\bar{J} = \frac{i}{nF} \quad (7.33)$$

Eliminating \bar{J} between (7.32) and (7.33):

$$i = \frac{nF\bar{D}A}{\delta} (\bar{c}^* - \bar{c}) \quad (7.34)$$

This will be written as:

$$i = k_3(\bar{c}^* - \bar{c}) \quad (7.35)$$

where k_3 is given by:

$$k_3 = \frac{nF\bar{D}A}{\delta} \quad (7.36)$$

In the steady-state situation, when $p' = p_2'$, $\bar{c} = \bar{c}_2$, $i = i_2$ and $\frac{d\bar{N}}{dt} = 0$.

So using Equation (7.30):

$$Vk_1(k_2)^2\bar{c}_2p_2' = \frac{i_2}{nF} \quad (7.37)$$

And from (7.35)

$$i_2 = k_3(\bar{c}^* - \bar{c}_2) \quad (7.38)$$

Eliminating i_2 between (7.37) and (7.38):

$$Vk_1(k_2)^2\bar{c}_2p_2' = \frac{k_3(\bar{c}^* - \bar{c}_2)}{nF}$$

So

$$\bar{c}_2 = \frac{\bar{c}^*}{1 + \frac{Vk_1(k_2)^2 p_2' nF}{k_3}}$$

Or

$$\bar{c}_2 = \bar{c}^* \left(1 + \frac{Vk_1(k_2)^2 p_2' nF}{k_3} \right)^{-1} \quad (7.39)$$

Writing

$$\bar{z}_2 = \left(1 + \frac{Vk_1(k_2)^2 p_2' nF}{k_3} \right)^{-1} \quad (7.40)$$

Then

$$\bar{c}_2 = \bar{z}_2 \bar{c}^* \quad (7.41)$$

Note that \bar{z} is a function of p' and $\bar{z} \leq 1$. Likewise:

$$\bar{c}_1 = \bar{z}_1 \bar{c}^* \quad (7.42)$$

We may write:

$$\frac{d\bar{c}}{dt} = \frac{1}{V} \frac{d\bar{N}}{dt} \quad (7.43)$$

Eliminating i between (7.30) and (7.35) for $p' = p_2'$

$$\frac{d\bar{N}}{dt} = -Vk_1(k_2)^2 \bar{c} p_2' + \frac{k_3(\bar{c}^* - \bar{c})}{nF} \quad (7.44)$$

From (7.43) and (7.44):

$$\frac{d\bar{c}}{dt} = \frac{1}{V} \left[-\bar{c} \left(Vk_1(k_2)^2 p_2' + \frac{k_3}{nF} \right) + \frac{k_3}{nF} \bar{c}^* \right] \quad (7.45)$$

$$= \frac{k_3}{VnF} \left[-\bar{c} \left(\frac{nFVk_1(k_2)^2 p_2'}{k_3} + 1 \right) + \bar{c}^* \right] \quad (7.46)$$

Then using Equation (7.40):

$$\frac{d\bar{c}}{dt} = \frac{k_3}{VnF\bar{z}_2} (-\bar{c} + \bar{z}_2 \bar{c}^*) \quad (7.47)$$

Followed by (7.41):

$$\frac{d\bar{c}}{dt} = \frac{k_3}{VnF\bar{z}_2} (\bar{c}_2 - \bar{c}) \quad (7.48)$$

Integrating:

$$\int_{\bar{c}_1}^{\bar{c}} \frac{d\bar{c}}{(\bar{c}_2 - \bar{c})} = \frac{k_3}{VnF\bar{z}_2} \int_{t_1}^t dt \quad (7.49)$$

$$-\ln[\bar{c}_2 - \bar{c}]_{\bar{c}_1}^{\bar{c}} = \frac{k_3}{VnF\bar{z}_2} (t - t_1) \quad (7.50)$$

$$\ln \frac{\bar{c}_2 - \bar{c}}{\bar{c}_2 - \bar{c}_1} = -\frac{k_3}{VnF\bar{z}_2} (t - t_1) \quad (7.51)$$

It follows from (7.35) and (7.51) that

$$\ln \frac{i_2 - i}{i_2 - i_1} = -\frac{k_3}{VnF\bar{z}_2} (t - t_1) \quad (7.52)$$

This is the required equation.

The theory allows prediction of the behaviour of the system as follows:

A) From (7.37) and (7.41):

$$i_2 = nFVk_1(k_2)^2 \bar{z}_2 \bar{c}^* p_2' \quad (7.53)$$

This shows that steady current is proportional to $\bar{z}_2 p_2'$ (rather than p_2' only, as indicated earlier from the obtained results) where \bar{z}_2 is given by (7.40).

B) Equation (7.52) indicates that a plot of $\ln(i_2 - i)$ for $i_2 > i_1$ [or $\ln(i - i_2)$ for $i_1 > i_2$] versus time should show a straight line of slope $-\frac{k_3}{VnF\bar{z}_2}$. As \bar{z}_2 is a function of p_2' the slope is expected to vary with hydrogen partial pressure.

The significance of the parameter \bar{z} is now briefly considered. Clearly, Equation (7.40) shows that \bar{z} must take a value between zero and unity but its actual value in a given cell depends upon certain characteristics of the system.

Interestingly, the physical meaning of parameter \bar{z} is closely related to the Damkohler number, which is a dimensionless number used in chemical reaction engineering^{152,153}. The general definition of Damkohler number, Da, is given by the following ratio¹⁵³:

$$\text{Da} = \frac{\tau_C}{\tau_M} \quad (7.54)$$

where τ_C is the characteristic time of the chemical reaction, τ_M is the mixing time that can be controlled by hydrodynamics or by diffusion.

In systems that include the interphase mass-transfer (via diffusion), a second Damkohler number, Da_{II} , is defined by the following ratio¹⁵⁴:

$$\text{Da}_{\text{II}} = \frac{k_w}{k_f a_s} \quad (7.55)$$

where k_w is the rate coefficient in $\text{m}^3(\text{kg}_{\text{cat}})^{-1} \text{s}^{-1}$, k_f is the mass-transfer coefficient in m s^{-1} and a_s is the specific external surface area of the catalyst pellet in $\text{m}^2(\text{kg}_{\text{cat}})^{-1}$.

The second Damkohler number, Da_{II} , is the one relevant to this study, as it compares the rate of chemical reaction and rate of mass-transfer.

Therefore using Equation (7.36), the term $\frac{vk_1(k_2)^2 p_2' nF}{k_3}$ that determines the value of \bar{z} via

Equation (7.40) can be represented by the expression $\frac{vk_1(k_2)^2 \delta p_2'}{AD}$. At a given temperature, this expression is dependent upon geometric factors (V/A), mass transfer factors (via δ/D which decreases with increasing convection), and a kinetic factor (k_1), complementary to the factors a_s , k_f and k_w respectively in the definition of Da_{II} (see above).

The larger the value of k_3 (i.e. large A ; small δ) then \bar{z} tends towards unity; conversely, the smaller the value of k_3 (i.e. small A ; large δ) then \bar{z} tends towards small values with a limiting value of zero. The value of \bar{z} determines the output current of the cell as shown in Equation (7.53).

7.6.1. Experimental validation of model for CE mode

Application of Equation (7.52) to experimental data for oxidation of hydrogen and injection of oxygen anodically at -0.90 V vs. RE at 780 °C (shown in Figure 7.2) resulted in reasonable straight lines ($R^2_{\text{average}} > 0.98$) (Figure 7.14-Figure 7.16). Note that the R-squared value is a measure of the goodness of fit of the data to a straight line. The standard error of the slope is $3 \times 10^{-6} \text{ s}^{-1}$. The slopes obtained from Figure 7.14-Figure 7.16 are summarised in Table 7.1.

Table 7.1 Reciprocal time constants for various p_2' values.

p_2' / kPa	0	8	15	26
Slope / 10^{-3} s^{-1}	0.97	1.11	1.39	1.92
Average slope / 10^{-3} s^{-1}	0.97	1.05	1.06	1.92
Time constant / s	1031	926	820	521

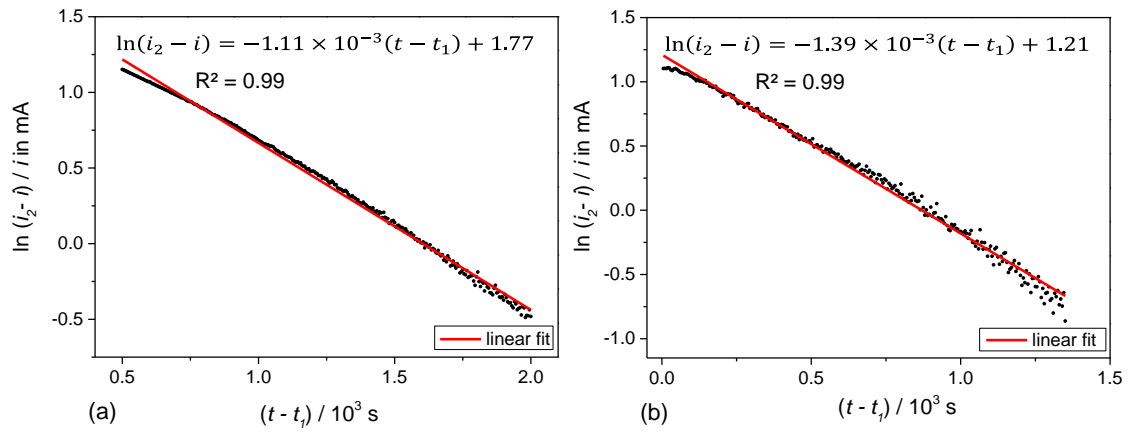


Figure 7.14. Step change in hydrogen partial pressure: from 0 to 8 kPa (total flow rate 2.6 ml s⁻¹) (a); from 8 to 15 kPa (total flow rate 2.8 ml s⁻¹) (b).

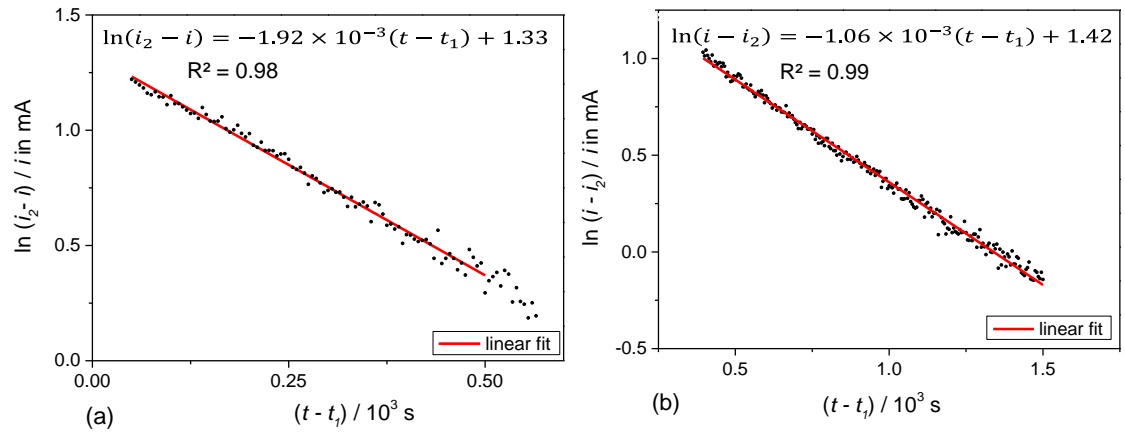


Figure 7.15. Step change in hydrogen partial pressure: from 15 to 26 kPa (total flow rate 3.2 ml s⁻¹) (a); from 26 to 15 kPa (total flow rate 2.8 ml s⁻¹) (b).

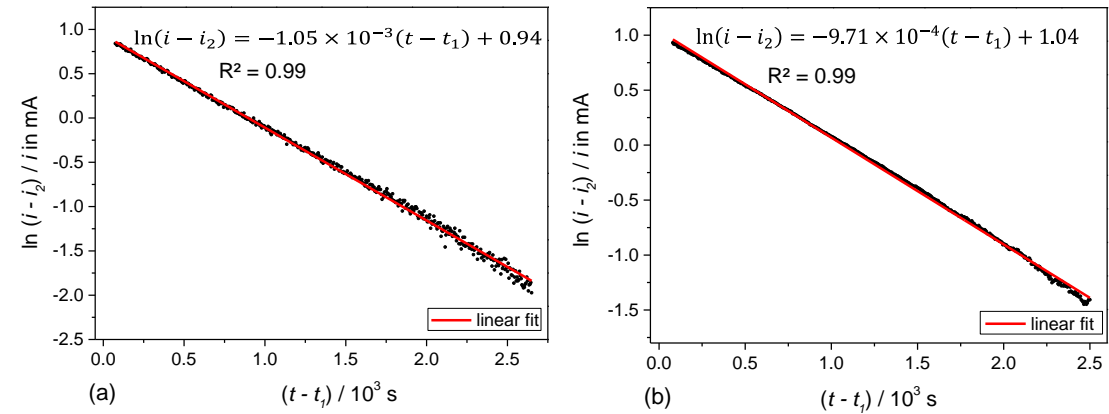


Figure 7.16. Step change in hydrogen partial pressure: from 15 to 8 kPa (total flow rate 2.6 ml s⁻¹) (a); from 8 kPa to 0 (total flow rate 2.3 ml s⁻¹) (b).

It is notable that the time constants (reciprocal of the slopes in Figure 7.14–Figure 7.16) for step changes in hydrogen partial pressure show a decrease with increasing $p(\text{H}_2)$ (as \bar{z}_2 decreases) as expected from (7.52) and (7.40). Slopes (reciprocal time constants) vs. p_2' are shown in Figure 7.17.

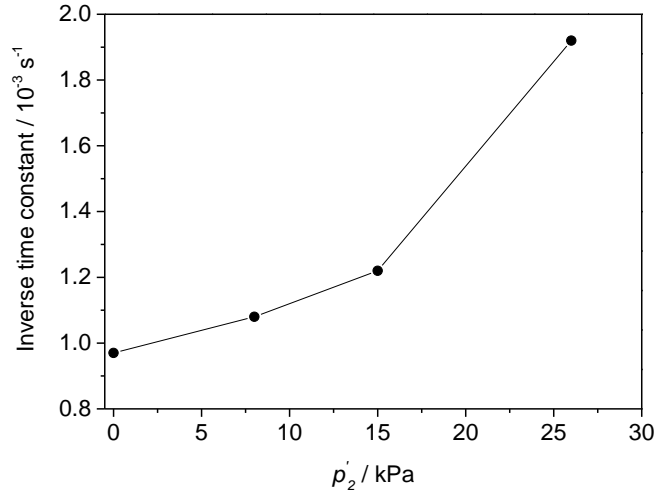


Figure 7.17. The reciprocal time constant versus p_2' .

Equation (7.53) predicts proportionality between steady current, i_2 and $\bar{z}_2 p_2'$. But \bar{z}_2 is itself a function of p_2' (according to (7.40)) and hence a plot of i_2 vs. p_2' should show deviation from a straight line. Clearly, for the range of p_2' values employed in the measurements (Figure 7.4) the deviation is small.

Equation (7.40) may be written:

$$\bar{z}_2 = (1 + \bar{K} p_2')^{-1} \quad (7.56)$$

where

$$\bar{K} = \frac{V k_1 (k_2)^2 n F}{k_3} \quad (7.57)$$

Differentiating Equation (7.53) with respect to p_2' :

$$\frac{di_2}{dp_2'} = n F V k_1 (k_2)^2 \bar{c}^* \frac{d}{dp_2'} (\bar{z}_2 p_2') \quad (7.58)$$

leads to

$$\frac{di_2}{dp_2'} = n F V k_1 (k_2)^2 \bar{c}^* (1 + \bar{K} p_2')^{-2} \quad (7.59)$$

Therefore for $p_2' = 0$ (i.e. at the origin):

$$\left(\frac{di_2}{dp_2'} \right)_{p_2'=0} = n F V k_1 (k_2)^2 \bar{c}^* \quad (7.60)$$

Furthermore, differentiating (7.53) with respect to $\bar{z}_2 p_2'$:

$$\frac{di_2}{d(\bar{z}_2 p_2')} = n F V k_1 (k_2)^2 \bar{c}^* \quad (7.61)$$

So comparing (7.60) and (7.61) it follows that

$$\left(\frac{di_2}{dp_2'}\right)_{p_2'=0} = \frac{di_2}{d(\bar{z}_2 p_2')} = nFV k_1 (k_2)^2 \bar{c}^* \quad (7.62)$$

where \bar{z}_2 is given by (7.56).

So Equation (7.62) shows that the slope of the tangent to the curve of i_2 versus p_2' at the origin is $nFV k_1 (k_2)^2 \bar{c}^*$ which is identical to the slope of the straight line plot of i_2 versus $\bar{z}_2 p_2'$.

The difficulty of applying Equation (7.62) to find the value of $nFV k_1 (k_2)^2 \bar{c}^*$, which is required in Section 7.6.2.1 for validation of the model, is that \bar{z}_2 is not known as a function of p_2' except at $p_2'=0$ where $\bar{z}_2 = \text{unity}$ (i.e. the value of \bar{K} in Equation (7.56) is not known). So the following procedure was adopted to address this problem.

- A value for \bar{K} was assumed.
- Using this value of \bar{K} together with the data in Figure 7.4, i_2 was plotted versus $\bar{z}_2 p_2'$.
- The best line through the data points was determined by a linear regression analysis which provided the slope of the line, the intercept at $p_2' = 0$ and the R-squared value. The last-mentioned is a measure of the goodness of fit of the data to a straight line.
- The above was repeated for other values of \bar{K} , and then the slope, intercept and R-squared values were plotted versus \bar{K} .
- The \bar{K} value, which provided the value for R-squared closest to unity, was determined from the plots and this was denoted \bar{K}_{best} .
- \bar{K}_{best} is the most likely value of \bar{K} . It is however not possible to put an uncertainty on its value based upon any well-defined criterion. As a result, the range of possible values of the parameter was set by selecting a value of R-squared less than the maximum value which then set a range of \bar{K} values; by appropriate choice of the R-squared value it was ensured that this range was substantial so as to have reasonable confidence that the range encompassed the true value of \bar{K} . The endpoints of the range were designated \bar{K}_{max} and \bar{K}_{min} .
- A value of $nFV k_1 (k_2)^2 \bar{c}^*$ together with its likely range was calculated using the determined slopes of the plots of i_2 versus $\bar{z}_2 p_2'$ at the \bar{K} values given by \bar{K}_{best} , \bar{K}_{max} and \bar{K}_{min} .

Results generated by applying the above procedure are shown in Figure 7.18-Figure 7.19.

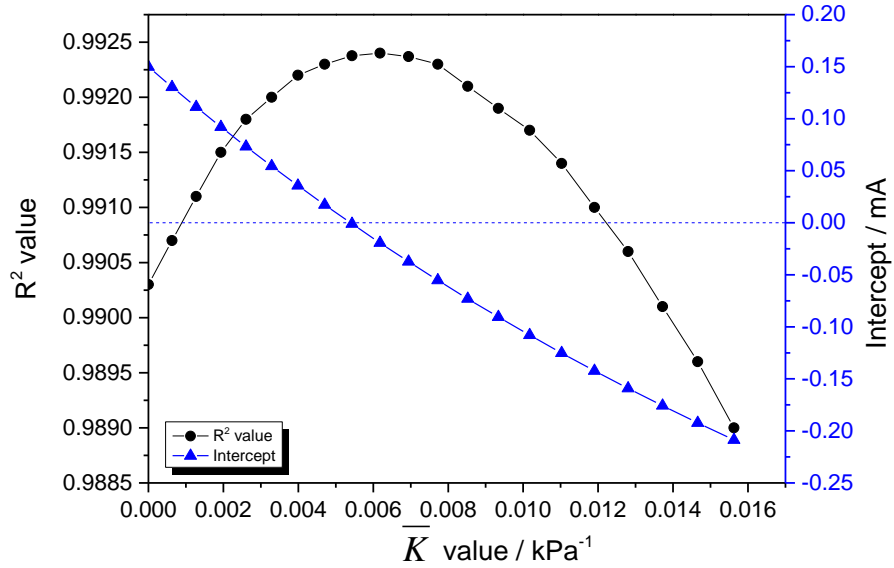


Figure 7.18. Determined values of R^2 and intercept for the plots of i_2 versus $\bar{z}_2 p'_2$ versus \bar{K} for a range of values.

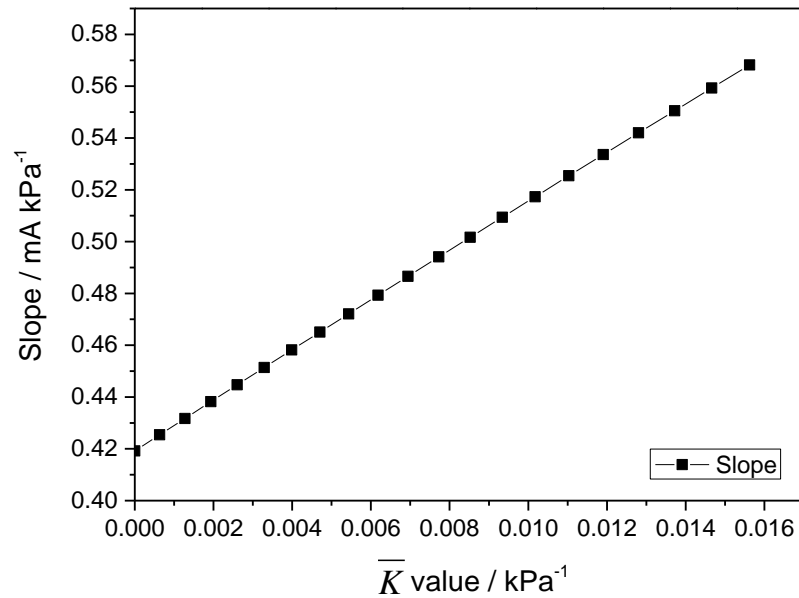


Figure 7.19 Determined values for the slope of plots of i_2 versus $\bar{z}_2 p'_2$ plotted as a function of \bar{K} .

In accordance with the procedure set out above, the \bar{K} was estimated to take the value $\bar{K} = 0.007 \pm 0.007$. This gave values for \bar{K}_{max} and \bar{K}_{min} of 0.014 and 0.000 respectively. Furthermore, at $\bar{K} = 0.007$ the intercept (Figure 7.18) is close to zero providing additional confidence that this best value of \bar{K} is not greatly different from the true value. The slope from Figure 7.19 for $\bar{K} = 0.007 \pm 0.007$ is $0.48 \pm 0.06 \text{ mA kPa}^{-1}$ which is the required value for $nFV k_1 (k_2)^2 \bar{c}^*$; this value is applied in Section 7.6.2.1 for validation of the model.

Using the values for $\bar{K} = 0.007 \pm 0.007$ together with equations (7.53) and (7.56) the resulting computed curves for i_2 versus p'_2 are shown together with the original experimental data in Figure 7.20.

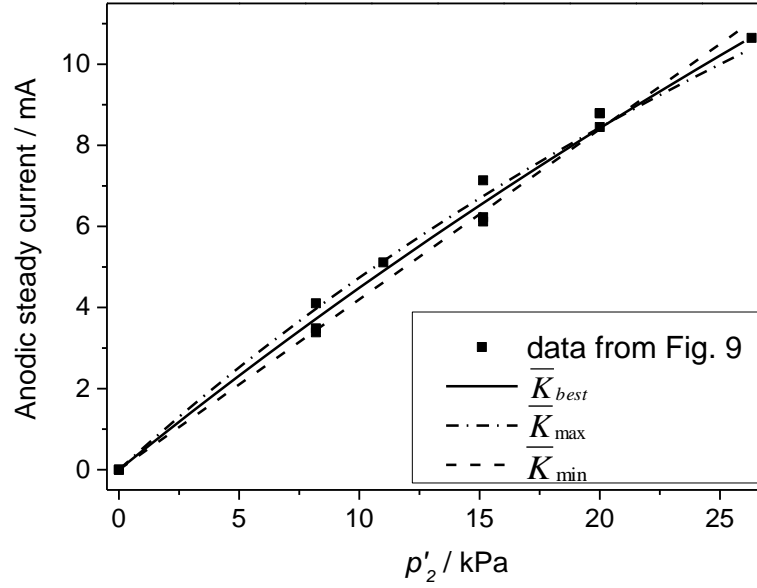


Figure 7.20. The ‘refined’ plot: steady anodic current versus p'_2 . Compare Figure 7.4.

7.6.2. Additional mechanistic theory for CE mode

A further case is now considered where the inert gas, Ar, is first bubbled through the tin for sufficient time to reduce the hydrogen concentration to a value close to zero. Then, while holding the potential at a constant value, E , a gas mixture of Ar/H₂ with hydrogen partial pressure p'_2 is bubbled continuously, starting at time $t = t_1$, through the tin and the anodic current (due to injection of oxygen to replace that consumed by hydrogen) is measured as a function of time.

At $t = t_1$, $\bar{c} = \bar{c}^*$ and thus $i = 0$ (see Equation (7.7))

Equation (7.30) becomes

$$\left[\frac{d\bar{N}}{dt} \right]_{t=t_1} = -Vk_1(k_2)^2 \bar{c}^* p'_2 \quad (7.63)$$

Differentiating Equation (7.35):

$$\left[\frac{di}{dt} \right]_{t=t_1} = -k_3 \frac{d\bar{c}}{dt} \quad (7.64)$$

From (7.43), (7.63) and (7.64):

$$\left[\frac{di}{dt} \right]_{t=t_1} = k_1(k_2)^2 k_3 \bar{c}^* p'_2 \quad (7.65)$$

Alternatively, a similar equation may be derived as follows:

Equation (7.52) becomes

$$\ln \left(1 - \frac{i}{i_2} \right) = -\frac{k_3}{VnF\bar{z}_2} (t - t_1) \quad (7.66)$$

as $p'_1 = 0$ and $i_1 = 0$ at $t = t_1$. For $\frac{i}{i_2} \ll 1$ the logarithm linearises as follows:

$$\ln\left(1 - \frac{i}{i_2}\right) \cong -\frac{i}{i_2} \quad (7.67)$$

So

$$\frac{i}{i_2} \cong \frac{k_3}{VnF\bar{z}_2}(t - t_1) \quad (7.68)$$

Differentiating and combining with (7.53):

$$\left[\frac{di}{dt}\right]_{\frac{i}{i_2} \ll 1} \cong k_1(k_2)^2 k_3 \bar{c}^* p'_2 \quad (7.69)$$

Thus

$$\left[\frac{di}{dt}\right]_{\frac{i}{i_2} \ll 1} \cong \left[\frac{di}{dt}\right]_{t=t_1} \quad (7.70)$$

Equation (7.67) is a fair approximation for i/i_2 values up to 0.2. Thus a plot of i versus t is expected to show a straight line for values of current up to at least one fifth of the steady current for a given hydrogen partial pressure.

Equations (7.65) and (7.70) predict that $\left[\frac{di}{dt}\right]_{t=t_1}$ or $\left[\frac{di}{dt}\right]_{\frac{i}{i_2} \ll 1}$ should be proportional to p'_2 ;

a plot of $\left[\frac{di}{dt}\right]_{t=t_1}$ vs. p'_2 is expected to reveal a slope of $k_1(k_2)^2 k_3 \bar{c}^*$, which will be denoted as s_1 .

Equation (7.53) indicates that a plot of i_2 vs. $\bar{z}_2 p'_2$ has a slope of $nFV k_1(k_2)^2 \bar{c}^*$, which will be denoted as s_2 . It follows that:

$$\frac{s_1}{s_2} = \frac{k_3}{VnF} \quad (7.71)$$

Thus the magnitude of $\frac{k_3}{VnF}$ from Equation (7.71) can be compared to the reciprocal time constant determined from the slopes of plots of $\ln(i_2 - i)$ vs. t [or $\ln(i - i_2)$ vs. t] at $p'_2 = 0$ (see Equation (7.52)).

7.6.2.1. *Experimental validation of additional mechanistic theory*

In order to validate this extension of the theory, the cell was first flushed with a mixture of H₂/Ar to remove any residual SnO₂, followed by Ar only while the tin electrode was held at -0.90 V vs. RE at 780 °C; the ongoing parasitic leak of oxygen inevitably occurring was measured using the technique described in Section 7.3.1. The $p(\text{H}_2)$ was then stepped from

zero to 10 kPa and back to zero; from zero to 20 kPa and back to zero and finally from zero to 30 kPa and back to zero. The current response was monitored with time (Figure 7.21).

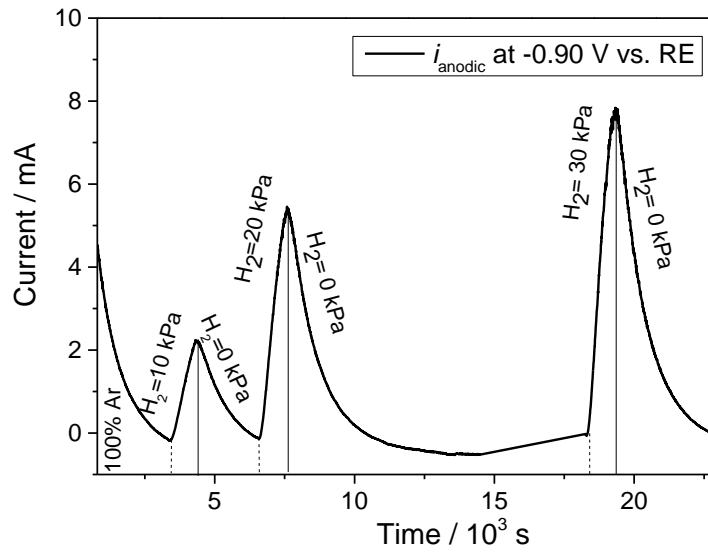


Figure 7.21. Anodic current versus time in LTA SOFC at 780 °C with instantaneous step change of $p(\text{H}_2)$ from 0 to 10 kPa, then to back to zero, repeated with 20 kPa and 30 kPa.

The following current – time curves (Figure 7.22a-Figure 7.22c) were extracted from the data in Figure 7.21. Anodic current immediately after the switch of the hydrogen from zero to a particular partial pressure (10, 20 and 30 kPa) is shown versus time.

All three current-time curves resulted in straight lines ($R^2 > 0.98$), the slopes (di/dt) of which were then plotted against hydrogen partial pressure to derive the value of s_i (Figure 7.22d; Equation (7.65)). It should be noted that the straight line in Figure 7.22d is based upon only 3 points but that each point is determined using a substantial data set; furthermore, as predicted the intercept is small ($-0.18 \times 10^{-3} \text{ mA s}^{-1}$) indicating direct proportionality between di/dt and p'_2 .

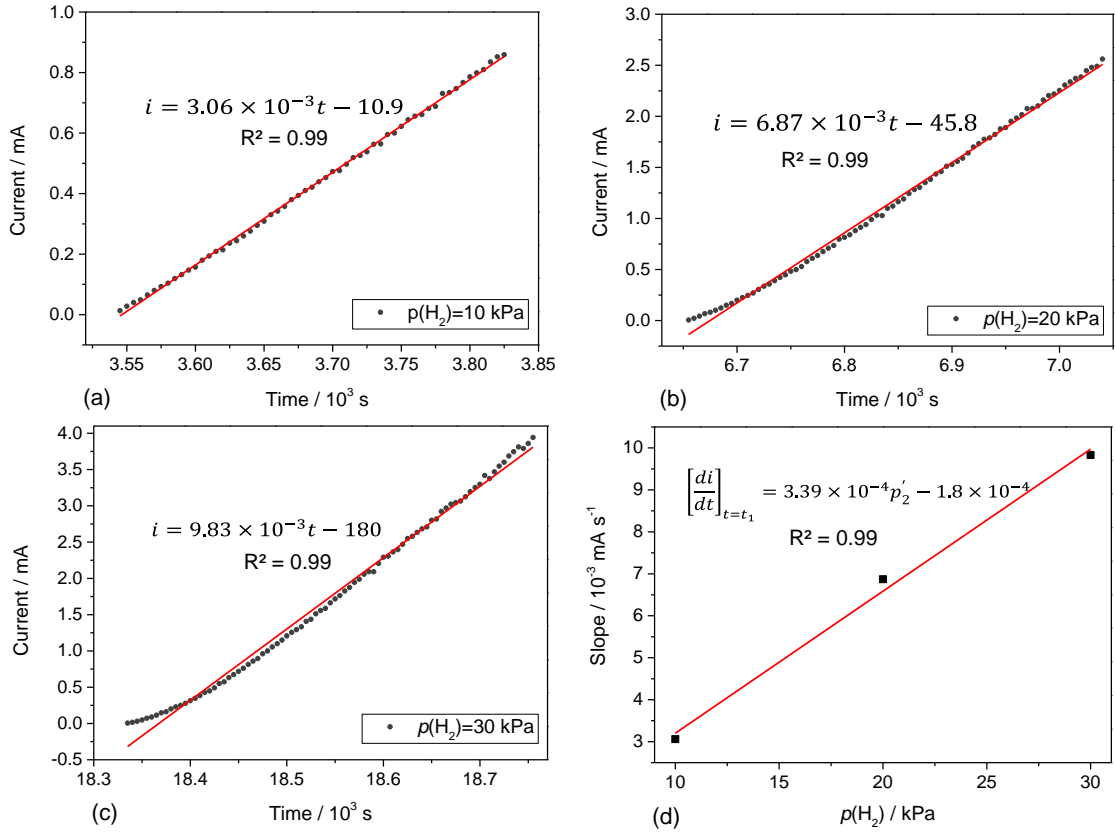


Figure 7.22. Current-time curves after switching the hydrogen partial pressure from 0 to 10 kPa (a); 20 kPa (b); 30 kPa(c). Slopes of the lines in (a-c) vs. p(H₂) are shown in (d).

The data are interpreted using Equations (7.65) and (7.70):

$$s_1 = k_1(k_2)^2 k_3 \bar{c}^* = 3.4 \times 10^{-4} \text{ mA s}^{-1} \text{ kPa}^{-1}$$

It is shown in Section 7.6.1 that

$$s_2 = nFV k_1(k_2)^2 \bar{c}^* = 0.48 \pm 0.06 \text{ mA kPa}^{-1}$$

Thus applying (7.71):

$$\frac{s_1}{s_2} = \frac{k_3}{VnF} = \frac{3.4 \times 10^{-4}}{0.48 \pm 0.06} = (0.71 \pm 0.09) \times 10^{-3} \text{ s}^{-1}$$

This value may be compared with the value of the reciprocal time constant at $p_2' = 0$ ($\bar{z}_2 = 1$) which is $0.97 \times 10^{-3} \text{ s}^{-1}$ (see Table 7.1).

The similarity of the determined values for the reciprocal time constant, $\left(\frac{k_3}{VnF}\right)$: 0.71×10^{-3} and $0.97 \times 10^{-3} \text{ s}^{-1}$, is remarkable considering that the values were determined by unrelated methods and the simplicity of the model employed. This indicates that the principles and assumptions upon which the model is based are broadly correct.

It is difficult to place accuracy on the assumptions employed in the **CE** model. However, the correlation between the results from static (steady currents vs. p(H₂)) and dynamic measurements (step changes in p(H₂) with analysis of current vs. time and di/dt determination) is remarkable, and provides confidence in the validity of the assumptions implied.

7.7. Conclusion

Studies of the oxidation of hydrogen in a SOFC with molten tin anode were carried out. The anode was operated at -0.90 V versus an air RE, which is within an 'inert' potential window. Steady anodic currents were essentially proportional to hydrogen partial pressure and independent of total gas flow rate. Two models were considered for either (i) direct anodic oxidation of dissolved hydrogen or (ii) homogeneous reaction between dissolved hydrogen and oxygen followed by anodic injection of oxygen to replace that removed by the chemical reaction. The former model was rejected as it required the incorporation of the hydrogen/ argon fuel gas in the form of a persistent foam which was not detected. Oxygen solubility values are compatible with the latter model which was validated using steady-state and dynamic experimentally-generated data.

The development of the theoretical framework has generated the parameter \bar{z} . This parameter does not have fundamental significance but is of technological importance when designing LMA SOFC reactors. Theory shows that \bar{z} depends upon geometric factors (including electrode area and the volume of tin), mass-transfer (diffusion layer thickness and diffusion coefficient of dissolved oxygen) and kinetic factors in the cell; its physical meaning is related to the Damkohler number, widely applied in chemical reaction engineering. The value of \bar{z} is required in order to obtain a fuller understanding of experimentally-generated results.

This study has clarified the behaviour of the oxygen-hydrogen-tin system in the 'inert window' and provides a firm basis for proceeding with studies via the Rotating Electrolyte Disc (RED).

8. Additional validation of *CE* model

In the previous chapter a model for the processes taking place in the liquid metal anode involving hydrogen oxidation in liquid tin anode SOFCs in mode *CE* was proposed and validated. A new key parameter, the dynamic oxygen utilisation coefficient, (\bar{z}) was also introduced which has important implications regarding understanding and design of these systems. This chapter demonstrates the development and application of a method named anodic injection coulometry (AIC), for the determination of \bar{z} , as well as providing additional validation of the chemical – electrochemical (*CE*) model by measurement of the oxygen solubility in liquid tin for comparison with literature values.

8.1. Introduction

Solid oxide fuel cells (SOFCs) with liquid metal anodes (LMAs) have substantial potential for power generation. The advantages over combustion systems and other types of fuel cell have been reviewed recently¹³⁰. The technology is able to provide high efficiency and low environmental impact with flexibility regarding fuels, including solid fuel such as coal¹⁸. It is clear that the development of pilot plants and industrial systems requires an in-depth understanding and solutions to a number of technological challenges.

In the previous Chapter, the fundamental electrochemistry of a simple system, using hydrogen as fuel, was explored. It was demonstrated that the oxidation of hydrogen takes place via a chemical-electrochemical (*CE*) mode, whereby hydrogen undergoes homogeneous oxidation by oxygen dissolved in the liquid tin followed by anodic oxygen injection to replace oxygen removed by the chemical reaction. A model was developed which was validated using experimental data. A new key parameter, termed the dynamic oxygen utilisation coefficient, (\bar{z}), evolved during model development which is important for LMA fuel cell design.

In this paper, the model is developed further and a method is proposed, named anodic injection coulometry (AIC), similar in principle to the well-known technique of anodic stripping voltammetry (ASV)¹⁵⁵, to determine \bar{z} . This allows the solubility of oxygen in the melt to be measured and provides additional validation of the model and *CE* mechanism.

8.2. Background literature concerning oxygen and hydrogen solubilities

Solubility of diatomic gases in liquid metals has previously been investigated by various methods.^{149,156,157} It is known that dissolution of diatomic gases in liquid metals involves dissociation into single atoms, according to Sievert's law^{150,151,158,159}. For example hydrogen dissolves as follows:



Sievert's law states that concentration of dissolved gas in liquid metal is proportional to the square root of the gas partial pressure, i.e.:

$$c' = K_s \sqrt{p(H_2)} \quad (8.2)$$

where c' is the concentration of dissolved hydrogen, $p(H_2)$ is the hydrogen gas pressure and K_s is the temperature-dependent constant (Sievert's constant).

Studies on hydrogen and oxygen solubility in liquid tin have been explored in the literature review of this thesis (see Section 2.3.3).

Oxygen solubility in liquid tin data reported by Belford and Alcock⁷⁹ and Ramanarayanan and Rapp⁸⁰ are shown in Figure 8.1.

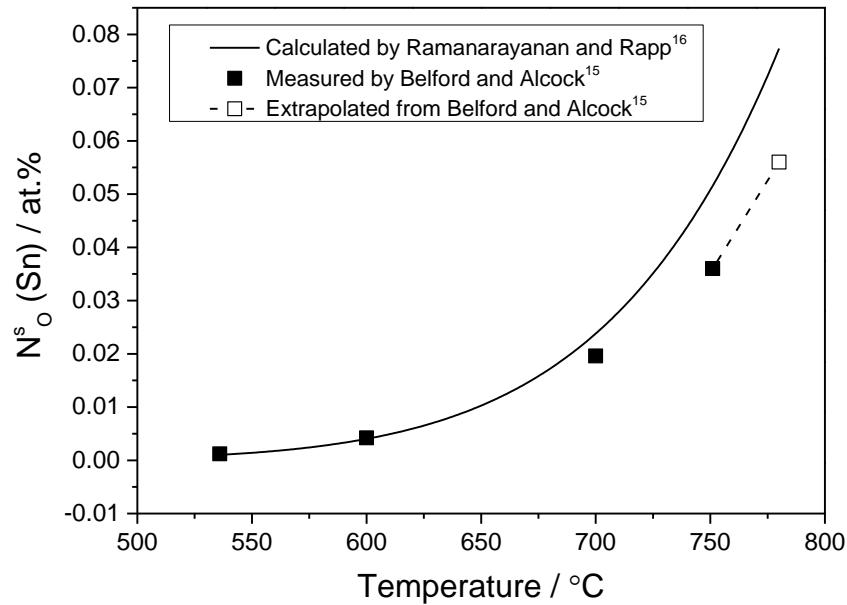


Figure 8.1 Reported solubility of oxygen in liquid tin.

These literature values at 780 °C calculated from formulae given by Belford and Alcock⁷⁹ and Ramanarayanan and Rapp⁸⁰ (i.e. 0.06 and 0.08 at.%, respectively, Figure 8.1) are used for the comparison with experimentally measured solubility data for oxygen determined in the present chapter.

A detailed review of oxygen solubility in liquid tin (given in Section 0 of this thesis) shows a substantial range of literature values derived from various Sn-O phase diagrams, including both measured and predicted data. Importantly, solubility of oxygen in liquid tin is a parameter of technological significance for operation of LMA SOFCs; this is because operation of the liquid tin anode involves oxidation of fuel by the dissolved oxygen⁶. Hence the solubility of oxygen in tin governs the quantity of oxygen which is stored (available to react with fuel) in the liquid tin anode prior to formation/ precipitation of solid tin oxide.

The solid oxide builds up progressively upon further polarisation of the anode and eventually blocks the anode / electrolyte interface^{6,72}. This phenomenon was found to be the major cause of performance degradation of SOFCs with liquid tin anode^{72,73}. Therefore an in-depth understanding of oxygen solubility in liquid metal anodes is of great importance for the development of this class of fuel cell, where oxygen solubility is a vital parameter for design of such systems.

This chapter presents further investigation into the role of dissolved oxygen in liquid tin anode SOFCs when operated in **CE** mode. This includes determination of the key parameter, \bar{z} , as well as calculation of oxygen solubility. To this end, two related regimes of operation are proposed. These regimes are run in a mixed mode (i.e. potentiostatic and open-circuit), whereby electrode potential is switched between a fixed value E and open-circuit. During the open-circuit periods hydrogen reacts with oxygen dissolved in tin. In the first regime (Regime 1) the flow of H_2 is constant, whereas in the second (Regime 2) it is intermittent. This uses additional theory developed specifically for each regime as well as theory developed previously¹⁶⁰ (see Chapter 7, Section 7.6).

8.3. Experimental procedure

Experimental work employed SOFC with liquid tin anode in mode **CE** at 780 °C as described previously¹⁶⁰ (in Chapter 7).

8.4. Results and discussion

This chapter presents further validation of the theory developed to describe **CE** mode hydrogen oxidation in LMA-SOFCs. Anodic injection coulometry (AIC) (with similarities to anodic stripping voltammetry) is proposed as a method for determination of dynamic oxygen utilisation coefficient, \bar{z} , postulated in the **CE** model¹⁶⁰. The method involves AIC under two different modes of oxygen injection (termed Regimes 1 and 2). Subsequent analysis of the experimental data in both regimes enables the calculation of \bar{z} . The theory developed previously is extended and then applied for the determination of the solubility of oxygen in liquid tin.

8.4.1. Determination of the dynamic oxygen utilisation coefficient using anodic injection coulometry

In the previous chapter it was shown that \bar{z} depends upon geometric factors (electrode area and liquid metal volume), diffusion layer thickness (and hence degree of convection) and hydrogen partial pressure. Though not fundamental, it is important to determine its value in order to obtain an understanding of experimentally-generated results. In a broader sense, this parameter is expected to be important for the design of systems consisting of two processes: fuel oxidation via dissolved oxygen and oxygen replacement via electrochemical injection at the liquid anode / electrolyte interface.

In the theoretical treatment, hydrogen and oxygen are denoted by single prime and bar superscripts respectively, for example c' and \bar{c} (as previously employed in Chapter 7).

8.4.1.1. Regime 1

Consider the following, four-stage operation (see Figure 8.2): prior to Point A, argon is bubbled through liquid tin for a sufficient time to allow the current to reduce to a value close to zero while holding the tin electrode at an anodic potential E , typically -0.90 V vs. RE (air electrode). It has been shown that this potential places the system in the CE mode of operation¹⁶⁰. During the intervals A - B, B - C and C - D, hydrogen at partial pressure p'_2 is bubbled through the tin. The interval A - B is sufficiently long to allow the current to reach a steady value, i_2 . During the interval B - C, of length $t_3 - t_2$, the tin electrode is switched to open circuit (OC). Then, during the interval C - D, the potential of the tin electrode is held at anodic potential E , during which time the current is monitored. The period C - D is sufficiently long to allow the current to return to a value close to the steady value, i_2 . The charge, Q_1 , shown as the shaded area in Figure 8.2 is then calculated.

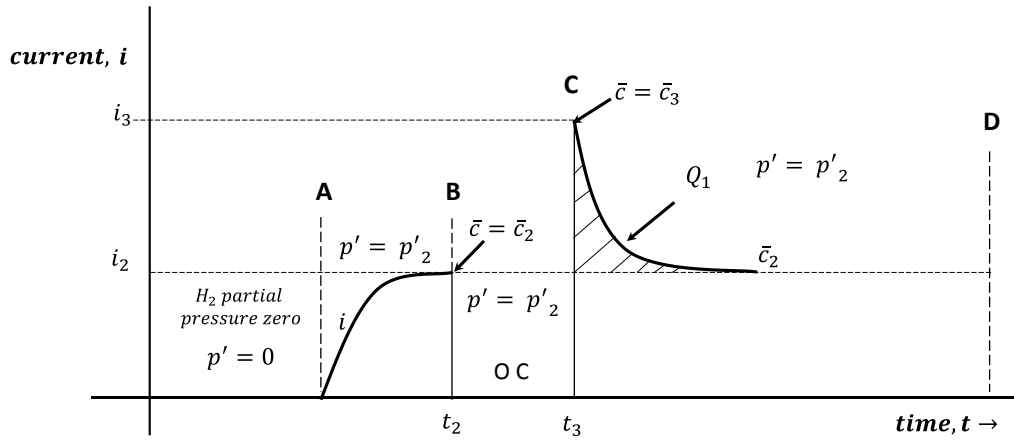


Figure 8.2 Schematic representation of Regime 1 conditions applied to the working cell: same hydrogen partial pressure, p'_2 is applied from A to D; potential is held at a value E everywhere except in B - C.

The interval A-B was treated previously in Chapter 7 (Section 7.6.1). The interval B - C is treated as follows. At open circuit, $i=0$, so the equation expressing the rate of removal of oxygen via chemical reaction with hydrogen and the addition of oxygen via anodic injection (Equation (7.30)) (when treated from B - C) becomes:

$$\frac{d\bar{N}}{dt} = -Vk_1(k_2)^2\bar{c}p_2' \quad (8.3)$$

Using Equation (7.43) shown before:

$$\frac{d\bar{c}}{dt} = \frac{1}{V} \frac{d\bar{N}}{dt}$$

We obtain:

$$\frac{d\bar{c}}{dt} = -k_1(k_2)^2\bar{c}p_2' \quad (8.4)$$

Integrating (8.4):

$$\int_{\bar{c}_2}^{\bar{c}_3} \frac{d\bar{c}}{\bar{c}} = -k_1(k_2)^2 p_2' \int_{t_2}^{t_3} dt \quad (8.5)$$

$$\ln \frac{\bar{c}_3}{\bar{c}_2} = -k_1(k_2)^2 p_2'(t_3 - t_2)$$

Or

$$\bar{c}_3 = \bar{c}_2 \exp[-k_1(k_2)^2 p_2'(t_3 - t_2)] \quad (8.6)$$

The region C-D is now treated, where $p' = p_2'$. The steps used as follows:

- i) The starting value of \bar{c} , which is \bar{c}_3 is given by Equation (8.6).
- ii) An expression is derived for \bar{c} as a function of time.
- iii) Using the expression for \bar{c} , and equations (7.35),(7.38) and (7.41) to reveal the term $(i - i_2)$ as a function of time.
- iv) Integrate $(i - i_2)$ from t_3 to ∞ to obtain Q_t .

Equation (7.51) that was derived previously provides the relationship between \bar{c} and t as follows:

$$\ln \frac{\bar{c}_2 - \bar{c}}{\bar{c}_2 - \bar{c}_1} = -\frac{k_3}{VnF\bar{z}_2} (t - t_1)$$

and replacing \bar{c}_1 by \bar{c}_3 and t_1 by t_3 we obtain:

$$\bar{c}_2 - \bar{c} = (\bar{c}_2 - \bar{c}_3) \exp\left[-\frac{k_3}{VnF\bar{z}_2} (t - t_3)\right] \quad (8.7)$$

From Equations (7.35) and (7.38) derived in the previous Chapter we can write:

$$i - i_2 = k_3(\bar{c}_2 - \bar{c}) \quad (8.8)$$

Then with (8.7) we obtain:

$$i - i_2 = k_3(\bar{c}_2 - \bar{c}_3) \exp\left[-\frac{k_3}{VnF\bar{z}_2} (t - t_3)\right] \quad (8.9)$$

Substituting for \bar{c}_3 from (8.6) into (8.9) and using Equation (7.41) we obtain:

$$\begin{aligned} i - i_2 &= k_3 \bar{z}_2 \bar{c}^* \{1 - \exp[-k_1(k_2)^2 p_2'(t_3 - t_2)]\} \\ &\times \exp\left[-\frac{k_3}{VnF\bar{z}_2} (t - t_3)\right] \end{aligned} \quad (8.10)$$

The charge shown by the shaded area in the diagram (Figure 8.2) is given by:

$$Q_1 = \int_{t_3}^{\infty} (i - i_2) dt \quad (8.11)$$

$$Q_1 = -VnF(\bar{z}_2)^2 \bar{c}^* \{1 - \exp[-k_1(k_2)^2 p_2'(t_3 - t_2)]\} \times \left\{ \exp \left[-\frac{k_3}{VnF\bar{z}_2} (t - t_3) \right] \right\}_{t_3}^{\infty} \quad (8.12)$$

Or

$$Q_1 = VnF(\bar{z}_2)^2 \bar{c}^* \{1 - \exp[-k_1(k_2)^2 p_2'(t_3 - t_2)]\} \quad (8.13)$$

Equation (8.13) is the required solution.

8.4.1.2. Corroborating experimental results in Regime 1

To validate the above theory the LTA SOFC was operated in Regime 1. After Point A (Figure 8.2) a mixture of H₂ (16 kPa) and Ar was bubbled constantly through liquid tin while holding a potential of WE at -0.90 V vs. RE. Once the anodic current had stabilised at a steady value, the tin electrode was switched to open circuit (OC) remaining so for 1500 s before controlling the potential again at -0.90 V vs. RE. Once the anodic current had returned to within 10 μA of its steady value, the electrode was again switched to OC and held for 900 s. The above procedure was repeated with varying OC times (Figure 8.3).

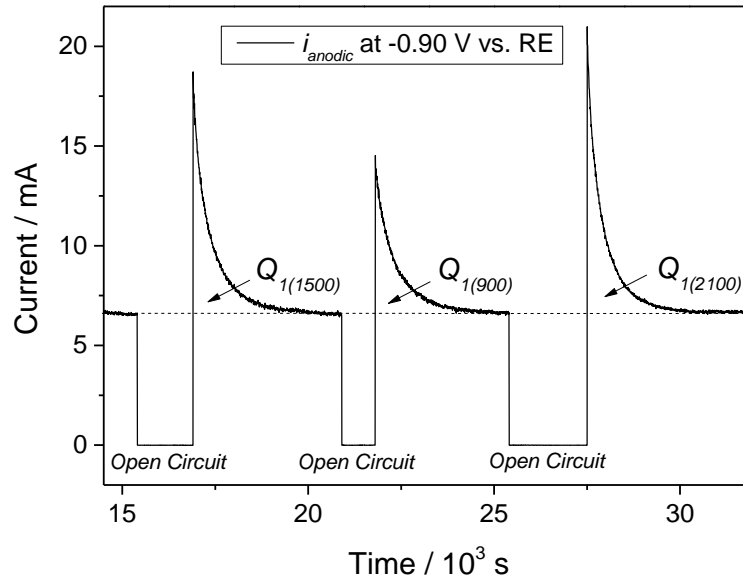


Figure 8.3 Operation of the working cell under Regime 1 with 16 kPa $p(\text{H}_2)$ at 780 °C.

The values of Q_i were calculated applying numerical integration of the area under the current-time curve (currents were measured at 5 s intervals) and are summarised in Table 8.1.

Table 8.1 Q_I values obtained from with 16 kPa $p(\text{H}_2)$ for Regime 1 operation.

OC time / s	900	1500	2100
Q_I values / C	3.98	5.35	5.71

8.4.1.3. Regime 2

For Regime 2, consider a four stage process (see Figure 8.4). During the interval A – B the potential of tin electrode is held at the potential E and argon is flowed for sufficient time to reduce the current to a value close to zero. At B the tin electrode is then switched to open circuit and the flowing gas to an argon-hydrogen mixture with hydrogen partial pressure p'_2 for a period t_3-t_2 . At C the flowing gas is returned to 100% argon and the potential of the electrode switched to the value E . The current is measured as a function of time for a time sufficient for the current to return to a value close to zero. The charge, Q_2 , shown as the shaded area in Figure 8.4 is then calculated. Note that no hydrogen is bubbled into the tin during the period when the charge Q_2 is determined.

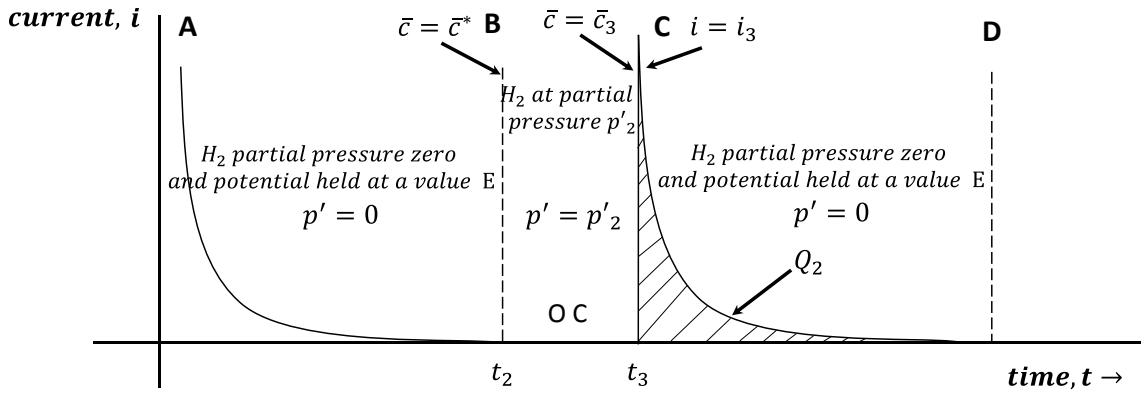


Figure 8.4. Schematic representation of Regime 2 conditions applied to the working cell flushed with constant flow of argon.

Interval A - B is not considered in this treatment. For the interval B – C Equation (8.5) is used, replacing \bar{c}_2 by \bar{c}^* , (where \bar{c}^* is the saturated concentration of oxygen at OC in the bulk of liquid tin at $p'=0$):

$$\int_{\bar{c}^*}^{\bar{c}_3} \frac{d\bar{c}}{\bar{c}} = -k_1(k_2)^2 p_2' \int_{t_2}^{t_3} dt \quad (8.14)$$

Then integrating

$$[\ln \bar{c}]_{\bar{c}^*}^{\bar{c}_3} = -k_1(k_2)^2 p_2' [t]_{t_2}^{t_3}$$

$$\ln \frac{\bar{c}_3}{\bar{c}^*} = -k_1(k_2)^2 p_2' (t_3 - t_2)$$

$$\bar{c}_3 = \bar{c}^* \exp[-k_1(k_2)^2 p_2' (t_3 - t_2)] \quad (8.15)$$

Region C – D is now treated, where $p' = 0$. It follows that the charge, Q_2 , shown in the diagram (Figure 8.4) is given by

$$Q_2 = (\bar{c}^* - \bar{c}_3)VnF \quad (8.16)$$

Substituting for \bar{c}_3 from (8.15) into (8.16):

$$Q_2 = VnF\bar{c}^*\{1 - \exp[-k_1(k_2)^2 p_2'(t_3 - t_2)]\} \quad (8.17)$$

This is the required solution which may be compared with Equation (8.13).

8.4.1.4. Corroborating experimental results in Regime 2

To validate the above theory the LTA SOFC was operated in Regime 2. A mixture of H_2 (16 kPa) and Ar was bubbled through the melt while the tin electrode was held at open circuit for 1500 s. Then the tin electrode was switched from OC to -0.90 V vs. RE and the H_2 was removed from the flow (argon continued to bubble into the tin). Once the measured anodic current (due to anodic injection of oxygen to replace oxygen consumed by reaction with hydrogen) had reduced to zero, the electrode was switched to OC and remained so for 900 s with flow of 16 kPa $p(H_2)$ (Figure 8.5). The above procedure was repeated for OC intervals of 1500 and 2100 s. The flow of argon was constant throughout the experiment including the open circuit periods.

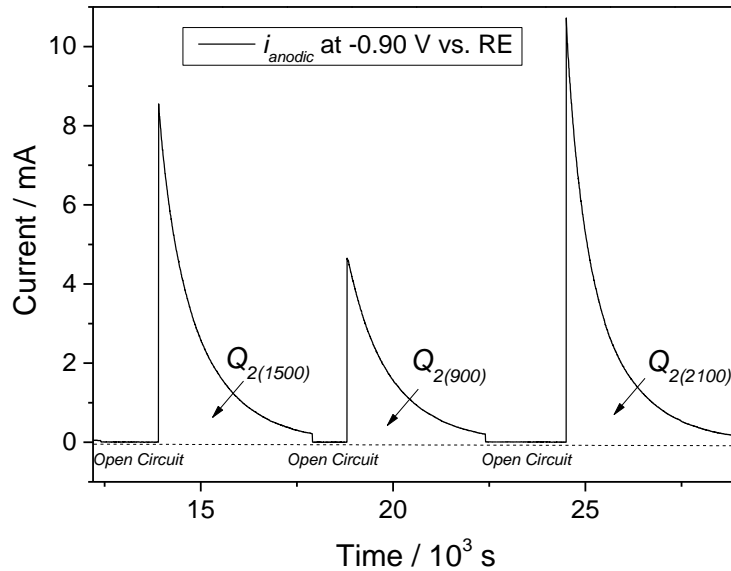


Figure 8.5 Operation of the working cell under Regime 2 with 16 kPa $p(H_2)$ at 780 °C.

The values of Q_2 were calculated in the same way as Q_1 values via numerical integration of the area under the current-time curve (currents again were measured at 5 s intervals) and are summarised in Table 8.2.

Table 8.2. Q_2 values obtained with 16 kPa $p(\text{H}_2)$ for Regime 2 operation.

OC time / s	900	1500	2100
Q_2 values / C	5.11	8.05	8.9

8.4.1.5. Regime 3

This case is included for completeness. However no experiments were performed to support the theory developed for Regime 3 as this is not required for determination of \bar{z} . This regime, which is a combination of the previous two regimes, is illustrated in Figure 8.6.

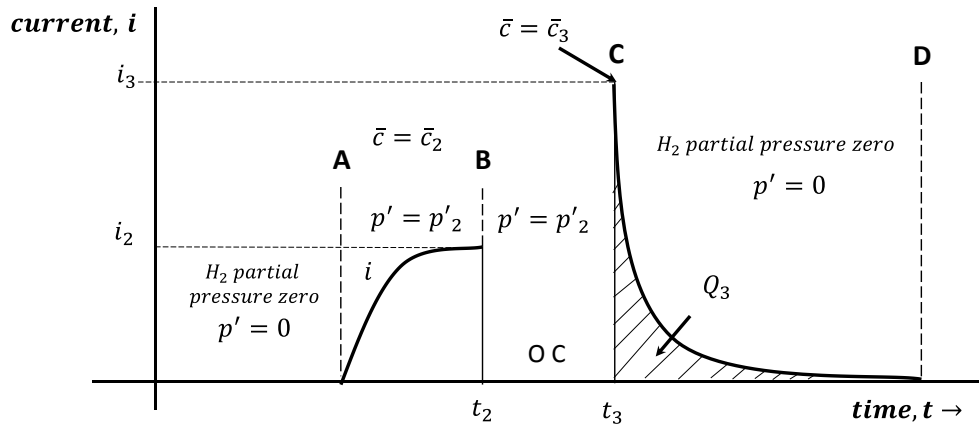


Figure 8.6 Schematic representation of Regime 3 conditions applied to the working cell flushed with constant flow of argon; potential is held at a value E everywhere except in B - C.

Prior to Point A argon is bubbled through tin and the electrode is held at an anodic potential E , typically -0.90 V with respect to an air electrode, while sufficient time is allowed for the current to reduce to a value close to zero. During the intervals A – B and B - C, hydrogen at partial pressure p'_2 is bubbled through the tin. The interval A - B (with potential maintained at E) is sufficiently long to allow the current to reach a steady value, i_2 . During the interval B - C, of length $t_3 - t_2$, the tin electrode is switched to open circuit. At Point C the flowing gas is returned to 100% argon and the tin electrode switched from OC to the potential E . Thereafter, the current is measured as a function of time until the current returns to a value close to zero. The charge Q_3 , shown as the shaded area in Figure 8.6 is then calculated. Note that no hydrogen is bubbled into the tin during the period when the charge Q_3 is determined.

Following Regime 1, the oxygen concentration \bar{c}_3 at C given by (8.6) which together with Equation (7.41) leads to:

$$\bar{c}_3 = \bar{z}_2 \bar{c}^* \exp[-k_1(k_2)^2 p_2'(t_3 - t_2)] \quad (8.18)$$

For the interval C – D as for Regime 2 the partial pressure of hydrogen equals to zero (i.e. $p' = 0$). It follows that the charge, Q_3 , shown in the diagram (Figure 8.6) is given by

$$Q_3 = (\bar{c}^* - \bar{c}_3)VnF \quad (8.19)$$

So from (8.18) and (8.19):

$$Q_3 = VnF\bar{c}^*\{1 - \bar{z}_2 \exp[-k_1(k_2)^2 p_2'(t_3 - t_2)]\} \quad (8.20)$$

This is the required solution and may be compared with (8.13) and (8.17)

Summary of the principal results in 8.4.1.1- 8.4.1.5.

The important equations in the above sections are those that allow interpretation of the coulombic charge under the final parts of the regimes, i.e. C – D. These are as follows:

$$\text{Regime 1} \quad Q_1 = VnF(\bar{z}_2)^2 \bar{c}^*\{1 - \exp[-k_1(k_2)^2 p_2'(t_3 - t_2)]\} \quad (8.13)$$

$$\text{Regime 2} \quad Q_2 = VnF\bar{c}^*\{1 - \exp[-k_1(k_2)^2 p_2'(t_3 - t_2)]\} \quad (8.17)$$

$$\text{Regime 3} \quad Q_3 = VnF\bar{c}^*\{1 - \bar{z}_2 \exp[-k_1(k_2)^2 p_2'(t_3 - t_2)]\} \quad (8.20)$$

8.4.1.6. *Experimental determination of dynamic oxygen utilisation coefficient, \bar{z}*

The development of the theoretical framework described earlier in Section 7.6, Chapter 7 has identified the parameter \bar{z} . For a given hydrogen partial pressure, p_2' , and $(t_3 - t_2)$, \bar{z} may be determined using (8.13) and (8.17) as follows:

$$(\bar{z}_2)^2 = \frac{Q_1}{Q_2} \quad (8.21)$$

Taking the values of Q_1 and Q_2 from Table 8.1 and Table 8.2, the value of \bar{z}_2 from (8.21) is equal to 0.83 for hydrogen partial pressure of 16 kPa.

The estimated uncertainty on the obtained values of Q_1 and Q_2 is $\pm 5\%$, resulting in an uncertainty in the \bar{z}_2 value of 3.5 % (i.e. $\bar{z}_2 = 0.83 \pm 0.03$).

The relationship between a value of \bar{z}_2 and p_2' was shown in Equation (7.56) as follows:

$$\bar{z}_2 = (1 + \bar{K}p_2')^{-1} \quad (7.56)$$

Taking \bar{z}_2 as 0.83 for 16 kPa $p(\text{H}_2)$ and inserting into (7.56) leads to a value of \bar{K} of 0.012 kPa⁻¹. This value is within the range of values of \bar{K} ($0.000 < \bar{K} < 0.014$ kPa⁻¹) deduced in Chapter 7.

8.4.2. Measurement of the oxygen solubility in liquid tin using electrochemical model for CE mode

Having obtained a value for \bar{z}_2 , the solubility of oxygen in tin (oxygen content at an electrode potential of -0.90 V versus air electrode) may be determined as shown below. The value calculated may then be compared with literature values and used to provide additional validation and confirmation of the model developed and tested in Chapter 7.

An expression for the number of moles of dissolved oxygen in liquid tin, may be developed using the Equations (7.38) and (7.41) as follows:

$$i_2 = k_3(\bar{c}^* - \bar{c}_2) \quad (7.38)$$

$$\bar{c}_2 = \bar{z}_2 \bar{c}^* \quad (7.41)$$

Eliminating \bar{c}_2 between (7.38) and (7.41) leads to:

$$i_2 = k_3 \bar{c}^* (1 - \bar{z}_2) \quad (8.22)$$

We can write this as

$$i_2 = \frac{k_3 \bar{c}^* V n F (1 - \bar{z}_2)}{V n F} \quad (8.23)$$

Rearranging (8.23):

$$\bar{c}^* = \frac{i_2}{(1 - \bar{z}_2) n F V} \left(\frac{V n F}{k_3} \right) \quad (8.24)$$

This is an expression for the saturated concentration of oxygen in liquid tin, \bar{c}^* , in terms of the steady current, i_2 , the time constant at $p=0$ (when $\bar{z}_2=1$), $\frac{V n F}{k_3}$, the volume of tin, V , and the parameter \bar{z}_2 .

Recalling Equation relating the steady anodic current and $p(\text{H}_2)$ that was presented in Figure 7.4 (current in mA hydrogen partial pressure in kPa):

$$i_{steady} = 0.42 p(\text{H}_2) + 0.15 \quad (8.25)$$

the value of i_2 for 16 kPa can be determined from that.

Similarly the time constant, $\frac{V n F}{k_3}$, for $p(\text{H}_2)=0$ was reported as 1031 s (refer to Table 7.1).

Substituting the value of $\bar{z}_2 = 0.83$ determined in the previous section for 16 kPa $p(\text{H}_2)$, the solubility of oxygen, \bar{c}^* is found to be $5.7 \times 10^{-5} \text{ mol cm}^{-3}$ or 0.10 at.% .

The potential of the working electrode was chosen to be close (within 10 mV) to the equilibrium potential of the Sn/SnO₂ couple. At this potential the oxygen concentration is expected to be close to the saturated value. Moving to more positive potentials would result in precipitation of SnO₂ (see Figure 6.3).

The calculated value (0.10 at.% at 780 °C) is comparable to those reported by Ramanarayanan and Rapp⁸⁰ (0.08 at.%) and Belford and Alcock⁷⁹ (0.06 at.%), respectively. This serves as additional confirmation for the validity of the electrochemical model developed for **CE** mechanism in the previous Chapter.

8.5. Conclusion

Operation of LMA SOFC fuelled with hydrogen in mode **CE** was investigated using the newly-developed anodic injection coulometry technique applied in two regimes of operation. Analysis of experimentally-generated data (Q_1 and Q_2 values measured in Regimes 1 and 2, respectively) resulted in the value of dynamic oxygen utilisation coefficient, \bar{z} , determined for 16 kPa hydrogen as 0.83. The oxygen solubility in liquid tin at 780 °C was measured to be 0.10 at.%, which is similar to literature values, serving as additional confirmation of the validity of the model for **CE** mode operation.

9. Water electrolysis in reverse LME SOFCs

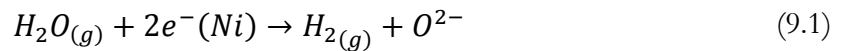
This chapter examines reduction of water (steam) in reverse liquid tin anode SOFCs (or solid oxide electrolyzers – SOEs). Possible mechanisms for the electrolysis of water in LMA are proposed. The most likely mechanism is considered to be dissolution of water (fast process), followed by slow, rate-determining, dissociation of water to hydrogen and oxygen and then by diffusion-controlled cathodic extraction of the oxygen generated by the dissociation of water. Hydrogen generated by the electrolysis was carried out of the cell with the carrier gas. Saturation of the carrier gas with water vapour was achieved using water bottles held at either at room temperature or at temperatures below ambient using a water bath (cooled with ice) with thermostat. Partial pressure of water vapour was varied to investigate its effect on measured current. Initial results showed that, upon changing the water vapour content of the carrier gas, measured current- time curves followed an exponential function, with time constants somewhat shorter than those measured for hydrogen oxidation (followed by anodic injection of oxygen). Currents eventually stabilised; steady currents were found to be proportional to partial pressure of water vapour. An electrochemical model has been developed for interpretation of the water reduction data. The model was validated with experimental results and overall good agreement was found. Initial studies only are presented here and additional work is required for a more complete understanding of water electrolysis in reverse LMA SOFCs.

9.1. Introduction

There are numerous studies on water electrolysis for production of hydrogen using solid oxide membranes¹⁶¹. The use of solid oxide electrolyzers (SOE) is advantageous due to availability and application of heat that is emitted (wasted) during various industrial processes. However, high energy requirement for water (steam) dissociation remains to be the greatest challenge^{162,163}. Many studies have suggested the use of gaseous hydrocarbons to reduce the open circuit voltage in solid oxide steam electrolyzers (SOSE)^{162,163}. One of the most relevant studies was made by Pati *et al.* where instead of solid anode with gaseous carbonaceous fuel, the SOSE was operated on solid hydrocarbon fuel^{53,56} fed into a liquid metal anode to provide an interface for solid fuel oxidation.

Water electrolysis for production of syngas (a mixture of H₂ and CO) from steam and hydrocarbon waste in such cells was achieved using a solid oxide electrolyte, Ni-YSZ cathode and liquid tin anode^{53,56}. Oxidation of fuel in liquid metal anode reduces the concentration of dissolved oxygen in the metal anode and aids the dissociation of steam to hydrogen⁵³.

The steam is fed to the cathode (Ni-YSZ) and undergoes the reaction as follows:



Oxygen ions are then oxidised at the interface with the melt as follows:



Dissolved oxygen diffuses through the liquid metal to react with the reductant (fuel) via reaction as follows:



The schematic of the operation of a solid oxide electrolyser with LMA was described earlier in the literature review (Chapter 2; Figure 2.16). The electrolysis of steam using the liquid metal electrode has not previously been reported.

This chapter aims to investigate the possibility for water (steam) electrolysis within the liquid metal electrode. The approach applied in the present study whereby water (steam) dissociates in a liquid metal electrode has not been tested previously in typical solid oxide electrolyzers (SOE) and hence provides some new insights into the application of liquid metal electrodes for water electrolysis.

9.2. Experimental procedure

In the present chapter, all experimental work entails operation of LTA SOFC cell at a constant operating temperature of 810 °C. Experimental set-up and components of the working cell were similar to the ones described in Chapter 4. However, some modifications

to the original set-up were made to fulfil the requirements for the practical work on the dissociation of water in the bulk of the liquid tin anode followed by cathodic reduction of oxygen at the liquid tin / YSZ interface. In particular the humidification of argon was achieved by the use of water bottles held at room temperature or inside a temperature-controlled water bath.

A schematic of the experimental rig used in this work is shown in Figure 9.1. Argon was humidified by bubbling through water contained in bottles held at room temperature or suspended in a 5 litre heated circulating water bath (T100-ST-5, Grant Instruments, UK) which enabled humidification at a range of temperatures; temperatures below ambient were achieved by the addition of ice to the bath. The humidified argon was piped to the oxygen sensor after which it was mixed with hydrogen and supplied to the cell (Figure 3.6) held at operating temperature by an electric furnace.

9.2.1. Humidification of the carrier gas (Ar)

The degree of humidification of argon was controlled by bubbling the gas through one of two sets of water bottles (one kept at room temperature and the other suspended in a water bath), where inside the bath the temperature of water could be adjusted from 0 to 100 °C. Water bottles were held at room temperature (ca. 25 °C) while the temperature inside the water bath was set to 0, 10 and 15 °C. The precision of the temperature in the water bath was ± 0.05 °C. The use of bottles suspended either inside the water bath or in the air (held at room temperature) enabled rapid changes in water partial pressure, which is important when determining time constants. The respective saturated vapour pressures at each temperature are summarised in Table 9.1. In practice, the water bath was not operated at temperatures above ambient as this resulted in condensation of water in the pipes (heated lines were not used).

Saturation of the argon at 25 °C was confirmed by bubbling the gas through two water bubblers in series at room temperature (25 °C) and condensing the contained water vapour as follows: a known volume of the gas was passed through a pre-weighed U-shaped drying tube (inner diameter 13 mm, Duran glass) with stopcock plugs and side hose connector (6mm) (Carl Roth, Anncis Ltd., UK) immersed in an ice-salt bath (temperature ca. -10 °C). After passing a specified volume of humidified gas through the tube the stopcocks were closed and after drying the external surfaces of the tube and allowing sufficient time for it to return to room temperature, it was reweighed. The increase in weight due to condensation of water indicated that the partial pressure of water vapour was 3.2 kPa at 25

°C (in agreement with the value given by standard tables) showing that the gas was fully saturated with H₂O.

Table 9.1 Saturated water vapour pressure at set temperature values from standard tables.

Temperature / °C	0	10	15	25	26	28
$p(\text{H}_2\text{O})$ / kPa	0.6	1.2	1.7	3.2	3.4	3.8

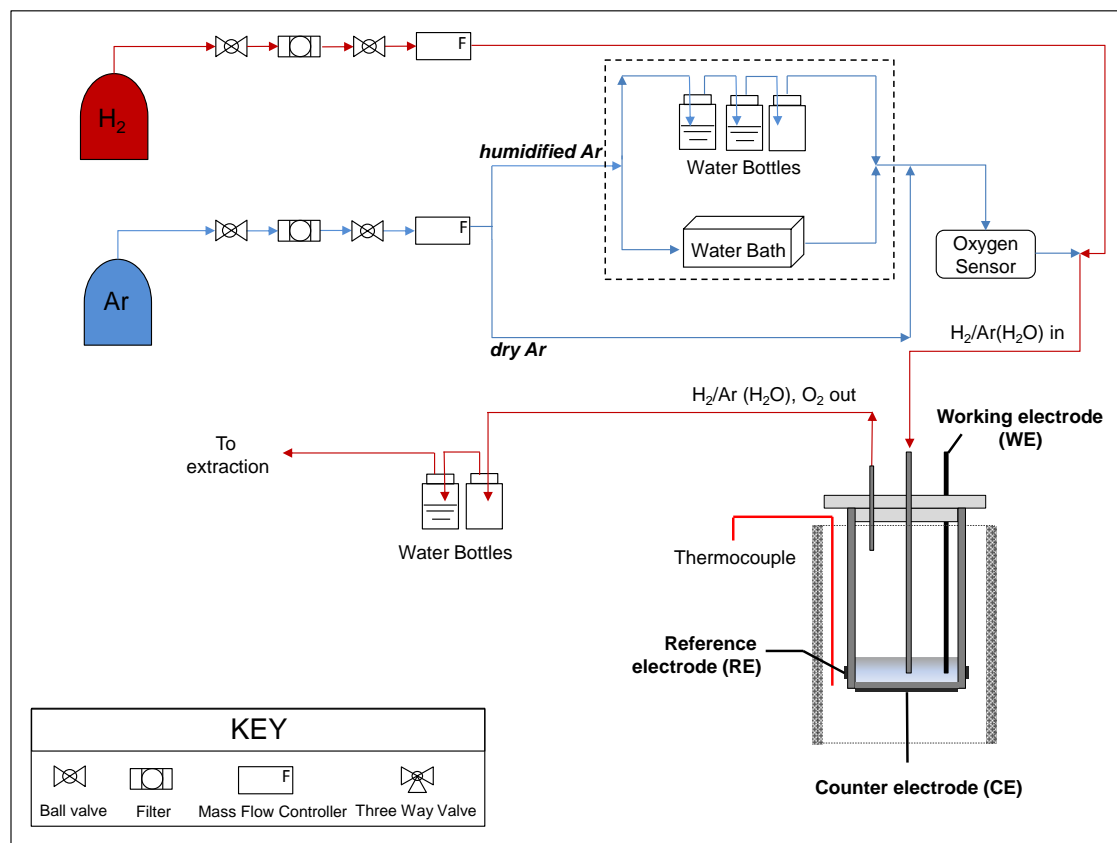


Figure 9.1 Process flow diagram for dissociation of water in LMA SOFC cell followed by cathodic reduction of oxygen (with optional use of H₂ for additional removal of tin oxide).

9.3. Results and discussion

9.3.1. Water reduction in LTA SOFC

The water bath was operated at temperatures of 0, 10, and 15 °C (below the room temperature of 26 °C) which eliminated condensation inside the tubing. The LTA SOFC cell was run at 810 °C and dry argon at a flow rate of 1 ml s⁻¹ was supplied to the cell. A potential of -1.1 V vs. RE was applied to the working electrode (WE).

The flow of argon was switched between water bottles held at room temperature (26 °C) and others suspended in the water bath at temperatures below ambient. The temperature of each set of water bottles was maintained constant throughout each experiment.

The observed cathodic current with time is shown in Figure 9.2. Initially it gradually decreased in magnitude from ca. -10 mA and stabilised at ca.-1.0 mA with dry argon (Figure 9.2).

The flow of argon was then switched to bubble through bottles in the water bath which was set to 0 °C. This resulted in a steady current of -1.8 mA. The flow of argon was then changed so that it was supplied through two water bottles (held at room temperature) and the cathodic current increased in magnitude to -4.6 mA associated with 3.4 kPa $p(\text{H}_2\text{O})$. The procedure was repeated whereby the carrier gas was supplied from bottles at 0, 10 and 15 °C. The estimated accuracy of measured currents is $\pm 50 \mu\text{A}$.

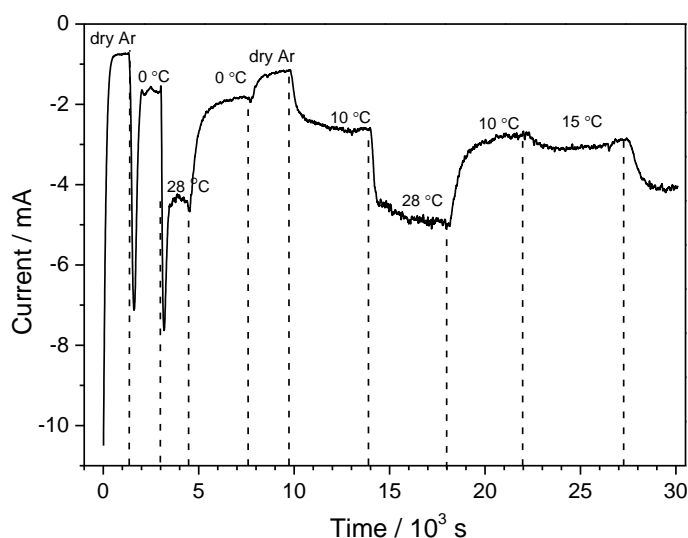


Figure 9.2 Cathodic current at -1.1 V vs. RE at 810 °C with changes of $p(\text{H}_2\text{O})$.

The steady currents as a function of $p(\text{H}_2\text{O})$ (corrected for the reduction current attributed to parasitic oxygen concentration in the melt) are shown in Figure 9.3. Linearity between the steady cathodic current and $p(\text{H}_2\text{O})$ is evident ($R^2 > 0.98$). The uncertainty on the points in this Figure is estimated $\pm 75 \mu\text{A}$ in the current and $\pm 0.2 \text{ kPa}$ in $p(\text{H}_2\text{O})$.

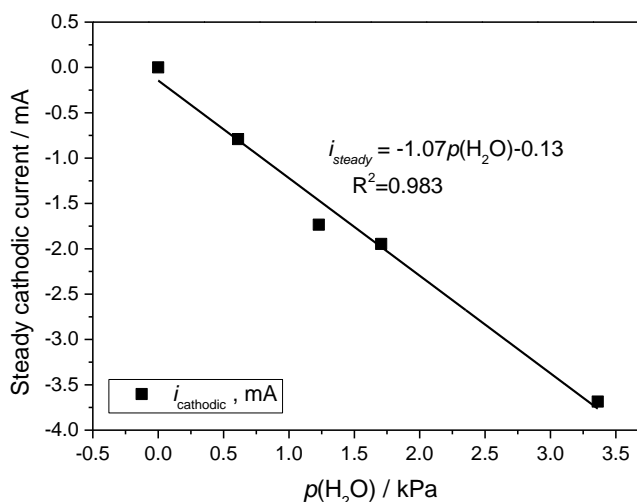


Figure 9.3 Steady cathodic current data as a function of $p(\text{H}_2\text{O})$ corrected for parasitic oxygen current.

Interestingly, measured steady cathodic currents during water reduction (at -1.1 V) were greater in magnitude (by a factor of 2.5) than steady anodic currents for hydrogen oxidation (at -0.90 V) for a given partial pressure of either hydrogen or water vapour.

9.3.2. Water reduction in Regime 1

Operating conditions of Regime 1 (refer to Chapter 8) were applied for water reduction at 810 °C. Instead of anodic overvoltage, a potential of -1.1 V vs. RE was applied to the tin electrode with open circuit (OC) intervals of 300, 1500, 900 and 2100 seconds (Figure 9.4). The water vapour pressure was maintained constant at a value of 3.8 kPa corresponding to 28 °C with a flow of Ar 1 ml s⁻¹. The estimated accuracy of current measurements is $\pm 10\mu\text{A}$.

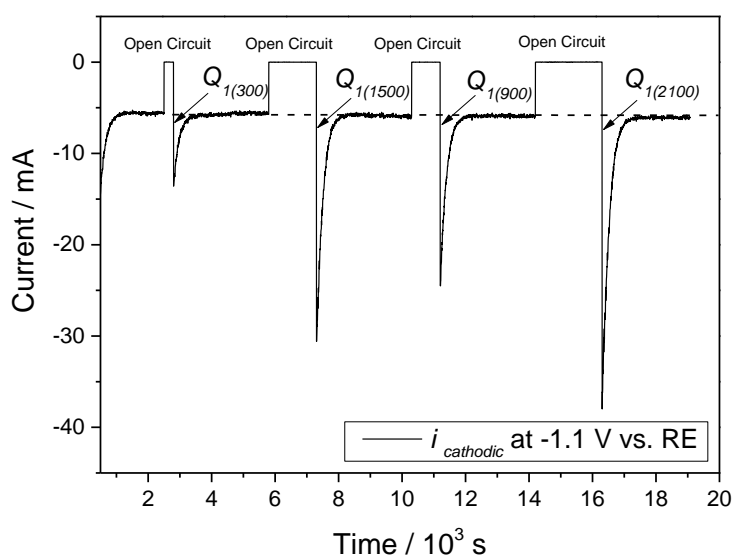


Figure 9.4 Operation of LTA SOFC under Regime 1 with constant 3.8 kPa $p(\text{H}_2\text{O})$.

Q_1 values (coulombic charge to reduce dissolved oxygen generated during the open-circuit periods due to the water dissociation process in liquid tin) were calculated by numerical integration of the area under the current vs. time curve (Figure 9.4) and are summarised in Table 9.2. The estimated uncertainty on the obtained values of Q_1 is $\pm 2.5\%$.

Table 9.2 Q_1 values obtained from with 3.8 kPa $p(\text{H}_2\text{O})$ for Regime 1 operation.

OC time / s	300	900	1500	2100
Q_1 values / C	1.3	3.6	5.2	7.1

The obtained values of Q_1 increase in magnitude as the open-circuit period rises indicating that dissolved oxygen concentration increases with time. A plot of measured Q_1 values (in mC) versus the open circuit intervals resulted in a straight line with a slope of -4.3 mC s^{-1} (Figure 9.5). This slope divided by the vapour pressure of water vapour leads to the value -

1.1 mA kPa⁻¹ in agreement with the slope of Figure 9.3. This important finding is relevant to the development of an electrochemical model for interpretation of experimentally-generated results. The estimated accuracy of Q_I values is ± 100 mC.

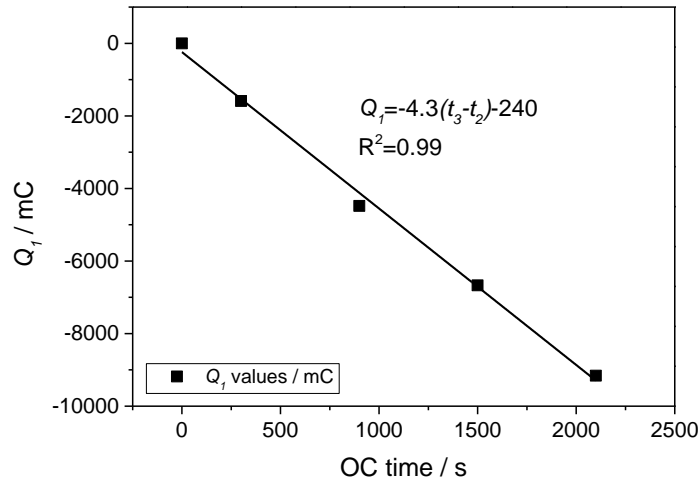


Figure 9.5 Measured Q_I values as a function of OC intervals.

9.3.3. Electrochemical model for water electrolysis

The **CE** model was developed for the oxidation of hydrogen to water in Chapter 7. Measurements have been made for the reverse process, reduction of water to hydrogen. Results showed steady current proportional to partial pressure of water vapour. Also step changes in partial pressure of water vapour resulted in exponential-type current-time curves. Thirdly, Q_I values increased with open-circuit period and showed values consistent with steady currents.

A simple theory is developed below for initial interpretation of the results. Two possible mechanisms were considered analogous to those proposed for hydrogen oxidation earlier:

- i) Rate-determining dissolution of water followed by diffusion-controlled cathodic reduction at the zirconia-tin interface.
- ii) Fast dissolution of water in the tin with concentration proportional to partial pressure of water vapour, i.e. Henry's law behaviour (Sievert's law only applicable to diatomic gases), followed by rate-determining homogeneous reduction of water and then diffusion-controlled cathodic reduction of oxygen at the zirconia-tin interface .

Either of these mechanisms would result in a steady current proportional to the partial pressure of water vapour but Mechanism (ii) is thought to be more likely particularly as it is the one analogous to that validated for hydrogen oxidation and this is the one developed below.

The reaction equation is:



This injects oxygen into the tin. $[H]_{Sn}$ is removed by the following associative process with the hydrogen gas being carried out of the system by the flowing Ar carrier gas:



If the Sn electrode is held at a potential, E , typically -1.1 V vs. air electrode, then the oxygen generated via Reaction (9.4) is removed by cathodic reduction at the Sn-YSZ interface:



This is a similar process to that occurring as a result of H_2 oxidation, except the diffusion of oxygen and the current are in the reverse direction (refer to Equation (7.28) and Figure 7.13).

In the theoretical treatment, water concentration is denoted by double prime and oxygen concentration by a bar.

Concentration profiles in the tin at the interface may be represented by the following figure.

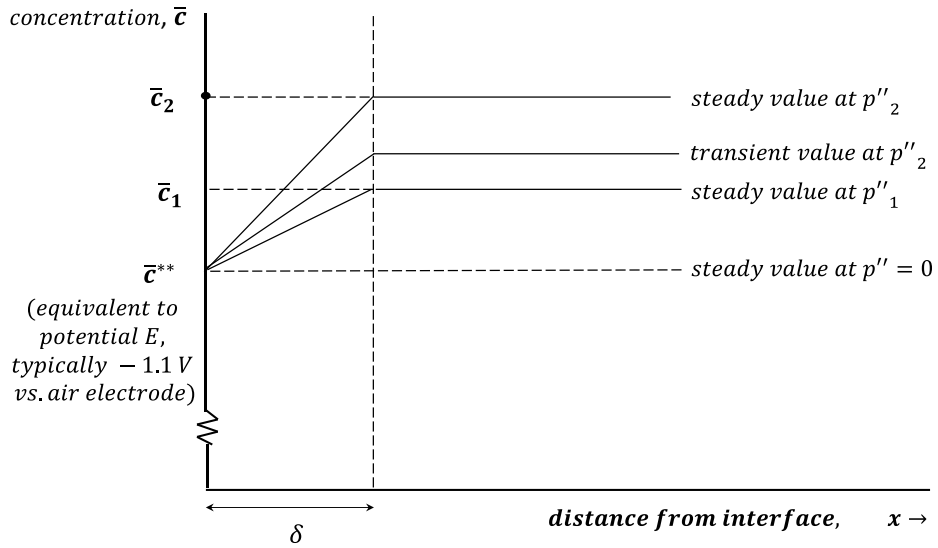


Figure 9.6 Schematic of the dissolved oxygen concentration profile at a given applied potential E during the water reduction process. The diffusion layer thickness is shown as δ . (Compare with Figure 7.13).

The rate of generation of oxygen via Reaction (9.4) is Vk_4c'' (i.e. k_4c'' per unit volume of tin) where k_4 is the homogeneous rate constant for the reaction.

The rate of injection of oxygen via Reaction (9.6) is i/nF ($n=2$, note that i is negative).

Thus the net rate of injection of oxygen via the two reactions is $Vk_4c'' + i/nF$. The concentration of water, c'' , for a given water partial pressure, p'' , is given by (Henry's law):

$$c'' = k_5p'' \quad (9.7)$$

where k_5 is a constant for a given temperature.

Expressing the total amount (gram atoms) of [O] in the tin as \bar{N} , it follows that

$$\frac{d\bar{N}}{dt} = V k_4 k_5 p'' + \frac{i}{nF} \quad (9.8)$$

Applying Fick's first law to the diffusion of [O] to the interface (\bar{J} negative) (Figure 9.6):

$$\bar{J} = -\bar{D}A \frac{d\bar{c}}{dx} \quad (9.9)$$

\bar{D} , A and $\frac{d\bar{c}}{dx}$ have their usual significance.

So (9.9) becomes:

$$\bar{J} = -\bar{D}A \left(\frac{\bar{c} - \bar{c}^{**}}{\delta} \right) \quad (9.10)$$

Concentration \bar{c}^{**} is defined as the equilibrium concentration of [O] at potential E , the potential at which the tin electrode is held (typically -1.1 V vs. air electrode in this case).

Equating the current with the flux via Faraday's law:

$$\bar{J} = \frac{i}{nF} \quad (9.11)$$

Eliminating \bar{J} between (9.10) and (9.11):

$$i = \frac{nF\bar{D}A}{\delta} (\bar{c}^{**} - \bar{c}) \quad (9.12)$$

Or

$$i = k_3 (\bar{c}^{**} - \bar{c}) \quad (9.13)$$

where k_3 is given by

$$k_3 = \frac{nF\bar{D}A}{\delta} \quad (9.14)$$

In the steady-state situation, when $p'' = p_2''$, $\bar{c} = \bar{c}_2$, $i = i_2$ and $\frac{d\bar{N}}{dt} = 0$, then using (9.8)

$$i_2 = -VnFk_4k_5p_2'' \quad (9.15)$$

This shows that steady current is directly proportional to the partial pressure of water vapour (as found experimentally and with negative slope, Figure 9.3).

The model is now developed to obtain an expression for the transient behaviour (changing from p_1'' to p_2''). The mathematics is simplified by defining a new variable, \bar{c} , where

$$\bar{c} = \bar{c}^{**} - \bar{c} \quad (9.16)$$

So Equation (9.13) becomes

$$i = k_3 \bar{c} \quad (9.17)$$

When $p'' = p_2''$, $i = i_2$ and Equation (9.17) becomes:

$$i_2 = k_3 \bar{c}_2 \quad (9.18)$$

Eliminating i_2 between (9.15) and (9.18):

$$\bar{c}_2 = -\frac{-VnFk_4k_5p_2''}{k_3} \quad (9.19)$$

And similarly:

$$\bar{c}_1 = -\frac{-VnFk_4k_5p_1''}{k_3} \quad (9.20)$$

Note that $\frac{d\bar{c}}{dx} = -\frac{d\bar{c}}{dx}; \frac{d\bar{c}}{dt} = -\frac{d\bar{c}}{dt}$.

Recalling that

$$\frac{d\bar{c}}{dt} = \frac{1}{V} \frac{d\bar{N}}{dt} \quad (9.21)$$

So

$$\frac{d\bar{c}}{dt} = -\frac{1}{V} \frac{d\bar{N}}{dt} \quad (9.22)$$

Using Equation (9.8) with $p'' = p_2''$, with (9.19), (9.17) and (9.22):

$$-V \frac{d\bar{c}}{dt} = -\frac{k_3\bar{c}_2}{nF} + \frac{k_3\bar{c}}{nF}$$

$$\frac{d\bar{c}}{dt} = \frac{k_3}{VnF} (\bar{c}_2 - \bar{c}) \quad (9.23)$$

Separating the variables and integrating:

$$-\int_{\bar{c}_1}^{\bar{c}} \frac{d\bar{c}}{\bar{c} - \bar{c}_2} = \frac{k_3}{VnF} \int_{t_1}^t dt$$

$$\ln[\bar{c} - \bar{c}_2]_{\bar{c}_1}^{\bar{c}} = \frac{k_3}{VnF} (t - t_1)$$

$$\ln \frac{\bar{c} - \bar{c}_2}{\bar{c}_1 - \bar{c}_2} = \frac{k_3}{VnF} (t - t_1) \quad (9.24)$$

Using (9.17)

$$\ln \frac{i - i_2}{i_1 - i_2} = \frac{k_3}{VnF} (t - t_1) \quad (9.25)$$

This is the required equation.

9.3.4. Experimental validation of the model on water reduction in LMA SOFC

The electrochemical mode developed for water reduction in LMA SOFC was validated against the experimental data.

Application of Equation (9.25) derived for reduction of water on the experimental data for water dissociation and cathodic reduction of oxygen at -1.1 V vs. RE at 810 °C (the reverse process of hydrogen oxidation) (shown in Figure 9.2) resulted in reasonable straight lines ($R^2_{\text{average}} > 0.94$) (Figure 9.7-Figure 9.8). Note that the R-squared value is a measure of the goodness of fit of the data to a straight line. The standard error of the slope is $5 \times 10^{-5} \text{ s}^{-1}$. The analysis was applied only to the smoothest parts of the current-time curve, as the remainder of the current-time curve was excessively noisy. The slopes obtained in Figure 9.7- Figure 9.8 are summarised in Table 9.3.

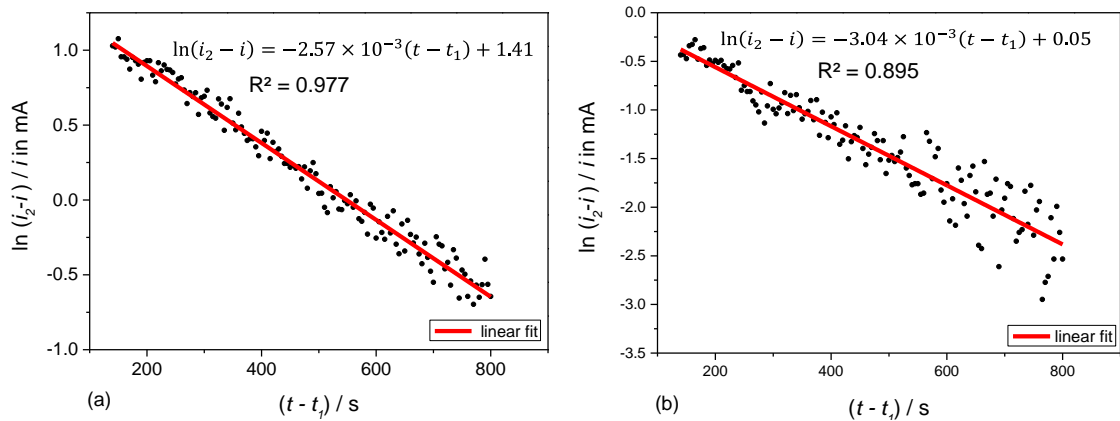


Figure 9.7 Step change in $p(\text{H}_2\text{O})$: from 3.78(28 °C) to 0.61(0 °C) kPa (a); from 0.61kPa (0 °C) to zero (dry Ar) (b).

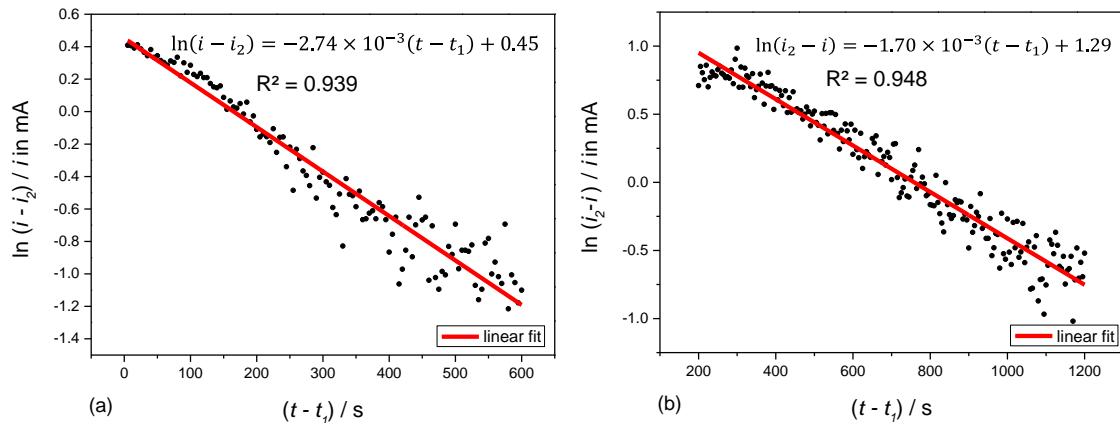


Figure 9.8 Step change in $p(\text{H}_2\text{O})$: from zero (dry Ar) to 1.23 kPa (10 °C) (a); from 3.78 kPa (28 °C) to 1.23 kPa (10 °C) (b).

Table 9.3. Reciprocal time constants for various destination $p(\text{H}_2\text{O})$ values.

$p(\text{H}_2\text{O})/ \text{kPa}$	0	0.6	1.2
Slope / 10^{-3} s^{-1}	3.04	2.57	2.74
Average slope / 10^{-3} s^{-1}			1.70
Time constant / s	329	389	503

The theory developed for H₂O reduction is similar to the one for H₂ oxidation where reciprocal time constant was shown as $\frac{k_3}{VnF\bar{z}_2}$ vs. $\frac{k_3}{VnF}$ (see Equation (9.25)). So the same time constant ($\bar{z}_2=1$) should be found for hydrogen oxidation and water reduction. However, for the limited and noisy data available, the time constant for water reduction was found to be significantly lower than that for hydrogen oxidation (compare data in Table 7.1 and Table 9.3). The experiment was also more difficult to perform with water because a step change in partial pressure of water vapour was not straightforward.

In the present study, liquid metal cathode was applied for electrolysis of water and on the anode side (Pt solid electrode) molecular oxygen was generated. This process can be combined with the approach proposed by Pati *et al.*⁵³ and hence both cathode and anode will be liquid metals. In that case the energy requirements for water electrolysis should reduce, while the liquid metal anode can operate with various carbonaceous fuels (even contaminated) and generate CO. Then the overall reaction for such system would be:



where R – is the carbonaceous fuel (reductant),

If for instance solid carbon is utilised on the anode side, then the system generates H₂ and CO. In line with stability and deterioration concerns of solid anodes (e.g. Ni-YSZ) with hydrocarbons, the suggested system provides an interesting alternative to common solid oxides steam electrolyzers. However, more research is required to understand the performance of liquid metal electrodes for both anodic and cathodic reactions.

9.4. Conclusion

Studies of the electrolysis of water in a reverse SOFC with liquid tin anode were carried out. The tin electrode was operated at -1.1 V versus air electrode. Water vapour pressure, $p(H_2O)$, has been varied using the water bottles and water bath where the temperature of water had been adjusted. It was shown that it is preferable to set the temperature of the water bath to a value below room temperature, where the lines are unheated. This resulted in reasonably smooth current – time curves. Steady cathodic currents were proportional to water vapour pressure, $p(H_2O)$ for the limited range investigated.

An electrochemical model for water reduction (the reverse of that shown to be applicable to hydrogen oxidation) was developed as a theoretical framework for interpretation of experimental data. Rapid dissolution of water in the liquid tin anode followed by rate-determining dissociation to hydrogen and oxygen followed by diffusion-controlled cathodic reduction of oxygen has been demonstrated as the likely mechanism for water reduction in a reverse LMA SOFC.

Application of the model resulted in shorter time constants for cathodic reduction of oxygen at the liquid tin / YSZ interface compared with ones for oxygen injection during hydrogen oxidation reported in Chapter 7.

Water reduction in Regime 1 resulted in Q_t values (the total charge for reduction of dissolved oxygen due to its accumulation in tin from water reduction) that increased directly proportionally with OC periods, which was expected. There was an important and significant correlation between the rate of oxygen accumulation in the tin on open-circuit due to dissociation of water vapour and the steady current measured on closed-circuit at equilibrium.

10. Rotating Electrolyte Disc system design and testing

Experimental and modelling work presented in the previous Chapters 7-9 has clarified the behaviour of the oxygen-hydrogen/water-tin system in the ‘inert window’ and provided a firm basis for proceeding with studies via the Rotating Electrolyte Disc (RED) technique being developed specifically to examine the mass-transport and kinetics processes within the liquid metal electrode.

This chapter includes the rationale for a novel rotating electrolyte disc (RED) technique, an inverted system based on standard rotating disc electrode (RDE) theory, to study various transport and kinetic processes within liquid metal electrodes in the LMA SOFC. The chapter provides details of the evolution of developed RED designs. Experimental validation of the engineering aspects of the RED apparatus was made in an aqueous system. The results obtained confirmed that the first prototype RED apparatus was built correctly and performance similar to conventional commercial RDE set-ups was achieved. Testing of the RED in molten tin anode is anticipated. Model systems that were explored in Chapters 7-9 are now proposed to be tested with the RED.

10.1. Introduction

With respect to uncertainties in performance of liquid metal anode SOFCs reported earlier (Section 2.3.5), greater understanding of electrochemical reactions, redox, and transport processes within liquid metal electrodes is needed. There are a number of research challenges, including: mass transport of dissolved oxygen (and other gases) or oxidized species in the liquid metal; reaction kinetics between metal oxide and fuel within the liquid anode; kinetics of oxygen transfer at the liquid metal anode - electrolyte interface, etc.

The mechanism and kinetic characteristics of solid electrode reactions with solution phase electroactive species is typically derived via application of the well-established rotating disc electrode (RDE) technique^{99,164,165}. The robust theory of the RDE has been extensively utilised for aqueous electrochemical systems¹⁰⁸. However, its application to examine the mechanisms of operation of SOFCs with LME has not been previously reported.

A novel technique that is based on standard RDE theory has been developed in this study to address research questions on transport and kinetics of electrochemical reactions within the liquid metal electrode. In the proposed design, a solid electrolyte disc rotates in a liquid metal electrode (e.g. tin), as opposed to a solid electrode disc rotating in a liquid electrolyte. This underlying operating principle makes the proposed concept novel and unique. To reflect that feature the technique is termed “Rotating Electrolyte Disc”.

The RED is designed to determine parameters controlling mass transport of dissolved oxygen (and other gases) and oxidised species, including metal oxide in the liquid metal; the technique also provides the possibility of the investigation of heterogeneous and homogeneous reaction kinetics as well as the influence of electrode contaminants. Investigation of anodic reaction kinetics can provide additional options to optimize conventional tubular design of LME SOFCs and in turn contribute to further improvement of fuel cell performance. The application of the RED in LMA SOFCs involves operation with molten metal above 700 °C, as opposed to aqueous electrolyte at ambient temperature, which is interesting and challenging at the same time.

This chapter presents the development and construction of the rotating electrolyte disc (RED) apparatus to be tested in LMA SOFCs. In order to see if the proposed RED design performed satisfactory from a hydrodynamic point of view, the engineering aspects of the RED were tested in an aqueous electrochemical system. Operation in this conventional RDE mode represents an important step towards the final system. A model system where the RED can be applied is proposed.

10.1.1. Background to application of RDE technique

Since the solution of the convective diffusion equations of electroactive species to the surface of rotating disc electrode by Levich in 1942^{165,166}, the application of the RDE technique gained much interest and was applied in various fields of electrochemistry¹⁶⁷. So far, the RDE remains the most favoured method for investigation of kinetics and mechanisms of electrode processes due to its simplicity, high accuracy along with rigorous theory¹⁰⁸. It is advantageous over other methods as it allows the study of electrochemical reactions at higher rates and wider potential range.

Typical configuration of RDE consists of a disc electrode of interest – Pt, Au, glassy carbon, etc. shielded in a cylinder of insulating material (e.g. Teflon)¹⁶⁸ as shown in Figure 10.1a. Electrical connection to the electrode is typically achieved via a silver-carbon brush spring-loaded to the surface of a steel shaft. A bearing block is used to minimize vibrations upon rotation. A further development of the RDE resulted in the rotating ring-disc electrode (RRDE). In the RRDE a disc electrode is surrounded with a conducting ring, whereby the ring is electrically isolated from the disc via an insulator (Figure 10.1b) and operated at a different potential. Reaction products are transported in the liquid flow from disc to ring where they undergo electrochemical reaction. The RRDE is particularly useful for separation and analysis of intermediates of a multistage electrochemical reaction, for instance in organic electrochemistry¹⁰⁸. The collection efficiency of the RRDE, is the fraction of intermediate formed at the disc that is collected at the ring, and was a term introduced by Albery and Brett^{169,170}.

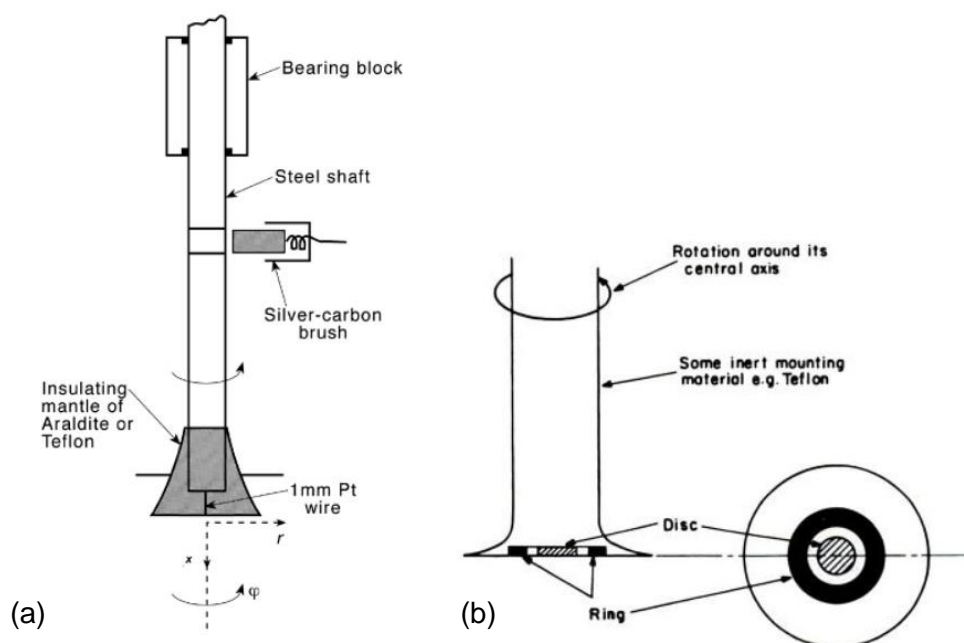


Figure 10.1 (a) Schematic of a rotating disc electrode of the classical Riddiford design where the electrode is a platinum wire of 1 to 3 mm radius¹⁶⁸; (b) schematic of rotating ring-disc electrode¹⁷¹ (the broken arrow indicates the electrolyte-flow lines induced by rotation).

The RDE and RRDE have been widely applied to study diffusion, reaction kinetics, volume reaction kinetics, etc. Diffusion studies involved determination of diffusion coefficients for a wide range of molecules and ions in various media, e.g. diffusion of Ag^+ ions¹⁷², ferri- and ferrocyanide species in polymers¹⁷³. Many studies explored the diffusion in molten salt systems^{174–177} using RDE. The practicality of the RDE technique was shown not only in the field of analytical electrochemistry, but also in corrosion studies¹⁷⁸, development of PEM fuel cells catalyst^{179–182}, biochemistry¹⁸³, neuroscience¹⁸⁴, etc.

10.2. Development of the RED set-up

The RDE method has been developed and applied widely in aqueous electrochemical systems. The theoretical principles of the RDE technique were given in Section 3.4.4.

10.2.1. Requirements for operating conditions

For construction of the experimental set-up that conforms to the RDE theory the following conditions should be met¹⁰⁸:

- Laminar flow conditions: for a given disc radius, a laminar flow can be maintained at certain rotation speed. Transition from laminar to turbulent flow is assumed¹⁰⁸ to occur if the Reynolds number (Re) is within the range of 1.5×10^5 and 3.1×10^5 . At higher Re numbers, the flow is turbulent. Vibration and surface roughness of the electrode may also cause turbulence in the flow¹⁰⁸. Hence, the shape of the insulator should be chosen carefully, as it may affect the flow of liquid in proximity to the disc perimeter. Riddiford and Blurton¹⁶⁵ showed that the optimum shapes for RDE (to prevent turbulence in proximity of the disc perimeter) are concave, conic and simple cylindrical shapes.
- Suppression of migration and ohmic drop in solution: analyte concentration should be significantly lower than total electrolyte concentration; this would increase ionic conductivity and the diffusion of active species would be constant.
- Choice of optimal electrode size and cell volume: the theory for RDE was derived assuming infinite plane rotating in semi-infinite volume of liquid. In practice, both are limited in dimensions and hence the optimum disc radius, rotation speed and the cell volume should be chosen.
- The effect from mechanical defects: vibration, eccentricity and surface roughness of the rotating electrode should be monitored though their effect on the mass transport is considered small¹⁰⁸.

10.2.2. Evolution of the designs for the RED setup

This section presents the evolution of designs developed to build the RED setup for measurements in LME SOFC.

In aqueous RDE studies the electrode disc is normally metal, which is held within a non-conductive sheath, often PTFE (Figure 10.1a). In the present system, the sheath is substituted by solid electrolyte, i.e. 8YSZ. To encompass this feature, and also to meet hydrodynamic and thermal requirements for operation of RED in molten metal, the first design (Design 1) proposed was as shown in Figure 10.2.

The design envisaged the use of a so-called 'YSZ sheath' that was made of layers of green 8YSZ tape (Viking Chemicals, Follenslev, Denmark). The 8YSZ rings (20 mm × 10 mm) cut from the tape were hydrated with distilled water to induce a 'sticky' consistency, layered vertically, dried at room temperature, and sintered at 1400 °C for two hours. However, a zirconia sheath made in this way tended to buckle and distort upon firing and as a result, this preparation process was not pursued further.

Other components essential to the operation of the overall system under the hydrodynamic control regime, while maintaining high temperature, are demonstrated in Figure 10.2. The RED setup is designed to be operated vertically inside an electrical furnace. The rotating tube (alumina tube) is attached to a motor (not shown) by a gear wheel and is rotated over a range of frequencies. Electrical connection to the Pt electrode (located on the inner side of the electrolyte disc) is made via a carbon brush (that is in constant contact with a brass collar). Roller bearings are proposed to minimise vibration of the rotating tube at high rotation rates, provided that the rotating shaft is long enough to keep the roller bearings away from the hot zone. The use of roller bearings could lead to difficulties in sealing the system. The supply of argon is proposed to solve this by flushing the system continuously and so removing any residual oxygen. In addition, electrochemical extraction of oxygen from the melt is suggested via an external porous platinum electrode on the outer surface of the YSZ tube (closed at one end) containing the tin.

The major disadvantages of Design 1 were:

- roller bearings impose problems with oxygen leakage into the system;
- the long rotating shaft with unbalanced sheath may cause vibration/bending of the rotating tube at high rotation rates.

In Design 1, the centre of gravity of the sheath and rotating tube will inevitably not lie on the axis of rotation and on spinning will cause the tube to 'flap about', and so disturb the hydrodynamic flow pattern across the base of the disc. The effect is worsened upon

- the rotating tube can be made as long as needed and thereby keep the upper parts of the system relatively cool;
- replacement of the sheath by a thin YSZ disc with flat surface minimizes the unbalancing effect on the rotating tube and also improves the flatness of the surface and uniformity of the thickness of disc.

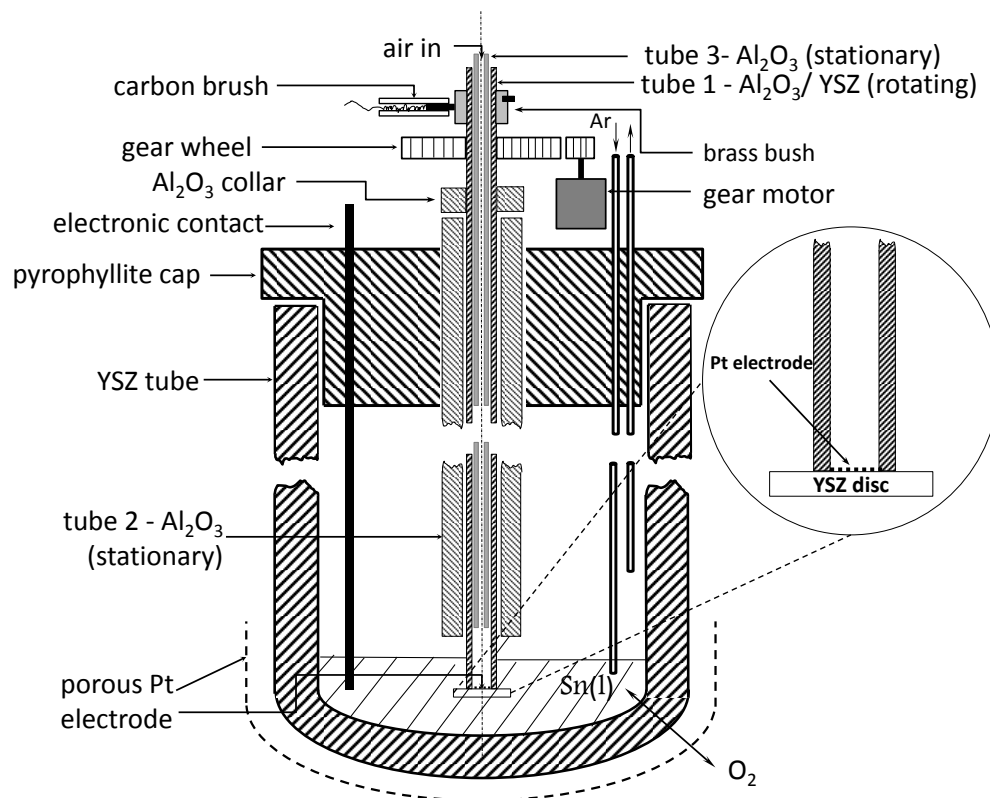


Figure 10.3 The improved design of RED - Design 2.

10.3. The RED modified for aqueous electrochemical systems

To confirm that the developed RED design (see Figure 10.3) would provide results that are in good agreement with standard RDE theory, an RED setup was tested in aqueous systems. The operation in such systems is fairly straightforward, as experiments can be done at ambient temperature; this simplifies the original design in many aspects mentioned below.

10.3.1. Construction of the RED setup for aqueous systems

In order to demonstrate the validity of the concept and design for high temperature studies, the RED setup was firstly tested using an aqueous system at ambient temperature. Therefore the design shown in Figure 10.3 was simplified to convert the RED prototype to

one usable for aqueous systems (see Figure 10.4). The rig consists of one rotating alumina tube with a disc electrode at the bottom, one stationary (alumina) tube, small gear motor and gear wheel, carbon brush, and a brass bush.

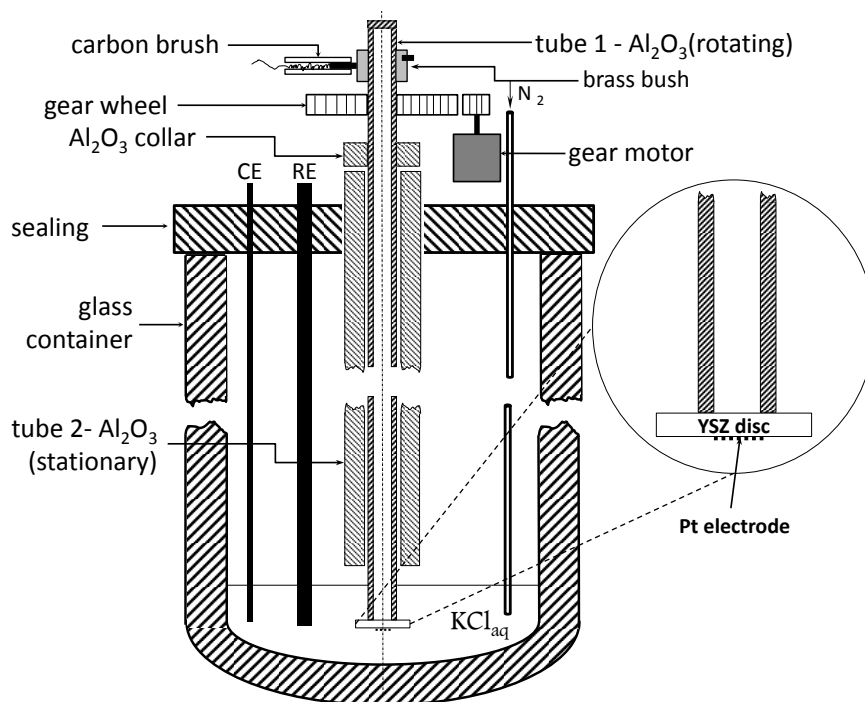


Figure 10.4 Design for simplified RED setup in aqueous systems.

The construction was made through the steps described below. The electrode was made with platinum ink coated onto a 20 mm diameter 8YSZ disc (Fuel Cell Components, USA). In order to ensure a continuous electrical connection to the rotating electrode, the Pt ink was applied to both surfaces of the disc and on the edge (see Figure 10.5).

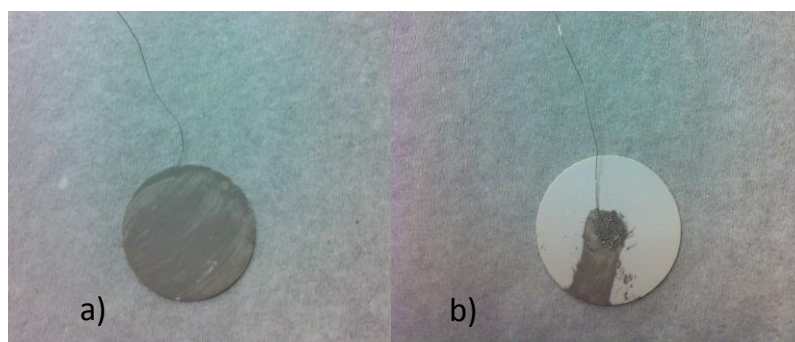


Figure 10.5 The outer side of YSZ disc painted with Pt ink (a) and inner side (b) where Pt mesh and wire are attached.

Electrical contact to one side of the electrode was made with platinum wire (0.25 mm dia., 99.9% Pt, Peak Sensors Ltd) of 4 cm long and platinum mesh attached to the YSZ disc with platinum ink. Subsequently the electrode disc was sintered at 1000 °C for 1 hour, ramping up and down at 1°C per minute. A second Pt wire (25 cm long) ran inside the

rotating tube and out through the top to the bush, where it was fixed with a grub screw. The free end of the second wire was twisted together with the wire attached to the YSZ disc (as explained earlier). At every stage of processing, continuous electrical connection was checked with a laboratory multimeter. The connection from the bush was made using a spring-loaded carbon brush and from there to the potentiostat.

The brass bush (a good sliding fit with the rotating tube) was made in-house (Department of Chemical Engineering Workshop). The metal bush, PTFE washer and alumina collar were glued to the top of rotating tube using Rapid Araldite adhesive (RS Components, UK), while the electrode disc was similarly affixed to the bottom. The Araldite adhesive was made by mixing epoxy and hardener in equal amounts and it set (cured) at room temperature in approximately one hour. The PTFE washer was used as lubricant to reduce any friction between the two alumina tubes, whereas the alumina collar was used to define/fix the operating position of the rotating tube within the stationary tube.

For good operation of the rig, care was taken to ensure that the plane of the gear wheel and of the zirconia/ platinum disc were perpendicular to the axis of rotation. This was particularly important regarding the disc as otherwise the ideal hydrodynamic conditions considered in the Levich theory were no longer fulfilled. This was confirmed by slowly rotating the inner tube manually, a visual observation providing a precise check on the correct alignment of components.

An active electrode disc was prepared as follows. Firstly the alumina tube was rotated through a complete revolution while using a stationary marker to touch the electrode; this defined a circle (8 mm diameter) chosen to be slightly larger than the required electrode (6 mm diameter). A disc of 6 mm diameter was punched from electrical insulating tape and stuck centrally within the drawn circle. The whole disc was then coated using a PTFE spray (RS Components, UK). The disc of insulating tape was then removed leaving the precisely-defined active circular disc electrode for carrying out the electrochemical tests. Being hydrophobic the PTFE isolated all surfaces except the exposed 6 mm diameter electrode. The setup as described above is shown in Figure 10.6.

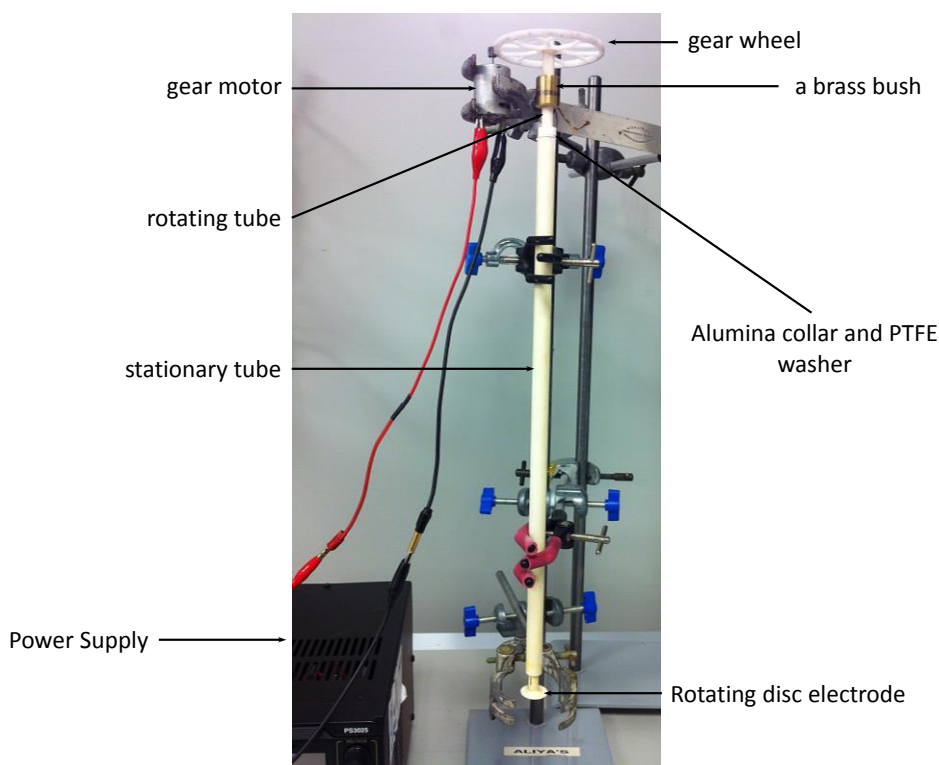


Figure 10.6 The prepared RED setup for aqueous electrochemical testing.

Besides the working electrode which is the rotating disc, a counter electrode (Pt mesh and Pt wire), reference electrode (Saturated Calomel Electrode (SCE) with 0.249 V potential vs. SHE with standard electrical connectors to the potentiostat) were applied.

Results from testing the RED set-up with Pt disc electrode in 3 M KCl solution are shown in the next Section. The rotation speed rate was regulated by adjusting the voltage supplied to the gear motor, though the rates of rotation were not measured at that stage.

After several tests the Pt electrode detached from the surface of YSZ disc and so was replaced with an improved arrangement as follows. A flat, 100 μ m thick, 20 mm diameter gold disc was affixed with Rapid Araldite (RS Components, UK) to the underside of the rotating electrolyte disc. To enhance electrical connection to the working electrode (gold disc) conducting Araldite (RS Components, UK) was coated on the rear surface of the gold to make electrical contact to the platinum wire and platinum track. The gold electrode was masked off as described above using a non-conducting paint (nail varnish) except for an 8 mm diameter circular disc of gold (centre aligned with the axis of rotation) which remained exposed and served as the working electrode (Figure 10.7).

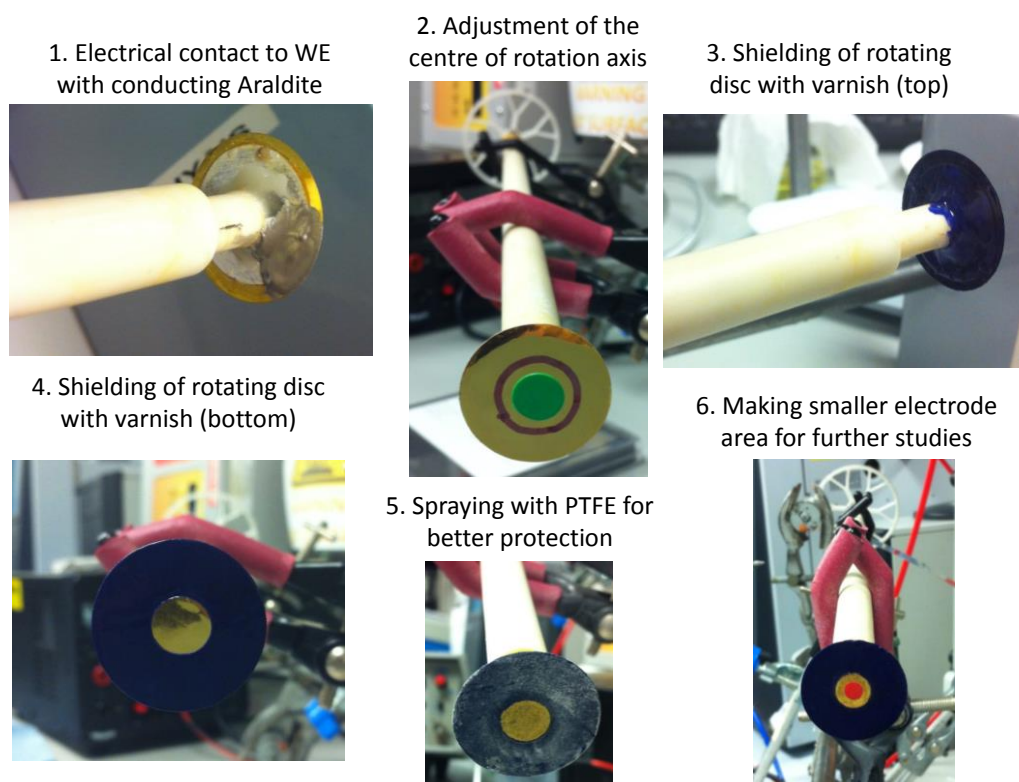


Figure 10.7 Stages in making the gold disc electrode of 8 mm diameter.

Rotation speed measurements were achieved using a 3 mm diameter neodymium disc magnet (RS Components, UK) attached to the bush, Hall effect sensor (2SS52, RS Components, UK) and universal counter timer 9900 (Racal-Dana Instruments Ltd., UK) (Figure 10.8). The readings from the time counter were checked with an oscilloscope and a stroboscope for consistency.

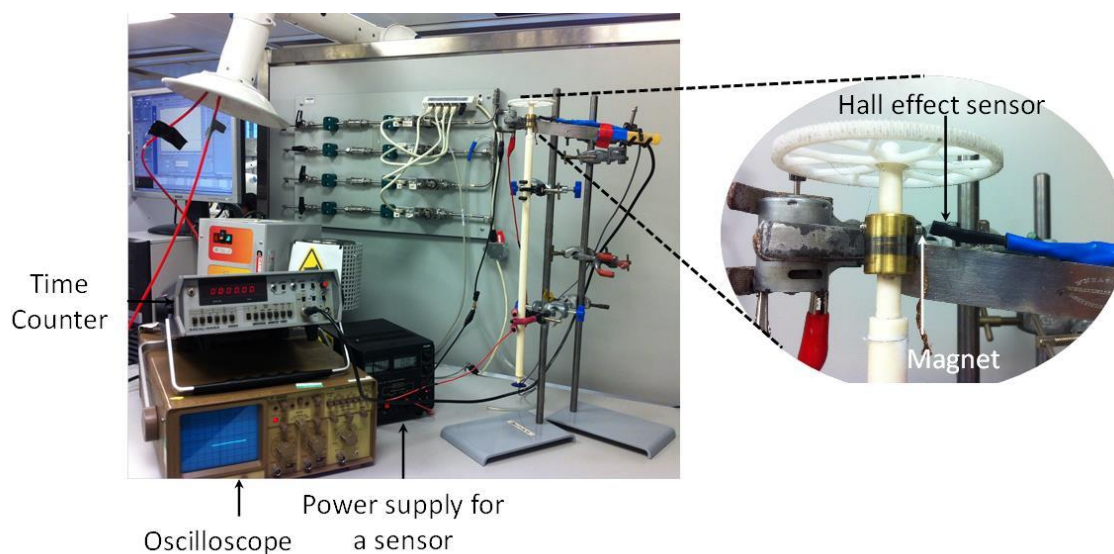


Figure 10.8 Experimental set-up for rotation speed measurement using Hall effect sensor and a time counter

10.3.2. RED measurements in aqueous system

The RED setup was applied to study the mass transfer characteristics of the $\text{Fe}^{3+}/\text{Fe}^{2+}$ redox reaction in solutions of ferrous and ferric chloride of various concentrations in acidified 1 and 3 M KCl medium initially using a platinum and later gold disc electrodes.

An equimolar solution of ferrous and ferric chloride (0.014 M) with 3 M KCl as supporting electrolyte and a platinum disc electrode (WE) on the base of YSZ disc were investigated. Platinum wire and piece of platinum mesh were used as the counter electrode (CE) and a saturated calomel electrode (SCE) was employed as a reference electrode (RE). The potential difference of SCE measured vs. reversible hydrogen electrode (RHE) was measured to be 0.249 V. The area of the platinum working electrode was 0.28 cm^2 .

Note that ferric and ferrous chlorides were chosen as analogues to potassium ferri and ferro cyanides ($\text{K}_3\text{Fe}(\text{CN})_6$ and $\text{K}_4\text{Fe}(\text{CN})_6$) that are typically used in standard RDE measurements¹⁸⁵ but were avoided here due to their hazardous nature. The supporting electrolyte¹⁸⁶ was a solution of 3 M potassium chloride in deionised water, containing 0.014 M of ferric chloride and ferrous chloride. Oxygen in the cell was purged by firstly bubbling nitrogen through the solution and then continuously blanketing the solution with a constant flow of nitrogen throughout the experiment. Rotated disc voltammograms (Figure 10.9) were obtained using various rotation speeds at room temperature. Applying the linear sweep voltammetry technique the potential was swept from -0.4 V up to +1.4 V versus SCE with a scan rate of 10 mV s^{-1} . The system was operated at progressively increasing rotation speeds. The estimated accuracy of currents measurements is $\pm 10\ \mu\text{A}$.

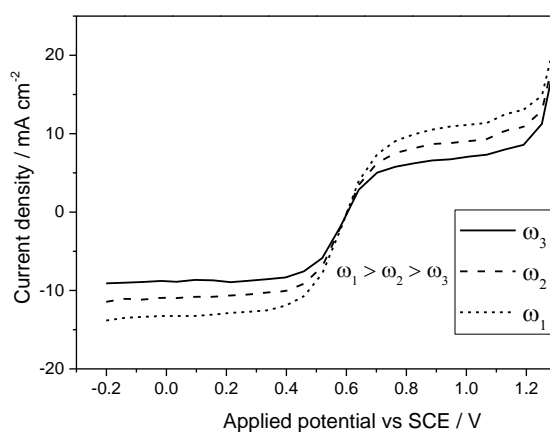


Figure 10.9 LSVs with increasing rotation rate for the ferrous-ferric redox couple using 0.014 M Fe^{2+} / 0.014 M Fe^{3+} in 3M KCl (data obtained via 6 mm Pt disc electrode).

The obtained data (see Figure 10.9) show that the developed design for RED setup conforms to standard RDE behaviour, indicating a limiting current density which increased with rotation speed, ω , in both the anodic and cathodic sweeps. Next, having developed the method for rotation speed measurement, the above experiment was repeated using a

solution of ferrous and ferric chloride in acidified 1 M KCl solution using a gold disc electrode (8 mm diameter) (Figure 10.10). In place of the SCE reference, a dipping platinum wire was used so that potentials were measured versus the equilibrium potential of the ferrous-ferric couple pertaining in each solution. This reference was simple and convenient with no junction potential; it operated most successfully and had the unusual feature that all sweeps showed a zero current at zero applied potential versus the platinum RE.

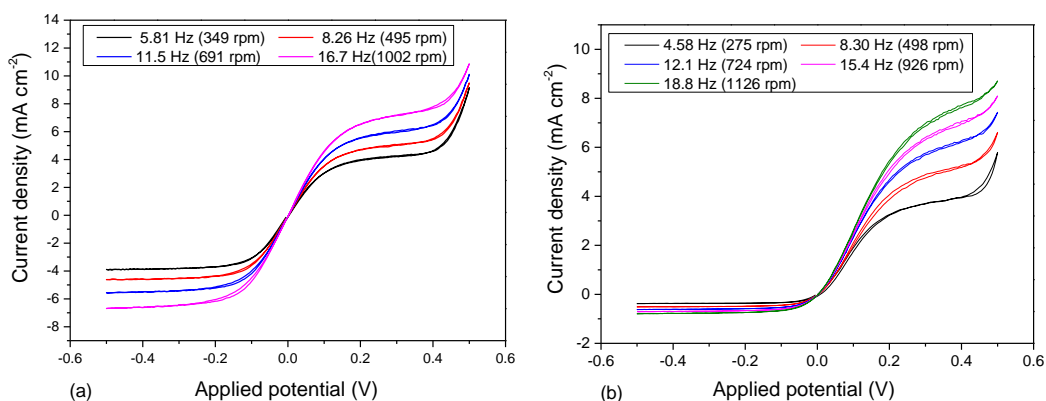


Figure 10.10 Cyclic voltammograms for a range of rotation rates for the ferrous-ferric redox couple using 0.02 M Fe^{2+} / 0.02 M Fe^{3+} (a) and 0.02 M Fe^{2+} / 0.002 M Fe^{3+} in 1M KCl plus 0.01 M HCl (b) (data obtained via 8 mm Au disc electrode). The reference electrode was a dipping platinum wire so that potentials shown were versus the equilibrium potential of the particular ferrous-ferric couple under investigation.

The rapid increase in current at potentials of $\geq +0.4$ V potential in Figure 10.10a indicates the onset of O_2 evolution. Sweeps in the negative-going direction did not reach potentials at which hydrogen is evolved (-0.77 V for equimolar concentrations of Fe^{2+} and Fe^{3+}). Flatter positive-going voltammograms were achieved when the concentration of Fe^{2+} was reduced as shown in Figure 10.11a, b and these data were used for analysis in respect of this ion.

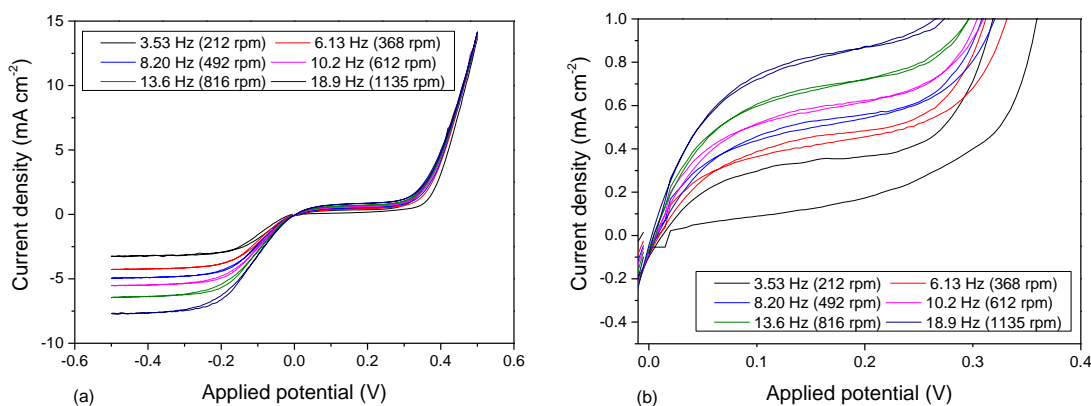


Figure 10.11 Cyclic voltammograms for a range of rotation rates for the ferrous-ferric redox couple using 0.002 M Fe^{2+} / 0.02 M Fe^{3+} in 1M KCl plus 0.01 M HCl (a); expanded view (b) (data obtained via 8 mm Au disc electrode). The reference electrode was as for Figure 10.10.

Diffusion coefficients for Fe^{2+} and Fe^{3+} were determined from Levich plots (Figure 10.12).

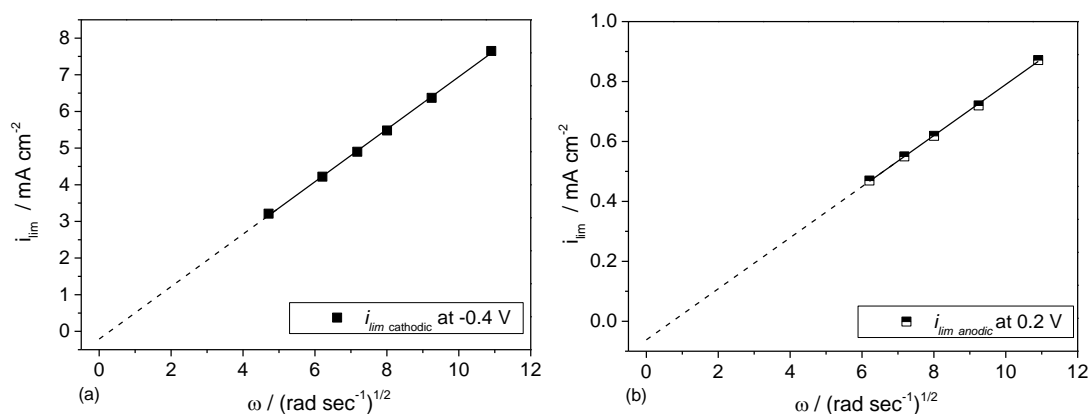


Figure 10.12 Plots of limiting current density for Fe^{3+} reduction (a) and Fe^{2+} oxidation (b) vs. square root of rotation speed.

The diffusion coefficients for Fe^{3+} and Fe^{2+} were calculated from the slopes of the Levich plots to be 4.4×10^{-6} and $5.8 \times 10^{-6} \text{ cm}^2 \text{ s}^{-1}$ respectively, which are similar to those reported by Spiro and Creeth¹⁸⁷(see Table 10.1). The standard error in the diffusion coefficient data is estimated to be $\pm 10\%$. The correlation with literature values is satisfying, though in this work, RDE measurements in aqueous systems were made to validate the apparatus and not to obtain definitive values of the diffusion coefficients.

Table 10.1 Comparison of diffusion coefficients for Fe^{2+} and Fe^{3+} ions with literature.

	UCL ¹³² (present work)	Spiro and Creeth ¹⁸⁷
$D(\text{Fe}^{3+})/10^{-6} \text{ (cm}^2 \text{ s}^{-1})$	4.45	4.86
$D(\text{Fe}^{2+})/10^{-6} \text{ (cm}^2 \text{ s}^{-1})$	5.81	5.78
Medium (mol dm^{-3})	1 M KCl, 0.01 M HCl	0.05 M HClO_4

10.4. Application of RED to LME SOFCs

10.4.1. Construction of RED for LME SOFCs

Construction of RED setup for high temperatures was based on the design shown in Figure 10.3 (Design 2) and the previous setup for aqueous systems (Figure 10.6). Some parts used in the RED for aqueous study were replaced by thermally stable materials. As such, the disc at the bottom could not be glued with epoxy resin (stable up to 200 °C) and was replaced by high temperature ceramic cement (Ceramabond 552, Aremco Products, USA).

Electrical connection to the rotating electrode was complicated by the third alumina tube (tube 3, Figure 10.3) placed inside the rotating tube for supply of air to electrode surface. If the Pt wire were to run all the way through the inside of the rotating tube (tube 2, Figure 10.3) as in the case of RED for the aqueous system, the wire would also rotate and as a result would wrap around the stationary central tube causing it to break.

To avoid this it was decided to engineer a platinum track on the outer side of rotating tube; Pt ink was painted along and inside a groove in the alumina tube which was cut with a diamond tipped drill. Connection from the bottom disc to the track was made with Pt wire. Electrical connection at the top (to a brass bush) was made by fixing one end of Pt wire to the Pt track and other end to the bush. Connection of the wire to the track at the top of the tube was made with conducting adhesive (silver loaded Araldite, RS Components, UK). The constructed RED set-up based on Design 2 for LME SOFC is shown in Figure 10.13(a). Once assembled the RED apparatus was used in a LMA SOFC cell at 770 °C as shown in Figure 10.13 (b).

Testing of the RED in LMA SOFC resulted in several problems that were due to constraints in the size of furnace and poor sealing of the electrolyte disc to the bottom of the rotating tube. From one aspect, the furnace used in the first instance enabled the application of relatively small (19 mm outer diameter) and hence less expensive YSZ tube that contained the RED immersed into liquid tin (Figure 10.3). However, from the other aspect, the small size of the furnace gave very little flexibility and generated unfavourable conditions of liquid flow around the disc, which upon rotation may lead to formation of vortices that may introduce distortion to the liquid flow^{108,109,186}. Once tin was molten, the RED was inserted inside the YSZ tube, which caused cracking of the latter due to thermal shock. In addition, gas tight sealing of the YSZ disc at the bottom of rotating alumina tube was not achieved. This was probably due to mismatch of thermal expansion coefficients between 8YSZ ($11 \times 10^{-6}/\text{ }^\circ\text{C}$) and alumina ($8.4 \times 10^{-6}/\text{ }^\circ\text{C}$), which resulted in a porous seal.

To resolve practical challenges, a larger furnace was purchased and this has opened up new possibilities in designing the latest system. The new design aimed to address disadvantages from Design 2 and also to take into account technical problems arisen from initial testing of RED in LMA SOFC.



Figure 10.13 The ready RED set-up in operation of LME SOFCs.

10.4.2. Final design for RED for LME SOFCs

The latest design (Design 3) is shown Figure 10.14 and its rationale in comparison with Design 2 (Figure 10.3) is summarised as follows.

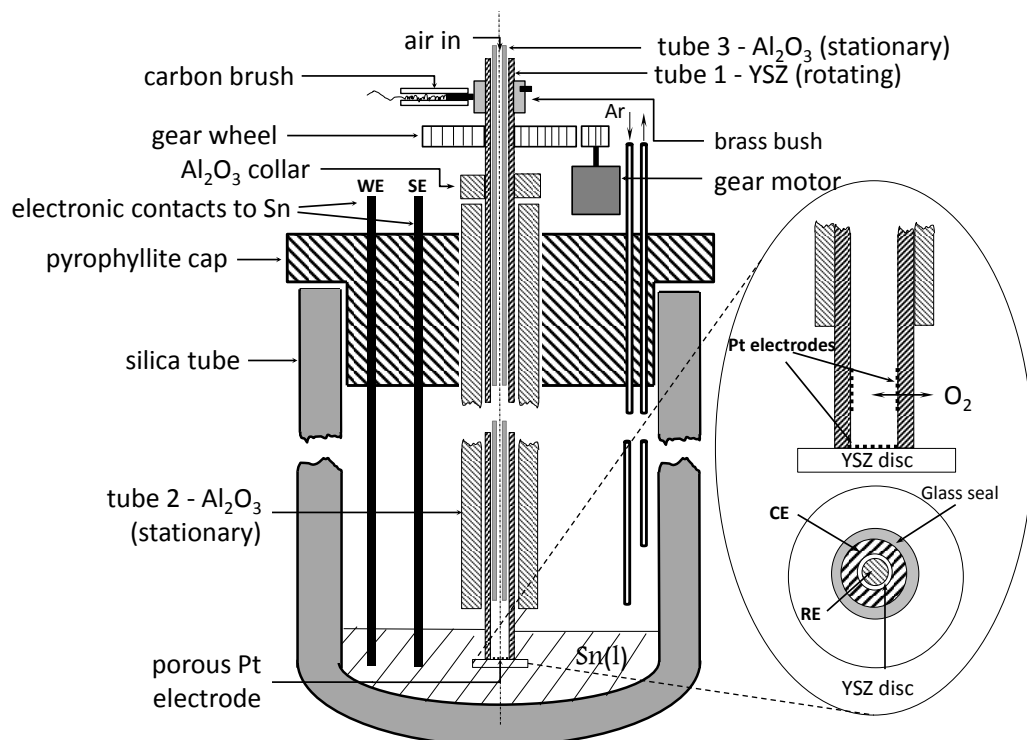


Figure 10.14 The latest design of RED - Design 3.

Application of a larger furnace allowed the use of a larger container (silica instead of zirconia having an advantage in terms of cost) for tin and the RED minimising edge effects regarding the hydrodynamics, as well as turbulence of the flow.

The second major change in Design 3 was replacement of the rotating tube material from alumina to YSZ in order to eliminate thermal expansion difference of the two components (tube and disc) and should prevent breakage of the seal. A glass-ceramic sealant has been sourced to replace the ceramic cement, which may improve the sealing and resolve the sealing problem.

The possibility to pump oxygen in/out of tin is proposed via application of the same YSZ rotating tube to avoid use of an extra YSZ tube that would have been immersed into the liquid metal for pumping of oxygen into and out of the tin.

Another important improvement of the latest design is the placement of the reference electrode within the WE disc. Also, a second electronic contact to tin is proposed to be used for sensing the electrode connections. This will eliminate any ohmic drop in the current collector that is in contact with the tin.

Electrical connections from the electrodes coated on the inner side of the rotating YSZ tube (for oxygen pump) and from the YSZ discs (from CE and RE) require four brass bushes and four carbon brushes that are electrically isolated from each other. Note that the glass-ceramic seal employed between the YSZ disc and YSZ tube will totally isolate pumping and working electrodes from each other. Work is underway to construct the RED apparatus based upon Design 3.

10.4.3. Electrochemical system for RED studies

It is suggested that the assembled RED system should be tested in the following system to explore mass-transport and kinetics processes within the liquid tin anode SOFC:

(Working Electrode) $(\text{H}_2)/\text{Ar}$, $[\text{O}]_{\text{Sn}}$ | LMA | YSZ, Pt, air (Counter Electrode)

Following the latest design of RED, the potential applied via the pumping electrode sets the concentration of dissolved oxygen, $[\text{O}]_{\text{Sn}}$, in tin. Counter and reference electrodes (Pt air electrodes) are painted on the inner surface of the rotating electrolyte disc in accordance with the latest design.

Oxygen is pumped in/out of the system to maintain the concentration of oxygen in tin at a fixed value and below the solubility limit, and so prevent oxidation of liquid tin to tin oxide or dioxide in the bulk. This is achieved by using rotating YSZ tube as oxygen pump with Pt electrode painted on its inner side and liquid tin electrode on its outside (Design 3; Figure

10.14). For similar reasons, argon will be blown into the silica container to keep the O₂ level very low.

Having examined oxidation of H₂ and water dissociation in LMA SOFCs (see Chapters 7-9), the assembled RED set-up is intended to investigate kinetics and mass-transport of either anodic injection of oxygen (as part of oxidation of H₂ in LTA SOFC) or cathodic oxygen reduction (in case of water dissociation) reactions as shown in Equation (10.1).



It is planned to operate the system in a narrow potential window whereby formation of tin oxide is eliminated (mode **CE**). The measurement of the diffusion coefficient of dissolved oxygen is anticipated. The determination is important as it will be obtained via a direct method rather than an indirect one as applied by Abernathy *et al.*⁶

10.5. Conclusion

A novel rotating electrolyte disc (RED) has been proposed as an inverted Rotating Disc Electrode (RDE) technique where a solid electrolyte disc rotates in a liquid electrode, as opposed to a solid electrode rotating in a liquid electrolyte. This unique apparatus is being developed for examination of transport properties and mechanisms within the liquid metal anode. The oxidation of hydrogen and/or electrolysis of water observed in LMA SOFC are proposed for examination via RED. In particular, the anodic injection of oxygen and cathodic extraction/ reduction of oxygen are two reactions to be quantified by applying RDE theory.

Prior to construction of the RED apparatus, various designs were suggested and progressively improved. Once the finalised design for RED was proposed, the engineering aspects of RED were tested in a simple aqueous system. For that, a modified version of RED was built and tested in an electrochemical system with ferrous and ferric chloride solutions in KCl electrolyte media. The obtained data show that the developed design conforms to standard RDE behaviour (increasing rotation speed ω increased the observed limiting current density). The diffusion coefficients for Fe³⁺ and Fe²⁺ were calculated from the slopes of the Levich plots to be 4.4×10^{-6} and 5.8×10^{-6} cm² s⁻¹ respectively, which are similar to literature values.

Having been tested in aqueous system, the RED was constructed according to Design 2 and tested in LMA SOFC. Electrochemical data could not be obtained due to technical problems arising from imperfections of Design 2 and also some practical issues, such as poor sealing between the YSZ disc and alumina tube. This and other disadvantages have

been addressed in the latest design of RED. The full details of the final design are outlined, and the construction of the RED in accordance with it is in progress.

11. Conclusion and future work

This thesis presents experimental findings from operation of liquid metal anode solid oxide fuel cells (LMA SOFCs) fuelled with hydrogen in Electrochemical-Chemical (*EC*) and Chemical-Electrochemical (*CE*) modes, as well as on operation of a reverse SOFC with liquid metal electrode for water electrolysis. A novel Rotating Electrolyte Disc (RED) technique is proposed to provide fuller understanding of the fundamental operation of LMA SOFCs. Initial results, including the testing of RED in an aqueous electrochemical system are discussed. This section summarises the main contributions of the obtained results.

11.1. Conclusion

There is growing awareness of the detrimental consequences of carbon dioxide emissions that drives development of environmentally friendly technologies for power generation from fossil fuels. LMA SOFCs offer the possibility of direct and highly efficient electrochemical conversion of solid fuels into electrical energy, with reduced levels of pure CO₂ (not diluted with NO_x gases). As an alternative to conventional power generating technologies, the LMA SOFC fuelled with hydrogen has been considered in this study. The use of hydrogen is considered as a model system for studying this technology to provide a basis for studies involving solid carbon fuel.

This novel type of solid oxide fuel cell with liquid metal electrodes (anodes) has the advantage of greater fuel tolerance, the ability to operate on solid fuel as well as to perform in battery mode in case of temporary fuel starvation. A range of metals have been reviewed including tin, the anode material on which most research has been performed. The key concepts of this technology are discussed along with the open research challenges that need to be addressed for its scale-up and commercialisation. Despite numerous studies, understanding of the reaction kinetics at the liquid metal-fuel and liquid metal-electrolyte interfaces, as well as oxygen diffusivity through the liquid metal layer, needs further systematic investigation.

Electrochemical cells, and a workstation developed for electrochemical characterisation of LMA SOFCs, have been developed and tested and investigation of the ionic conductivity

of the solid electrolyte chosen for this project (yttria-stabilised zirconia) has been made. First, potentiometric measurements using 10 mol.% yttria-stabilised zirconia (10YSZ) symmetrical cells as an oxygen sensor resulted in close agreement between measured and calculated concentration of oxygen for the applied range of gas flow rates. Then a series of linear sweep voltammeteries from -1.0 to 1.0 V for temperature range (500 - 800 °C) yielded current-voltage curves whereby the conductivity for 10YSZ increased progressively up to 800 °C (this included the overpotential on Pt electrodes). Lastly, the precise determination of YSZ ionic conductivity was performed using the Electrochemical Impedance Spectroscopy (EIS) technique. The EIS spectra showed substantial reduction in bulk resistance of electrolyte in agreement with the Arrhenius relationship. Ionic conductivity of 6 mol.% YSZ at 1000 °C was calculated to be $6.58 \times 10^{-2} \text{ S cm}^{-1}$ which was in agreement with reported value of $6.67 \times 10^{-2} \text{ S cm}^{-1}$ for 7.5 mol.% YSZ. These results assisted in evaluating the electrolyte based on mechanical and electrical properties. As a result, the original 6mol.% YSZ electrolyte was replaced with the more conductive 8 mol.% YSZ electrolyte.

Measurements of open circuit potential as a function of temperature for liquid tin anode SOFC (operated in battery mode) resulted in close agreement with thermodynamic predictions. This result confirmed the validity of the workstation and cell components required for testing of LMA SOFCs. Another outcome was the validation of the use of a glassy carbon rod as a current collector from liquid tin, which remained inert and had no alloying/ corrosion issues throughout numerous experiments.

An optimisation of the workstation was performed to investigate and minimise inevitable leak of oxygen into the LMA SOFC system. Experimental work involved the measurement of permeation rates of air (oxygen) through plastic tubing incorporated in the developed experimental rig. The concentration of leaked oxygen was found to be inversely proportional to the gas flow rate. Apart from oxygen that leaked from ambient air, additional pumping of oxygen was made using the YSZ oxygen pump. The amount of pumped oxygen was found to be consistent with Faraday's law, which confirmed reliability and accuracy of the electrochemical oxygen pump. Parasitic ingress of oxygen decreased upon reduction in the length of silicone peroxide tubing and later via its complete replacement with hard nylon tubing. A methodology to account for the effect of oxygen leakage into the fuel cell on the overall current was also developed. It was found that about 57% of the pumped current (translated to oxygen) is attributed to the change in fuel cell reduction current. The developed technique was an important step that allowed the effect

of leaked oxygen to be separated from other processes occurring in the liquid tin anode. This practice was successfully utilised throughout the whole study.

Followed by the experimental optimisation, a classification for the mechanisms for oxidation of gaseous fuel (hydrogen) in liquid metal anode SOFCs depending on the reaction conditions was described in Chapter 6. The proposed mechanisms are suggested to be true for all metal anodes associated with formation of solid metal oxide upon polarisation. Four different modes of operation (and hence mechanisms for oxidation) were identified: direct electrochemical oxidation of fuel gas at the liquid metal anode/ YSZ interface (**E** mode); homogeneous oxidation of fuel in the bulk of the liquid anode by dissolved oxygen, followed by electrochemical injection of oxygen to replace the consumed oxygen (**CE** mode); electrochemical oxidation of liquid metal at the anode/ electrolyte interface, followed by chemical oxidation of fuel by metal oxide in the bulk of the metal (Electrochemical-Chemical mode 1 (**EC1**)); and electrochemical oxidation of liquid metal at a rate significantly higher than metal oxide reduction with fuel, which may lead to the formation of a blocking metal oxide layer (Electrochemical-Chemical mode 2 (**EC2**)). Operation of a liquid tin anode SOFC in the commonly applied **EC** modes was performed. The obtained polarisation curve resulted in a “turning point” on the potential axis, beyond which the current density reduced dramatically and hence the fuel cell performance dropped. The decline in current density was attributed to the formation of a blocking layer of SnO₂ at the liquid tin / electrolyte interface. The findings from the polarisation curve were in agreement with reported studies. This result pointed to the requirement for a study where operation was in a potential region in which there was no formation of tin oxide, which entails **E/ CE** modes as the only possibilities. This enables the elimination of formation of the blocking layer and investigation of significant parameters for fuel oxidation within the liquid metal anode.

The oxidation of hydrogen in LMA SOFCs was examined in Chapter 7. Steady anodic currents were essentially proportional to hydrogen partial pressure and independent of total gas flow rate. Two models were considered for either (i) direct anodic oxidation of dissolved hydrogen (**E** mode) or (ii) homogeneous reaction between dissolved hydrogen and oxygen, followed by anodic injection of oxygen to replace that removed by the chemical reaction (**CE** mode). The former model was rejected as it required the incorporation of the hydrogen / argon fuel gas in the form of a persistent foam which was not detected. The latter model was validated using steady-state and dynamic experimentally-generated data and resulted in the evolution of the parameter \bar{z} . This parameter, termed the dynamic oxygen utilisation coefficient, does not have fundamental

significance but is likely to be of technological importance when designing LMA SOFC reactors. It is shown that \bar{z} parameter is closely related to the Damkohler number which compares the rates of chemical reaction and mass-transfer in the process.

The model for **CE** mode was further validated in Chapter 8. For that, a method termed anodic injection coulometry (AIC) was proposed and developed to determine the parameter \bar{z} , which depends upon geometric (electrode area and volume of tin), mass-transfer (diffusion layer thickness and diffusion coefficient of dissolved oxygen) and kinetic factors in the cell. The LMA SOFC was operated in two regimes, whereby anodic injection of oxygen at the liquid tin / YSZ interface was measured with time at a fixed applied potential (after a specific period of hydrogen dissolution at open circuit). The potential of the liquid tin was chosen to be close (within 10 mV) to the equilibrium potential of the Sn/SnO₂ couple. At this potential the oxygen concentration is expected to be close to the saturated value, as moving to more positive potentials would result in precipitation of SnO₂. Theoretical treatment of the coulombic anodic injection charge from each regime enabled the value of \bar{z} to be determined and was found to 0.83 for hydrogen partial pressure of 16 kPa; it also enabled a measurement of oxygen solubility in liquid tin at 780 °C of 0.10 at.% to be made. The obtained value was found to be similar to literature values. The estimated uncertainty on \bar{z}_2 value is 3.5 % (i.e. $\bar{z}_2 = 0.83 \pm 0.03$).

A novel concept for water (steam) electrolysis using the liquid metal electrode solid oxide system is demonstrated in Chapter 9. It is suggested that water dissolves in the tin whereupon it dissociates into hydrogen (which is carried away in the inert gas stream) and dissolved oxygen in monoatomic form. This increases the dissolved oxygen concentration which drives cathodic oxygen extraction. Initial experimental data showed that measured current-time curves followed an exponential function with time constants slightly higher than ones measured for hydrogen oxidation (followed by anodic injection of oxygen). More experimental and modelling work is required to fully understand the operation of reverse LMA SOFCs for water electrolysis.

The experimental and modelling work presented so far has clarified the behaviour of the oxygen-hydrogen/water tin system in the ‘inert window’ and provided a firm basis for proceeding with studies via the Rotating Electrolyte Disc (RED).

The final part of this study presents the development of a novel Rotating Electrolyte Disc (RED) technique for determination of parameters controlling mass transport of dissolved oxygen (and /or other gases) and oxidised species including metal oxide in the liquid metal; the technique also provides the possibility for investigation of heterogeneous and homogeneous reaction kinetics, as well as the influence of electrode contaminants. In the

proposed design, a solid electrolyte disc rotates in a liquid metal electrode (e.g. tin), as opposed to a solid electrode disc rotating in a liquid electrolyte, making this concept unique. Evolution of designs for novel RED apparatus and construction for high temperature studies is presented. In order to demonstrate the validity of the concept and design for high temperature systems, the engineering aspects of the RED apparatus were tested in an aqueous electrochemical system (equimolar solution of ferrous and ferric chloride with KCl as supporting electrolyte and a gold disc electrode on the base of the zirconia disc). The obtained data show that the developed design conforms to standard RDE behaviour (increasing rotation speed ω increased the observed limiting current density).

The diffusion coefficients for Fe^{3+} and Fe^{2+} as calculated from the slopes of the Levich plots were found to be 4.4×10^{-6} and $5.8 \times 10^{-6} \text{ cm}^2 \text{ s}^{-1}$ respectively, which are similar to those reported in the literature. The standard error in the diffusion coefficient data is estimated to be $\pm 10\%$. The model system for application of RED for investigation of LME SOFCs has been discussed.

11.2. Recommendations for future work

This project has been aimed at understanding the mechanisms of operation in liquid metal anode solid oxide fuel cells (LMA SOFCs). Options for future work in this area are split into three phases: short-term, medium-term and long-term.

In the short-term, construction of the rotating electrolyte disc (RED) apparatus based upon the latest design, proposed in this study, can be done. This work involves three main aspects: sealing of the rotating electrolyte disc affixed to the bottom of rotating tube, development of electrical connection from three electrodes system and construction of mechanical parts that enable rotation of the RED setup in liquid tin up to 1800 rpm at temperatures $>700 \text{ }^\circ\text{C}$.

This work is followed by application of built RED apparatus for studies in LMA SOFCs. This encompasses experimental work on oxygen reduction reaction at rotating electrolyte/liquid tin interface at various rotation speeds. The concentration of oxygen can be set via the potential applied to the liquid tin electrode, while the diffusion layer thickness is fixed via rotation speed. Applying the Levich, Koutecki-Levich analysis it is possible to elucidate mass transport (diffusion coefficient of dissolved oxygen) and kinetic (if any) parameters for the oxygen reduction reaction.

The next step in the application of the RED can be done in the model system developed in this thesis (Chapters 7 and 8), whereby oxidation of hydrogen takes place in an LMA SOFC operated in mode *CE*. The data generated with the RED can be compared to

previous data from a stationary system. Most importantly, the results will provide an insight into the mechanisms underpinning transport and kinetic phenomena within the liquid metal anode during the fuel oxidation process. The measurement of diffusion coefficient of dissolved oxygen can be compared to the one found in the step above and ideally should remain constant.

The work outlined above may take six months and requires only one PhD student.

The medium-term work is outlined as follows and would require a team of up to a dozen researchers. The time scale for a medium-term work may be up to five-six years.

The first step would be the optimization of an existing workstation built for stationary electrochemical testing of LMA SOFCs. One of the challenges in this study was parasitic ingress of oxygen into the fuel cell despite substantial improvement of the rig, such as replacement of silicone tubing with impermeable nylon tubing. Therefore it is essential to replace all plastic tubing with stainless steel tubing and most importantly to apply stainless steel joints, valves, etc. In addition the supplied fuel (gaseous mixture of inert gas and fuel) should be passed through a titanium furnace to reduce the oxygen level down to few (ca. 5-10) ppm.

The optimization of the workstation should be followed by further experimental work on hydrogen oxidation in LMA SOFCs in ***CE*** mode (as described in Chapters 7 and 8) at various operating potentials (less positive than -0.90 V vs. RE employed in this study). This can be done in order to examine the effect of potential on the time-constants and test the validity of the model in wider potential range. In addition, it would be interesting to alter the geometry of the cell (e.g. electrode area and tin volume) to see if the value of dynamic oxygen utilization coefficient is consistent with predictions from the ***CE*** model.

In addition, variation in the operating temperature and applied potential (further away or closer to the Sn/SnO₂ equilibrium potential) may potentially result in the range of oxygen solubility measured with greater accuracy than the one in this work, as this time the oxygen leakage will be reduced to minimum.

The following step should involve improvement of the current electrochemical model for ***CE*** mode including refinement of the assumption on identification of the rate-determining step in hydrogen oxidation process. In the present model this assumption was made because the supplied fuel was dry (i.e. contained only traces of water) and hence the backward reaction (water reduction) was ignored. This assumption may not be absolutely true and in order to investigate it additional work with humidified hydrogen can be done. Combining the results from both models (hydrogen oxidation in ***CE*** mode and water electrolysis) should result in a model with more defined boundary conditions.

The basis of an improved model can be applicable for modelling of a more complicated system involving other gaseous fuels (e.g. carbon monoxide) which are of practical interest. A model that incorporates oxidation of carbon monoxide instead of hydrogen should be developed in conjunction with practical work on evaluation of the performance of LMA SOFC with other fuels such as carbon monoxide and solid carbon.

Large deposits of coal worldwide provide a niche for this technology in the global market, particularly in the coal-dependent countries. With regards to fuel cell testing using solid carbon, the effect of carbon particles size on the performance should be evaluated.

Greater attention is needed to explore one of the benefits of this technology – anode tolerance to fuel impurities⁵⁹. Initial studies may involve evaluation of LMA performance in presence of common contaminants (e.g. sulphur), which according to the literature should electrochemically oxidise in the bulk of liquid anode and serve as additional energy source (acting as a fuel).

Application of carbonaceous fuels (gaseous or solid) requires the analysis of the gas outlet from the fuel cell using the gas chromatographer or mass spectrometer. This would provide additional information concerning the kinetics of the reduction of dissolved oxygen and /or metal oxide and enable their comparison with the anode oxidation kinetics. It would also allow the practical efficiency of the fuel oxidation processes with both solid carbon and gaseous CO to be measured.

In addition to a tubular design (applied in the present work), a pellet cell design can be introduced to perform electrochemical characterisation of LMA SOFCs. In such a design, a thin electrolyte pellet is affixed to the bottom of zirconia tube with high temperature, non-porous sealant. Once *in-situ* electrochemical characterisation has been made, the pellet can be dismantled from the supporting tube and be exposed to further *ex-situ* physical characterisation. Analysis of Sn|SnO₂|YSZ interphases using scanning electron microscopy along with energy-dispersive X-ray spectroscopy (EDX) would provide more detailed information on structure of the electrodes, formation of a blocking layer, etc. compared to the previously applied tubular cell.

In parallel to studies on oxidation of fuel in chemical –electrochemical (**CE**) mode, the operation of LMA SFOCs in common in literature electrochemical –chemical (**EC**) modes is appropriate.

The application of the electrochemical impedance spectroscopy (EIS) may be particularly interesting to differentiate various losses in the LMA SOFC operated in both **CE** and **EC** modes. The EIS data on operation of LMA SOFC in **EC** modes has been measured previously; however, no EIS data is available for LMA system operating in the **CE** mode.

Development of a model for *EC* modes would be valuable, as it may generate additional parameters to be taken into consideration for design of LMA SOFCs with improved performance.

Electrolytic performance of liquid metal electrode systems can be of practical interest. Further experimental work is required on water (steam) electrolysis using the liquid metal electrode. In particular, a wider partial pressure range of water should be applied (using the heated lines) with minimal inclusion of parasitic oxygen to investigate the mechanism for water electrolysis. If initial studies show promising results, further exploration of two liquid metal electrodes (cathode and anode) for steam electrolysis and fuel oxidation (similar to conventional solid oxide steam electrolyzers) can be made. It is optional to examine water electrolysis and may not be part of this work plan as the main focus of this study is fuel cell operation.

Once fundamental data on mechanisms and transport properties of LMA SOFCs are obtained in work under short term and medium term time scale, their implication for the scale-up of the technology would be appropriate. The obtained findings should complement the development of commercial cells and stacks. For that the development of multi-scale and multi-physics models (using COMSOL software, for example) can be undertaken. Thermal imaging technique may be applied additionally for examination of the heat transfer process.

The long-term goals for an improved development of LMA SOFC technology include development and testing of LMA SOFC stacks, techno-economic analysis of LMA SOFC stacks in terms its performance, capital and maintenance costs. One of the biggest challenges in the development of the stacks might be the poor wetting properties of tin. In the present study, only large volume of molten tin anode was used. Therefore an optimization work would be necessary to identify the optimum thickness of liquid anode, as well as conditions at which its surface tension is the lowest.

As such, for successful implementation of LMA SOFCs, its economics has to be competitive with existing mature technologies (e.g. power plants). Therefore, analysis of the capital costs of stack manufacture, maintenance costs and future electricity costs will provide a basis for improvements to the design of LMA SOFCs. At later stages trialing of the pilot plant with built LMA SOFC stacks can be made. The rough estimate on the time frame for long-term is about 20 years.

Nomenclature

Parameters and Variables	Description	Section
a	(a) Rate of electrochemical oxidation of metal to metal oxide (b) Tafel equation constant	6.2 2.2.4
a_i	Activity of a specie i	2.2.3
a_s	Specific external surface area of the catalyst pellet in Equation(7.55)/m ² (kgcat) ⁻¹	7.6
\bar{a}	Intercept (concentration of O ₂ in the carrier gas, N ₂)	5.2.1
A	(a) Area of reaction interface/ cm ² (b) Disc electrode surface area/ cm ² (c) Cross-sectional area of component i / cm ² (d) Area of permeable membrane / cm ²	7.4 3.4.4 2.2.4 5.2
b	(a) Rate of chemical reduction of metal oxide to metal (b) Tafel equation constant	6.2 2.2.4
c'	Concentration of hydrogen in the bulk of the melt / mol cm ⁻³	7.4
c'_1	Steady value of c' at p'_1	Appendix C
c'_2	Steady value of c' at p'_2	7.4
c'_3	Steady value of c' at p'_3	Appendix C
c''	Concentration of water in the bulk of the melt / mol cm ⁻³	9.3.3
\bar{c}	a) Concentration of oxygen in the bulk of the melt / mol cm ⁻³ b) Concentration of leaking oxygen / ppm	7.6 5.2.1
\bar{c}_1	Steady concentration of oxygen in the bulk of the melt at p'_1 / mol cm ⁻³	7.6
\bar{c}_2	Steady concentration of oxygen in the bulk of the melt at p'_2 / mol cm ⁻³	7.6
\bar{c}_3	Initial concentration of oxygen after switch from OC to potential, E / mol cm ⁻³	8.4.1
\bar{c}^*	Saturated concentration of oxygen at potential E in the bulk of the melt at $p'=0$ / mol cm ⁻³	7.6
\bar{c}^{**}	Equilibrium concentration of dissolved oxygen at potential E in the bulk of the melt at $p''=0$ / mol cm ⁻³	9.3.3
c^{*}	Saturated concentration of hydrogen in the bulk of the melt / mol cm ⁻³	Appendix C
c^{*}_1	Saturated concentration of hydrogen in the bulk of the melt at p'_1 / mol cm ⁻³	Appendix C
c^{*}_2	Saturated concentration of hydrogen in the bulk of the melt at p'_2 / mol cm ⁻³	7.4
\bar{c}	The difference between the equilibrium oxygen concentration at potential E and concentration in the bulk (Equation 9.16)	9.3.3
\bar{c}_1	The value of \bar{c} at $p'' = p_1''$	9.3.3
\bar{c}_2	The value of \bar{c} at $p'' = p_2''$	9.3.3
C	Concentration of analyte in bulk solution / mol cm ⁻³	3.4.4
D	Diffusion coefficient / cm ² s ⁻¹	
\bar{D}	Diffusion coefficient of oxygen in the melt/ cm ² s ⁻¹	7.6
D'	Diffusion coefficient of hydrogen in the melt / cm ² s ⁻¹	7.4

Nomenclature

Da	Damkohler number	7.6
Da _{II}	The second Damkohler number	7.6
E	Potential / V	
E_a	Activation energy for conduction/ kJ mol ⁻¹	4.2.1
E_{cell}	Cell potential / V	2.2.4
E_N	Nernst Potential / V	2.2.3
E_{rev}	Reversible potential / V	2.2.2
f	Frequency / number of revolutions per second	3.4.3
F	Faraday's constant / 96,485 C mol ^{-eq} ⁻¹	2.2.2
ΔG	Total Gibbs free energy change / J mol ⁻¹	2.2.2
ΔG_r^0	Gibbs free energy change of reaction / J mol ⁻¹	2.3.2
$\Delta G_{M-MO_n}^0$	Gibbs free energy for metal oxidation reaction (M+ (n/2)O ₂ → MO _n)	2.3.2
ΔH	Total Enthalpy of reaction / J mol ⁻¹	2.2.2
i	Anodic oxidation or cathodic reduction current / mA	
$i_{cathodic}$	Parasitic oxygen reduction current / mA	7.3.1
i_d	Diffusion-controlled current / A (Equation (3.6))	3.4.4
i_k	Kinetic current / A	3.4.4
i_1	Steady anodic current at p_1' / mA	7.4
i_2	a) Steady anodic current at p_2' / mA b) Steady cathodic current at p_2'' / mA	7.4 9.3.3
i_3	Initial (maximum) anodic current after switch from OC to potential, E / mA	8.4.1
I	Pumped current / A	5.2.1
$I(m)$	Amplitude of current sinusoidal oscillation / A	3.4.3
$I(t)$	Current sinusoidal oscillations / A	3.4.3
j	Current density / A cm ⁻²	2.2.4
j_0	Exchange current density / A cm ⁻²	2.2.4
j_{lim}	Limiting current density / A cm ⁻²	2.2.4
J	Permeation rate (flux) of gas through a membrane / cm ³ s ⁻¹	5.2
\bar{J}	Flux of oxygen in the melt / mol s ⁻¹	7.6
\bar{J}	Flux of hydrogen in the melt / mol s ⁻¹	7.4
k	Boltzmann constant / J K ⁻¹	4.2.1
k_f	a) Rate constant in Equation (3.8) b) Mass-transfer coefficient/ m s ⁻¹ in Equation (7.55)	3.4.4 7.6
k_1	Rate constant for homogeneous oxidation of hydrogen in liquid metal / s ⁻¹ mol ⁻² cm ⁶	7.6
k_1'	Rate constant for the dissolution of hydrogen in liquid metal / cm ³ s ⁻¹	7.4
k_2	Equilibrium constant for hydrogen dissolution in liquid metal / mol cm ⁻³ kPa ^{-0.5} (Equation (7.29))	7.6
k_2'	Proportionality constant in Equation (7.7) / C cm ³ (mol-eq ⁻¹ s) ⁻¹	7.4
k_3	Proportionality constant in Equation (7.36) / C cm ³ (mol-eq ⁻¹ s) ⁻¹	7.6
k_3'	Henry's law constant / mol (cm ³ kPa) ⁻¹ (Equation (7.19))	7.4
k_4	Homogeneous rate constant for Reaction (9.4) / mol (cm ³ kPa) ⁻¹	9.3.3
k_5	Henry's law constant / mol (cm ³ kPa) ⁻¹ (Equation 9.7)	9.3.3
k_w	Rate coefficient in Equation (7.55) / m ³ (kg _{cat}) ⁻¹ s ⁻¹	7.6
\bar{K}	Sub-parameter of \bar{z}_2 , defined by Equations (7.56) and (7.57) and dependent upon geometric and convective factors/ kPa ⁻¹	7.6.1
K_s	Sievert's constant / mol cm ⁻³ Pa ^{-0.5} (Equation (8.2))	8.2
l	Total length of permeable tubing / cm	5.2.1
l_i	Conductivity path length in cell component i / m	2.2.4
n	Number of electrons transferred in electrochemical reaction	

Nomenclature

n	Stoichiometric number	2.3.2
N'	Number of moles of hydrogen	7.4
\bar{N}	Number of moles of oxygen	5.4.2
N_O^S	Solubility of oxygen / at. %	2.3.3
p_i	Partial pressure of a gas i / kPa	2.2.2
p'	Partial pressure of hydrogen / kPa	7.4
p'_1	Partial pressure of hydrogen at $t = 0$ / kPa	7.4
p'_2	Partial pressure of hydrogen at $t = t_1$ / kPa	7.4
p''	Water vapour partial pressure / kPa	9.3.3
p_1''	Partial pressure of water vapour at $t = 0$ / kPa	9.3.3
p_2''	Partial pressure of water vapour at $t = t_1$ / kPa	9.3.3
Δp	Pressure difference	5.2
$p_{O_2\text{sample}}$	Partial pressure of oxygen in sample gas (Equation (5.10))	5.2.2
$p_{O_2\text{ref}}$	Measured concentration of oxygen in reference gas / ppm (Equation (5.10))	5.2.2
P	Permeability coefficient / $\text{cm}^3 \text{ s}^{-1} \text{ Pa}^{-1}$	5.2
$P\Delta V$	Expansion or compression work / J mol^{-1}	2.2.2
Q	Total heat added or removed from a system / J mol^{-1}	2.2.2
Q_1	Coulombic charge in Regime 1 (after switch of potential from OC to E) / C	8.4.1
Q'_1	Coulombic charge in Regime 1 (after switch of potential from OC to E) / C (E mode)	Appendix C
Q_2	Coulombic charge in Regime 2 (after switch of potential from OC to E) / C	8.4.1
Q'_2	Coulombic charge in Regime 2 (after switch of potential from OC to E) / C (E mode)	Appendix C
Q_3	Coulombic charge in Regime 3 (after switch of potential from OC to E) / C	8.4.1
Q'_3	Coulombic charge in Regime 3 (after switch of potential from OC to E) / C (E mode)	Appendix C
R	Universal gas constant / $\text{J mol}^{-1} \text{ K}^{-1}$	
R_{cell}	Total resistance of a cell / Ω	2.2.4
r	Radius of permeable tubing / cm	5.4.3
r_1	External radius of permeable tubing / cm	5.4.3
r_2	Internal radius of permeable tubing / cm	5.4.3
s_1	Slope of $\left[\frac{di}{dt}\right]_{t=0}$ vs. p'_2 , equivalent to $k_1(k_2)^2 k_3 \bar{c}^*$	7.6.2
s_2	Slope of i_2 vs. p'_2 , equivalent to $nFVk_1(k_2)^2 \bar{z}_2 \bar{c}^*$	7.6.2
S	Absorption coefficient in Equation (5.1) / cm Pa^{-1}	
ΔS	Total entropy change / J (mol K)^{-1}	2.2.2
t	Time / s	
t_{ion}	Transport number of a mobile ion	4.2.1
t_1	Time at which $p(H_2)$ changes from p'_1 to p'_2 / s	7.4
t_2	Time at which potential is switched from E to OC / s	8.4.1
t_3	Time at which potential is switched from OC back to E / s	8.4.1
T	Absolute temperature / K	
ΔU	Total change in in internal energy / J mol^{-1}	2.2.2
ν	Kinematic viscosity / $\text{cm}^2 \text{ sec}^{-1}$	3.4.4
ν_i	Stoichiometric factor of a specie i	2.3.2
V	a) Volume of gas that penetrates through membrane / cm^3 b) Volume of the melt (liquid tin) / cm^3	5.2 7.4
$V(m)$	Amplitude of voltage sinusoidal oscillation / V	3.4.3

Nomenclature

$V(t)$	Voltage sinusoidal oscillations / V	3.4.3
w'	Measure of the balance between the rates of hydrogen dissolution in liquid metal and its removal by anodic oxidation (Equation (7.10))	7.4
W	Total work / J mol ⁻¹	2.2.2
W_{elec}	Electrical work / J mol ⁻¹	2.2.2
x	Ratio of the two rates: electrochemical oxidation of metal to metal oxide and chemical reduction of metal oxide to metal	6.2
X	Flow rate of gas / ml s ⁻¹	5.2.1
Y	(a) Admittance / Ω^{-1}	3.4.3
Y	(b) Permeation rate of oxygen through plastic tubing/cm ³ s ⁻¹	5.2.1
Y_{Re}	Real part of impedance / Ω^{-1}	3.4.3
Y_{Im}	Imaginary part of admittance / Ω^{-1}	3.4.3
\bar{z}	Dynamic oxygen utilisation coefficient defined by the Equation (7.40)	7.6
\bar{z}_2	A value of \bar{z} at $p' = p'_2$	7.6
Z	Impedance / Ω	3.4.3
Z_{Im}	Imaginary part of impedance / Ω	3.4.3
Z_{Re}	Real part of impedance / Ω	3.4.3

Greek symbols

α	Charge transfer coefficient	2.2.4
δ	Diffusion layer thickness / cm	7.4
η	Overvoltage (potential loss) / V	2.2.4
σ	a) Electronic conductivity / S m ⁻¹ b) Ionic conductivity / S m ⁻¹	2.2.4 4.2.1
σ_0	Pre-exponential factor in Equation (4.6.)	4.2.1
τ	Permeable membrane thickness / cm	5.2
τ_C	Characteristic time of the chemical reaction in Equation (7.54) / s	7.6
τ_M	Mixing time that can be controlled by hydrodynamics or by diffusion in Equation (7.54) / s	7.6
φ	Phase shift between voltage and current sinusoidal signal / °	3.4.3
ω	a) Angular frequency / Hz b) Angular velocity of rotation / revolutions per second (rad s ⁻¹)	3.4.3 3.4.4
Ω	Resistance / Ohm	4.4.3

Subscripts

a	Anode
act	Activation
b	Boiling
$bulk$	Bulk
c	Cathode
$conc$	Concentration
e	Electrode
gb	Grain boundary
H_2	Hydrogen
H_2O	Water /Steam
l	Liquid

<i>lim</i>	Limiting
<i>m</i>	Metal
<i>n</i>	Stoichiometric number
O_2	Oxygen
<i>ohmic</i>	Ohmic
<i>react</i>	Reaction zone
<i>steady</i>	Steady
<i>ref</i>	Reference
<i>rev</i>	Reversible

Superscripts

'	Hydrogen
”	Water/steam
-	Oxygen

Abbreviation

Description

AFC	Alkaline fuel cell
CE	Counter electrode
CHP	Combined heat and power
CHPP	Combined heat and power plant
CNC	Computer Numerical Control
DCFC	Direct carbon fuel cell
EMF	Electromotive force / V
GT	Gas turbine
ID	Internal diameter
LHV	Low heating value
LMA	Liquid metal anode
LME	Liquid metal electrode
LTA	Liquid tin anode
MCFC	Molten carbonate fuel cell
OCP	Open circuit potential / V
OCV	Open circuit voltage / V
OD	Outer diameter
PAFC	Phosphoric acid fuel cell
PEMFC	Polymer electrolyte membrane fuel cell
RDE	Rotating disc electrode
RE	Reference electrode
RED	Rotating electrolyte disc
SE	Sensing electrode
SOE	Solid oxide electrolysis
SOFC	Solid oxide fuel cell
SOSE	Solid oxide steam electrolysis
WE	Working electrode
YSZ	Yttria-stabilised zirconia

References

1. Intergovernmental Panel on Climate Change, (2001)
http://www.ipcc.ch/publications_and_data/publications_and_data_reports.shtml.
[Accessed: May 2015]
2. UK Government, (2015) <http://www.gov.uk/government/publications/2010-to-2015-government-policy-greenhouse-gas-emissions/2010-to-2015-government-policy-greenhouse-gas-emissions>. [Accessed: May 2015]
3. International Energy Agency (IEA), (2014)
http://www.worldenergyoutlook.org/media/weowebiste/2014/141112_WEO_FactSheets.pdf. [Accessed: April 2015]
4. D. Cao, Y. Sun, and G. Wang, *J. Power Sources*, **167**, 250–257 (2007).
5. S. Singhal and K. Kendall, *High Temperature Solid Oxide Fuel Cells Fundamentals, Design and Applications*, 1st ed., Elsevier, Oxford, (2003), p. 89–92.
6. H. Abernathy, R. Gemmen, K. Gerdes, M. Koslowske, and T. Tao, *J. Power Sources*, **196**, 4564–4572 (2011).
7. M. Lo Faro, V. Antonucci, P. L. Antonucci, and A. S. Aricó, *Fuel*, **102**, 554–559 (2012).
8. S. Park, J. M. Vohs, and R. J. Gorte, *Nature*, **404**, 265–267 (2000).
9. D. K. Niakolas, *Appl. Catal. A Gen.*, **486**, 123–142 (2014).
10. T. S. Li and W. G. Wang, *J. Power Sources*, **196**, 2066–2069 (2011).
11. D. J. L. Brett, M. Manage, E. Agante, N. P. Brandon, E. R. Brightman, J. C. Brown, and I. Staffell, in *Functional materials for sustainable energy applications*, J. A. Kilner, S. J. Skinner, S. J. C. Irvine, and P. P. Edwards, Editors, p. 249–274, Woodhead Publishing Limited, Cambridge (2012).
12. W. A. G. McPhee, M. Boucher, J. Stuart, R. S. Parnas, M. Koslowske, T. Tao, and B. A. Wilhite, *Energy & Fuels*, **23**, 5036–5041 (2009).
13. T. Tao, M. Koslowske, W. McPhee, L. Bateman, M. Slaney, and J. Bentley, in *Coal Based Fuel Cell Technology: Status, Needs and Future Applications*, p. 93–103 (2007).
14. T. Tao, in *Solid Oxide Fuel Cells IX*, S. C. Singhal and J. Mizusaki, Editors, p. 353–362, The Electrochemical Society, Pennington, N.J. (2005).
15. T. Tao, M. Slaney, L. Bateman, and J. Bentley, *ECS Trans.*, **7**, 1389–1397 (2007).
16. T. Tao, L. Bateman, J. Bentley, and M. Slaney, *ECS Trans.*, **5**, 463–472 (2007).
17. T. Tao, W. A. McPhee, M. T. Koslowske, L. S. Bateman, M. J. Slaney, and J. Bentley, *ECS Trans.*, **12**, 681–690 (2008).

References

18. A. Jayakumar, R. Küngas, S. Roy, A. Javadekar, D. J. Buttrey, J. M. Vohs, and R. J. Gorte, *Energy Environ. Sci.*, **4**, 4133–4137 (2011).
19. A. Jayakumar, J. M. Vohs, and R. J. Gorte, *Ind. Eng. Chem. Res.*, **49**, 10237–10241 (2010).
20. A. Jayakumar, S. Lee, A. Hornés, J. M. Vohs, and R. J. Gorte, *J. Electrochem. Soc.*, **157**, B365–B369 (2010).
21. M. LaBarbera, M. Fedkin, and S. Lvov, *ECS Trans.*, **35**, 2725–2734 (2011).
22. D. J. L. Brett, A. Atkinson, N. P. Brandon, and S. J. Skinner, *Chem. Soc. Rev.*, **37**, 1568–78 (2008).
23. S. Kakac, A. Pramuanjaroenkij, and X. Zhou, *Int. J. Hydrogen Energy*, **32**, 761–786 (2007).
24. K. Huang and J. B. Goodenough, *Solid oxide fuel cell technology*, Woodhead Publishing Limited, CRC Press LLC, Oxford, Cambridge, New Delhi, (2009), p. 1–7, 10–19.
25. R. O’Hayre, S.-W. Cha, W. Colella, and F. B. Prinz, *Fuel Cell Fundamentals*, John Wiley&Sons, Inc., New Jersey, (2006), p. 10–12.
26. S. J. Peighambardoust, S. Rowshanzamir, and M. Amjadi, *Review of the proton exchange membranes for fuel cell applications*, (2010), p. 9349–9384.
27. US Department of Energy Energy Efficiency & Renewable Energy, *Comp. Fuel Cell Technol.* (2011)
http://www1.eere.energy.gov/hydrogenandfuelcells/fuelcells/pdfs/fc_comparison_chart.pdf. [Accessed: Oct 2012]
28. S. A. Hajimolana, M. A. Hussain, W. M. A. W. Daud, M. Soroush, and A. Shamiri, *Renew. Sustain. Energy Rev.*, **15**, 1893–1917 (2011).
29. G. Prentice, *Electrochemical Engineering Principles*, Prentice Hall, New Jersey, (1991), p. 177–182.
30. R. Bove and S. Ubertini, *J. Power Sources*, **159**, 543–559 (2006).
31. S. Grosso, L. Repetto, and P. Costamagna, in *Modeling Solid Oxide Fuel Cells: Methods, Procedures and Techniques*, R. Bove and S. Ubertini, Editors, p. 189–192, Springer (2008).
32. T. S. Zhao, K. D. Kreuer, and T. Van Nquyen, *Advances in Fuel Cells*, Elsevier B.V, Oxford, (2007), p. 33–35.
33. S. Murthy and A. G. Fedorov, *J. Power Sources*, **124**, 453–458 (2003).
34. S. P. S. Badwal and F. T. Ciacchi, *Ionics (Kiel)*, **6**, 1–21 (2000).
35. J. W. Fergus, R. Hui, X. Li, D. P. Wilkinson, and J. Zhang, *Solid Oxide Fuel Cells Materials Properties and Performance*, CRC Press Taylor and Francis Group, Boca Raton, (2009), p. 5–7.
36. J. B. Hedrick, *U.S. Geol. Surv.*, 1–7 (1997).

37. S. P. S. Badwal, *Solid State Ionics*, **52**, 23–32 (1992).
38. J. A. Kilner and R. J. Brook, *Solid State Ionics*, **6**, 237–252 (1982).
39. J. T. S. Irvine and P. Connor, in *Solid Oxide Fuel Cells: Facts and Figures: Past Present and Future: Perspectives for SOFC Technologies*, J. Irvine and P. Connor, Editors, p. 163–169, Springer, London (2013).
40. J. W. Fergus, *J. Power Sources*, **162**, 30–40 (2006).
41. W. Strickler and W. G. Carlson, **47**, 122–127 (1963).
42. S. P. S. Badwal, *J. Mater. Sci. Letters*, **6**, 1419–1421 (1987).
43. E. Barsoukov and J. Ross Macdonald, *Impedance Spectroscopy Theory, Experiment, and Applications*, Second., A John Wiley & Sons, Inc., New Jersey, (2005), p. 530–537.
44. J. R. Macdonald, *Electrochim. Acta*, **35**, 1483–1492 (1990).
45. J. R. Macdonald and D. R. Franceschetti, *J. Electroanal. Chem. Interfacial Electrochem.*, **307**, 1–11 (1991).
46. J. E. Bauerle, **30**, 2657–2670 (1969).
47. T. Wang, R. F. Novak, and R. E. Soltis, *Sensors Actuators B*, **77**, 132–138 (2001).
48. M. M. Mench, *Fuel Cell Engines*, John Wiley&Sons, Inc., New Jersey, (2008), p. 23.
49. L. Kouchachvili and M. Ikura, *Int. J. Hydrogen Energy*, **36**, 10263–10268 (2011).
50. M. N. Manage, D. Hodgson, N. Milligan, S. J. R. Simons, and D. J. L. Brett, *Int. J. Hydrogen Energy*, **36**, 5782–5796 (2011).
51. S. Gopalan, G. Ye, and U. B. Pal, *J. Power Sources*, **162**, 74–80 (2006).
52. S. D. Ebbesen and M. Mogensen, *J. Power Sources*, **193**, 349–358 (2009).
53. S. Pati, S. Gopalan, and U. B. Pal, *Int. J. Hydrogen Energy*, **36**, 152–159 (2011).
54. Q. Fu, C. Mabilat, M. Zahid, A. Brisse, and L. Gautier, *Energy Environ. Sci.*, **3**, 1382 (2010).
55. F. Bidrawn, G. Kim, G. Corre, J. T. S. Irvine, J. M. Vohs, and R. J. Gorte, *Electrochem. Solid-State Lett.*, **11**, 167–170 (2008).
56. S. Pati, K. J. Yoon, S. Gopalan, and U. B. Pal, *J. Electrochem. Soc.*, **156**, B1067–B1077 (2009).
57. N. P. Brandon and D. J. Brett, *Philos. Trans. A. Math. Phys. Eng. Sci.*, **364**, 147–59 (2006).
58. P. R. Shearing, D. J. L. Brett, and N. P. Brandon, *Int. Mater. Rev.*, **55**, 347–363 (2010).

59. T. T. Tao, M. T. Koslowske, J. Bentley, J. Brodie, and C. MacKean, *ECS Trans.*, **41**, 125–135 (2012).
60. K. T. Jacob, *ECS Trans.*, **35**, 573–582 (2011).
61. T. Tao, M. T. Koslowske, and J. Bentley, in *219th ECS Meetings*, p. 1 (2011).
62. R. Gemmen, H. Abernathy, K. Gerdes, M. Koslowske, W. A. G. McPhee, and T. Tao, in *Advances in Solid Oxide Fuel Cells V*, N. P. Bansal and P. Singh, Editors, p. 37–52, John Wiley & Sons, New Jersey (2009).
63. A. Javadekar, A. Jayakumar, R. J. Gorte, J. M. Vohs, and D. J. Buttrey, *J. Electrochem. Soc.*, **159**, A386–A389 (2012).
64. H. Wang, Y. Shi, and N. Cai, *J. Power Sources*, **245**, 164–170 (2014).
65. T. Cao, Y. Shi, H. Wang, and N. Cai, *J. Power Sources*, **284**, 536–546 (2015).
66. H. Wang, T. Cao, Y. Shi, N. Cai, and W. Yuan, *Energy*, **75**, 555–559 (2014).
67. H. Wang, Y. Shi, W. Yuan, T. Cao, N. Cai, and X. Liang, *ECS Trans.*, **57**, 2913–2922 (2013).
68. T. Cao, H. Wang, Y. Shi, and N. Cai, *Fuel*, **135**, 223–227 (2014).
69. H. Wang, Y. Shi, and N. Cai, *Int. J. Hydrogen Energy*, **38**, 15379–15387 (2013).
70. M. Colet Lagrille, U. Doraswami, and G. H. Kelsall, *ECS Trans.*, **41**, 137–148 (2012).
71. S. C. Rayman, M. Koslowske, L. Bateman, T. Tao, and R. E. White, *ECS Trans.*, **33**, 93–121 (2011).
72. S. Khurana, M. LaBarbera, M. V. Fedkin, S. N. Lvov, H. Abernathy, and K. Gerdes, *J. Power Sources*, **274**, 1049–1054 (2015).
73. H. Wang, Y. Shi, and N. Cai, *J. Power Sources*, **246**, 204–212 (2014).
74. R. C. Sharma and Y. A. Chang, *J. Phase Equilibria*, **7**, 269–273 (1986).
75. J. Kestin, M. Sokolov, and W. A. Wakeham, *J. Phys. Chem. Ref. Data*, **7**, 941–948 (1978).
76. K. Nogi, K. Ogino, A. McLean, and W. A. Miller, *Metall. Trans. B*, **17**, 163–170 (1986).
77. M. B. Bever, J. Member, and C. F. Floe, *Trans. Am. Inst. Min. Met. Eng.*, **156**, 149–159 (1944).
78. K. Iwase, *Sci. Reports Tohoku Imp. Univ.*, **15** (1926).
79. T. N. Belford and C. B. Alcock, *Trans. Faraday Soc.*, **61**, 443–453 (1965).
80. T. A. Ramanarayanan and R. A. Rapp, *Metall. Trans.*, **3**, 3239–3246 (1972).

References

81. S. Cahen, N. David, J. M. Fiorani, A. Maître, and M. Vilasi, *Thermochim. Acta*, **403**, 275–285 (2003).
82. M. G. Bonicelli, G. Ceccaroni, F. Gauzzi, and G. Mariano, *Thermochim. Acta*, **430**, 95–99 (2005).
83. Z. M. Jarzebski and Marton, *J. Electrochem. Soc.*, 199–205 (1976).
84. J.-H. Lee, S.-J. Park, and K. Hirota, *J. Am. Ceram. Soc.*, **73**, 2771–2774 (1990).
85. L. Wang and Q. Mei, *J. Mater. Sci. Technol.*, **22**, 569–571 (2006).
86. A. E. Arkel, E. A. Flood, and F. H. Bright, *Can. J. Chem.*, **31**, 1009–10019 (1953).
87. K. Huang, M. Feng, and J. B. Goodenough, *Solid State Ionics*, **89**, 17–24 (1996).
88. N. M. Sammes, G. A. Tompsett, H. Näfe, and F. Aldinger, *J. Eur. Ceram. Soc.*, **19**, 1801–1826 (1999).
89. M. A. Colet Lagrille, thesis, Imperial College London (2013).
90. S. C. Marschman and D. C. Lynch, *Can. J. Chem. Eng.*, **62**, 875–879 (1984).
91. A. D. Javadekar, thesis, University of Delaware (2012).
92. I. V. Yentekakis, P. G. Debenedetti, B. Costa, M. Konsolakis, and V. Kiouisis, *Ionics (Kiel)*, **5**, 460–471 (1999).
93. M. Ni, M. Leung, and D. Leung, *Int. J. Hydrogen Energy*, **33**, 2337–2354 (2008).
94. J. Winkler, P. V. Hendriksen, N. Bonanos, and M. Mogensen, *J. Electrochem. Soc.*, **145**, 1184–1192 (1998).
95. S. B. Adler, *J. Electrochem. Soc.*, **149**, E166–E172 (2002).
96. G. Offer, D. Brett, and N. Brandon, *ECS Trans.*, **7**, 1645–1652 (2007).
97. Hochttemperatur-Werkstoffe, *Glas. Carbon* <http://www.htw-germany.com/technology>. [Accessed: Oct 2013]
98. C. G. Zoski, *Handbook of Electrochemistry*, First Edit., Elsevier, Amsterdam, (2007), p. 431–454.
99. A. J. Bard and L. R. Faulkner, *Fundamentals and Applications*, First Edit., John Wiley&Sons, Inc., New York, (1980), p. 136–280.
100. Q.-A. Huang, R. Hui, B. Wang, and J. Zhang, *Electrochim. Acta*, **52**, 8144–8164 (2007).
101. J. R. Macdonald, *Ann. Biomed. Eng.*, **20**, 289–305 (1992).
102. D. D. Maconald, *Electrochim. Acta*, **51**, 1376–1388 (2006).

103. M. Orazem and B. Tribollet, *Electrochemical Impedance Spectroscopy*, John Wiley&Sons, Inc., New Jersey, (2008), p. 155–162.
104. S. Fritz, *Electroanalytical methods*, 2nd ed., Springer, London, (2010), p. 159–176.
105. J. Gonzalez, C. Real, L. Hoyos, R. Miranda, and F. Cervantes, *J. Electroanal. Chem.*, **651**, 150–159 (2011).
106. T. I. Quickenden and X. Jiang, *Electrochim. Acta*, **29**, 693–700 (1984).
107. R. Vargas, C. Borrás, J. Mostany, and B. R. Scharifker, *Electrochim. Acta*, **80**, 326–333 (2012).
108. V. Y. Filinovsky and Y. V. Pleskov, in *Comprehensive treatise of electrochemistry*, E. Yeager, J. O. M. Bockris, B. E. Conway, and S. Sarangapani, Editors, p. 293–352, Plenum Press, New York (1984).
109. A. J. Bard and L. R. Faulkner, *Electrochemical methods: Fundamentals and Applications*, John Wiley&Sons, Inc., (1980), p. 280–298.
110. A. Cirera, C. Lopez-Gándara, and F. M. Ramos, *J. Sensors*, **2009**, 1–15 (2009).
111. W. C. Maskell, *J. Phys. E.*, **20**, 1156–1168 (1987).
112. W. C. Maskell, in *Techniques and Mechanisms in Gas Sensing*, P. T. Moseley, J. O. W. Norris, and D. E. Williams, Editors, p. 1–45, Taylor & Francis, Bristol (1991).
113. C. Zhang, C. J. Li, G. Zhang, X. J. Ning, C. X. Li, H. Liao, and C. Coddet, *Mater. Sci. Eng. B Solid-State Mater. Adv. Technol.*, **137**, 24–30 (2007).
114. J. W. Fergus, R. Hui, X. Li, and D. P. Wilkinson, *Solid Oxide Fuel Cells Materials Properties and Performance*, CRC Press Taylor and Francis Group, Boca Raton, (2009), p. 4.
115. D. Vladikova and Z. Stoyanov, *Advanced Impedance Techniques in SOFC Studies*, p. 201–210.
116. D. E. Vladikova, Z. B. Stoyanov, A. Barbucci, M. Viviani, P. Carpanese, J. A. Kilner, S. J. Skinner, and R. Rudkin, *Electrochim. Acta*, **53**, 7491–7499 (2008).
117. P. Hofmann and K. D. Panopoulos, *J. Power Sources*, **195**, 5320–5339 (2010).
118. S. Bebelis, N. Kotsionopoulos, A. Mai, D. Rutenbeck, and F. Tietz, *Solid State Ionics*, **177**, 1843–1848 (2006).
119. A. Barbucci, M. Viviani, P. Carpanese, D. Vladikova, and Z. Stoyanov, *Electrochim. Acta*, **51**, 1641–1650 (2006).
120. A. Barbucci, R. Bozzo, G. Cerisola, and P. Costamagna, *Electrochim. Acta*, **47**, 2183–2188 (2002).
121. M. J. Jørgensen, S. Primdahl, and M. Mogensen, **44**, 4195–4201 (1999).
122. Y. Arachi, H. Sakai, O. Yamamoto, Y. Takeda, and N. Imanishai, **121**, 133–139 (1999).

123. B. A. Boukamp, *Solid State Ionics*, **20**, 31–44 (1986).
124. C.-C. T. Yang, W.-C. J. Wei, and A. Roosen, *Mater. Chem. Phys.*, **81**, 134–142 (2003).
125. V. Stannett, *J. Memb. Sci.*, **3**, 97–115 (1978).
126. R. M. Felder and G. S. Huvar, in *Methods of Experimental Physics: Polymers.*, R. A. Fava, Editor, p. 315–377, Academic Press, New York (1980).
127. J. G. Wijmans and R. W. Baker, *J. Memb. Sci.*, **107**, 1–21 (1995).
128. P. Wood-Adams, *Diffus. Permeability Polym. (Course Notes)* (2006).
129. W. C. Maskell and B. C. H. Steele, *J. Appl. Electrochem.*, **16**, 475–489 (1986).
130. A. Toleuova, V. Yufit, S. Simons, W. C. Maskell, and D. J. L. Brett, *J. Electrochem. Sci. Eng*, **3**, 91–105 (2013).
131. I. Barin, *Thermochemical Data of Pure Substances*, VCH Verlagsgesellschaft mbH, Weinheim, (1995).
132. A. Toleuova, V. Yufit, S. J. R. Simons, W. C. Maskell, and D. J. L. Brett, *ECS Trans.*, **58**, 65–70 (2013).
133. D. Weaire and S. Hutzler, *Introduction to the physics of foams*, Oxford University Press, Oxford, (1999), p. 202–207.
134. J. Banhart, *Prog. Mater. Sci.*, **46**, 559–632 (2001).
135. V. C. Srivastava and K. L. Sahoo, *Mater. Sci.*, **25**, 733–753 (2007).
136. G. J. Davies and S. Zhen, *J. Mater. Sci.*, **18**, 1899–1911 (1983).
137. J. Banhart, D. Bellmann, and H. Clemens, *Acta Mater.*, **49**, 3409–3420 (2001).
138. J. Banhart, *Adv. Eng. Mater.*, **15**, 82–111 (2013).
139. F. Garcia-Moreno, S. T. Tobin, M. Mukherjee, C. Jimenez, E. Solorzano, G. S. Vinod Kumar, S. Hutzler, and J. Banhart, *Soft Matter*, **10**, 6955–6962 (2014).
140. L. Helfen, T. Baumbach, P. Pernot, P. Cloetens, H. Stanzick, K. Schladitz, and J. Banhart, *Appl. Phys. Lett.*, **86**, 1–3 (2005).
141. Y. Feng, H. Zheng, Z. Zhu, and F. Zu, *Mater. Chem. and Phys.*, **78**, 196–201 (2002).
142. F. G. Cuevas, J. M. Montes, J. Cintas, and P. Urban, *J. Porous Mater.*, **16**, 675–681 (2009).
143. N. Babcsan, I. Meszaros, and N. Hegman, *Mater. Sci. Eng. Technol.*, **34**, 391–394 (2003).
144. K. P. Dharmasena and H. N. G. Wadley, *J. Mater. Res.*, **17**, 625–631 (2002).

References

145. J. A. Lee, W. C. Maskell, and F. L. Tye, in *Membrane Separation processes*, P. Meares, Editor, p. 423–426, Elsevier Scientific Publishing Co., Amsterdam (1976).
146. Polymax Ltd., *Rubber Nitrile O-ring datasheet* (2015) <http://www.polymax.co.uk/o-rings/rubber-nbr-oring/>. [Accessed: Nov 2014]
147. Cambridge Glassblowing Ltd., *Glas. Prop. data sheet* (2015) <http://www.camglassblowing.co.uk/glass-properties/>. [Accessed: Nov 2014]
148. S. (Rob) Hui, J. Roller, S. Yick, X. Zhang, C. Decès-Petit, Y. Xie, R. Maric, and D. Ghosh, *J. Power Sources*, **172**, 493–502 (2007).
149. G. Jiang, Y. Li, and Y. Liu, *Trans. Nonferrous Met. Soc. China*, **21**, 1130–1135 (2011).
150. C. Wagner, *Thermodynamics of alloys*, Addison-Wesley Press, (1952).
151. H. M. Lee, *Metall. Trans. A*, **7A**, 431–433 (1976).
152. H. S. Fogler, *Elements of Chemical Reaction Engineering*, Fourth., Pearson Education, Upper Saddle River, NJ, (2006), p. 158.
153. M. J. Madou, *Fundamentals of Microfabrication and Nanotechnology: Solid-State Physics, Fluidics and Analytical Techniques in Micro-and Nanotechnology*, Third., CRC Press Taylor and Francis Group, Boca Raton, FL., (2011), p. 475.
154. G. B. Marin and G. S. Yablosnky, *Kinetics of Chemical Reactions*, Wiley-VCH Verlag & Co. KGaA, Weinheim, (2011), p. 57.
155. T. R. Copeland and R. K. Skogerboe, *Anal. Chem.*, **46**, 1257–1268 (1974).
156. H. Liu, M. Bouchard, and L. Zhang, *J. Mater. Sci.*, **30**, 4309–4315 (1995).
157. W. M. Boorstein and R. D. Pehlke, *Metall. Trans.*, **5**, 399–405 (1974).
158. F. C. Campbell, *Elements of Metallurgy and Engineering Alloys*, AMS International, (2008), p. 105–106.
159. W. F. Hosford, *Physical Metallurgy*, CRC Press Taylor and Francis Group, Boca Raton, (2005), p. 36–37.
160. A. Toleuova, W. C. Maskell, V. Yufit, P. R. Shearing, and D. J. Brett, *J. Electrochem. Soc.*, **162**, F988–F999 (2015).
161. M. Momirlan and T. Veziroglu, *Renew. Sustain. Energy Rev.*, **6**, 141–179 (2002).
162. W. Wang, J. M. Vohs, and R. J. Gorte, *Top. Catal.*, **46**, 380–385 (2007).
163. J. Martinez-Frias, A. Q. Pham, and S. M. Aceves, *Int. J. Hydrogen Energy*, **28**, 483–490 (2003).
164. A. C. Riddiford, in *Advances in Electrochemistry and Electrochemical Engineering*, P. Delahay and C. W. Tobias, Editors, p. 47–116, Interscience Publishers, New York (1966).

165. K. F. Blurton and A. C. Riddiford, *J. Electroanal. Chem.*, **10**, 457–464 (1965).
166. V. G. Levich, *Physicochemical Hydrodynamics*, Prentice Hall Inc., New Jersey, (1962), p. 60–78.
167. F. Opekar and P. Beran, *J. Electroanal. Chem.*, **69**, 1–105 (1976).
168. R. G. Compton and C. E. Banks, *Understanding Voltammetry*, 2nd ed., Imperial College Press, London, (2011), p. 294–295.
169. W. J. Albery and C. M. A. Brett, *J. Electroanal. Chem. Interfacial Electrochem.*, **148**, 201–210 (1983).
170. W. J. Albery and C. M. A. Brett, *J. Electroanal. Chem.*, **148**, 211–220 (1983).
171. J. Bockris and A. K. N. Reddy, *Modern Electrochemistry: An Introduction to an Interdisciplinary Area*, Plenum Press, New York, (1970), p. 1071.
172. R. R. M. Johnston and M. Spiro, *J. Phys. Chem.*, **986**, 3784–3790 (1967).
173. J. Legrand, E. Dumont, J. Comiti, and F. Fayolle, *Electrochim. Acta*, **45**, 1791–1803 (2000).
174. P. G. Zambonin and G. Signorile, *J. Electroanal. Chem. Interfacial Electrochem.*, **35**, 251–259 (1972).
175. E. Desimoni, F. Paniccia, and P. G. Zambonin, *J. Electroanal. Chem. Interfacial Electrochem.*, **38**, 373–379 (1972).
176. J. E. L. Bowcott and B. A. Plunkett, *Electrochim. Acta*, **14**, 883–887 (1969).
177. J. Phillips, R. J. Gale, R. G. Wier, and R. A. Osteryoung, *J. Anal. Chem.*, **48**, 1266–1268 (1976).
178. S. H. Alwash, V. Ashworth, M. Shirkhazadeh, and G. E. Thompson, *Corros. Sci.*, **27**, 383–390 (1987).
179. S. L. Gojković, S. K. Zeinevic, and R. F. Savinell, *J. Electrochem. Soc.*, **145**, 3713 (1998).
180. U. A. Paulus, T. J. Schmidt, H. A. Gasteiger, and R. J. Behm, *J. Electroanal. Chem.*, **495**, 134–145 (2001).
181. F. Gloaguen, F. Andolfatto, R. Durand, and P. Ozil, *J. Appl. Electrochem.*, **24**, 863–869 (1994).
182. F. Gloaguen, P. Convert, S. Gamburgzev, O. A. Velev, and S. Srinivasan, *Electrochim. Acta*, **43**, 3767–3772 (1998).
183. C. Earles and J. O. Schenk, *Anal. Biochem.*, **264**, 191–198 (1998).
184. C. E. Hagan, J. F. Neumaier, and J. O. Schenk, *J. Neurosci. Methods*, **193**, 29–38 (2010).

References

185. D. H. Angell and T. Dickinson, *J. Electroanal. Chem. Interfacial Electrochem.*, **35**, 55–72 (1972).
186. P. Delahay, *New Instrumental Methods in Electrochemistry*, Interscience Publishers, New York, (1954), p. 227–229.
187. M. Spiro and A. M. Creeth, *J. Chem. Soc. Faraday Trans.*, **86**, 3573–3576 (1990).

Appendix

A. Electrical furnace temperature profile

In an electrical furnace mounted vertically the temperature distribution over the total furnace length is not uniform. Therefore to identify the hottest zone in the furnace the temperature profile inside the electrical vertical furnace was measured using a K-type thermocouple (separately from the furnace's thermocouple) for two different set points of 600 °C and 700 °C and the results are illustrated in Figure A.1.

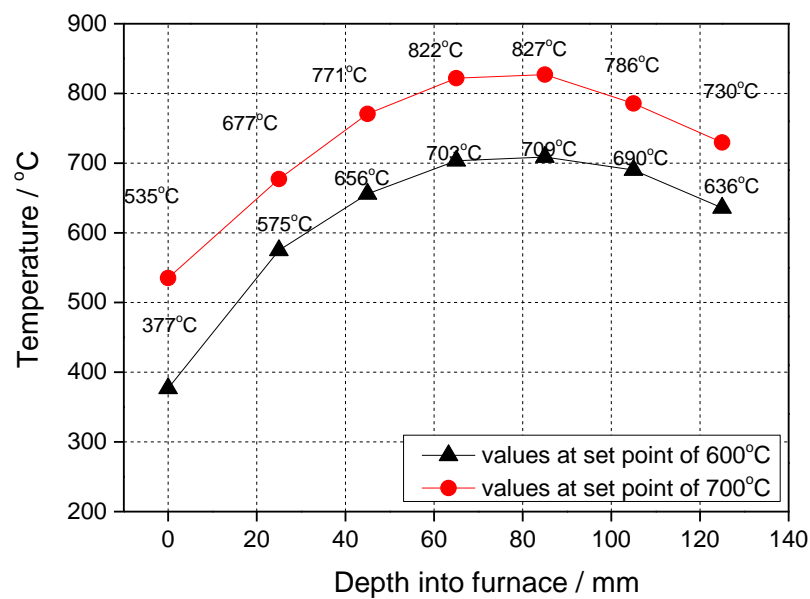


Figure A.1 Measured temperature profile inside the furnace for set points of 600 and 700 °C.

From Figure A.1 an electrochemical cell is decided to be placed only in the middle part of the furnace which is about 80 mm from the top of the furnace. However, for more accurate temperature reading a K-type thermocouple is placed parallel to the measured system (e.g. fuel cell, symmetrical cell or silica tube cell).

B. Determination of permeability coefficient for plastic tubing

Steady-state diffusion is quantified by Fick's first law of diffusion:

$$J = -DA \frac{dc}{dx} \quad (\text{B.1})$$

where J is the flux through area A , D is the diffusion coefficient and dc/dx is the concentration gradient.

Diffusion of gas through a membrane is given by the equation corresponding to equation (B.1) is as follows:

$$J = -PA \frac{dp}{dx} \quad (\text{B.2})$$

where P is the permeability coefficient and dp/dx is the gaseous pressure gradient (which is also a partial pressure gradient).

Consider the permeation through a plastic tube with the element radius, r and thickness, dr . Note that concentration of O_2 inside the tubing is assumed to be zero, $\bar{c} = 0$.

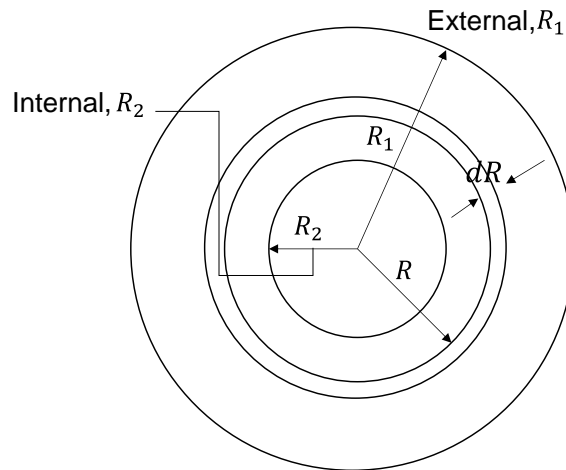


Figure B.1 Schematic representation of plastic tubing with external (r_1) and internal (r_2) radii and element radius, r and thickness, dr .

Applying Equation (B.2):

$$J = -P 2\pi Rl \frac{dp}{dr} \quad (\text{B.3})$$

Separating the variables (note that J is constant for $r_2 < r < r_1$) and integrating:

$$\int_{r_2}^{r_1} \frac{dr}{r} = - \int_0^{0.21 \times 10^5} \frac{2\pi l P}{J} dp \quad (\text{B.4})$$

where for this analysis p is the O₂ partial pressure in Pa.

$$[\ln r]_{r_2}^{r_1} = -\frac{2\pi l P}{J} [p]_0^{0.21 \times 10^5} \quad (\text{B.5})$$

$$\ln\left(\frac{r_1}{r_2}\right) = -\frac{2\pi l P}{J} (21,000) \quad (\text{B.6})$$

But $J=Y$, so

$$P = \frac{Y \ln(r_1/r_2)}{21,000(2\pi l)} \quad (\text{B.7})$$

This is the required equation for permeability coefficient.

C. Electrochemical model for Anodic Oxidation of Hydrogen in Electrochemical mode

Model 1

The assumptions made are as follows:

- i) the process (anodic oxidation) is diffusion-limited so that the concentration of hydrogen at the interface is close to zero at the chosen operating potential of the anode;
- ii) the solubility of hydrogen in tin accords with Henry's law;
- iii) the system is considered to be in quasi-equilibrium;
- iv) the dissolution of hydrogen in tin is governed by a first-order rate equation;
- v) the rate of removal of hydrogen from tin by anodic oxidation is negligible compared with the rate of dissolution;
- vi) the diffusion of H₂ to the electrolyte interface occurs through a diffusion layer of constant thickness as a result of convection induced by bubbling and thermal effects.

In the theoretical treatment in this series, hydrogen and water are denoted by single prime and double prime superscripts respectively, for example c' and c'' .

Consider the following: hydrogen is bubbled through the liquid tin at partial pressure p_1' , a potential, E , is applied to the Sn / YSZ interface and a steady current, i_1 , is observed. The partial pressure of H₂ is then increased to p_2' and the current, i , increases with time and eventually stabilises at i_2 (Figure 7.5).

In the model the diffusion layer thickness at quasi-equilibrium is δ .

When H₂ at partial pressure of p_2' is bubbled through tin, it dissolves in the tin and eventually saturates the solution; the saturated concentration of H₂ is c_2^{*} . The general unsaturated concentration is written as c' .

For a sufficient total flow rate of gas, the rate of dissolution of hydrogen in the tin is proportional to the difference of the saturated concentration and the actual concentration at any given time. If the amount of H₂ (in moles) in the tin is expressed as N' , we may write:

$$\frac{dN'}{dt} = k_1'(c_2^{*} - c') \quad (\text{C.1})$$

where k_1' is the rate constant for dissolution.

We assume that the dissolved concentration of hydrogen at the electrochemical interface is negligible when a potential, E (typically -0.90 V vs. RE, in the **E** mode of operation) is

applied, so the current, i , is controlled by diffusion through the diffusion layer of thickness δ . The flux, J' , is given by Fick's first law, which is expressed as:

$$J' = -D'A \frac{dc'}{dx} \quad (C.2)$$

where D' is the diffusion coefficient, A is the area of the interface and $\frac{dc'}{dx}$ is the concentration gradient within the diffusion layer. So the flux is given by:

$$J' = -\frac{D'Ac'}{\delta} \quad (C.3)$$

Equating the flux with current via Faraday's law:

$$J' = -\frac{i}{nF} \quad (C.4)$$

where i is the current; n is the number of electrons transferred per hydrogen molecule, i.e. $n = 2$.

Combining (C.3) and (C.4) leads to:

$$i = \frac{nFD'Ac'}{\delta} \quad (C.5)$$

This will be written as:

$$i = k'_2 c' \quad (C.6)$$

where k'_2 is given by:

$$k'_2 = \frac{nFD'A}{\delta}$$

Furthermore:

$$\frac{dc'}{dt} = \frac{1}{V} \frac{dN'}{dt} \quad (C.7)$$

where V is the volume of the solution.

Combining (C.1) and (C.7):

$$\frac{dc'}{dt} = \frac{1}{V} k'_1 (c_2^{*'} - c') \quad (C.8)$$

Rearranging and integrating:

$$\int \frac{dc'}{c_2^{*'} - c'} = \frac{k'_1}{V} \int dt$$

The switch from p_1' to p_2' occurs at t_f . So:

$$\int_{c_1^{*'}}^{c'} \frac{dc'}{c_2^{*'} - c'} = \frac{k_1'}{V} \int_{t_1}^t dt$$

$$-\ln \frac{c_2^{*'} - c'}{c_2^{*'} - c_1^{*'}} = \frac{k_1'}{V} (t - t_1) \quad (\text{C.9})$$

From (C.6) and (C.9) it follows that:

$$-\ln \frac{i_2 - i}{i_2 - i_1} = \frac{k_1'}{V} (t - t_1) \quad (\text{C.10})$$

In a steady-state condition $\frac{dN'}{dt} = 0$ and equation (C.1) shows that $c' = c^{*'}$; using (C.6)

$$i = k_2' c^{*'}. \quad (\text{C.11})$$

So $i_1 = k_2' c_1^{*'}$ and $i_2 = k_2' c_2^{*'}$

Applying the assumption that Henry's law is applicable to the system:

$$c^{*'} = k_3' p' \quad (\text{C.12})$$

where k_3' is a constant for a given temperature.

Thus:

$$i_2 = k_2' c_2^{*'}. \quad (\text{C.13})$$

Predictions from Model 1:

- iii) Steady current is proportional to hydrogen partial pressure (Equation (7.20)).
- iv) Plot of $\ln \frac{i_2 - i}{i_2 - i_1}$ versus t should show a straight line of slope $-\frac{k_1'}{V}$ through the origin (according to Equation (C.10)). Note that $\frac{V}{k_1'}$ is the time constant for the curve of i versus t when a step-change is made in hydrogen partial pressure.

Model 2

Model 1 incorporated the assumption that the rate of removal of hydrogen by anodic oxidation is negligible compared with its rate of dissolution (assumption v)). This assumption has been removed from the following analysis (Model 2). A consequence of the removal of this assumption is that in the steady-state condition, where the current attains a steady value, the concentration of hydrogen in the molten tin is less than the concentration at saturation. We retain assumptions i), ii), iii), iv) and vi).

So now Equation (C.1) is modified to:

$$\frac{dN'}{dt} = k_1' (c_2^{*'}. - c') - \frac{i}{nF} \quad (\text{C.14})$$

When $c' = c'_2$, $i = i_2$ and $\frac{dN'}{dt} = 0$; note that $c'_2 < c_2^{*}$

It follows that:

$$k'_1(c_2^{*'} - c'_2) = \frac{i_2}{nF}$$

and

$$c'_2 = c_2^{*'} - \frac{i_2}{nF k'_1} \quad (\text{C.15})$$

from (C.6):

$$i_2 = k'_2 c'_2 \quad (\text{C.16})$$

Eliminating i_2 between (C.15) and (C.16):

$$c'_2 = c_2^{*'} - \frac{k'_2 c'_2}{nF k'_1} \quad (\text{C.17})$$

Rearranging:

$$c'_2 = \frac{c_2^{*'}}{\left(1 + \frac{k'_2}{k'_1 nF}\right)} \quad (\text{C.18})$$

Write:

$$w' = \left(1 + \frac{k'_2}{k'_1 nF}\right)^{-1} \quad (\text{C.19})$$

Then

$$c'_2 = w' c_2^{*'} \quad (\text{C.20})$$

By the same reasoning:

$$c'_1 = w' c_1^{*'} \quad (\text{C.21})$$

Eliminating i between (C.14) and (C.6):

$$\frac{dN'}{dt} = k'_1(c_2^{*'} - c') - \frac{k'_2 c'}{nF} = k'_1 c_2^{*'} - k'_1 c' \left(1 + \frac{k'_2}{k'_1 nF}\right)$$

Using (C.19) and (C.20) leads to:

$$\frac{dN'}{dt} = k'_1 \left(\frac{c'_2}{w'} - \frac{c'}{w'}\right) = \frac{k'_1}{w'} (c'_2 - c') \quad (\text{C.22})$$

Note that (C.1) and (C.22) are of the same form, but with the constant k'_1 replaced by $\frac{k'_1}{w}$

and c_2^{*} by c'_2 in (C.22) where c'_2 is given by (C.20).

So (C.8) becomes:

$$\frac{dc'}{dt} = \frac{1}{Vw'} k_1' (c_2' - c') \quad (\text{C.23})$$

Integrating:

$$\int_{c_1'}^{c'} \frac{dc'}{(c_2' - c')} = \frac{k_1'}{Vw'} \int_{t_1}^t dt$$

$$- \ln \frac{(c_2' - c')}{(c_2' - c_1')} = \frac{k_1'}{Vw'} (t - t_1) \quad (\text{C.24})$$

From (C.6) it follows that:

$$- \ln \frac{(i_2 - i)}{(i_2 - i_1)} = \frac{k_1'}{Vw'} (t - t_1) \quad (\text{C.25})$$

(Compare equation (C.10))

Predictions from Model 2:

These are as for Model 1, except that prediction ii) is modified to iia) as follows:

iia) A plot of $\ln \frac{i_2 - i}{i_2 - i_1}$ versus t should show a straight line of slope $-\frac{k_1'}{Vw'}$ through

the origin (according to equation (C.25)).

Note that $\frac{Vw'}{k_1'}$ is the time constant for the curve of i versus t when a step-change is made in hydrogen partial pressure.

Additional Mechanistic Theory

A further case is now considered where an inert gas, Ar, is first bubbled through the tin for sufficient time to reduce the hydrogen concentration to a value close to zero. The potential of tin is held at constant value E at which residual hydrogen, if present, undergoes anodic oxidation to water. Then, while holding the potential at this value, gas mixture of Ar/H₂ with hydrogen partial pressure p_2' is bubbled continuously, starting at time t equal to zero through the tin and the anodic current measured as a function of time.

At $t=0$, $c'=0$ and thus $i=0$ (Equation (C.6) with $c'=0$) Equation (C.14) becomes

$$\left[\frac{dN'}{dt} \right]_{t=0} = k_1' c_2'^* \quad (\text{C.26})$$

As hydrogen is supplied to the tin the concentration of hydrogen begins to increase from zero and it follows from (C.6) that

$$\frac{di}{dt} = k'_2 \frac{dc'}{dt} \quad (\text{C.27})$$

and

$$\frac{dc'}{dt} = \frac{1}{V} \frac{dN'}{dt} \quad (\text{C.7})$$

Combining (C.26), (C.27) and (C.7)

$$\left[\frac{di}{dt} \right]_{t=0} = \frac{k'_1 k'_2 c_2^{*'}}{V} \quad (\text{C.28})$$

Also from (C.12)

$$c_2^{*'} = k'_3 p'_2 \quad (\text{C.29})$$

Eliminating $c_2^{*'}$ between (C.28) and (C.29)

$$\left[\frac{di}{dt} \right]_{t=0} = \frac{k'_1 k'_2 k'_3}{V} p'_2 \quad (\text{C.30})$$

Equation (C.30) predicts that $\left[\frac{di}{dt} \right]_{t=0}$ should be proportional to p'_2 ; a plot of $\left[\frac{di}{dt} \right]_{t=0}$ vs. p'_2 is expected to reveal a slope of $\frac{k'_1 k'_2 k'_3}{V}$.

It has also been shown above that

$$i_2 = k'_2 c'_2 \quad (\text{C.16})$$

$$c'_2 = w' c_2^{*'} \quad (\text{C.20})$$

Combining these equations with (C.29):

$$i_2 = k'_2 k'_3 w' p'_2 \quad (\text{C.31})$$

Equation (C.31) predicts a straight line through the origin with slope $k'_2 k'_3 w'$ for a plot of i_2 vs. p'_2 . The ratio of the slopes of the above two plots using Equations (C.30) and (C.31) provides a value of $\frac{k'_1}{V w'}$ (see Equation (C.25)). So it should be possible to compare values of $k'_1/V w'$ determined by two different methods.

Determination of the apparent solubility of H₂ in liquid tin and the parameter w' using anodic stripping voltammetry

The development of the theoretical framework in the previous section has generated the parameter w' . This parameter expresses the balance between addition of hydrogen to the tin

via dissolution and the removal of hydrogen from the tin via anodic oxidation to water. Theory shown above postulates that w' depends upon geometric factors, applied potential and diffusion layer thickness (and hence degree of convection). Though not fundamental it is important to determine its value in order to obtain an understanding of experimentally-generated results. In broader sense this parameter will be important for the design of systems consisting of two processes: physical dissolution of the gas in the melt and electrochemical oxidation or reduction of the active gas via the liquid anode.

For the determination of w' parameter as well as hydrogen solubility three regimes of operation of LMA SOFC were proposed. The theory has been worked out for each of the regimes, which is used together with experimental data for the calculation of w' in different cells and apparent solubility of H_2 in liquid tin.

Regime 1

Consider the following operation where there are four stages (see Figure C.1). Prior to A, argon is bubbled through liquid tin for a sufficient time to reduce the concentration of hydrogen to a value close to zero and the tin electrode is held at an anodic potential E , typically -0.90 V vs. RE (air electrode); the current at A is close to zero. During the intervals A - B, B - C and C - D, hydrogen at partial pressure p'_2 is bubbled through the tin. The interval A - B is sufficiently long to allow the current to reach a steady value i_2 . During the interval B - C, of length $t_3 - t_2$, the tin electrode is switched to open circuit (OC). Then during the interval C - D, the potential of the tin electrode is held at anodic potential E , during which time the current is monitored. The period C - D is sufficiently long to allow the current to return to the steady current i_2 .

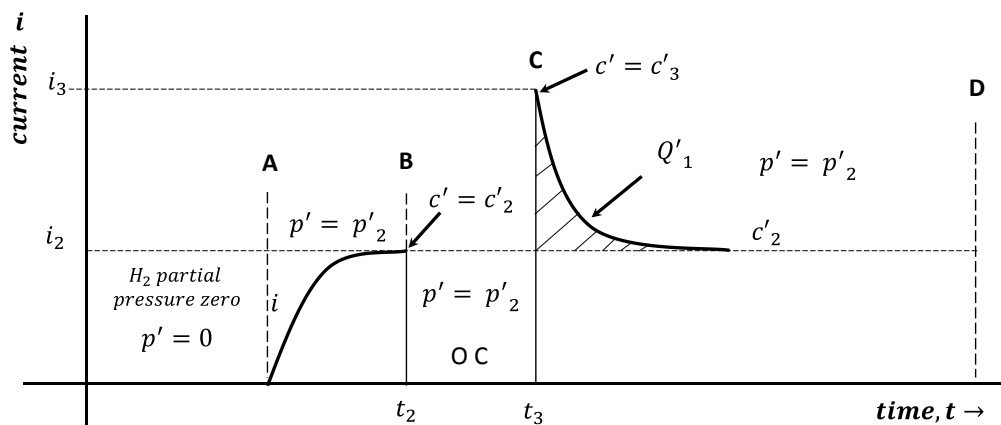


Figure C.1 Schematic of Regime 1 conditions applied to the working cell (E mode). Same hydrogen partial pressure, p'_2 is applied from A to D. Potential is held at a value E everywhere except in B - C.

From the E model steady concentration of hydrogen in the bulk is c'_2 at time t_2 :

$$c'_2 = w' c_2^* \quad (C.20)$$

From B to C (at open circuit) $i=0$, so the equation that expressed the rate of dissolution of hydrogen to the tin via and the removal of hydrogen from the tin via anodic oxidation to water was shown above:

$$\frac{dN'}{dt} = k'_1(c_2^{*'} - c') - \frac{i}{nF} \quad (\text{C.14})$$

when treated from B - C Equation (C.14) becomes:

$$\frac{dN'}{dt} = k'_1(c_2^{*'} - c') \quad (\text{C.32})$$

From previous model:

$$\frac{dc'}{dt} = \frac{1}{V} \frac{dN'}{dt} \quad (\text{C.7})$$

Using (C.32) and (C.7):

$$\frac{dc'}{dt} = \frac{1}{V} k'_1(c_2^{*'} - c') \quad (\text{C.33})$$

Integrating (C.33)

$$-\ln(c_2^{*'} - c') \Big|_{c'_2}^{c'_3} = \frac{k'_1}{V} [t]_{t_2}^{t_3}$$

$$-\ln \frac{c_2^{*'} - c'_3}{c_2^{*'} - c'_2} = \frac{k'_1}{V} (t_3 - t_2) \quad (\text{C.34})$$

This becomes using (C.34) and (C.20):

$$-\ln \frac{c_2^{*'} - c'_3}{c_2^{*'} (1 - w')} = \frac{k'_1}{V} (t_3 - t_2) \quad (\text{C.35})$$

$$-\ln \frac{1 - c'_3/c_2^{*'}}{(1 - w')} = \frac{k'_1}{V} (t_3 - t_2)$$

$$\frac{1 - c'_3/c_2^{*'}}{(1 - w')} = \exp \left\{ -\frac{k'_1}{V} (t_3 - t_2) \right\}$$

$$1 - \frac{c'_3}{c_2^{*'}} = (1 - w') \exp \left\{ -\frac{k'_1}{V} (t_3 - t_2) \right\}$$

$$\frac{c'_3}{c_2^{*'}} = 1 - (1 - w') \exp \left\{ -\frac{k'_1}{V} (t_3 - t_2) \right\}$$

$$c'_3 = c_2^{*'} \left[1 - (1 - w') \exp \left\{ -\frac{k'_1}{V} (t_3 - t_2) \right\} \right] \quad (\text{C.36})$$

Using Equation (C.20):

$$c'_3 - c'_2 = c_2^{*'} \left[1 - (1 - w') \exp \left\{ -\frac{k'_1}{V} (t_3 - t_2) \right\} - w' \right]$$

$$c'_3 - c'_2 = c_2^{*'} (1 - w') \left[1 - \exp \left\{ -\frac{k'_1}{V} (t_3 - t_2) \right\} \right] \quad (\text{C.37})$$

Note that $(t_3 - t_2)$ may be varied over a wide range.

The region from C-D is now treated. In this region, Equation (C.14) applies, i.e.:

$$\frac{dN'}{dt} = k'_1 (c_2^{*'} - c') - \frac{i}{nF} \quad (\text{C.14})$$

Furthermore invoking Equation (C.25):

$$-\ln \frac{(c'_2 - c')}{(c'_2 - c'_1)} = \frac{k'_1}{Vw'} (t - t_1) \quad (\text{C.25})$$

and replacing c' by c'_3 and t_1 by t_3 :

$$\ln \frac{(c' - c'_2)}{(c'_3 - c'_2)} = -\frac{k'_1}{Vw'} (t - t_3) \quad (\text{C.38})$$

Where from (C.37) and (C.20):

$$c'_3 - c'_2 = \frac{c_2^{*'}}{w'} (1 - w') \left[1 - \exp \left\{ -\frac{k'_1}{V} (t_3 - t_2) \right\} \right] \quad (\text{C.39})$$

Substituting for $c'_3 - c'_2$ from (C.39) into (C.38) and invoking Equation (C.6) which was derived previously as follows:

$$i = k'_2 c' \quad (\text{C.6})$$

Obtain:

$$\ln \frac{i - i_2}{i_2 \left(\frac{1 - w'}{w'} \right) \left[1 - \exp \left\{ -\frac{k'_1}{V} (t_3 - t_2) \right\} \right]} = -\frac{k'_1}{Vw'} (t - t_3) \quad (\text{C.40})$$

So

$$i - i_2 = i_2 \left(\frac{1 - w'}{w'} \right) \left[1 - \exp \left\{ -\frac{k'_1}{V} (t_3 - t_2) \right\} \right] \exp \left\{ -\frac{k'_1}{Vw'} (t - t_3) \right\} \quad (\text{C.41})$$

The charge shown by the shaded area in the diagram is given by:

$$Q'_1 = \int_0^{\infty} (i - i_2) dt = i_2 \frac{1 - w'}{w'} \left[1 - \exp \left\{ -\frac{k'_1}{V} (t_3 - t_2) \right\} \right] \times \int_{t_3}^{\infty} \exp \left\{ -\frac{k'_1}{Vw'} (t - t_3) \right\} dt \quad (\text{C.42})$$

Or

$$\begin{aligned}
 \frac{Q'_1}{i_2} &= \frac{1-w'}{w'} \left[1 - \exp \left\{ -\frac{k'_1}{V} (t_3 - t_2) \right\} \right] \\
 &\quad \times \int_{t_3}^{\infty} \exp \left\{ -\frac{k'_1}{Vw'} (t - t_3) \right\} dt \\
 &= \frac{1-w'}{w'} \left[1 - \exp \left\{ -\frac{k'_1}{V} (t_3 - t_2) \right\} \right] \\
 &\quad \times \left\{ -\left[\frac{Vw'}{k_1} \exp \left\{ -\frac{k'_1}{Vw'} (t - t_3) \right\} \right]_{t_3}^{\infty} \right\} \\
 \frac{Q'_1}{i_2} &= (1-w') \left[1 - \exp \left\{ -\frac{k'_1}{V} (t_3 - t_2) \right\} \right] \left[\frac{V}{k'_1} \right] \\
 \frac{Q'_1}{i_2} &= \frac{V(1-w')}{k'_1} \left[1 - \exp \left\{ -\frac{k'_1}{V} (t_3 - t_2) \right\} \right] \quad (C.43)
 \end{aligned}$$

Q'_1/i_2 has the units of time. Equation (C.43) is the required solution.

Regime 2

Consider the following operation where there are four stages (see Figure C.2). During the interval A – B the anodic potential is held at E , argon is flowed for sufficient time to reduce the hydrogen concentration in the molten tin and the current to a value close to zero. At B the tin electrode is then switched to open circuit and the flowing gas to an argon-hydrogen mixture with hydrogen partial pressure p'_2 for a period t_3-t_2 . At C the flowing gas is returned to 100% argon and the potential of the electrode switched to the anodic value E . The current is measured as a function of time for a time sufficient for the current to return to a value close to zero. The charge Q_2 shown as the shaded area in Figure C.2 is then calculated. Note that no hydrogen is bubbled into the tin during the period when the charge Q_2 is determined.

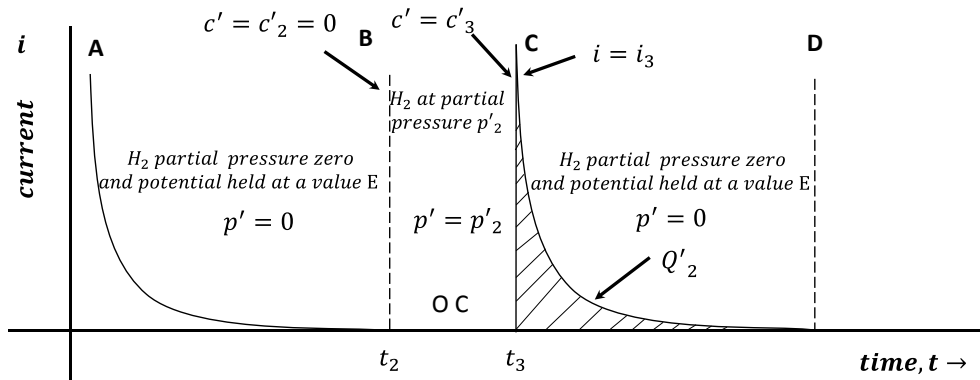


Figure C.2 Schematic of Regime 2 conditions applied to the working cell (E mode) with constant flow of argon.

For the interval B – C Equation (C.32) pertains:

$$\frac{dN'}{dt} = k'_1(c_2^{*'} - c') \quad (\text{C.32})$$

and

$$\frac{dc'}{dt} = \frac{k'_1}{V}(c_2^{*'} - c') \quad (\text{C.33})$$

Integrating (C.33):

$$\begin{aligned} -[\ln(c_2^{*'} - c')]_0^{c'_3} &= \frac{k'_1}{V} [t]_{t_2}^{t_3} \\ -\ln \frac{c_2^{*'} - c'_3}{c_2^{*'}} &= \frac{k'_1}{V} (t_3 - t_2) \end{aligned} \quad (\text{C.44})$$

Compare with (C.34)

$$\begin{aligned} -\ln \left(\frac{1 - c'_3}{c_2^{*'}} \right) &= \frac{k'_1}{V} (t_3 - t_2) \\ \frac{c'_3}{c_2^{*'}} &= 1 - \exp \left[-\frac{k'_1}{V} (t_3 - t_2) \right] \\ c'_3 &= c_2^{*'} \left[1 - \exp \left\{ -\frac{k'_1}{V} (t_3 - t_2) \right\} \right] \end{aligned} \quad (\text{C.45})$$

Compare (C.45) with (C.37). Note that w' does not appear in (C.45).

We now treat region C – D. Equation (C.14) is modified to

$$\frac{dN'}{dt} = k'_1(0 - c') - \frac{i}{nF} \quad (\text{C.46})$$

The zero in (C.46) reflects the fact that the gas composition contains no hydrogen in this region.

Eliminating i between (C.46) and (C.6):

$$\begin{aligned} \frac{dN'}{dt} &= -k'_1 c' - \frac{k'_2 c'}{nF} \\ &= -c' \left(k'_1 + \frac{k'_2}{nF} \right) \\ &= -k'_1 c' \left(1 + \frac{k'_2}{k'_1 nF} \right) \\ &= -\frac{k'_1 c'}{w'} \end{aligned}$$

Using Equation (C.7) becomes:

$$\frac{dc'}{dt} = -\frac{k'_1 c'}{Vw'} \quad (\text{C.47})$$

Compare it with (C.33)

Integrating (C.47):

$$\int_{c'_3}^{c'} \frac{dc'}{c'} = - \int_{t_3}^t \frac{k'_1}{Vw'} dt$$

$$[\ln c']_{c'_3}^{c'} = \left[-\frac{k'_1 t}{Vw'} \right]_{t_3}^t$$

$$\ln \frac{c'}{c'_3} = -\frac{k'_1}{Vw'} (t - t_3) \quad (\text{C.48})$$

Using (C.6):

$$\ln \frac{i}{i_3} = -\frac{k'_1}{Vw'} (t - t_3) \quad (\text{C.49})$$

Or

$$i = i_3 \exp \left\{ -\frac{k'_1}{Vw'} (t - t_3) \right\} \quad (\text{C.50})$$

The charge, Q'_2 , shown in the diagram is given by

$$Q'_2 = \int_{t_3}^{\infty} i dt = \int_{t_3}^{\infty} i_3 \exp \left\{ -\frac{k'_1}{Vw'} (t - t_3) \right\} dt$$

$$Q'_2 = \frac{-Vw' i_3}{k'_1} \left[\exp \left\{ -\frac{k'_1}{Vw'} (t - t_3) \right\} \right]_{t_3}^{\infty} = \frac{Vw' i_3}{k'_1} \quad (\text{C.51})$$

Writing $c_2^* = c'_2/w'$ equation (C.45) becomes:

$$c'_3 = \frac{c'_2}{w'} \left[1 - \exp \left\{ -\frac{k'_1}{V} (t_3 - t_2) \right\} \right] \quad (\text{C.52})$$

Applying (C.6), Equation (C.52) becomes:

$$i_3 = \frac{i_2}{w'} \left[1 - \exp \left\{ -\frac{k'_1}{V} (t_3 - t_2) \right\} \right] \quad (\text{C.53})$$

Substituting for i_3 in (C.51)

$$\frac{Q'_2}{i_2} = \frac{V}{k'_1} \left[1 - \exp \left\{ -\frac{k'_1}{V} (t_3 - t_2) \right\} \right] \quad (\text{C.54})$$

Compare (C.54) with (C.43)

Regime 3

This case is included for completeness. However no experiments are performed to support theory developed in this section (for Regime 3). Figure C.3 describes the regime which is a combination of the previous two regimes.

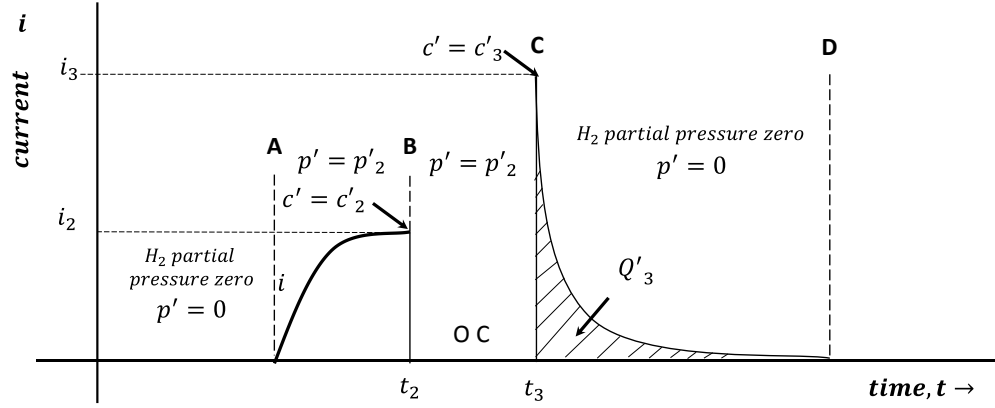


Figure C.3 Schematic of Regime 3 conditions applied to the working cell (E mode) with constant flow of argon. Potential is held at a value E everywhere except in B-C.

Prior to A argon is bubbled through tin for a sufficient time to reduce the concentration of hydrogen to a value close to zero and the tin electrode is held at an anodic potential E , typically -0.90 V, with respect to an air electrode; the current at A is close to zero. During the intervals A - B, B - C, hydrogen at partial pressure p_2 is bubbled through the tin. The interval A - B is sufficiently long to allow the current to reach a steady value i_2 . During the interval B - C, of length $t_3 - t_2$, the tin electrode is switched to open circuit. At C the flowing gas is returned to 100% argon and the potential of the electrode switched to the anodic value E . The current is measured as a function of time for a time sufficient for the current to return to a value close to zero. The charge Q_3 , shown as the shaded area in Figure C.3 is then calculated. Note that no hydrogen is bubbled into the tin during the period when the charge Q_3 is determined.

Following Regime 1 we have the hydrogen concentration c'_3 at C given by (C.36):

$$c'_3 = c_2^* \left[1 - (1 - w') \exp \left\{ -\frac{k'_1}{V} (t_3 - t_2) \right\} \right] \quad (\text{C.36})$$

For the Region C - D Equation (C.51) applies and leads to

$$Q_3 = \frac{Vw'i_3}{k'_1} \quad (\text{C.55})$$

The next equation ((C.17)) has been derived previously:

$$c'_2 = c_2^* - \frac{k'_2 c'_2}{nFk'_1}$$

Using (C.36), (C.6) and (C.20):

$$i_3 = \frac{i_2}{w'} \left[1 - (1 - w') \exp \left\{ -\frac{k'_1}{V} (t_3 - t_2) \right\} \right] \quad (\text{C.56})$$

(Compare it to Equation (C.53))

Note that i_3 in (C.51) $\neq i_3$ in (C.55). Substituting for i_3 from (C.56) into (C.55):

$$Q'_3 = \frac{Vi_2}{k_1} \left[1 - (1 - w') \exp \left\{ -\frac{k'_1}{V} (t_3 - t_2) \right\} \right]$$

Or

$$\frac{Q'_3}{i_2} = \frac{V(1 - w')}{k_1} \left[1 - \exp \left\{ -\frac{k'_1}{V} (t_3 - t_2) \right\} \right] + \frac{w'V}{k_1} \quad (C.57)$$

Comparing (C.57) and (C.43) it is noted that they are identical apart from the additional term $\frac{w'V}{k_1}$ in (C.57).

The important equations in the above sections are those that allow interpretation of the coulombic charge under the final parts of the regimes, i.e. C – D. These are as follows:

$$\text{Regime 1} \quad \frac{Q'_1}{i_2} = \frac{V(1 - w')}{k_1} \left[1 - \exp \left\{ -\frac{k'_1}{V} (t_3 - t_2) \right\} \right] \quad (C.43)$$

$$\text{Regime 2} \quad \frac{Q'_2}{i_2} = \frac{V}{k_1} \left[1 - \exp \left\{ -\frac{k'_1}{V} (t_3 - t_2) \right\} \right] \quad (C.54)$$

$$\text{Regime 3} \quad \frac{Q'_3}{i_2} = \frac{V(1 - w')}{k_1} \left[1 - \exp \left\{ -\frac{k'_1}{V} (t_3 - t_2) \right\} \right] + \frac{w'V}{k_1} \quad (C.57)$$

Determination of the parameter w'

The development of this theoretical framework has generated the parameter w' . This parameter expresses the balance between addition of hydrogen to the tin via dissolution and the removal of hydrogen from the tin via anodic oxidation to water.

For a given value of $(t_3 - t_2)$ and the same p'_2 value (and i_2 value) (C.43) and (C.54) show that:

$$w' = 1 - \frac{Q'_1}{Q'_2} \quad (C.58)$$

The given value of $(t_3 - t_2)$ may be then varied and the w' value determined for each case. The w' value would be expected to be independent of $(t_3 - t_2)$.